Synergy joint degree between the Departments of Civil Engineering of the University of Strathclyde and the University of Glasgow

Numerical modelling of coupled behaviour in unsaturated soils

A Thesis presented for the Degree of Doctor of Philosophy

by

Martí Lloret Cabot

2011

Supervision at Strathclyde University:

Dr Marcelo Sánchez and Dr Minna Karstunen

Supervision at Glasgow University:

Prof Simon Wheeler

En primer lloc, a la paciència,

la mare de la ciència;

però també,

al pare i a la mare,

a en Ferran i la C.,

a en Jordi, a l'Arnau i la V., a en Marc i l'A., a l'Anna i en M. i a en Roger.

This thesis is the result of the author's original research. It has been composed by the author and has not been previously submitted for examination which has led to the award of a degree.

Signed:

Date:

ABSTRACT

Unsaturated soils are present in a wide range of geotechnical applications such as slopes, highways or earth dams, in addition to many other geo-environmental applications such as underground disposal of radioactive waste or landfills. Despite a significant number of improvements in understanding unsaturated soil behaviour over the last five decades, there are still several aspects to be addressed and to be better understood, including in the areas of constitutive modelling, development of experimental procedures and improvement of numerical techniques.

This work concentrates on two of these aspects: constitutive modelling of unsaturated soils accounting for the coupling between mechanical and water retention response; and associated numerical and computational aspects employed to solve engineering problems involving unsaturated soil mechanics.

Wheeler et al. (2003) proposed a coupled elasto-plastic constitutive model for the mechanical and water retention behaviour of unsaturated soils and this model constitutes the basis of the work developed within this thesis. For isotropic stress states this coupled model employs as stress state variables mean Bishop's stress p^* and modified suction s^*. In the model, plastic volumetric strains occur when the stress state reaches a *LC* yield curve and plastic changes of degree of saturation S_r occur when the stress state reaches a *SD* or *SI* yield curve. Coupled movements of the yield curves represent the influence of plastic changes of degree of saturation on mechanical behaviour and the influence of plastic volumetric strains on water retention behaviour.

According to this constitutive model, during many types of loading or wetting under isotropic stress states the soil state will ultimately arrive at the corner between the *LC* and *SD* yield curves. Analysis of the model suggests that such states should fall on a unique planar normal compression surface in $v:lnp^*:lns^*$ space and also on a second unique planar surface in $S_r:lnp^*:lns^*$ space. The experimental results of Sivakumar (1993) from constant suction isotropic loading of compacted speswhite kaolin are presented in these spaces, and are shown to lie on planar surfaces, as predicted by the model. Presenting experimental normal compression results in this way gives an ideal method for determining the values of the key soil parameters k_1, k_2, λ_s and κ_s in the model.

A simple extension of the Wheeler et al. (2003) model to the stress conditions of the triaxial test, by including the role of deviator stress q, has been proposed by Lloret et al.

(2008b) and Raveendiraraj (2009). According to this extended model, critical states will commonly occur at the intersection of the *LC* yield surface and the *SD* yield surface, and such critical states should fall on a second pair of unique planar surfaces in the $v{:}ln p^*{:}ln s^*$ and $S_r{:}ln p^*{:}ln s^*$ spaces. The experimental critical state data of Sivakumar (1993) have been plotted in these spaces and the results obtained are presented and discussed.

The new constitutive model has been extended to general 3D stress conditions and generalised stress-strain relationships required for numerical integration of the model are presented. Furthermore, 3D extended functions to identify the different elasto-plastic mechanisms of the model are proposed. A partial validation of this extended model is also presented using the experimental results of Sivakumar (1993).

Two strain-driver algorithms for the integration of the generalised model are presented including first and second order error schemes. The complete formulation of these explicit algorithms is described and the computed results from both integration schemes is compared and discussed.

Finally, the generalised fully coupled constitutive model has been implemented within the finite element program CODE_BRIGHT (Olivella et al., 1996) to solve boundary value problems involving unsaturated soil. The performance of the new implemented model is analysed and discussed by considering application to a boundary value problem involving wetting of a cylindrical soil specimen.

ACKNOWLEDGEMENTS

First of all I would like to thank *Synergy* as this scheme offered me the possibility to enjoy a joint supervision between the University of Strathclyde and the University of Glasgow. Next, I would like to thank Marcelo Sánchez for his supervision at Strathclyde, which is essentially related to the second half of this document. He encouraged and convinced me to study within the area of unsaturated soils. Also his continued interest and perseverance have been crucial to finally achieving the aims initially proposed within the awarded Synergy project. I would also like to give a very special thanks to Simon Wheeler who gave me supervision at Glasgow University. His ability in making simpler complex concepts has been undoubtedly helpful during all of this work. Also his clarity in explaining has been reflected on my current understanding of unsaturated soil behaviour. I would also like to acknowledge the crucial support of Minna Karstunen who took on a supervisory role after Marcelo's move to Texas. Thanks to her and Marcelo I also became involved with the Geo-Excel project and spent several months at the Universidade Federal de Pernambuco (UFPE) in Recife, Brazil. From UFPE I would especially like to thank Leonardo Guimaraes for his support and valuable discussions during the final stages of my PhD research. I would also like to thank the computational geomechanics group and, in particular, Igor, Julliana and Nayra.

Thanks to the *Mac Roberston* scholarship I had the possibility to visit A&M Texas University in College Station, in Texas, USA. In College Station I was able to meet with my supervisor Marcelo and we were able to finalise the fundamental final part of this research. I would also like to mention in particular the support and help received from Giovanna Biscontin.

The MUSE (Mechanics of Unsaturated Soils for Engineering) project gave me the opportunity to interact with people of several European universities including, Durham University in the UK, Università di Trento in Italy, Ecole Nationale des Ponts et Chaussées (ENPC) in France, Universitat Politècnica de Catalunya (UPC) in Spain and Università di Napoli “Federico II” in Italy. From UPC in Barcelona, I would like to mention and thank Enrique Romero for his interesting discussions on the experimentally observed wetting-collapse induced behaviour, a fundamental feature of unsaturated soils; and also for sharing some of the experimental results presented in this work. Also from the ENPC I would like to thank the organizers Vincenzo De Gennaro, Jean-Michel Pereira and Pierre

Delage for inviting me to present my research at the 3rd Workshop of Young Doctors in Geomechanics (WHYDOC, 08).

A special mention must go to the PhD students and researchers at the University of Strathclyde who have shared this journey with me: Gráinne, Marcín, Caroline, Alvis, Siva, Antoine, Daniela, Heather, Marco and Harald. I would also like to thank the post-doctoral fellow Manoel, as his support was crucial in helping me to get started with the programming. I am particularly grateful to him and to Gráinne for the many discussions we had on unsaturated soils and many other research topics. In this regard, I would like to thank here my friend Boris.

I would also like to mention the support received from all my friends in Glasgow for their patience in my rather repetitive talks on unsaturated soils during these years. A special mention goes to Jordi, Dani, Gelu, Pau, Ana, Olaya, Marta, Juan Carlos, Ravi, Javi, Xavi, Jose and Graham.

Finally, I would like to thank my family for their continual support and understanding during my PhD studies: my grandmothers, *la iaia i l'àvia*, my parents, Jordi and Anna Maria, my large number of brothers Ferran, Jordi, Arnau, Marc, and Roger and, especially, my sister Anna who helped me with the preparation of the AutoCAD drawings presented in this work.

Table of contents

LIST OF SYMBOLS

$\bar{\mathbf{B}}$	Generalised matrix containing hardening rules and couplings
$\boldsymbol{D}^{e}$	Elastic matrix
$\boldsymbol{D}^{ep}$	Elasto-plastic matrix
$\boldsymbol{D}^{\star}_{e}$	Generalised elastic matrix
$\boldsymbol{D}^{\star}_{ep}{}^{LC}$	Generalised elasto-plastic matrix for yielding on the LC yield surface alone
$\boldsymbol{D}^{\star}_{ep}{}^{\beta}$	Generalised elasto-plastic matrix for yielding on the SD or SI yield surface alone
$\boldsymbol{D}^{\star}_{ep}{}^{LC+\beta}$	Generalised elasto-plastic matrix for simultaneous yielding on the LC and the SD or SI yield surfaces
e	Void ratio
f	Yield surface
F_{LC}, LC	Loading Collapse yield surface of the Wheeler et al. (2003) model
F_{SD}, SD	Suction Decrease yield surface of the Wheeler et al. (2003) model
F_{SI}, SI	Suction Increase yield surface of the Wheeler et al. (2003) model
f_1	Conical surface delimiting the boundary between stress paths involving yielding on the SI yield surface alone and those involving simultaneous yielding on SI and LC
f_2	Conical surface delimiting the boundary between stress paths involving yielding on the LC yield surface alone and those involving simultaneous yielding on SI and LC
f_3	Conical surface delimiting the boundary between stress paths involving yielding on the LC yield surface alone and those involving simultaneous yielding on SD and LC
f_4	Conical surface delimiting the boundary between stress paths involving yielding on the SD yield surface alone and those involving simultaneous yielding on SD and LC
g	Plastic potential
G	Elastic shear modulus

$g(\theta)$	Function depending on the Lode angle
H	Plastic modulus
$d\boldsymbol{h}$	Vector containing increments of the hardening parameters
$\boldsymbol{I}$	Identity matrix
$\boldsymbol{i}_{\alpha}^{i}$	Non-advective mass flux (i=w, a: α=l, g) ; w is water, a is air, l is liquid and g is gas
J	Second invariant of the Bishop's stress tensor
$\boldsymbol{j}_{\alpha}^{i}$	Total max flux of i-species in α-phase with respect to a fixed reference
$\boldsymbol{j'}_{\alpha}^{i}$	Total max flux of i-species in α-phase with respect to the solid phase
$\boldsymbol{K}_{\alpha}$	Permeability tensor (α=l,g)
$\boldsymbol{k}$	Intrinsic permeability tensor
$k_{r\alpha}$	α phase relative permeability (α=liquid, gas)
K	Bulk modulus
$\boldsymbol{m}$	Auxiliary vector $\mathbf{m}^{T}=(1,1,1,0,0,0)$
$\boldsymbol{m_{LC}}$	Auxiliary vector for the LC flow rule in the Wheeler et al. (2003) model
$\boldsymbol{m_{\beta}}$	Auxiliary vector for the SD or SI flow rule in the Wheeler et al. (2003) model
M	Gradient of the Critical State Line (CSL)
n	Porosity
p	Mean stress
p'	Mean effective stress
$\overline{p}$	Mean net stress
p^{*}	Mean Bishop's stress
p_{0}^{*}	Hardening parameter defining the location of the *LC* yield surface
q	Deviatoric stress

s	Matric suction
s^*	Modified suction
s_t	Total suction
s_D^*	Hardening parameter defining the location of the *SD* yield surface
s_I^*	Hardening parameter defining the location of the *SI* yield surface
S_r, S_I	Degree of saturation
dS_r^e	Elastic increment of degree of saturation
dS_r^p	Plastic increment of degree of saturation
T	Temperature
t	Time
$\boldsymbol{u}$	Solid displacement vector
u_y	Vertical displacements
u_x	Horizontal displacements
u_a	Pore air pressure
u_w	Pore water pressure
v	Specific volume
w	Water content
dW	Increment of work input
β	Parameter indicating SD or SI yield surface
Γ^*	Soil constant related to the critical states planar surface predicted by the Wheeler et al. (2003) model for simultaneous yielding on the LC and SD yield surfaces in the v:lnp*:lns* space
δ_{ij}	Kronecker delta
χ	Parameter related to degree of saturation in Bishop's (1959)

χ^*	Soil constant related to the isotropic normal compression planar surface predicted by the Wheeler et al. (2003) model for simultaneous yielding on the LC and SD yield surfaces in the S_r:lnp*:lns* space
$d\chi$	Plastic multiplier
$d\chi_{LC}$	Plastic multiplier associated with the LC
$d\chi_{SD}$	Plastic multiplier associated with the SD
$d\chi_{SI}$	Plastic multiplier associated with the SI
$d\chi_{LC}^{LC+\beta}$	Plastic multiplier associated with plastic changes of volumetric strains when simultaneous yielding is active
$d\chi_{\beta}^{LC+\beta}$	Plastic multiplier associated with plastic changes of degree of saturation when simultaneous yielding is active
$d\boldsymbol{\chi}$	Vector containing plastic multipliers associated with the mechanism active
ψ	Water potential
Ψ^*	Soil constant related to the critical states planar surface predicted by the Wheeler et al. (2003) model for simultaneous yielding on the LC and SD yield surfaces in the S_r:lnp*:lns* space
$d\varepsilon_{ij}$	Strain increment tensor
$d\varepsilon_1$, $d\varepsilon_2$, $d\varepsilon_3$	Principal strains
$d\varepsilon_v$	Increment of volumetric strain
$d\varepsilon_q$	Increment of shear strain
$d\varepsilon_v^e$	Elastic increment of volumetric strain
$d\varepsilon_q^e$	Elastic increment of shear strain
$d\varepsilon_v^p$	Plastic increment of volumetric strain
$d\varepsilon_q^p$	Plastic increment of shear strain
$d\tilde{\varepsilon}_{ij}^*$	Increment of generalised strains

γ_d	Dry unit weight
η	Stress ratio
κ	Gradient of elastic swelling lines in the v:lnp* plane (in the Wheeler et al. (2003) model)
κ_s	Gradient of elastic scanning lines in the S_r:lns* plane (in the Wheeler et al. (2003) model)
k_1, k_2	Coupling parameters in the Wheeler et al. (2003) model
λ	Conventional gradient of the saturated normal compression line
λ_s	Elasto-plastic gradient of the main drying or wetting curves in the in the S_r:lns* plane in the Wheeler et al. (2003) model
λ^*, k_1^*	Gradients of the isotropic normal compression (and critical states) planar surfaces predicted by the Wheeler et al. (2003) model for simultaneous yielding on the LC and SD yield surfaces in the v:lnp*:lns* space
λ_s^*, k_2^*	Gradients of the isotropic normal compression (and critical states) planar surfaces predicted by the Wheeler et al. (2003) model for simultaneous yielding on the LC and SD yield surfaces in the S_r:lnp*:lns* space
μ_w	Water viscosity
N^*	Soil constant related to the isotropic normal compression planar surface predicted by the Wheeler et al. (2003) model for simultaneous yielding on the LC and SD yield surfaces in the v:lnp*:lns* space
θ	Lode's angle
ρ_s	Solid density
ρ_α	Mass of α-phase per unit of volume of α-phase (α=l, g)
σ_{ij}	Total stress tensor
σ_1, σ_2, σ_3	Principal total stresses
σ_{ij}'	Effective stress tensor
σ_1', σ_2', σ_3'	Principal effective stresses

$\bar{\sigma}_{ij}$	Net stress tensor
$\bar{\sigma}_1$, $\bar{\sigma}_2$, $\bar{\sigma}_3$	Principal net stresses
σ_{ij}^*	Bishop's stress tensor
σ_1^*, σ_2^*, σ_3^*	Principal Bishop's stresses
$d\tilde{\sigma}_{ij}^*$	Increment of generalised stresses
υ	Poisson's ratio
BBM	Barcelona Basic Model
CSL	Critical State Line
H-M	Hydro-Mechanical
MCC	Modified Cam Clay
TOL1	Tolerance for the intersection(s)
TOL2	Tolerance for the drift correction method
3D	Three dimensional

Chapter 1

INTRODUCTION AND BASIC DEFINITIONS

1. Introduction and basic definitions

1.1. Background and objectives of the research project

Basic definitions

Soils are typically modelled as multiphase porous media. When the pores, or spaces between the solid particles, are fully filled with liquid the soil is referred to as saturated and when these voids are partially filled with liquid and partially filled with gas the soil is referred to as unsaturated. In general the liquid present in the soil is water while the gas phase is typically air. There are, however, many other examples in nature in which the fluids between the particles are not only water and air but a mixture of other fluids such as oil or gaseous hydrocarbons. An equivalent general framework to that used for unsaturated soils may also be applied to describe these deformable multiphase systems, after including the appropriate constitutive relationships of the fluids and solids involved.

The presence of air between the soil particles adds complexity to classical soil mechanics problems where the soil is typically considered as fully saturated. In saturated cases, when describing the observed behaviour, it is not necessary to explicitly characterise the amount of water present in the soil pores as it occupies all the voids and, therefore, it is known by knowing the volume of pores. In unsaturated soils, however, it is important to characterise the amount of water between the particles because it may influence the unsaturated soil behaviour. There are a number of physico-chemical phenomena involved in the capacity of soils to retain water in the pore space; such as: surface tension phenomena (and associated capillary effects); water adsorption; double layer phenomenon; and other processes occurring at soil particle level. This thesis, however, will mainly focuses on the effect of capillary phenomenon on unsaturated soil behaviour.

The water retention behaviour describes the amount of water present in the soil by relating the water content (or degree of saturation) and the matric suction (i.e. pore air pressure minus pore water pressure). This relationship is intimately linked with the mechanical behaviour which relates stresses and strains including shear strength and volume change. More precisely, the degree of saturation (in addition to suction) influences the mechanical behaviour because it describes the number of inter-particle contacts affected by “meniscus water bridges”. These meniscus water bridges, are formed around particle contacts when soil is unsaturated and have an stabilising effect on the soil skeleton that is lost when an individual void is flooded with water (“bulk water”). On the other hand, the volumetric strains (mechanical behaviour) also influence the water

retention behaviour essentially through the dimensions of the voids. The size and volume of the voids is affected when stresses change and this variation has a direct influence on the water retention behaviour. It is fundamental to appropriately describe these couplings (or interactions) between mechanical and water retention behaviour for a proper characterisation of the unsaturated soil behaviour. This is generally achieved with the formulation of a constitutive model which expresses the basic phenomenological mechanisms involved in the physical system analysed. The formulation of a constitutive model is typically based on experimental observations, which are also employed in the validation process by comparing the model results with those measured in the laboratory.

In general, to carry out the validation of a constitutive model, it is required to previously integrate the model. This refers to the development of the mathematical equations expressing the unknown increments (typically increments of stresses and increments of degree of saturation) in terms of the known ones (typically increments of strains and increments of suction). This is achieved by programming an algorithm of the integrated constitutive model. A verification process, such as comparing the output with corresponding analytical solutions, is required to confirm correct implementation of the constitutive model. Then, to analyse practical engineering problems, it is necessary to include this algorithm into a numerical tool capable of solving non-linear initial/boundary value problems, such as software using the finite element method.

Occurrence and understanding of unsaturated soils

The unsaturated condition of the soil is present in many civil engineering constructions as it is the common condition of the soil on the surface above the water table, where most of the engineering structures interact. Other significant examples in civil engineering where unsaturated soil mechanics is relevant involve those construction projects in which compacted soil is used as fill material such as embankments, behind retaining walls or beneath foundations. Unsaturated soils are also present in a wide range of geotechnical applications such as slope stability analysis, landslides, highways, railways or earth dams, in addition to many other geo-environmental applications such as underground disposal of radioactive waste, ground energy systems, hydro-chemico-mechanical behaviour of landfills or analysis of contaminant transport above the water table level. It is, therefore, important to understand the behaviour of the soil when not fully saturated and to take it into account in the project design, during the construction stage and also during the life of the civil structure, in order to better protect constructions from potential risks. In general, the soil below the water table level is saturated while the soil above is under the effect of capillary pressures. However, the location of the water table level changes with climate or

weather, generally rising during wet seasons and lowering during drought periods. This variability, which has been more frequently observed lately, also affects soil behaviour. It is, then, important to improve our current understanding of these mechanisms influencing soil response, in order to determine their relevance on the design/construction/life-time stages of a civil engineering structure.

The importance and interest of unsaturated soil mechanics is also reflected in these last five decades of study. Significant improvements have been made over this period and a general understanding of unsaturated soil behaviour has been achieved. However, there are still several aspects to be addressed and to be better understood, including in the areas of constitutive modelling, development of experimental procedures, improvement of numerical techniques and engineering applications.

In particular, this work concentrates on two complementary aspects. On the one hand, constitutive modelling of unsaturated soils accounting for the observed coupling between mechanical and water retention response; and, on the other hand, on numerical techniques and computational issues associated with the solution of engineering problems involving unsaturated soil mechanics.

Objectives of the thesis

The primary aims of this research were as follows:

- To extend to 3D stress states the fully coupled constitutive model proposed by Wheeler et al. (2003) for isotropic stress conditions, and to extend the validation of the model by comparison against existing experimental data.
- To develop the incremental relationships of the state variables for the numerical integration of the generalised constitutive model.
- To propose an integration algorithm of the 3D coupled constitutive model and ensure its accuracy, robustness and efficiency by verifying it against analytical solutions.
- To implement this algorithm into an existing finite element program (CODE_BRIGHT, Olivella et al., 1996) for its use in the analysis of boundary value problems in geotechnical engineering.

As a consequence of the research carried out during this project the following objectives were also achieved:

- Development of the mathematical relationships predicted by the model for isotropic normal compression states and their validation against the experimental results presented in Sivakumar (1993).

- Development of the mathematical relationships predicted by the extended model for critical states and their validation by comparing them with the experimental data provided in Sivakumar (1993).

- Proposal of a formal methodology to determine from experimental test results the values of the soil parameters employed in the Wheeler et al. (2003) constitutive model.

1.2. Layout of the thesis

This current Chapter 1 is intended to provide a very general background describing the basic ideas behind the research, which are essential for the subsequent development of the thesis. There is also a brief description of the objectives along with the following layout of the document.

Chapter 2 of the thesis goes deeper into some fundamental aspects involved when modelling unsaturated soil behaviour. A review is presented highlighting the key advances and main improvements achieved over five decades of study of unsaturated soil mechanics. More precisely, this part focuses on mechanical behaviour, water retention behaviour and couplings observed between both. Following these descriptions, a detailed overview of the fully coupled constitutive model proposed by Wheeler et al. (2003) for isotropic stress states is also given, emphasising its most important contributions in comparison with prior existing models of unsaturated soils. Some of the complexities arising from the use of this constitutive model as the mathematical framework to be generalised, integrated and implemented into a finite element program, are initially discussed in this part of the document and are further illustrated within the following chapters.

A further exploration of this constitutive model has led to a separate second part of this Chapter 2, in which two normal compression relationships predicted by the model are developed. The proposed mathematical expressions are then compared and analysed with the isotropic normal compression experimental results shown in Sivakumar (1993). This analysis is carried out in the semi-log spaces S_r:lns^*:lnp^* and v:lnp^*:lns^* where S_r is the degree of saturation, v is the specific volume, p^* is the mean Bishop's stress (mean net stress plus degree of saturation times suction) and s^* is the modified suction (suction

times porosity). It is also shown in this second part of Chapter 2, that this form of plotting provides an ideal methodology for the determination of the values of the soil parameters of the Wheeler et al. (2003) model from experimental test data. It is important to mention here that this second part of Chapter 2 is an original contribution of the author, not included in the original publication of Wheeler et al. (2003).

Chapter 3 gives a very basic introduction to some of the most fundamental aspects of classical plasticity theory. Several of these aspects are subsequently applied in developing the elasto-plastic stress-strain and water retention relationships for isotropic stress conditions, employing the constitutive model described in Chapter 2. These relationships are then used to formulate a pair of stress-driver incremental subroutines. In one of them, the increments of Bishop's stress and the increments of modified suction are the inputs; while in the other, the inputs are increments of mean net stress and increments of matric suction. Both of these stress-driver algorithms are employed to analyse the computed response for elastic behaviour, elasto-plastic behaviour with only one plastic mechanism active and elasto-plastic behaviour with two plastic mechanisms acting simultaneously.

Chapter 4 initially presents a brief introduction of the well-known critical state models for saturated soils. This critical state framework is then used to propose a possible extension of the Wheeler et al. (2003) model to triaxial stress states. From this extended version of the model, a pair of critical state relationships are developed of similar form to the normal compression expressions shown in Chapter 2. These relationships are then analysed and compared in the same semi-log spaces considered in Chapter 2 with the experimental data provided in Sivakumar (1993) at critical states.

Chapter 5 proposes a 3D version of the fully coupled constitutive model of Wheeler et al. (2003). Extending the ideas developed within Chapter 3, this Chapter 5 provides the generalised stress-strain relationships required for the numerical integration of the model along with the 3D extended functions identifying the different elasto-plastic domains. A partial validation of this extended model is finally presented using the experimental results shown in Sivakumar (1993).

Chapter 6 proposes two strain-driver algorithms for the integration of the generalised model. The complete formulation of these explicit algorithms is presented discussing some of their relevant computational aspects. Also a comparison of the computed performance between both integrations schemes is included at the end of the chapter.

Chapter 7 starts with a brief introduction of the existing finite element program CODE_BRIGHT (Olivella et al., 1996) including a very general description of the governing equations involved. This chapter also describes the modifications required within this program to include the strain-driver (i.e. increments of strains and increments of suction are the *known* or *driving* variables) type algorithms presented in Chapter 6. A case study using the new model implemented is analysed and discussed at the end of the chapter.

Chapter 8 presents the conclusions from the research carried out and makes recommendations for further future research.

Chapter 2

MECHANICAL AND WATER RETENTION BEHAVIOUR IN UNSATURATED SOILS

2. Mechanical and water retention behaviour in unsaturated soils

This chapter contains two major parts. A general overview of the most important aspects of unsaturated soil mechanics is given first; focussing on the advances made in understanding and modelling of the mechanical response, the water retention behaviour and the observed couplings between both. A detailed description of a constitutive model capable of considering these couplings within a single framework (Wheeler et al., 2003) is also given in this part. The second part covers the development of a set of normal compression relationships formulated on the basis of the mentioned constitutive model. The proposed mathematical expressions are then partially validated with the experimental data shown in Sivakumar (1993). This analysis is carried out in the semi-log spaces S_r:$ln s^*$:$ln p^*$ and v:$ln p^*$:$ln s^*$ where S_r is the degree of saturation, v is the specific volume, p^* is the mean Bishop's stress (mean net stress plus degree of saturation times suction) and s^* is the modified suction (suction times porosity). This form of plotting the results provides an ideal methodology for determining the values of some of the key parameters in the Wheeler et al. (2003) model from experimental data.

2.1. Introduction

The unsaturated condition prevails in many engineering problems of practical interest. To tackle properly such problems it is crucial to develop a good understanding of the influence of the different phases (i.e. liquid, gas and solid) present in the soil on the mechanical, retention and hydraulic behaviour of unsaturated soils. Perhaps the main complexity associated with the description of unsaturated soil behaviour comes from the strong interaction between the mechanical and the retention behaviour. Changes in the amount of water in the pore space are mainly controlled by fluid (i.e. water and air) pressure changes and also by the mechanical problem via changes of the pore volume (i.e. void ratio). Deformations of the soil mass depend not only on stress changes, but also on changes of retention variables, such as fluid pressures and degree of saturation.

Understanding properly the mechanical response, the water retention behaviour and interaction between both is, therefore, an essential step for a comprehensive description of unsaturated soil behaviour. The following sections are intended to provide a description of these concepts, establishing a basis to better understand the subsequent description of a fully coupled constitutive model (Wheeler et al., 2003) for unsaturated soils.

2.2. Phases in unsaturated soils

A fundamental and basic aspect when modelling unsaturated soils is the identification of the different phases (and interactions between them) acting in a representative volume of soil. In general, soil is modelled as a multiphase porous media where liquid, gas and solid are the three phases typically considered. As illustrated in Figure 2-1, the liquid phase may comprise, in general, free (or pore) water, dissolved air and dissolved salts. The gas phase comprises dry (free) air and water vapour, and the solid phase is composed of solid particles and adsorbed water. A brief discussion on each phase, describing their different components is given below to illustrate some of the complexity associated with unsaturated soils. Also the different interactions between phases and some of the major consequences on constitutive modelling are highlighted.

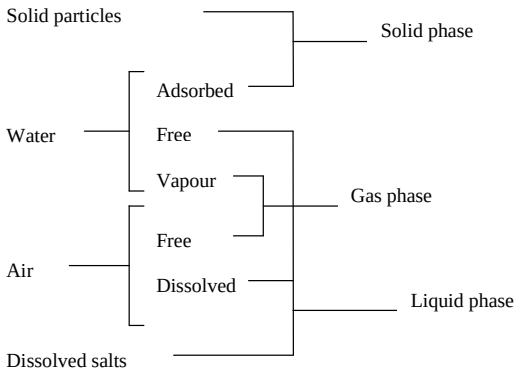

Figure 2- 1 Principal components of each phase in unsaturated soils (Yoshimi and Osterberg, 1963).

2.2.1. Solid phase

The soil particles comprise most of the solid phase and their characterisation is fundamental to understand soil behaviour. However, the characteristics of the soil particles may vary considerably. Properties such as their size and geometry, shape, mineralogy, chemistry or crystallography, may be essential in describing soil behaviour. Examples of this importance include the influence on macroscopic behaviour of the particle electric charge, its ability to adsorb cations and the variation of the diffuse double layer (Josa, 1988).

Clay minerals fractions, even occurring in small quantities, may have a significant influence on the overall behaviour of soil. Knowledge of their distribution and disposition is therefore important, as fabric affects the conditions of the water in the soil. More precisely, the mineralogical composition of the soil particles influences the adsorbed water and the internal geometry of the pore spaces controls the capillary water (Alonso et al., 1987). A possible classification of fabric cited in Alonso et al. (1987) is the following one proposed

by McGown and Collins (1975) based on Scanning Electron Microscopy (*SEM*) of natural soils. According to their work, the description of micro-fabric can be based on three types of forms: *elementary particle arrangements*, *particle assemblages* and *pore spaces* (see Figure 2-2).

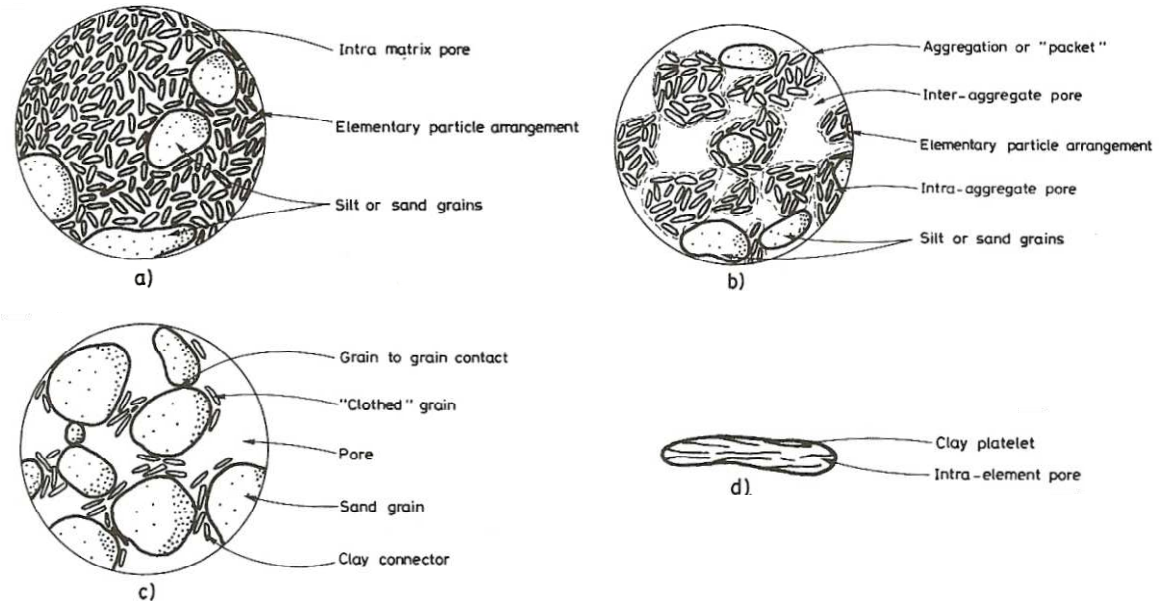

Figure 2- 2 Types of microfabric: a) clay matrix predominantly integrated by elementary particle arrangements of clay platelets and few grains of silt or sand; b) microfabric of clay predominantly integrated by aggregations of elementary particle arrangements; c) sand or silt matrix with clay connectors between individual grains; d) elementary particle arrangement in parallel configuration (Alonso et al., 1987).

The dominant components in expansive soils are the elementary clay arrangements and, in contrast, grain arrangements (often with clay particles and connectors) are typically observed in collapsible soils (Alonso et al., 1987). The particle assemblages are grouped in arrays of elementary particle configurations (*aggregations* when a grain-like configuration is formed, *matrices* if a three-dimensional structure is observed and *connectors* in the case of the configuration illustrated in Figure 2-2c). An interesting feature considered in this classification is that it allows the possibility of including different pore populations. Large pores observed between grains or packets (commonly referred to as *inter-aggregate* pores), and small pores comprising pore spaces between clay particles inside the packets which are typically referred to as *intra-aggregate* pores. This bi-modal distribution is commonly observed in compacted soil samples compacted dry of optimum whereas samples compacted wet of optimum exhibit a uni-modal pore size distribution (Juang and Holtz, 1986). This is important because different fabrics (i.e. uni-modal and bi-modal pore size distributions) produced during compaction wet or dry of optimum can significantly influence the mechanical behaviour of soils (Raveendiraraj, 2009). It is also

important in order to understand the water retention behaviour, as soil fabric has a significant influence on how the water is retained inside the soil. The work presented here, however, is intended to identify and describe the main basic aspects of unsaturated soil behaviour including mechanical and water retention couplings and does not explicitly describe the interrelation between intra- and inter-aggregate pores. Mathematical frameworks including this bi-modal distribution in their formulation may be found, for instance, in Sánchez (2004).

As described later, the solid particles also play an important role in understanding the shear strength of the soil, as tangential and normal forces are transmitted through soil particle contacts as a consequence of external loading.

2.2.2. Liquid phase

The liquid phase is mostly comprised by water. According to Romero (1999), interstitial water can be classified in different forms depending on the size of the pore spaces where the water is retained and also depending on the water interactions with the solid matrix of the clay. Water contained in inter-aggregate pores is typically referred to as *free* or *capillary water*. A characteristic of this fraction of water is that it may flow by hydraulic gradients. A second fraction of water is formed of that part retained in the pores within the aggregations and is referred to as *intercluster adsorbed water* (see Figure 2-1).

Water may contain dissolved salts and their cations are attracted by the double diffuse layer around the surface of clay particles. Differences in the pore water chemistry may significantly influence the mechanical response of soils. This research, however, focuses on the mechanical-retention coupling not including chemical effects. Further information on the chemical part and its coupling with the mechanical behaviour is given in Guimarães (2002).

Also present in the liquid phase will be air dissolved within the water. Under equilibrium conditions the amount of dissolved air will be governed by Henry's Law, as discussed further in Chapter 7.

In this work, liquid water will be studied as free water contained in the inter-aggregate pore space. In turn, this water may occur as *bulk water* when an individual void is flooded with water, like in saturated soils, or as *meniscus water* formed around particle contacts when an individual void is empty of water. As further discussed later, the occurrence of water as bulk water or as meniscus water bridges has a significant influence on the mechanical behaviour.

2.2.3. Gas phase

The gas phase is mostly comprised of dry air. More precisely, the air comprises a mixture of different gases but, in general, it is only considered as dry or free air. Gaseous air occupies the pore spaces not occupied by liquid water. The mechanical equilibrium of the liquid-gas interfaces involves a tensile force generated along the boundary (surface tension). The existence of surface tension means that the gas and liquid phases can be at different pressures if the interface is curved (see Figure 2-3). As discussed within the following sections, this interface has some specific properties which influence the mechanics of unsaturated soils.

Also in the gas phase will be water vapour, which will typically be in equilibrium with the liquid water through the psychrometric law. A more detailed description on this aspect is given in Chapter 7.

2.3. Mechanical behaviour of unsaturated soils

The mechanical behaviour of soils relates stresses and strains. This can be represented by the formulation of a mechanical constitutive model, aimed at describing the stress-strain behaviour, including volume change and shear strength. In general, the mathematical development of the mechanical constitutive model is based on the main physical principles involved and, once formulated, it can be validated with the results of experimental tests which may also be used to improve the constitutive relationships initially proposed. A fundamental aspect in the development of constitutive models is the correct choice of the stress state variables employed to describe the material behaviour as discussed in the following.

2.3.1. Stress state variables

When the soil pores are partially filled with liquid (typically water) and partially filled with gas (typically air) the soil is referred to as unsaturated. An unsaturated soil is thus constituted by three phases, which are the solid phase (composed of soil grains and aggregates and adsorbed water), the liquid phase (comprising water and dissolved air) and the gas phase (composed of dry air and water vapour). The interface between liquid and gas was considered by Fredlund and Morgersten (1977) as a fourth phase due to its particular properties. This interface is affected by the surface tension which is associated with capillary phenomena inside the pores. The characterisation of this phenomenon introduces an important stress variable known as matric (capillary) suction and defined as the difference between pore air pressure and pore water pressure (i.e. $s=u_a-u_w$). Figure 2-3 illustrates these concepts from an idealised infinitesimally small element of air-water

interface in equilibrium with forces exerted by air pressure, water pressure and surface tension.

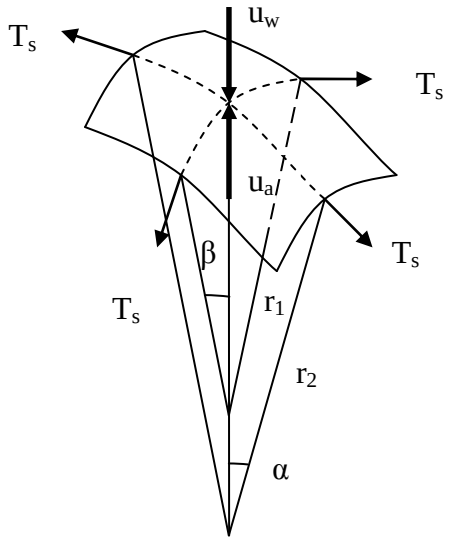

Figure 2- 3 Equilibrium of an infinitesimal element of gas-liquid interface.

Consideration of force equilibrium on the interface element leads to the following expression (typically referred to as the Young-Laplace equation) relating the matric suction to the surface tension T_s and the principal radii of curvature r_1 and r_2 of the interface (considered positive when measured on the air side and negative when measured on the water side):

$$u_a - u_w = T_s \left(\frac{1}{r_1} + \frac{1}{r_2} \right) \qquad (2.\ 1)$$

Total suction s_t is intimately related to the concept of water potential which can be defined as the amount of work per unit mass of pure water that must be done in order to transport, reversibly and isothermally, an infinitesimal quantity of water from one reference condition to a specified elevation and gas pressure (Gens, 2010). Thus, gradients of total water potential control the mass transfer of liquid water. Water potential and suction are equivalent concepts, but having units of energy per unit mass (L^2T^{-2}) and of pressure ($ML^{-1}T^{-2}$) respectively. In fact, as pointed out in Gens (2009), suction is obtained when expressing the water potential as energy per unit volume rather than as energy per unit mass and changing the sign (i.e. s_t=-ψ where ψ is the water potential expressed as energy per unit volume). This dual representation of the state of water in soils is useful in developing new measurement techniques or mechanical constitutive laws for unsaturated

soils (Alonso et al., 1987). In this direction, it is convenient to define the water potential as a combined contribution of several components (Review Panel, 1965):

$$\Psi = \Psi_z + \Psi_g + \Psi_o + \Psi_m \qquad (2.2)$$

The gravitational potential term ψ_z is associated to the difference in elevations (i.e. $\psi_z=\gamma_w z$ where z is the elevation with respect to a reference). The gas pressure potential ψ_g is related to the applied gas pressure (i.e.$\psi_g=u_a-u_{atm}$ where u_a and u_{atm} are the pore air pressure and the reference atmospheric pressure respectively). The osmotic potential ψ_o arises from differences in solute concentration between pore water and pure water (i.e. $\psi_o=\Delta cRT$ where Δc is the difference in concentration between the two solutions, R is the universal gas constant, 8.314 J/mol K, and T is the absolute temperature). The last term in equation (2.2), the matric potential ψ_m, includes the capillary absorption (i.e. $\psi_c=-(u_a-u_w)$) and surface adsorption phenomena (i.e. ψ_a).

As described in Gens (2009), the capillary and the adsorptive components are commonly lumped together into a single measurement of matric suction expressed as $s=u_a-u_w$, in spite of the fact that each component may have different effects on the mechanical behaviour. This is because it is difficult to separate them in practice although it is conceptually useful. In this sense, the development of increasing negative potentials occurring from high to low values of the degree of saturation should be viewed as a gradual process with no clear transition between the capillary and the adsorptive water regimes (Gens, 2009).

For non-expansive soils, matric suction changes are significantly more important than osmotic suction variations in controlling the mechanical behaviour of unsaturated soils (Alonso et al., 1987). This leads to the result that matric suction is considered as the component of suction employed as a stress state variable in most mechanical constitutive models. In expansive soils, where the pore fluid chemistry has an important influence on mechanical behaviour, the contribution of the osmotic suction component may be significant. In such soils, however, the influences of matric suction and of pore fluid chemistry on mechanical behaviour will need to be considered separately, and it will not be possible (when considering mechanical behaviour) to simply relate the behaviour to a single total suction variable i.e. the concept of total suction has meaning in the context of flow of liquid water but not in the context of mechanical behaviour. This research, however, is primarily concerned with the behaviour of non-expansive soils, and thus the term suction will here refer to matric (capillary) suction (i.e. $s=u_a-u_w$). An interesting and more detailed description on these issues is given in Gens (2009).

In saturated conditions, when all the pores are fully filled with water, the only stress variable required in describing the mechanical behaviour is the effective stress tensor, which is defined as the difference between total stress and pore water pressure:

$$\sigma'_{ij} = \sigma_{ij} - \delta_{ij} u_w \qquad (2.3)$$

where σ'_{ij} is the effective stress tensor, σ_{ij} is the total stress tensor, δ_{ij} is the Kronecker delta and u_w is the pore water pressure.

From a physical point of view the effective stress can be considered as the stresses transmitted through the grains or soil skeleton by inter-particle contact forces. Changes of these contact forces cause deformation of the soil skeleton and increase the friction generated at points of contact between the soil particles which gives the shear strength of the soil. Hence, it is reasonable to assume that variations of these contact forces cause a direct effect on the mechanical properties of the soil. This was formally announced by Terzaghi (1936) within the *effective stress principle* stating:

"*all the measurable effects, such as compression, distortion and a change of shearing resistance are exclusively due to changes in effective stress*".

However, in unsaturated soils, the existence of two fluid phases in the voids between the soil particles considerably increases the complexity of describing mechanical behaviour. Many early efforts in describing the unsaturated condition attempted to define an effective stress for unsaturated soils that satisfied Terzaghi's definition of effective stress in saturated soils. In this direction, several formulations directly inspired by the effective stress concept defined by Terzaghi (2.3) for the saturated condition, have been proposed for unsaturated soil. Probably the best known was suggested by Bishop (1959):

$$\sigma_{ij}' = \sigma_{ij} - \delta_{ij} \chi u_w - \delta_{ij} (1 - \chi) u_a \qquad (2.4)$$

where σ'_{ij} is the Bishop's effective stress tensor, χ is a material parameter which mainly depends on the degree of saturation and varies from 1 (saturated state) to 0 (dry state), u_a is the pore air pressure and u_w is the pore water pressure. Similarly to the case of saturated soils, the effective stress expression proposed by Bishop can be physically interpreted as an attempt to represent the stresses transmitted through the soil skeleton. The weighting factors χ and (1-χ) respectively applied to the pore water pressure and pore air pressure in equation (2.4), can be viewed (when looking at the influence of each pore pressure on the stresses transmitted through the soil skeleton) as representing a

weighting value of the voids fully occupied by water and those occupied by air (Wheeler et al., 2003).

This approach was capable of reasonably reproducing some features of the behaviour of unsaturated soil, such as the shear strength, but could not explain others, such as the irrecoverable volumetric compression which sometimes occurs upon wetting (Jennings and Burland ,1962). When an unsaturated soil sample is wetted the soil sample may experience swelling (under low confining stress) or a reduction in volume (under high confining stress). This duality of behaviour upon wetting probably makes it impossible to relate volume change with applied stress by using a single unique stress function (Burland, 1965). The lack of success in using a single stress variable to describe some of the basic features observed in unsaturated soil behaviour, led to new approaches employing two independent stress variables.

Fredlund and Morgenstern (1976) stated that two independent stress variables are required when modelling unsaturated soil behaviour. In particular, they proposed that any possible pair amongst $\sigma_{ij} - \delta_{ij}u_a$, $\sigma_{ij} - \delta_{ij}u_w$ and u_a-u_w could describe the mechanical behaviour of unsaturated soils. The most common pair used are net stress, $\sigma_{ij} - \delta_{ij}u_a$ and suction, u_a-u_w. Further support for this statement was provided by Fredlund and Morgenstern (1977) with experimental results observed in null tests, where no volume change of the soil was observed when changing pore air pressure, pore water pressure and total stress and keeping net stress and suction constant. Tarantino et al. (2000) provided also further experimental evidences supporting this statement.

Many attempts to describe the mechanical behaviour of unsaturated soils were made from the 1960s but it was not until Alonso et al. (1987) and Alonso et al. (1990) that a consistent and unified framework based on the theory of elasto-plasticity was developed. The constitutive model proposed by Alonso et al. (1990), known as the Barcelona Basic Model (*BBM*), is formulated in terms of suction ($s=u_a-u_w$) and net stress ($\bar{\sigma}_{ij} = \sigma_{ij} - u_a\delta_{ij}$) and it establishes the conceptual basis of constitutive modelling of unsaturated soils. Based on this framework a number of constitutive models employing the net stress tensor and suction were proposed later, aimed at improving or expanding the capabilities of the original *BBM* (e.g. Josa et al., 1992; Wheeler and Sivakumar, 1995; Cui and Delage, 1996; Sánchez et al., 2005, among others). Reviews on constitutive modelling of unsaturated soils can be found in Wheeler and Karube (1996), Gens et al. (2006) or, more recently, Sheng et al. (2008).

Following publication of the *BBM* by Alonso et al. (1990), there have also been many suggestions for alternative mechanical constitutive models which use some of the conceptual ideas but which employ alternative pairs of stress variables to the net stress tensor and the matric suction. Examples include Jommi (2000), Wheeler et al. (2003), Sheng et al. (2004), Khalili et al. (2004) and Tamagnini and Pastor (2005). The advantages and disadvantages of these alternative pairs of stress variables are discussed by Gens et al. (2006) and, also, Nuth and Laloui (2008a).

Houlsby (1997) suggested possible pairs of suitable stress variables for use in unsaturated soil mechanics, and corresponding appropriate strain increment variables, by considering the work input per unit volume of unsaturated soil. Houlsby showed that the increment of work input, *dW* per unit volume of unsaturated soil (neglecting the work dissipated by flow of fluids, the air compressibility term and ignoring the work of the air-water interface) can be written as:

$$dW = \left[\sigma_{ij} - \left(S_r u_w + \left(1 - S_r\right) u_a \right) \delta_{ij} \right] d\varepsilon_{ij} - \left(u_a - u_w\right) n dS_r = \sigma_{ij}^{*} d\varepsilon_{ij} - s^{*} dS_r \qquad (2.5)$$

where σ_{ij}^{*} is equivalent to the stress variable defined by equation (2.4) with the weighting factor χ replaced by the degree of saturation S_r and will be referred to as the Bishop's stress tensor, $d\varepsilon_{ij}$ is the strain increment tensor, n is the porosity and s^{*} will be referred to as the modified suction. Equation (2.5) shows that if Bishop's stress tensor and modified suction are employed as stress state variables to describe unsaturated soil behaviour, the appropriate pair of *work-conjugate* strain increment variables are increments of strains and decrements of the degree of saturation respectively. As pointed out in the original work (Houlsby, 1997) equation (2.5) can be re-arranged to provide other possible choices of stress and strain variables. In particular, if the net stress tensor and suction are used as stress state variables (as, for instance, in *BBM*), the appropriate pair of work-conjugate strain increment variables would be the strain increment tensor $d\varepsilon_{ij}$ (conjugate with the net stress tensor) and a complex strain increment variable ($-ndS_r+S_r d\varepsilon_v$), involving both the decrement of degree of saturation and the increment of volumetric strain, as conjugate with suction. As discussed in Houlsby (1997), this second strain increment variable is equal to $-dv_w / v$ where v is the specific volume ($1+e$) and v_w is ($1+S_r e$) defined by Wheeler (1991).

Perhaps one of the main limitations of the *BBM* family of models, which employ the net stress tensor and suction as the stress variables, is that they are not able to account for the influence of the degree of saturation (in addition to suction) on the mechanical

behaviour. In addition, when employed in the modelling of coupled hydro-mechanical boundary value problems they must be used in conjunction with a separate water retention constitutive model which typically would take no account of the influence of changes of void ratio on the water retention capacity. These two couplings (the influence of degree of saturation on mechanical behaviour and the influence of void ratio on water retention behaviour) are both crucial features of unsaturated soil behaviour experimentally confirmed by several authors (e.g. Romero, 1999; Jommi, 2000; Vaunat et al., 2000; Gallipoli et al., 2003b and Tarantino and Tomobolato, 2005). With the aim of including in the modelling of unsaturated soils such kinds of mechanical-retention couplings a number of advanced constitutive models, generally based on other sets of stress and strain variables, have been more recently proposed (e.g. Vaunat et al., 2000; Wheeler et al., 2003, Sheng et al., 2004). In particular, Wheeler et al. (2003) proposed a new fully coupled constitutive model which employs the stress variables σ_{ij}^* and s^* (and the corresponding appropriate strain variables) and which introduces the possibility to include, within a single constitutive model, not only the description of the main features of mechanical behaviour in unsaturated soils, but also most of the basic characteristics of the water retention behaviour. This coupled constitutive model of Wheeler et al. (2003) constitutes the basis of the work developed within the following chapters. This new perspective was one of the first formulations of a new family of more advanced constitutive models accounting for the coupling, at constitutive level, between mechanical and water retention behaviour (e.g. Sheng et al., 2004; Sun et al., 2007; Manzanal, 2008; Francois, 2008; Raveendiraraj, 2009; Buscarnera and Nova, 2009).

2.3.2. Volume change

The main features of volume change behaviour experimentally observed in unsaturated soils are summarised in the following sections. A brief description relating these features with significant aspects of constitutive modelling is also given.

2.3.2.1. Response under loading-unloading stress paths at constant suction

Unsaturated soils exhibit irreversible volumetric behaviour when loaded at constant suction beyond a certain net stress (the yield stress). From this stress state, plastic volumetric straining is observed if loading increases in the same way. It is also observed that if an unloading stress path at the same constant suction is then applied, swelling occurs and part of the volumetric changes are recovered (see response *b-c* in Figure 2-4). In the light of these experimental observations, it is reasonable to characterise this type of unloading behaviour (within an elasto-plastic framework) as reversible or elastic.

Furthermore, it is generally observed that the slope of these swelling lines do not significantly depend on suction (Alonso et al., 1990).

Also, if a re-loading stress path at the same value of suction is now applied, the volumetric response observed will approximately match with the previous swelling (now compressing instead of expanding) as plotted in Figure 2-4 as the response *c*-*d*. This type of behaviour illustrated in Figure 2-4 under oedometric conditions is also typically observed for isotropic stress paths as illustrated in Section 2.5.1. As shown later, it is also commonly observed that during a re-loading stress path, yielding takes place at the same stress state from where the previous unloading path started. It is interesting to note that these features of behaviour are very similar to those observed in saturated soils and (as further described in Chapter 3) they suggest elasto-plasticity as an adequate framework for its description (Gens and Potts, 1988).

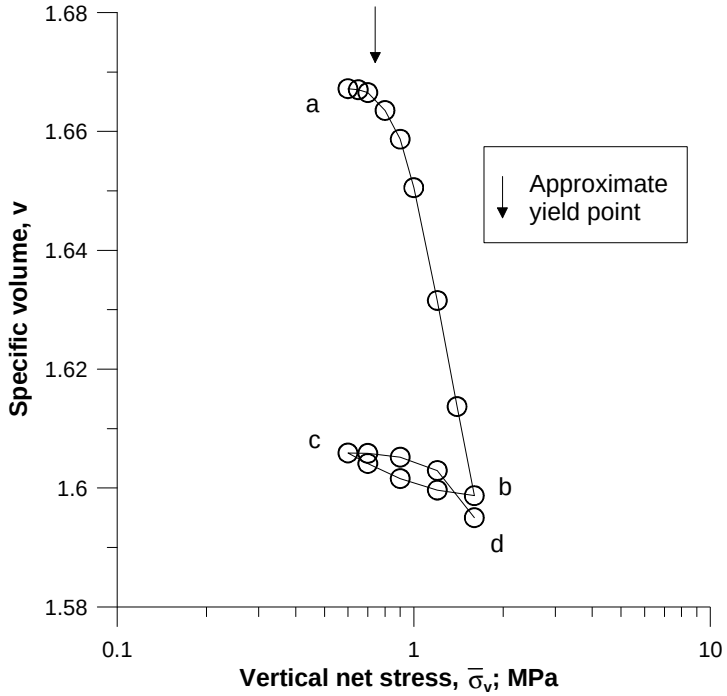

Figure 2- 4 Loading-unloading paths on high-porosity Boom clay at constant suction (Romero, 1999).

During isotropic loading paths at different values of suction, the yield stress increases with increasing suction. This particular feature of unsaturated soils is illustrated in Figure 2-5. It implies, from an elasto-plastic point of view, that the size of the elastic domain increases with increasing suction (Wheeler and Sivakumar, 1995).

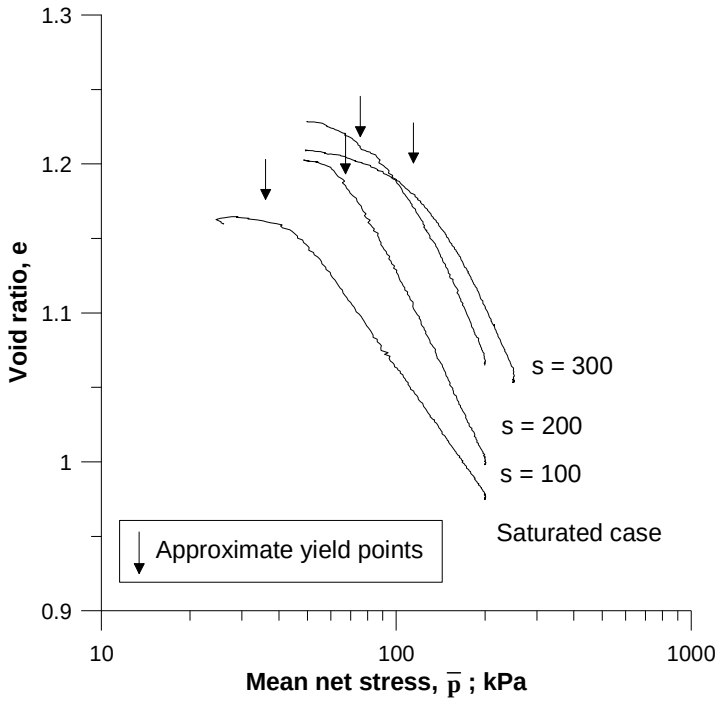

Figure 2- 5 Behaviour of speswhite kaolin during isotropic loading at different constant suctions (Sivakumar, 1993)

The locations and gradients of the normal compression lines in the plane v:ln $\bar{p}$ obtained from isotropic loading at constant suction are dependent on the suction level (see Figure 2-5), and can be expressed by:

$$v = N(s) - \lambda(s) \ln \bar{p} \qquad (2.6)$$

where $\bar{p}$ is the mean net stress and the intercept $N(s)$ and gradient $\lambda(s)$ both depend upon the value of suction.

2.3.2.2. Response under isotropic wetting paths at constant mean net stress

During a wetting path on a sample of unsaturated soil, swelling (see Figure 2-6) or collapse compression (see Figure 2-7) may occur. In general, swelling is observed at low values of net stress whereas, collapse compression occurs at higher values of net stress.

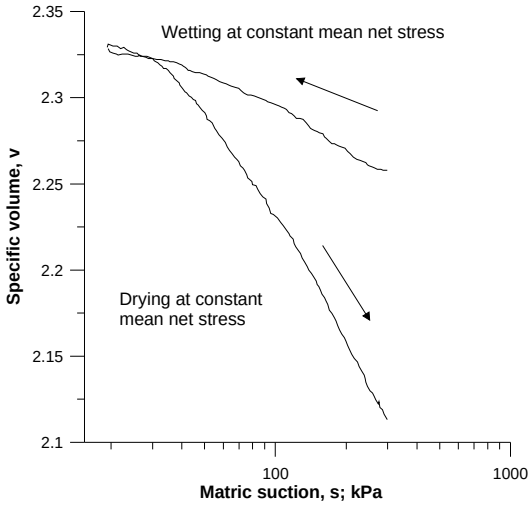

Figure 2- 6 Wetting-drying cycle on compacted bentonite-kaolin performed under isotropic stress state (Sharma, 1998).

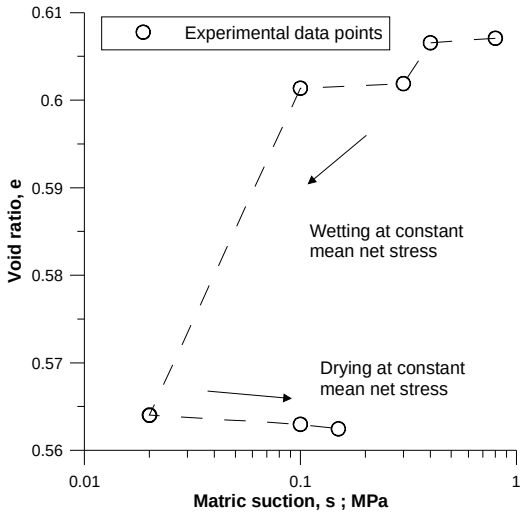

Figure 2- 7 Behaviour of a wetting-drying path on Barcelona clay at constant mean net stress (Barrera, 2002).

2.3.2.3. Response under isotropic drying paths at constant mean net stress

A decrease in volume (shrinkage) is observed during a drying path on a sample of unsaturated soil (see Figure 2-6 or Figure 2-7). According to Alonso et al. (1987) irrecoverable volumetric strains occur when suction is increased to values higher than those previously reached, which suggests the existence of a yield point. The reversible and irreversible behaviour that can be observed while drying an unsaturated soil sample is illustrated in Figure 2-6 (although note that, in this case, yielding on drying occurs at suction much lower than the maximum value previously applied – this point is discussed in Section 2.5.2).

2.3.2.4. Physical explanation and modelling with LC yield curve

In unsaturated soils, (free) water may occur as bulk water when an individual void is flooded with water like in saturated soils, or as meniscus water formed around particle contacts when an individual void is empty of water.

The occurrence of meniscus water bridges between the soil particles (formed where the neighbouring voids are air-filled) produces an additional component *ΔN* of normal force through the contact points resulting in a stabilising effect on the soil structure. Essentially as these normal contact forces increase, the friction generated at points of contact between the soil particles is also increased and this makes inter-particle slippage less likely, hence increasing yield stress (see Figure 2-8). This additional stability has a limiting value as suction tends to infinity (Wheeler et al., 2003) and it is lost when an individual void is flooded with water. More generally, in saturated soils where all the voids are fully filled with water, this stabilising effect has completely disappeared and pore water applies an isotropic pressure that produces a uniform effect on the soil skeleton (effective stress concept).

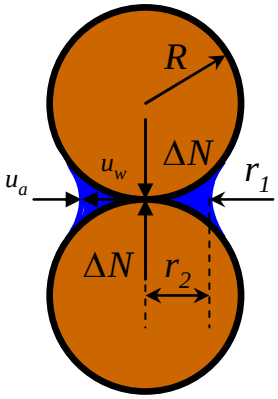

Figure 2- 8 Representation of the additional inter-particle force at contact point for idealised spherical soil particles.

The different forms of behaviour observed in unsaturated soils during wetting (swelling or collapse compression) can be explained by the occurrence of water as bulk water or as meniscus water. During a wetting process, pore water pressure increases within the bulk water causing swelling of the soil. On the other hand, the possible loss of meniscus water bridges as a consequence of this wetting process can trigger inter-particle slippage, resulting in volumetric compression (Raveendiraraj, 2009).

Based on the fact that aspects of mechanical behaviour listed above are inter-related, Alonso, Gens and Hight (1987) proposed a yield curve called the Loading-Collapse yield curve (*LC*). The *LC* yield curve represents plastic volumetric compression occurring either

during isotropic loading or during wetting as the same process (i.e. yielding on the *LC* yield curve). The mathematical formulation for the *LC* yield curve was later proposed by Alonso, Gens and Josa (1990) (see Section 2.3.4 for more detail).

2.3.3. Shear strength

The shear strength of a particular soil is higher when the soil is in an unsaturated condition than when it is in a saturated condition. From a physical point of view, and as described in Raveendiraraj (2009), this can be explained as follows. During a wetting process more and more air-filled voids become water-filled voids, losing stability at particle contacts because the number of meniscus water bridges affecting inter-particle contacts reduces. In the limit, soil becomes saturated and the stabilising effect is lost. Conversely, during a drying process, more and more water-filled voids become air-filled voids, leading to additional stability at particle contacts. At a certain stage while suction is being increased, most of the voids become air-filled (or, in other words, very few voids are filled with bulk water) and additional stability at inter particle contacts mainly depends on increasing suction. However, if suction is kept increasing, this additional stability reaches a limiting value, as described in Section 2.3.2.4. Hence, beyond a certain value of suction no significant increase of shear strength is observed. Indeed, at very high values of suction the shear strength may decrease, as meniscus water bridges are lost and some particle contacts become completely dry.

Several attempts to represent the shear strength variation of unsaturated soils have been proposed over the last 50 years. The first proposal was perhaps that of Bishop (1959) with his proposal for an effective stress equation for unsaturated soils (2.4) leading to the following shear strength expression:

$$\tau = c' + \left[\left(\sigma_n - u_a \right) + \chi \left(u_a - u_w \right) \right] \tan \phi' \qquad (2.7)$$

where τ is the shear strength of the soil, c' is the effective cohesion, Φ' is the effective internal frictional angle, $(\sigma_n - u_a)$ is the net stress normal to the plane of shearing, $(u_a - u_w)$ is matric suction and χ is a parameter dependent on the degree of saturation and varying between 0 and 1. Fredlund and Morgenstern (1977) put forward a new approach considering independently the contributions of suction and net normal stress on shear strength.

$$\tau = c' + \left(\sigma_n - u_a \right) \tan \phi' + \left(u_a - u_w \right) \tan \phi^b \qquad (2.8)$$

where Φ^b is the internal frictional angle associated with changes in matric suction, which was initially considered constant for a particular soil. However, as pointed out by several authors (e.g. Escario and Saez, 1986), Φ^b is not constant with suction, because when suction increases to very high values, the shear strength of this soil cannot increase infinitely, meaning that the value of Φ^b decreases with increasing suction after a certain value (a non-linear variation of shear strength with suction).

Some other proposals have been made since this period contributing to our current understanding of the shear strength of unsaturated soils. A detailed overview on these advances describing some engineering applications is given in Vanapalli (2009).

2.3.4. The Barcelona Basic Model

Alonso, Gens and Hight (1987) described and discussed, mainly from a phenomenological point of view, some of the most characteristic features observed in unsaturated soil behaviour and introduced at a qualitative level an elasto-plastic framework for unsaturated soils. This was subsequently further developed in the formulation of the commonly known Barcelona Basic Model (*BBM*) by Alonso, Gens and Josa (1990). The fundamental aspects of this mechanical constitutive model are described herein and further details can be found in the cited original work or also in the research presented by Josa (1988).

The Barcelona Basic Model (*BBM*) is probably the most commonly used constitutive model in unsaturated soil mechanics. This is because the *BBM* is able to include, within a single framework, many of the main characteristics of the mechanical behaviour of unsaturated soil. The mathematical framework of the model is based on elasto-plasticity and fundamental concepts of critical state models (see Chapters 3 and 4). Indeed, as suction decreases towards zero, the *BBM* tends to the well known Modified Cam Clay elasto-plastic model for saturated soils. It is implicitly assumed within the *BBM* that the soil is fully saturated whenever the suction is zero and only when the suction is zero. This may not be true in practice, as soils will typically show a finite air entry value of suction on drying and, conversely, may not achieve full saturation on wetting to zero suction.

A general description of *BBM* is given in the following, presenting first the predicted behaviour under isotropic stress states and subsequently generalising it to triaxial stress conditions.

Variations of specific volume *v* with mean net stress $\overline{p}$ for different values of suction *s* and along virgin isotropic loading paths (i.e. isotropic normal compression lines, *NCL*) are governed by the following expression:

$$v = N(s) - \lambda(s) \ln \frac{\overline{p}}{\overline{p}^c} \qquad (2.\ 9)$$

where *N(s)* is a reference value of the specific volume when the mean net stress equals a given reference value $\overline{p}^c$ and $\lambda(s)$ is the slope of the *NCL* which is assumed to vary with suction as expressed in the following equation:

$$\lambda(s) = \lambda(0)\left[(1-r)e^{-\beta s} + r\right] \qquad (2.\ 10)$$

where $\lambda(0)$ is the slope of the *NCL* for saturated conditions, *r* is a parameter giving the ratio of the value of $\lambda(s)$ at infinite suction to the saturated value $\lambda(0)$ and β is a parameter giving the rate of change of compression index $\lambda(s)$ with suction. It is interesting to note that (2.10) predicts a decrease of the compression index $\lambda(s)$ with increasing suction for values of *r* between 0 and 1, whereas if *r* is greater than 1 (2.10) predicts of $\lambda(s)$ an increase of $\lambda(s)$ with increasing suction as discussed in Wheeler et al. (2002).

Elastic variations of specific volume are governed by:

$$-dv^e = \kappa \frac{d\overline{p}}{\overline{p}} + \kappa_s \frac{ds}{(s + p_{atm})} \qquad (2.\ 11)$$

where κ is an elastic swelling index with respect to changes of $\overline{p}$, κ_s is an elastic index of the soil with respect to suction variations and p_{atm} is atmospheric pressure, introduced in order to avoid prediction of infinite elastic volumetric strains when suction approaches zero. The component of (2.11) involving κ_s describes elastic swelling on wetting and elastic shrinkage on drying.

Variations of the pre-consolidation mean net stress with suction are given by (2.12) which defines the Loading Collapse (*LC*) yield curve introduced in Section 2.3.2.4. The region identified inside the *LC* yield curve in the *s*- $\overline{p}$ plane (see Figure 2-9) defines the elastic domain under isotropic stress conditions.

$$\left(\frac{\overline{p}_0}{\overline{p}^c}\right) = \left(\frac{\overline{p}_0^*}{\overline{p}^c}\right)^{\left(\frac{\lambda(0)-\kappa}{\lambda(s)-\kappa}\right)} \qquad (2.\ 12)$$

where $\overline{p}_0^*$ is the value of pre-consolidation mean net stress for saturated conditions and $\overline{p}^c$ is a reference pressure.

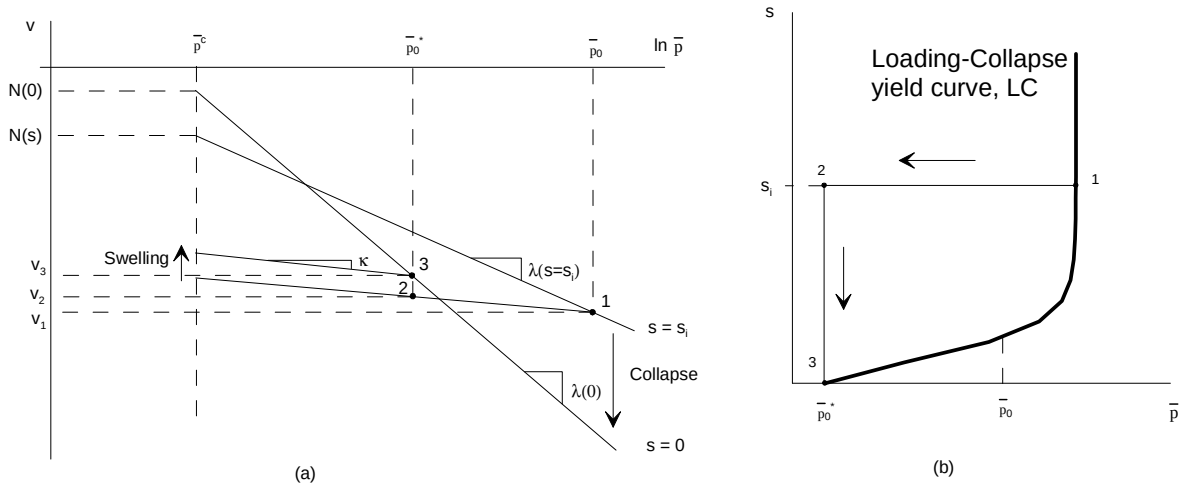

Figure 2- 9 Relationship between pre-consolidation stresses $\overline{p}_0$ and $\overline{p}_0^*$: (a) compression curves for saturated and unsaturated soil; (b) stress path and yield curve in ($\overline{p}$,s) stress plane (Alonso, Gens and Josa, 1990).

Extension of the model to triaxial stress states to include the effect of shearing is made by extending the Modified Cam Clay model from the saturated state (*s*=0) to non-zero values of suction. The resulting *LC* yield surface is assumed to have elliptical constant suction cross-sections and a linear increase of the tensile intercept with suction (see Figure 2-10 and Figure 2-11). This results in the following equation for the *LC* yield surface:

$$q^2 - M^2(\overline{p} + ks)(\overline{p}_0 - \overline{p}) = 0 \qquad (2.\ 13)$$

where *q* is the deviatoric stress, *k* is a parameter giving the assumed linear increase in tensile intercept with suction, *M* is the aspect ratio of the elliptical cross-sections and $\overline{p}_0$ is the isotropic yield stress at a given value of suction ($\overline{p}_0$ varies with suction according to the *LC* yield curve expression of (2.12)).

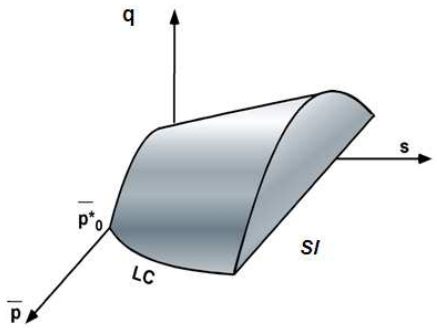

Figure 2- 10 Extended representation of the BBM yield surface (Sánchez, 2004).

Under these considerations, the critical state lines (*CSL*) for different values of suction (see Figure 2-11) are defined in the $q:\bar{p}$ plane by:

$$q = M\bar{p} + Mks \qquad (2.\ 14)$$

A simple linear increase of critical state strength with suction is therefore assumed, equivalent to the assumption of a constant Φ^b (see Section 2.3.3).

A Suction Increase (*SI*) yield surface is also included in the *BBM*, (see Figure 2-10 and Figure 2-11) to represent the occurrence of plastic shrinkage on drying to a higher value of suction than previously applied.

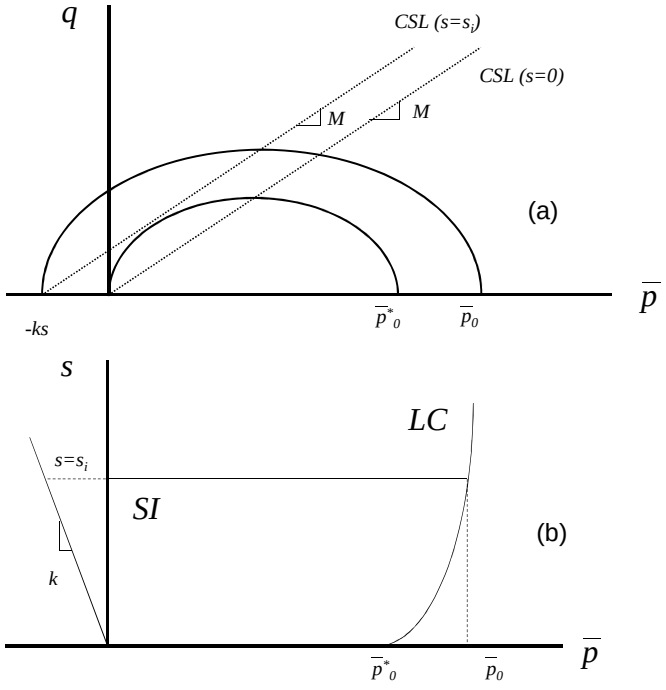

Figure 2- 11 LC and SI yield surfaces: (a) constant suction cross-sections; (b) q=0 cross-section (Alonso, Gens and Josa, 1990).

As the name implies, the main purpose (and achievement) of the Barcelona Basic Model is the formulation of a basic framework capable of reproducing the general behaviour of unsaturated soil. However, some of the assumptions made in order to simplify the model formulation led to some model limitations. A discussion on some of these limitations is given in Wheeler et al. (2002).

Many other alternative elasto-plastic constitutive models for unsaturated soils have been also proposed after the *BBM*. Interesting reviews and discussions on some of the most significant advances in constitutive modelling of unsaturated soils can be found, amongst others, in Gens (1996), Wheeler and Karube (1996), Jommi (2000) or Sheng et al. (2008).

2.4. Water retention behaviour of unsaturated soils

In unsaturated soils water is retained in the soil structure by both capillary absorption and surface adsorption on the active clay minerals (also influenced by osmotic effects resulting from the pore water chemistry) (Romero, 1999). According to Romero and Vaunat (2000) interstitial water contained in unsaturated soils can be distinguished in two components: the fraction occupying the inter-aggregate (significantly affected by loading processes) and the fraction of quasi-immobile water contained in the intra-aggregate level (with lower influence of the mechanical actions). The description of the water retention behaviour is the central aim of this section.

A fundamental constitutive law for a proper description of unsaturated soil behaviour is the water retention relationships which generally relate the amount of water retained in the soil pores to the suction s. The amount of water retained within the soil is typically expressed by either the water content w or the degree of saturation S_r. How w or S_r varies with suction s mainly depends on the geometry and distribution of the voids and on the physico-chemical interactions between pore water and soil. This correspondence between s and S_r is generally non-unique. It is experimentally observed that, for a given soil, at one particular value of suction, the values of degree of saturation will be different on a drying path and on a wetting path. This feature of the water retention behaviour is termed hydraulic hysteresis and it is illustrated in Figure 2-12. In this figure, the main drying curve gives the variation of degree of saturation with suction followed by a soil sample dried from an initially saturated state. Conversely, if a soil sample is wetted from a completely dry state, the observed variation of degree of saturation with suction traces the main wetting curve. Any reverse on the variation of suction from a main wetting or drying curve traces a different curve named a scanning curve (see Figure 2-12).

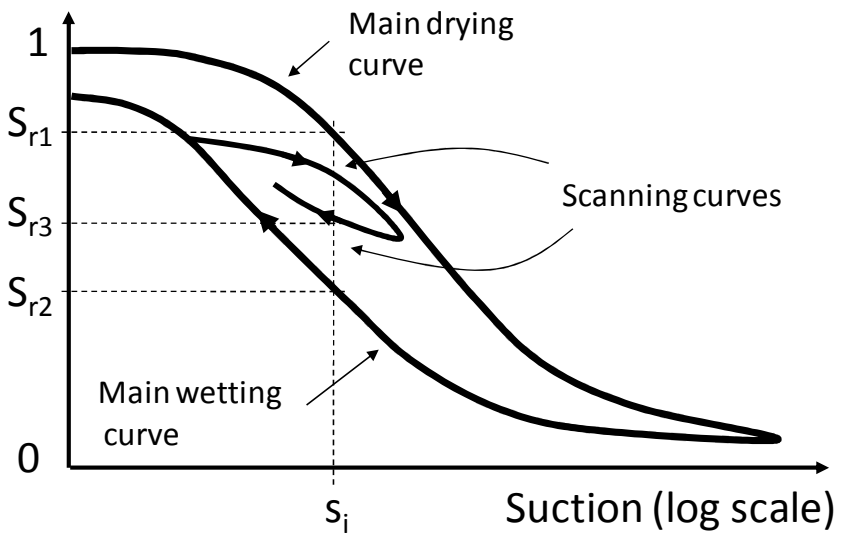

Figure 2- 12 Idealised representation of hydraulic hysteresis in the water retention behaviour (Tarantino, 2007).

A consequence of considering hydraulic hysteresis in the retention behaviour is that for a given value of suction many different values of the degree of saturation may occur: a maximum value S_{r1} on the main drying curve, a minimum value S_{r2} on the main wetting curve and intermediate values, such as S_{r3}, on scanning curves. These ideas are illustrated in Figure 2-12. In the light of this, if two different degrees of saturation are found for the same value of suction and the same net stress state, the stabilising effect of the meniscus water at inter-particle level would be different which may influence the mechanical response.

If changes of void ratio occur, there will be a shift in the positions of the main drying curve and main wetting curve. Lower values of the void ratio will shift the position of the main curves to higher suctions (to the right in Figure 2-12) as a higher value of suction will be required to empty or fill the smaller voids with water. This influence of the void ratio on the positions of the main drying and wetting curves has been observed by many authors (see for instance, Gallipoli et al., 2003a) and is further discussed in the following section when describing the influence of the mechanical behaviour on the water retention behaviour.

A more detailed description and deeper overview on the water retention behaviour can be found in Romero (1999) and also in Nuth and Laloui (2008b).

2.5. Coupling of mechanical and water retention behaviour at constitutive level

This section is aimed at describing the coupling at constitutive level between water retention behaviour and mechanical behaviour in unsaturated soils. These influences are observed in both directions. Mechanical behaviour influences water retention behaviour (essentially through variations of the void ratio) and water retention behaviour influences mechanical behaviour (mainly through variations of the degree of saturation). It is important to incorporate these couplings into a constitutive model in order to accurately describe and better understand the unsaturated soil behaviour.

2.5.1. Influence of mechanical behaviour on water retention behaviour

As already introduced, variations of the void ratio *e* change the capacity of the soil to retain water. In fact, as highlighted in Wheeler et al. (2003), changes in size of voids and of passageways between voids modifies the suction necessary to flood or empty the voids. These variations of *e* are essentially controlled by the stress-strain relationships and therefore the mechanical behaviour influences the S_r-*s* relationships. A shift of the main drying and wetting curves in the S_r-ln*s* plane is observed if the void ratio changes. For example, the main drying and wetting retention curves are shifted to higher suction values when the void ratio decreases as the required suction to flood or empty the voids tends to increase with decreasing void ratio. These influences have been observed by several authors (e.g. Romero, 1999; Romero and Vaunat, 2000; Jommi, 2000; Gallipoli et al., 2003a and Tarantino and Tomobolato, 2005). Figure 2-13 shows some of the results in the water retention plane presented in the work of Romero (1999) on statically compacted samples of kaolinitic-illitic soil. The work of Romero (1999) was aimed at investigating the influence of void ratio on main wetting and drying curves. Samples were compacted at a water content dry of optimum to two different dry unit weights (i.e γ_d=13.7 kN/m^3 and γ_d=16.7 kN/m^3) resulting in two different void ratios (i.e. *e*=0.93 and *e*=0.59 respectively). It is clearly observed in Figure 2-13 that the main wetting and drying curves corresponding to lower void ratios are shifted to higher values of suction compared to the corresponding curves for higher void ratios.

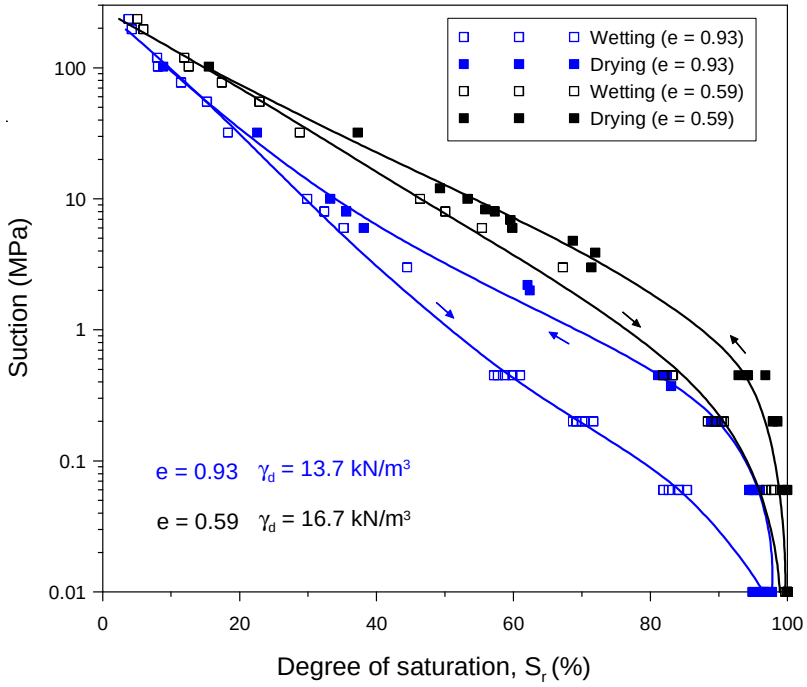

Figure 2- 13 Influence of void ratio on main wetting and drying curves for a kaolinitic-illitic soil (Romero, 1999).

It should also be noted that the water retention behaviour may also be presented in terms of the evolution of the water content w (rather than degree of saturation S_r) with suction s. This is illustrated in Figure 2-14, where the same experimental results from Romero (1999) shown in Figure 2-13 are now plotted in the w:ln$s$ plane. As argued in Raveendiraraj (2009), this alternative form of presenting the results of the water retention behaviour may be more useful for analyses in the high suction ranges because they may become independent of the void ratio (Romero and Vaunat, 2000) while plotting the water retention in terms of S_r may be more useful in low suction range because all curves approach S_r=1.0. Inspection of Figure 2-14 confirms that the main wetting curves for the two different void ratios analysed (i.e. e=0.93 and e=0.59) tend to merge into one for high suctions, and the same is observed for the main drying curves. Therefore, the previously described influence of the void ratio on the water retention behaviour, can be considered insignificant at high suctions, if the retention behaviour is expressed in terms of w instead of S_r. According to Romero and Vaunat (2000), plotting the results in the w:ln$s$ plane allows the identification of two separate zones: the intra-aggregate porosity region (where the water retention response is not dependent on the void ratio and retention curve parameters are mainly dependent on the specific surface of the soil particles) and the inter-aggregate porosity region (where the water retention response is dependent on void ratio and strongly influenced by mechanical actions). These regions are illustrated in Figure 2-14.

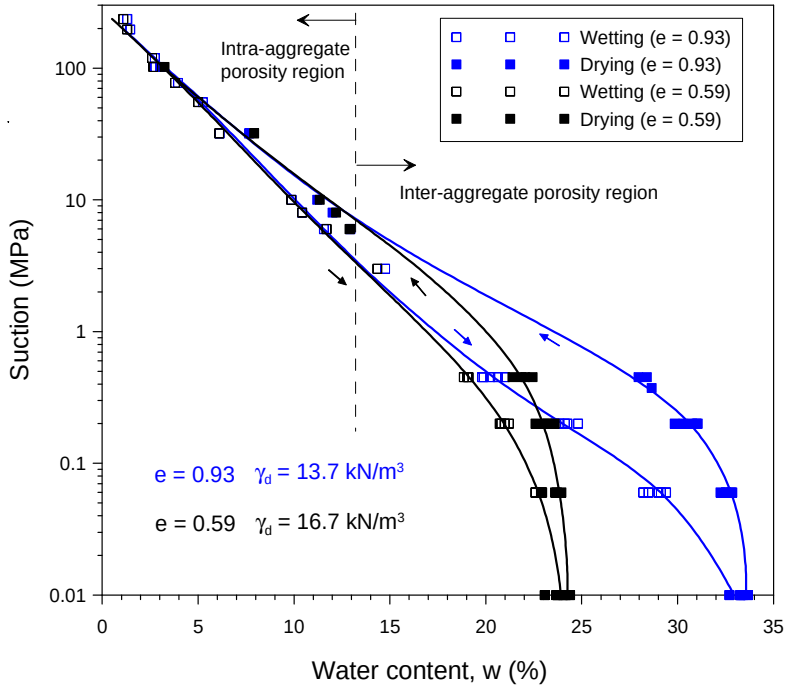

Figure 2- 14 Water retention curves for kaolinitic-illitic soil replotted in terms of water content (Romero, 1999).

2.5.2. *Influence of water retention behaviour on mechanical behaviour*

There is also an influence in the other direction. This is the water retention influencing the mechanical behaviour. The degree of saturation influences (in addition to suction) the mechanical response because it describes the number of inter-particle contacts affected by meniscus water bridges (Wheeler et al., 2003). As described in Section 2.2, these meniscus water bridges have a stabilising effect on the soil skeleton, that is lost when an individual void is flooded with water. These concepts were introduced by Wheeler et al. (2003) and incorporated in the fully coupled constitutive model described in Section 2.6.

An illustrative example of this influence is shown in Figure 2-15 where the results of Sharma (1998) on bentonite-kaolin samples are presented. Two different isotropic loading tests are shown. Figure 2-15a shows the results of a sample subjected to isotropic loading at constant suction with an intermediate unloading-reloading path at the same constant suction (*b*-*c*-*d*). To analyse the influence of the degree of saturation on subsequent isotropic loading, an equivalent test for the same soil and at the same value of suction, was carried out now including a wetting-drying cycle (*c*-*d*-*e*) after the unloading path (*b*-*c*). A subsequent loading was then applied (*e*-*f*) obtaining the results shown in Figure 2-15b.

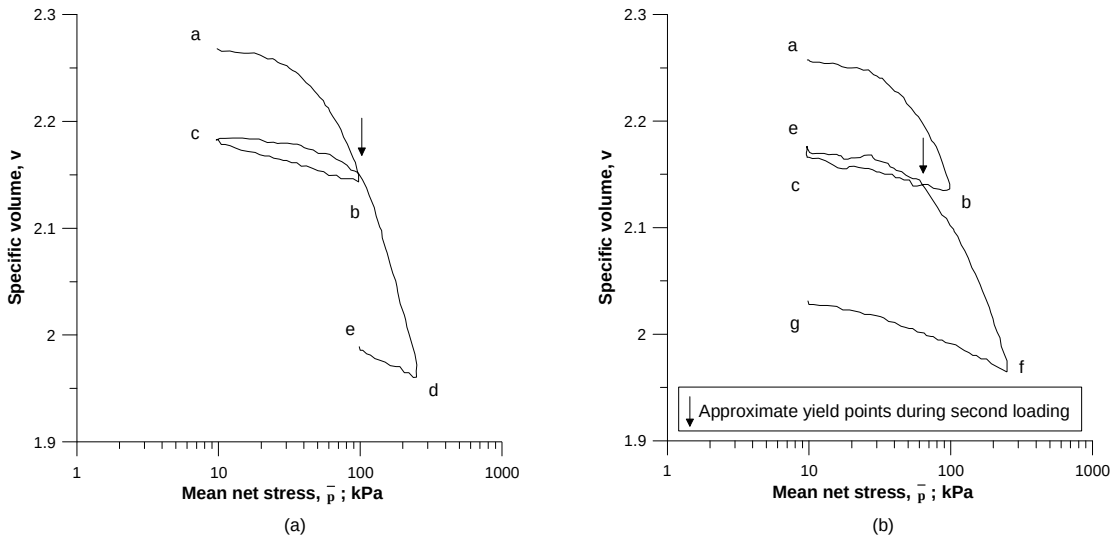

Figure 2- 15 Behaviour of bentonite-kaolin during isotropic loading at constant suction (Sharma, 1998): (a) no wetting-drying cycle applied; (b) wetting-drying cycle applied after unloading path b-c (Wheeler et al., 2003).

It is observed in Figure 2-15b that in the second isotropic loading (*e-f*), the initial yielding occurs at a mean net stress lower than the last value previously reached (point *b*). The reason for this observed behaviour is that a considerable irreversible increase of the degree of saturation as a consequence of the hydraulic hysteresis took place during the wetting-drying cycle *c-d-e*. This increase of S_r led to a reduction of the number of inter-particle contacts affected by meniscus water bridges, hence reducing the stability of the soil skeleton (Wheeler et al., 2003). It should also be mentioned here that Wheeler et al. (2003) described how the influence of S_r can also explain the occurrence of yielding on drying at suctions less than the maximum value previously applied (see Figure 2.6).

In order to give an introduction to following section (in which the model proposed by Wheeler et al. (2003) is described in detail), only the most significant features of coupling relevant to understand this model have been included and discussed within this section. Further descriptions on these issues may be found in Wheeler et al. (2003) or also in Raveendiraraj (2009).

2.6. Fully coupled constitutive model for isotropic stress states

Wheeler et al. (2003) proposed a coupled elasto-plastic constitutive model for the mechanical behaviour and water retention behaviour of unsaturated soils. A detailed description of this elasto-plastic framework is given in this section including: the state variables used; the yield surfaces, plastic mechanisms and couplings considered; the water retention model; the elastic relationships; the associated flow rules and the hardening laws.

2.6.1. Stress variables

It has been shown within the previous sections that a basic aspect in constitutive modelling is the choice of the stress variables. Based on the analysis presented by Houlsby (1997), which indicated that there are several appropriate sets of work-conjugate stress and strain variables (see Section 2.3) for unsaturated soils, Wheeler and co-workers proposed a fully coupled constitutive model for isotropic stress states expressed in terms of mean Bishop's stress p^* and modified suction s^* defined as follows:

$$p^* = p - S_r u_w - (1 - S_r) u_a = \bar{p} + S_r s \qquad (2.15)$$

$$s^* = n(u_a - u_w) = ns \qquad (2.16)$$

This pair of stress state variables (i.e. p^* and s^*) are work-conjugate with the volumetric strain increments $d\varepsilon_v$ and degree of saturation decrement $-dS_r$ respectively.

The mean Bishop's stress p^* can be viewed as the total stress minus a weighted average of pore water pressure and pore air pressure. In the absence of meniscus water bridges it might provide an average measure of stresses transmitted through the soil skeleton (like effective stress in saturated soils) and it is sometimes termed the "average soil skeleton stress" (Jommi, 2000). It does not include, however, the influence on the mechanical behaviour of the stabilising effect of the inter-particle meniscus water bridges. This influence of meniscus water bridges on mechanical behaviour is represented in the Wheeler et al. (2003) model through the role of plastic changes of degree of saturation (see below), which in turn are linked (through the water retention behaviour) to the second stress variable of modified suction s^*.

2.6.2. Yield surfaces, plastic mechanisms and couplings

The model of Wheeler et al. (2003) describes the mechanical and retention behaviour by two different plastic mechanisms that can be activated during loading, wetting or drying processes. One plastic mechanism is associated with slippage at inter-particle or inter-packet contacts, resulting in the occurrence of plastic volumetric strains. The other plastic mechanism is associated with flooding or emptying of voids with water, resulting in plastic changes of degree of saturation. These two plastic mechanisms, along with the couplings between them and the choice of stress state variables, are key features of the description of the interactions between the mechanical and the water retention behaviour.

The plastic mechanisms of the model are described by three different yield curves (Figure 2-16): a Loading Collapse yield curve *LC* (2.17); a Suction Increase yield curve *SI* (2.18) and a Suction Decrease yield curve *SD* (2.19).

$$F_{LC} = p^* - p_0^* = 0 \qquad (2.\ 17)$$

$$F_{SI} = s^* - s_I^* = 0 \qquad (2.\ 18)$$

$$F_{SD} = s_D^* - s^* = 0 \qquad (2.\ 19)$$

where p_0* is the hardening parameter defining the location of the *LC* yield curve and s_I^* and s_D^* are the hardening parameters defining the locations of the *SI* and *SD* yield curves respectively (see Figure 2-16).

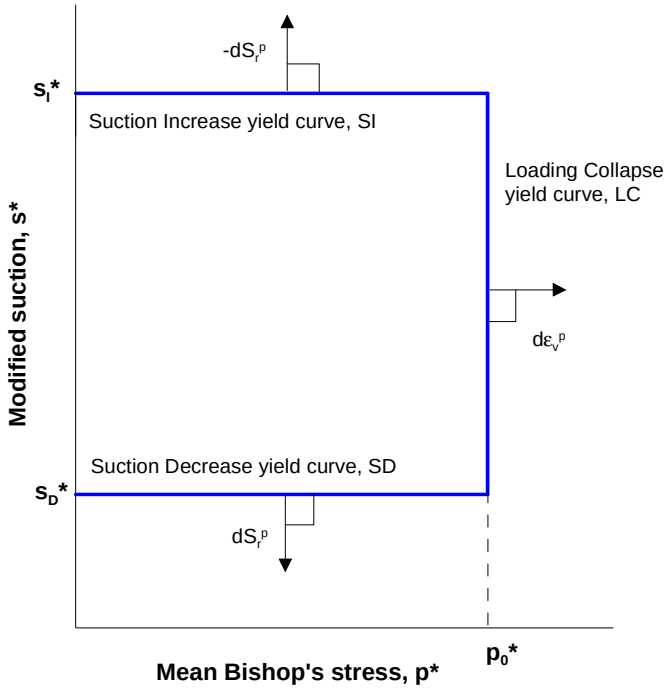

Figure 2- 16 Yield curves for isotropic stress states (Wheeler et al., 2003).

Yielding on the *LC* curve alone is associated with inter-particle or inter-aggregate slippage and causes plastic volumetric strain but no plastic change of degree of saturation. This yielding produces coupled upward movements of *SI* and *SD* curves which are controlled by a coupling parameter k_2:

$$\frac{ds_D^*}{s_D^*} = \frac{ds_I^*}{s_I^*} = k_2 \frac{dp_0^*}{p_0^*} \qquad (2.\ 20)$$

The coupled movements of *SD* and *SI* curves caused by yielding on the *LC* curve are illustrated in Figure 2-17. This is a key feature of how the model accounts for the influence of changes of void ratio (i.e. mechanical behaviour) on the water retention behaviour. More precisely, the occurrence of plastic volumetric strain while yielding on the *LC* curve reduces the dimensions of the voids and of the connecting passageways between voids, which increases the value of suction required for flooding or emptying of voids with water. This is represented in the model by upward movements of the *SD* and *SI* yield curves, which represent a shift in the main wetting and drying retention curves to higher suctions (see below).

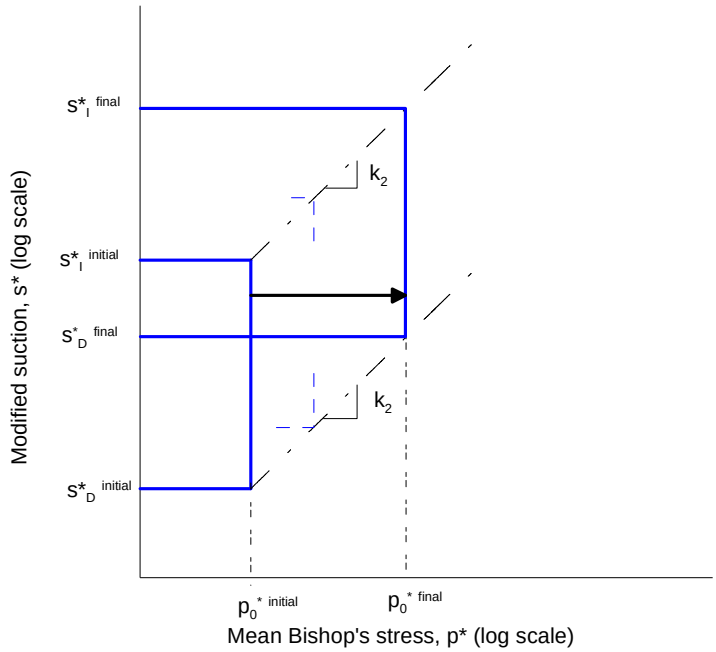

Figure 2- 17 Coupled movements of SD and SI yield curves caused by yielding on the LC yield curve (after Wheeler et al. 2003).

Coupling in the other direction (water retention influencing mechanical behaviour) is controlled by a second coupling parameter k_1 and it is considered in the model as follows. Yielding on the *SI* curve alone is associated with emptying of voids with water and causes plastic decreases of S_r but no plastic volumetric strains. This irreversible decrease of S_r produces a coupled upward movement of the *SD* curve and a coupled outward movement of the *LC* curve. The coupled upward movement of the *SD* curve maintains a constant spacing between *SI* and *SD* curves when s^* is plotted on a logarithmic scale:

$$\frac{ds_D^*}{s_D^*} = \frac{ds_I^*}{s_I^*} \qquad (2.\ 21)$$

The coupled outward movement of the *LC* curve is controlled by k_1:

$$\frac{dp_0^*}{p_0^*} = k_1 \frac{ds_I^*}{s_I^*} \qquad (2.\ 22)$$

These coupled movements are illustrated in Figure 2-18a. Finally, yielding on the *SD* curve alone is associated with flooding of voids with water and causes plastic increments of S_r but no plastic volumetric strains (equivalently to yielding on the *SI* curve alone). This yielding produces a coupled downward movement of the *SI* curve (proportional to the amount of yielding occurred on *SD*, (2.21)) and a coupled inward movement of the *LC* curve (2.22) controlled by k_1 (see Figure 2-18b). The occurrence of inelastic changes of degree of saturation affects the number of meniscus water bridges at inter-particle contacts and, therefore, modifies the stability of the soil skeleton.

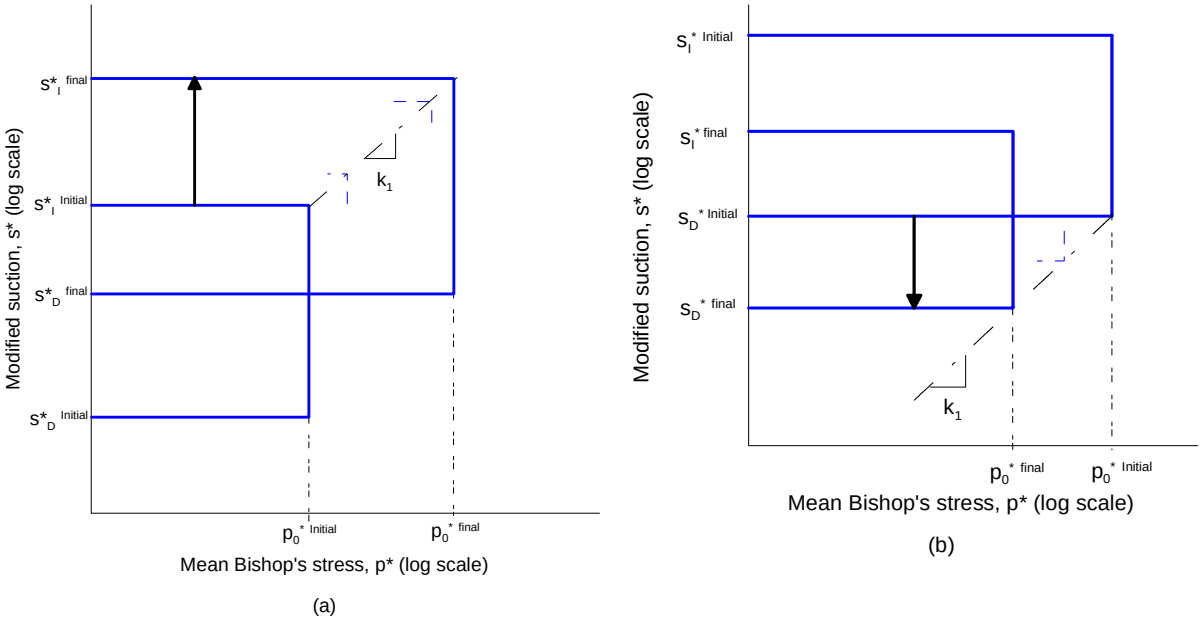

Figure 2- 18 (a) Coupled movements of SD and LC yield curves caused by yielding on SI curve; (b) coupled movements of SI and LC yield curves caused by yielding on SD curve (after Wheeler et al., 2003).

2.6.3. Elastic and plastic relationships and flow rules

Any isotropic stress path lying within the elastic domain defined by the three yield curves shown in Figure 2-16 will experience elastic variations of the volumetric strain and degree of saturation given by:

$$d\varepsilon_v^e = \frac{\kappa dp^*}{vp^*} \qquad (2.\ 23)$$

$$dS_r^e = -\frac{\kappa_s ds^*}{s^*} \qquad (2.\ 24)$$

where κ and κ_s are two elastic constants. An interesting consequence of these two equations is that elastic volumetric strains occur solely as a consequence of change of the mean Bishop's stress and, equivalently, elastic variations of the degree of saturation occur solely as a consequence of the changes of modified suction.

When the stress path reaches one of the three yield curves and overcomes it, yielding on this yield curve takes place and plastic changes of either volumetric strain or degree of saturation associated with yielding on the particular curve are computed. Plastic volumetric strains caused by yielding on the *LC* curve alone are given by:

$$d\varepsilon_v^p = \frac{(\lambda - \kappa)\, dp_0^*}{v p_0^*} \qquad (2.\ 25)$$

where λ is the slope of the normal compression line for saturated conditions. The flow rule for the *LC* curve corresponds to:

$$\frac{dS_r^p}{d\varepsilon_v^p} = 0 \qquad (2.\ 26)$$

Plastic changes of the degree of saturation caused by yielding on the *SI* or *SD* curve alone are given by:

$$dS_r^p = \frac{-(\lambda_s - \kappa_s)\, ds_I^*}{s_I^*} = \frac{-(\lambda_s - \kappa_s)\, ds_D^*}{s_D^*} \qquad (2.\ 27)$$

where λ_s is the gradient of the main wetting/drying curve in the S_r:ln s^* plane (see Figure 2-19). The flow rule for the *SI* and *SD* curves corresponds to:

$$\frac{d\varepsilon_v^p}{dS_r^p} = 0 \qquad (2.\ 28)$$

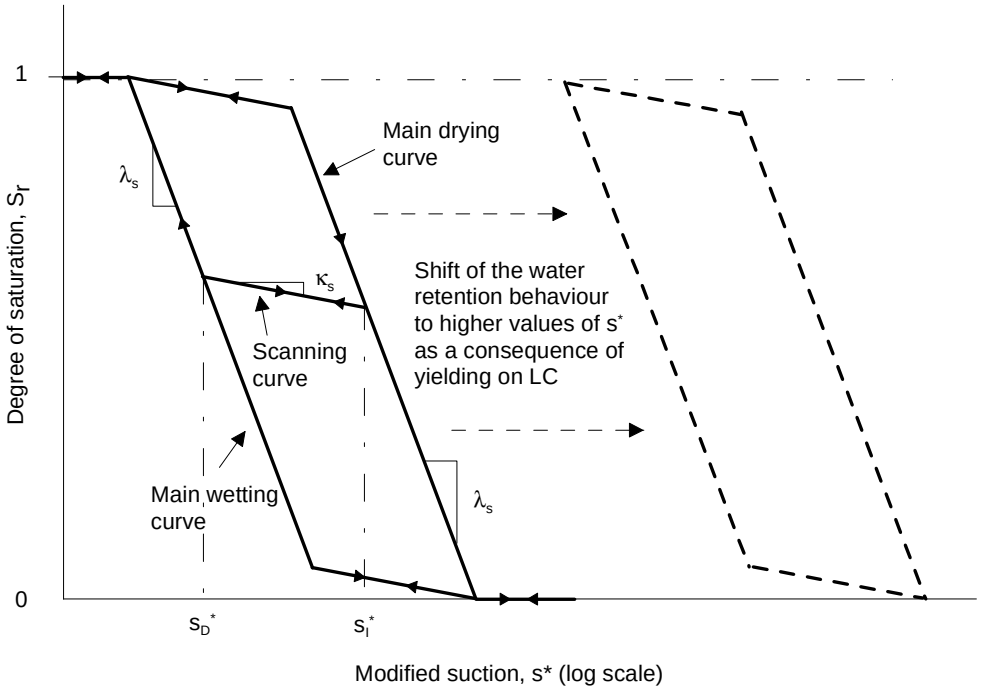

Figure 2- 19 Water retention model showing the shift to the right produced by plastic volumetric strains (after Wheeler et al., 2003).

Figure 2-19 illustrates the elasto-plastic representation of water retention behaviour within the model. The parameter κ_s gives the slope of elastic scanning curves in the S_r:lns^* plane, while λ_s is the corresponding gradient of the main wetting/drying curves. The values of the hardening parameters s_D^* and s_I^*, defining the locations of the *SD* and *SI* yield curves in the s^*:p^* plane (see Figure 2-16), change when moving along the main wetting curve or main drying curve (when yielding on the *SD* or *SI* yield curves). In particular, it can be observed in this plot that, in the absence of plastic volumetric strains as a consequence of yielding on *LC* curve, the values of the hardening parameters s_D^* and s_I^* decrease while wetting on the main wetting curve and increase when drying on the main drying curve but have limiting minimum and maximum values when the degree of saturation reaches 1 or 0.

Figure 2-19 also illustrates how the model accounts for the influence of plastic volumetric strains on the water retention behaviour. This is represented by shifting the main wetting/drying curves to higher values of modified suction when yielding on the *LC* yield curve takes place (see Figure 2-17). This shift is controlled by the coupling parameter k_2 as it defines the amount of coupled upward movement of *SD* and *SI* curves when yielding on the *LC* curve alone occurs (see Section 2.6.2).

It is important to note here a small inconsistency in the Wheeler et al. (2003) model identified in Raveendiraraj (2009) and associated with any occurrence of plastic

volumetric strains while the soil is fully saturated (i.e. S_r=1) or fully dry (i.e. S_r=0). This inconsistency is a consequence of a predicted irreversibility of subsequent elastic changes of S_r if plastic volumetric strains occur when the soil is either fully saturated or fully dry. The problem occurs because the model includes elastic changes of S_r when the soil is unsaturated, but assumes that the elastic changes of S_r are zero whenever S_r is 1 or 0 (see Figure 2-19). One way to overcome this problem is by simply assuming κ_s=*0* (so that elastic changes of S_r are always zero), but this leads, however, to a rather unrealistic modelling of the water retention behaviour. In order to better resolve this problem further research is required. A detailed discussion on these issues is given in Raveendiraraj (2009). It is also important to highlight here that in the work presented in the remainder of this thesis, the soil state remains unsaturated (i.e. $0<S_r<1$) and, therefore, this inconsistency has no direct effect on the analyses and results developed.

2.6.4. Hardening laws

In general, the overall movement of the *LC* yield curve is the result of a combination of two components: a direct one (due to any yielding on the *LC* curve itself) given by Equation (2.25) and a coupled one (due to any plastic change of degree of saturation) given by (2.22) and (2.27). The sum of these two components of movement governs the variation of the location of the *LC* yield curve and results in the following hardening rule:

$$dp_0^* = p_0^* \left[\frac{v d\varepsilon_v^p}{\lambda - \kappa} - \frac{k_1 dS_r^p}{\lambda_s - \kappa_s} \right] \qquad (2.29)$$

Similarly, the overall movements of the *SD* and *SI* yield curves are the result of two components: a direct one (due to any yielding on *SD* or *SI*) given by equation (2.27) and a coupled one (due to any plastic volumetric strain) given by (2.20) and (2.25). The sum of these two components of movement governs the variation of the location of the *SD* or *SI* yield curves and results in the second hardening rule:

$$ds_\beta^* = s_\beta^* \left[-\frac{dS_r^p}{\lambda_s - \kappa_s} + k_2 \frac{v d\varepsilon_v^p}{\lambda - \kappa} \right] \qquad \beta = SI / SD \qquad (2.30)$$

It is interesting to note that when yielding on the *LC* curve alone takes place, the movement of the *LC* curve is governed by (2.29) but with dS_r^p equal to 0. Similarly, the hardening rule associated with yielding on the *SD* or *SI* curve alone is given by (2.30) with $d\varepsilon_v^p$ equal to 0.

Equations (2.29) and (2.30) show the possibility of having two plastic mechanisms acting simultaneously, which occurs either when simultaneous yielding on *LC* and on *SD* takes place (i.e. the stress path has reached the bottom corner of Figure 2-16) or when simultaneously yielding on *LC* and *SI* (i.e. the stress path has reached the top corner of Figure 2-16). In both cases plastic volumetric strains and plastic changes of degree of saturation are developed. In such cases, Equations (2.29) and (2.30) can be combined (Wheeler et al. 2003) to show that the plastic increments of volumetric strain and degree of saturation are related to the movements of the yield curves by:

$$d\varepsilon_v^p = \frac{(\lambda-\kappa)}{v(1-k_1k_2)}\left(\frac{dp_0^*}{p_0^*}-k_1\frac{ds_I^*}{s_I^*}\right)=\frac{(\lambda-\kappa)}{v(1-k_1k_2)}\left(\frac{dp_0^*}{p_0^*}-k_1\frac{ds_D^*}{s_D^*}\right) \qquad (2.31)$$

$$dS_r^p = \frac{-(\lambda_s-\kappa_s)}{(1-k_1k_2)}\left(\frac{ds_I^*}{s_I^*}-k_2\frac{dp_0^*}{p_0^*}\right)=\frac{-(\lambda_s-\kappa_s)}{(1-k_1k_2)}\left(\frac{ds_D^*}{s_D^*}-k_2\frac{dp_0^*}{p_0^*}\right) \qquad (2.32)$$

2.7. Variation of v and S_r during simultaneous yielding on LC and SD

Simulations performed with the model of Wheeler et al. (2003), or even simply consideration of how the model behaves, soon leads to a conclusion that there are a wide variety of isotropic stress paths for which the stress point will ultimately arrive at the corner between *LC* and *SD* yield curves and subsequently lead to simultaneous yielding on *LC* and *SD*. For example, many "loading" paths will arrive first at the *LC* yield curve, but yielding on *LC* will then produce coupled upward movement of the *SD* yield curve, until the *SD* curve too is brought up to the stress point and then simultaneous yielding on *SD* commences. Similarly, many "wetting" stress paths will arrive first at the *SD* yield curve, but yielding on *SD* will then produce coupled inward movement of the *LC* yield curve, until the *LC* curve too is brought to the stress point and then simultaneous yielding on *LC* commences (this is the onset of collapse compression on wetting). Basically, any "loading" or "wetting" stress path which shows both substantial (i.e. plastic) volumetric straining and substantial (i.e. plastic) increase of degree of saturation involves simultaneous yielding on *LC* and *SD*. This can even involve loading paths involving modest increases of suction or wetting paths involving modest decreases of mean net stress.

In Section 2.7.2 it is shown that the model of Wheeler et al. (2003) implies that when simultaneous yielding on *LC* and *SD* is occurring there will be a unique relationship linking specific volume *v* to mean Bishop's stress p^* and modified suction s^*, and a second unique relationship linking degree of saturation S_r to p^* and s^*. These two relationships were first

derived by Wheeler (2009) and they define two planar surfaces, one in v:lnp^*:lns^* space and one in S_r:lnp^*:lns^* space. The equations are developed with the limitation that the soil remains under unsaturated conditions (i.e. $0<S_r<1$). This condition is to avoid the small inconsistency of the model discussed in Section 2.6.3 (irreversibility of elastic changes of S_r if plastic volumetric strains occur when the soil is fully saturated or fully dry). In Section 2.7.3, the model prediction of unique planar surfaces in v:lnp^*:lns^* space and in S_r:lnp^*:lns^* space during simultaneous yielding on *LC* and *SD* is validated by comparing with the results of Sivakumar (1993) on compacted speswhite kaolin. Finally, in Section 2.7.4, a new methodology is proposed to determine the values of the soil parameters in the model of Wheeler et al. (2003) from experimental data, and this is demonstrated with the experimental data of Sivakumar (1993).

2.7.1. Range of isotropic stress paths for which simultaneous yielding on LC and SD will occur

There are a surprisingly wide range of isotropic stress paths for which simultaneous yielding on *SD* and *LC* curves is predicted by the Wheeler et al. (2003) model. Consider a general starting point in stress space, defined in the lns^*:lnp^* plane, and then a variety of different stress paths from this starting point, with each stress path following a straight line in the lns^*:lnp^* plane. In most cases, the stress path will first arrive at one of the three yield curves (*LC*, *SD* or *SI*). However, if the stress path is continued indefinitely, in many cases the path will subsequently arrive at a corner between two yield curves (*LC* and *SD* or *LC* and *SI*) and this may then be followed by simultaneous yielding on the two curves. Figure 2-20 shows the ultimate situation that will be achieved if a given stress path direction in the lns^*:lnp^* plane is maintained indefinitely. Radial stress path directions in the lns^*:lnp^* plane can be divided into 6 different regions, one corresponding to elastic behaviour maintained indefinitely, three corresponding to yielding on a single curve (*LC*, *SD* or *SI*) maintained indefinitely, and two corresponding to yielding on two curves (*LC* and *SD* or *LC* and *SI*) ultimately achieved and then subsequently maintained indefinitely.

It is interesting to note that there is only a single unique stress path direction (decrease of lnp^* at constant lns^*) that can maintain elastic behaviour indefinitely. Similarly, there is only a single unique stress path direction (increase of both lnp^* and lns^*, with a stress path gradient of k_2 in the lns^*:lnp^* plane) that can maintain yielding on the *LC* yield curve alone indefinitely. It is also interesting to note that, whereas there is a fairly narrow range of stress path directions that will ultimately lead to simultaneous yielding on *LC* and *SI* maintained indefinitely, there is a very wide range of stress path directions that will ultimately lead to simultaneous yielding on *LC* and *SD* maintained indefinitely.

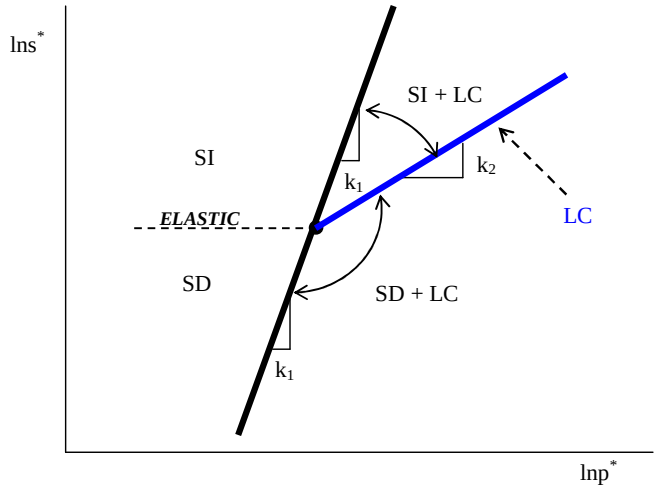

Figure 2- 20 Ultimate activation of yield curves if a constant gradient stress path in the lns:lnp* plane is maintained indefinitely.*

2.7.2. Predicted variation of v and S_r during simultaneous yielding on LC and SD

From (2.31) and (2.32), expressing plastic changes of $d\varepsilon_v^p$ and dS_r^p, and assuming simultaneously yielding on *LC* and *SD* (i.e. $p_0^*=p^*$ and $s_D^*=s^*$), the following expressions giving the plastic increments of specific volume dv^p and degree of saturation dS_r^p can be developed:

$$dv^p = \frac{-(\lambda-\kappa)}{(1-k_1k_2)}\left(\frac{dp^*}{p^*}-k_1\frac{ds^*}{s^*}\right) \qquad (2.\ 33)$$

$$dS_r^p = \frac{-(\lambda_s-\kappa_s)}{(1-k_1k_2)}\left(\frac{ds^*}{s^*}-k_2\frac{dp^*}{p^*}\right) \qquad (2.\ 34)$$

To find expressions for the total increments of v and S_r it is necessary to combine elastic components from (2.23) and (2.24) with the plastic components from (2.33) and (2.34) to give:

$$dv = dv^e + dv^p = -\kappa\frac{dp^*}{p^*} - \frac{(\lambda-\kappa)}{(1-k_1k_2)}\left(\frac{dp^*}{p^*}-k_1\frac{ds^*}{s^*}\right) \qquad (2.\ 35)$$

$$dS_r = dS_r^e + dS_r^p = -\frac{\kappa_s ds^*}{s^*} - \frac{(\lambda_s-\kappa_s)}{(1-k_1k_2)}\left(\frac{ds^*}{s^*}-k_2\frac{dp^*}{p^*}\right) \qquad (2.\ 36)$$

Integrating Equation (2.35), it is possible to develop the following equation giving the evolution of the specific volume v in terms of p^* and s^* when simultaneous yielding on *LC* and *SD* is occurring:

$$v = N^* - \lambda^* \ln p^* + k_1^* \ln s^* \qquad (2.37)$$

where:

$$\lambda^* = \kappa + \frac{\lambda - \kappa}{(1 - k_1 k_2)} = \frac{\lambda - \kappa k_1 k_2}{(1 - k_1 k_2)} \qquad (2.38)$$

$$k_1^* = k_1 \frac{\lambda - \kappa}{1 - k_1 k_2} \qquad (2.39)$$

and N^* is a soil constant. λ^* and k_1^* are two soil constants giving the gradients of a unique normal compression planar surface defined by (2.37) in v:lnp^*:lns^* space. Note that both constants, giving the gradients of this planar surface, are expressed as a combination of the original soil parameters λ, κ, k_1 and k_2 defined in the model, and therefore do not increase the number of independent constants in the model. A representation of this planar surface is given in Figure 2-21.

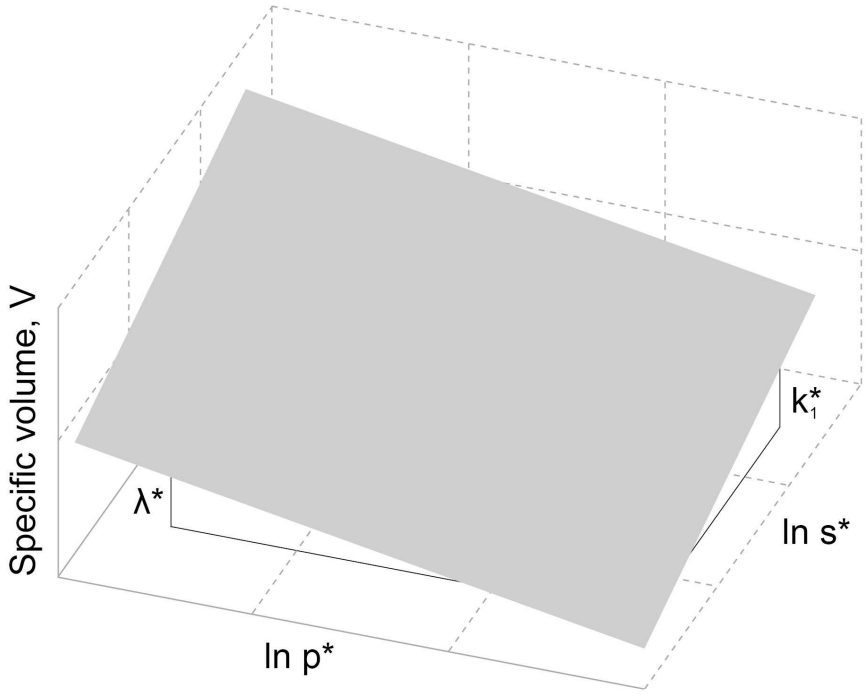

Figure 2- 21 Unique planar surface in v:lnp:lns* space when simultaneously yielding on LC and SD.*

Similarly, Equation (2.36) can be integrated to give an equation expressing the evolution of the degree of saturation in terms of p^* and s^* when simultaneous yielding on *LC* and *SD* is active, is occurring:

$$S_r = \chi^* - \lambda_s^* \ln s^* + k_2^* \ln p^* \qquad (2.40)$$

where

$$\lambda_s^* = \frac{\lambda_s - \kappa_s}{1 - k_1 k_2} + \kappa_s = \frac{\lambda_s - \kappa_s k_1 k_2}{1 - k_1 k_2} \qquad (2.41)$$

$$k_2^* = k_2 \frac{(\lambda_s - \kappa_s)}{(1 - k_1 k_2)} \qquad (2.42)$$

and χ^* is a soil constant. λ_s^* and k_2^* are two soil constants giving the gradients of a second unique planar surface (2.40), this time in S_r:lnp^*:lns^* space. λ_s^* and k_2^* are expressed as a combination of the original soil constants λ_s, κ_s, k_1 and k_2 defined in the model. A representation of this planar surface is given in Figures 2-22.

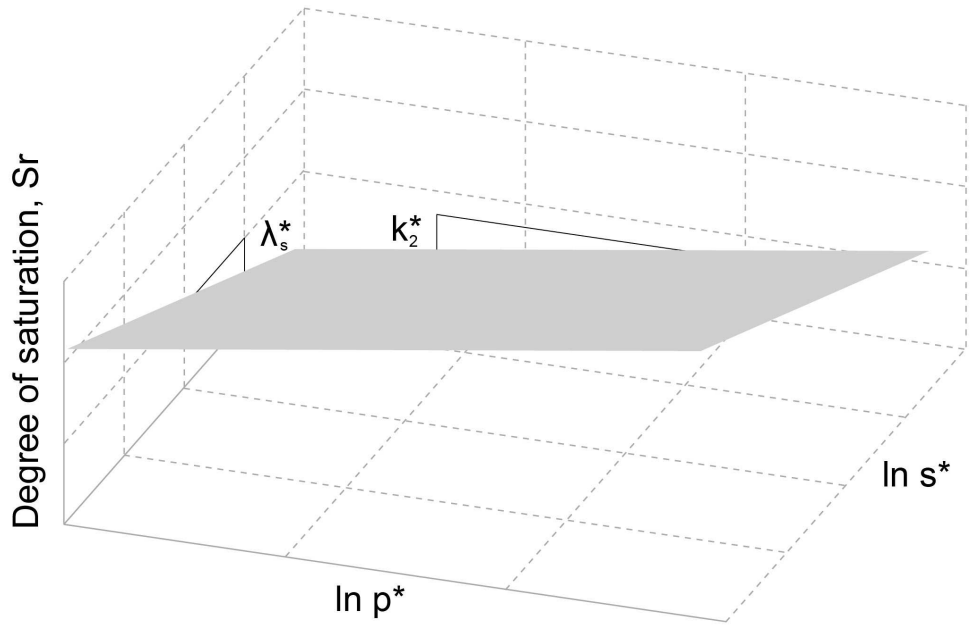

Figure 2- 22 Unique planar surface in S_r:lnp^*:lns^* space when simultaneously yielding on LC and SD.

In order to better emphasize some of the implications of the proposed pair of unique planar surfaces, and to illustrate how different stress paths traverse the surfaces, two different sets of basic stress paths are now considered.

Figure 2-23 shows 4 loading paths involving increase of p^* at four different values of modified suction (s_A^*, s_B^*, s_C^* and s_D^*). The initial locations of the *LC*, *SD* and *SI* yield curves are the same in all four cases. Figure 2-23a shows the stress paths (in the $\ln s^*$:$\ln p^*$ plane) and Figures 2-23b and 2-23c show the predicted variations of v and S_r respectively (both plotted against $\ln p^*$). In each case, yield point Y_1 represents yielding on the *LC* yield curve, and yield point Y_2 represents yielding on the *SD* curve. The initial stress state for sample *A* is on the *SD* curve, and in this case yielding on *LC* and *SD* commences simultaneously. In the other 3 cases the initial stress state is inside the *SD* yield curve and yielding on the *SD* curve commences at a later point than yielding on the *LC* curve (once the yielding on the *LC* curve has caused sufficient coupled upward movement of the *SD* curve to bring the *SD* curve up to the stress point). When yielding is occurring on the *LC* curve alone, the predicted variations of v and S_r (shown in Figures 2-23b and 2-23c respectively) have gradients of λ and zero respectively. However, once yielding is occurring on both *LC* and *SD* simultaneously, the variations of v and S_r (shown in Figures 2-23b and 2-23c respectively) have gradients of λ^* and k_2^* respectively. These lines of gradient λ^* and k_2^* in Figures 2-23b and 2-23c respectively represent cross sections taken at constant s^* of the two unique planar surfaces shown in Figures 2-21 and 2-22.

Figure 2-24 shows 4 wetting paths involving decrease of s^* at four different values of mean Bishop's stress (p_A^*, p_B^*, p_C^* and p_D^*). The initial locations of the *LC*, *SD* and *SI* yield curves are the same in all four cases. Figure 2-24a shows the stress paths (in the $\ln s^*$:$\ln p^*$ plane) and Figures 2-24b and 2-24c show the predicted variations of S_r and v respectively (both plotted against $\ln s^*$). In each case, yield point Y_1 represents yielding on the *SD* yield curve, and yield point Y_2 represents yielding on the *LC* curve. The initial stress state for sample *A* is on the *LC* curve, and in this case yielding on *LC* and *SD* commences simultaneously. In the other three cases the initial stress state is inside the *LC* yield curve and yielding on the *LC* curve commences at a later point than yielding on the *SD* curve (once the yielding on the *SD* curve has caused sufficient coupled inward movement of the *LC* curve to bring the *LC* curve to the stress point). When yielding is occurring on the *SD* curve alone, the predicted variations of S_r and v (shown in Figures 2-24b and 2-24c respectively) have gradients of λ_s and zero respectively. However, once yielding is occurring on both *LC* and *SD* simultaneously, the variations of S_r and v (shown in Figures 2-24b and 2-24c respectively) have gradients of λ_s^* and k_1^* respectively. These lines of gradients λ_s^* and k_1^* in Figures 2-24b and 2-24c respectively represent cross sections taken at constant p^* of the two unique planar surfaces shown in Figures 2-21 and 2-22.

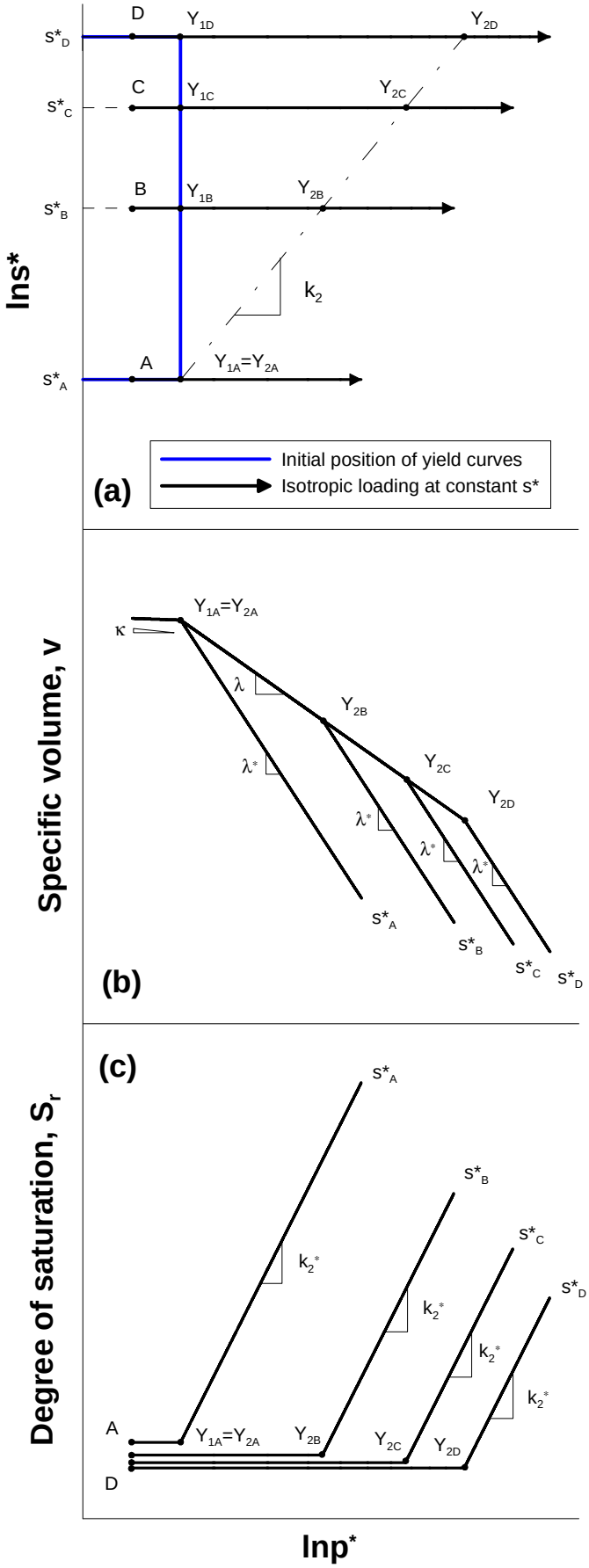

Figure 2- 23 Model response for isotropic loading paths at constant s^*.

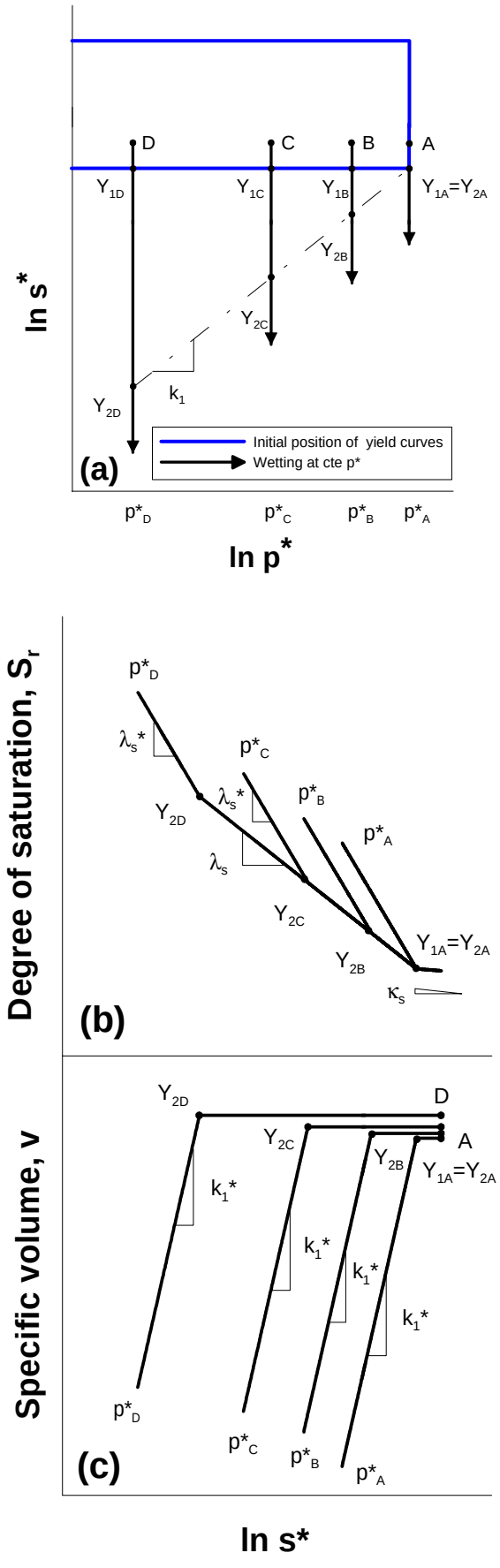

Figure 2- 24 Model response for isotropic wetting paths at constant p^*.

2.7.3. Experimental validation

It has been shown that (2.37) defines a unique planar surface in the semi-log space v:lnp^*:lns^* (see Figure 2-21). Similarly, (2.40) defines a second unique planar surface in the space S_r:lnp^*:lns^* (see Figure 2-22). This section, presents the experimental data of Sivakumar (1993) from constant suction isotropic loading of compacted speswhite kaolin in these spaces (i.e. v:lnp^*:lns^* and S_r:lnp^*:lns^*) and it is shown that these results lie on planar surfaces as predicted by the model.

Seventeen different isotropic compression test stages at constant non-zero values of suction were carried out by Sivakumar (1993) on samples of compacted speswhite kaolin. The results of these tests stages have been used in this work to explore the validity of the proposed relationships ((2.37) and (2.40)). A significant increase of S_r and decrease of v was observed when comparing the initial and the final states of each of these isotropic compression test stages (Sivakumar, 1993). Hence, according to the Wheeler et al. (2003) model, it is reasonable to assume that the soil state had arrived at the corner between the *LC* and *SD* yield curves at the end of each isotropic constant suction compression stage.

As part of the analysis, these final states have been plotted in the v:lnp^*:lns^* and S_r:lnp^*:lns^* spaces (see Figures 2-25 and 2-26). The least-square multi-regression method implemented in MATLAB has been used to best fit these experimental final states to planar surfaces, giving the following result:

$$v = 2.768 - 0.257 \ln p^* + 0.172 \ln s^* \qquad (2.43)$$

$$S_r = 0.755 - 0.206 \ln s^* + 0.159 \ln p^* \qquad (2.44)$$

From where, by comparison with (2.37) and (2.40), the values of the parameters N^*, χ^*, λ^*, λ_s^*, k_1^* and k_2^* are as summarised in Table 2.1.

Table 2. 1 Model parameter values for defining planar surfaces for compacted speswhite kaolin (Sivakumar, 1993).

N^*=2.768	λ^*=0.257	k_1^*=0.172
χ^*=0.755	λ_s^*=0.206	k_2^*=0.159

As mentioned these pair of relationships form two different planar surfaces in the v:lnp^*:lns^* and S_r:lnp^*:lns^* spaces, as illustrated in Figures 2-25 and 2-26, where the experimental results (represented as symbols) have also been plotted.

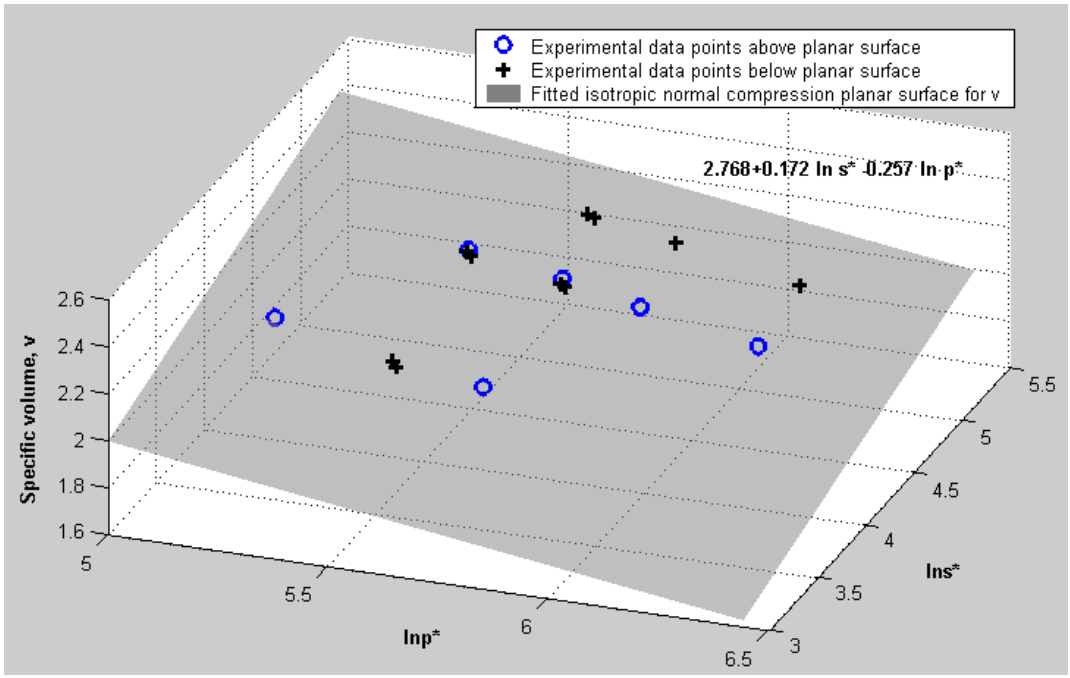

Figure 2- 25 Planar surface for v fitted to experimental results of Sivakumar (1993) at final states of isotropic compression.

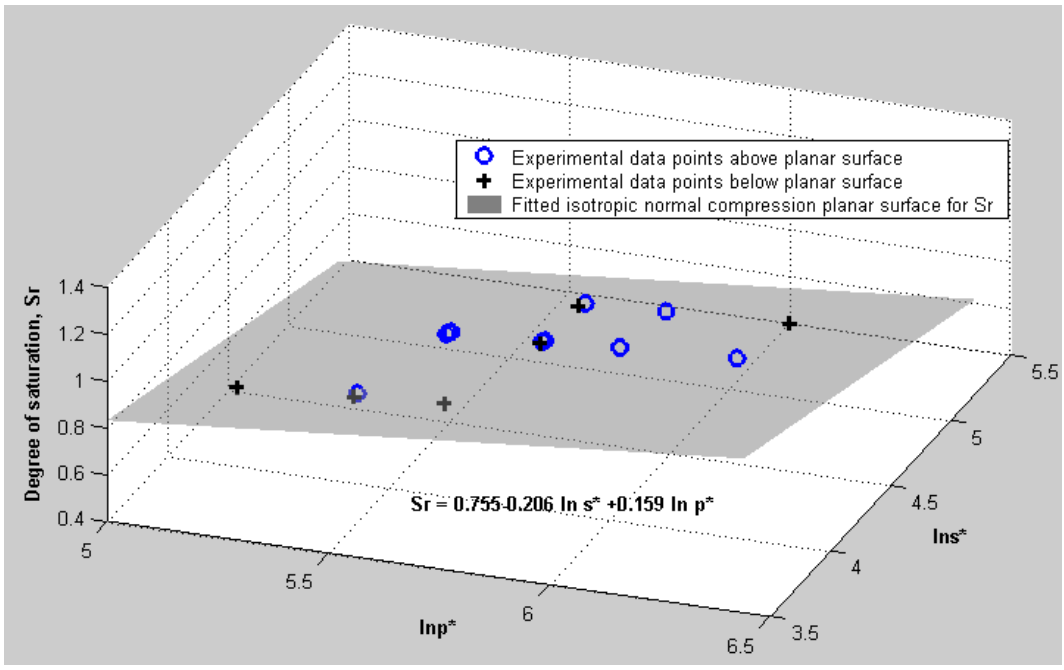

Figure 2- 26 Planar surface for S_r fitted to experimental results of Sivakumar (1993) at final states of isotropic compression.

It is difficult, from inspection of Figures 2-25 and 2-26, to form a visual impression of how well the two planar surfaces fit the experimental data. To aid this, the fitted relationships describing the planar surfaces and the corresponding experimental data have been re-plotted in Figures 2-27 and 2-28. Each of these figures is in two parts, essentially

representing a pair of orthogonal two-dimensional views of the planar surface. For example, Figure 2-27a shows v-0.172lns^* plotted against lnp^* (where 0.172 is the fitted value of k_1^*) and Figure 2-27b shows v+0.257lnp^* plotted against lns^* (where 0.257 is the fitted value of λ^*). In these two parts of Figure 2-27, the fitted planar surface for v has been reduced in each case to a single straight line, and it is now easy to gauge how well the planar surface fits the experimental data points. Inspection of Figures 2-27 and 2-28 indicates that the two planar surfaces (for v and S_r) provide excellent fits to the experimental results of Sivakumar (1993) at final states of isotropic compression.

The fact that the planar surfaces for v and S_r described by Equations (2.43) and (2.44) provide an excellent match to the experimental results of Sivakumar (1993) is a significant component of experimental validation of the Wheeler et al. (2003) model. The predicted existence and predicted form of the two unique planar surfaces arises from the combination of several key components of the model, most notably the existence and assumed mathematical forms of the two coupling relationships in the model (Equations (2-20), (2.21) and (2-22)). The results presented in Figures 2-25 – 2-28 therefore provide important experimental validation of, amongst other things, the specific mathematical forms selected for the coupling relationships (something that was not clear at the time of the original formulation of the model by Wheeler et al., 2003).

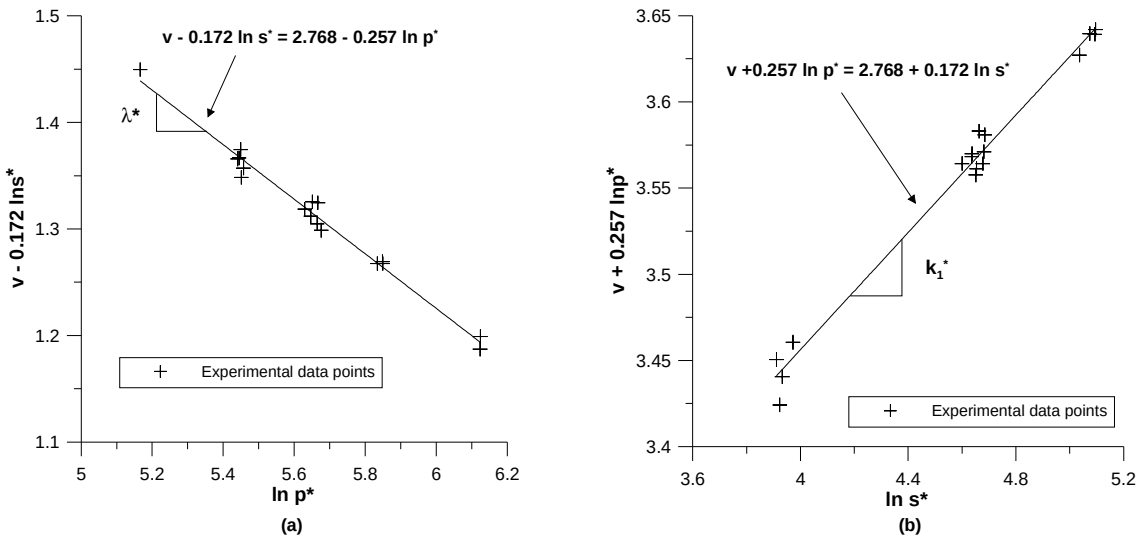

Figure 2- 27 Orthogonal two-dimensional views of planar surface for v compared with experimental results.

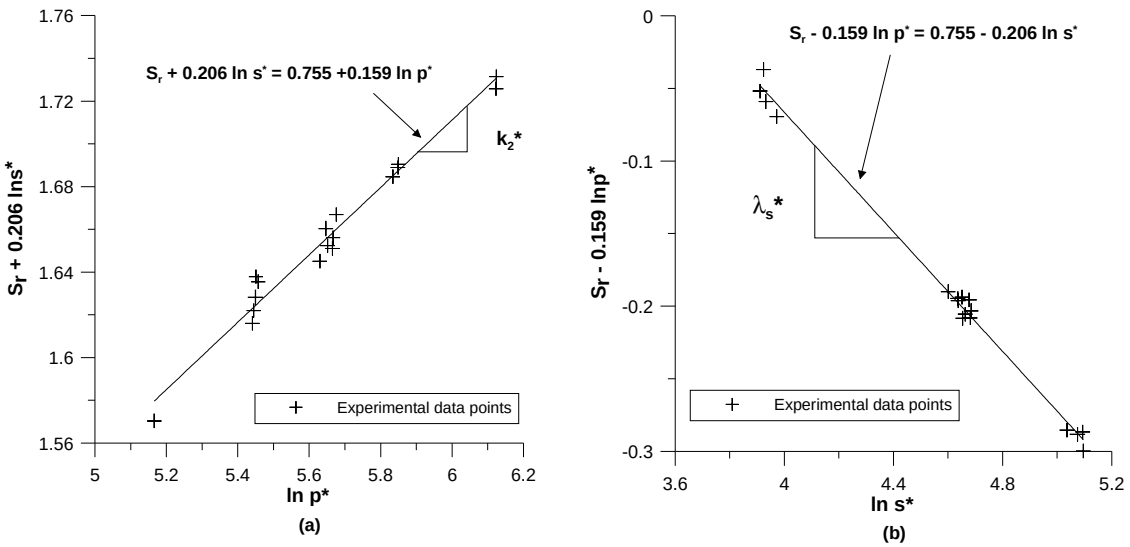

Figure 2- 28 Orthogonal two-dimensional views of planar surface for S_r compared with experimental results.

2.7.4. Determination of model parameter values

As detailed in this section, plotting experimental results at the end of isotropic normal compression stages in v:lnp^*:lns^* and S_r:lnp^*:lns^* spaces presents an ideal methodology for the determination of the soil parameters defined in the Wheeler et al. (2003) model.

To illustrate the proposed method the same seventeen experimental isotropic loading stages at constant non-zero values of suction presented in Sivakumar (1993) (and just introduced in the previous section) are employed i.e. the methodology is described by applying it in the estimation of the model parameter values for the soil tested by Sivakumar (1993). Also the initial state of the soil, including the initial values of the relevant hardening parameters, is estimated from the tests.

As previously described and illustrated (see Section 2.7.2.1), the final state of each of the experimental isotropic compression stages falls on two separate planar surfaces when plotted in the spaces v:lnp^*:lns^* (Figure 2-25) and S_r:lnp^*:lns^* (Figure 2-26). As also presented, the gradients of these two planar surfaces in two orthogonal directions provide optimised values of the four derived soil constants λ^*, k_1^*, λ_s^* and k_2^*, as summarised in Table 2.1.

Combining the expressions of these derived soil parameters (i.e. λ^*, k_1^*, λ_s^* and k_2^*) given by (2.38), (2.39), (2.41) and (2.42), and assuming that values of the soil parameters λ and κ are known from tests under saturated conditions (for the same soil), it is possible to express the remaining *unknown* soil parameters of the model (i.e. λ_s, κ_s, k_1 and k_2) in

terms of the previously estimated ones (i.e. λ^*, k_1^*, λ_s^* k_2^*, λ and κ). First, Equations (2.38) and (2.39) can be combined to given expressions for k_1 and k_2:

$$k_1 = \frac{k_1^*}{\lambda^* - \kappa} \qquad (2.45)$$

$$k_2 = \frac{\lambda^* - \lambda}{k_1^*} \qquad (2.46)$$

Once the values of k_1 and k_2 have been calculated, the values of λ_s and κ_s can be determined by combining Equations (2.41) and (2.42):

$$\lambda_s = \lambda_s^* - k_1 k_2^* \qquad (2.47)$$

$$\kappa_s = \lambda_s^* - \frac{k_2^*}{k_2} \qquad (2.48)$$

Note that, in this particular case, λ and κ (from the saturated conditions) are assumed to be known. However, other combinations are also possible depending on the pair of soil parameters previously estimated, in addition to the gradients of the planar surfaces previously determined (i.e. λ^*, k_1^*, λ_s^* and k_2^*). For example, if the values of κ_s and λ_s were already known (rather than the values of κ and λ) this would provide an alternative solution strategy. For this alternative approach, it would be important to appreciate that the values of κ_s and λ_s should be measured from water retention tests employing wetting and drying paths involving no plastic strains (i.e. with the stress path remaining inside the *LC* yield curve).

To proceed with the application of the preferred methodology it is now necessary to estimate the values of κ and λ for compacted speswhite kaolin tested by Sivakumar (1993). Six additional tests, carried out by Sivakumar (1993) under saturated conditions (see Figure 2-29) have been used to determine the values of κ and λ, which are presented below.

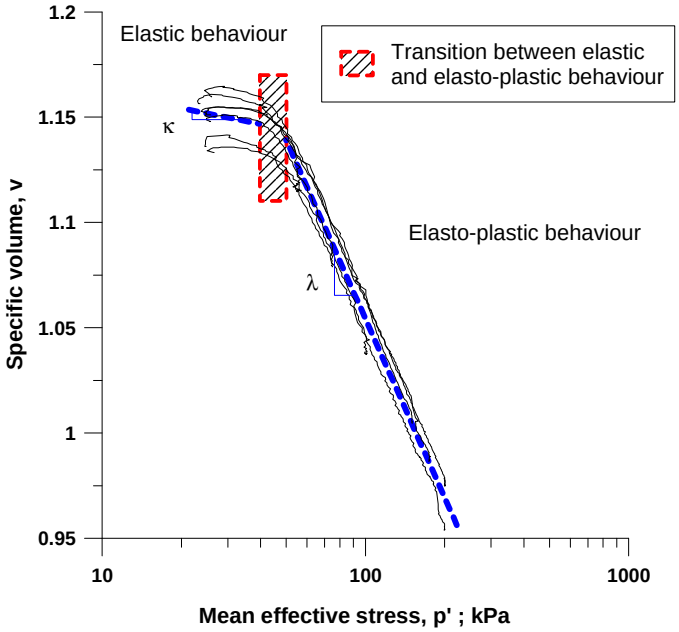

Figure 2- 29 Experimental results of isotropic loading stress paths for saturated conditions (after Sivakumar, 1993).

Figure 2-29 shows plots of six saturated isotropic compression tests used in the estimation of κ and λ. An idealisation of the approach employed to estimate these soil parameters is also included in this picture. All the compression curves from the saturated tests seem to include a pre-yield (elastic) section and a post-yield (elasto-plastic) section, with a smooth transition between. Straight lines have been fitted to each of the two sections of each curve (see Figure 2-30) with the transition section excluded from the fitting.

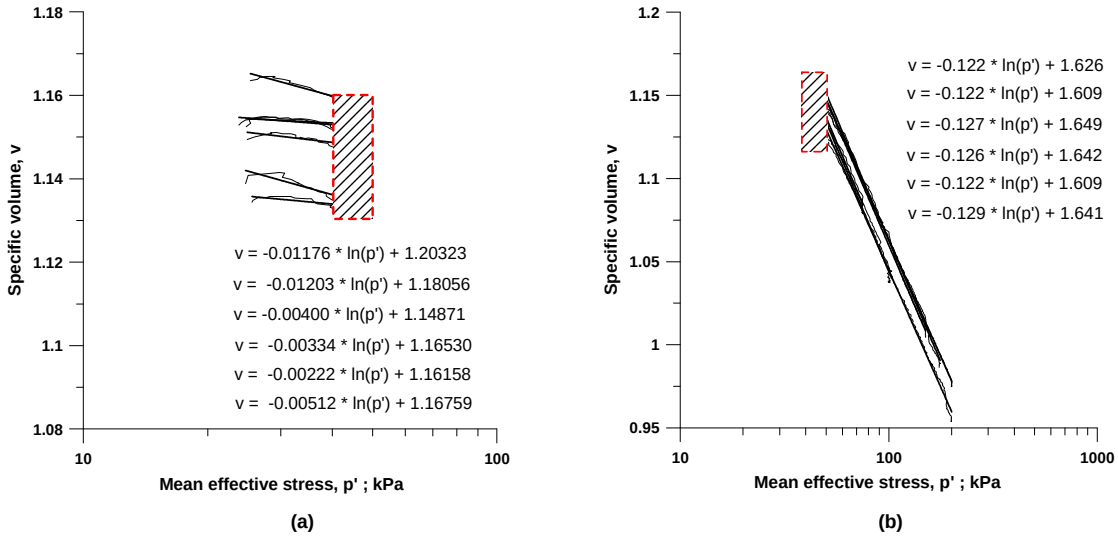

Figure 2- 30 Approximated linear relationships for saturated conditions: (a) Elastic behaviour; (b) Elasto-plastic behaviour.

Figure 2-30 presents the estimated swelling lines (Figure 2-30a) and normal compression lines (Figure 2-30b) for each of these six saturated tests of Sivakumar (1993). The average of the slopes from the six swelling lines estimated (see Figure 2-30a) and also the average of the slope from the six normal compression lines showed in Figure 2-30b are the final estimated values for κ and λ included in Table 2.2.

Combining now these values with those estimated from the planar surfaces (i.e. λ^*, k_1^*, λ_s^* and k_2^*) and using the relationships (2.45) to (2.48) the values of the rest of the soil parameters included in Table 2.2 can be estimated.

Table 2. 2 Estimated soil parameters from the experimental tests of Sivakumar (1993).

λ=*0.124*	λ_s=0.0971	κ_s=0.0004
κ=*0.006*	k_1=0.685	k_2=0.773

Also the initial state, including the values of the initial hardening parameters p_0^* and s_D^*, have been estimated from the seventeen unsaturated tests. The same initial state is considered for all the tests. This common initial state corresponds to an initial value of suction equal to the highest value of suction employed in the tests (i.e. s=300 kPa) and a mean net stress of 50 kPa (which was the value of mean net stress reached after initial equalisation; see Sivakumar, 1993). From this state, a wetting path at a constant mean net stress of 50 kPa can be initially modelled to reach the lower values of suctions at which the rest of the isotropic loadings were performed (see Figure 2-31).

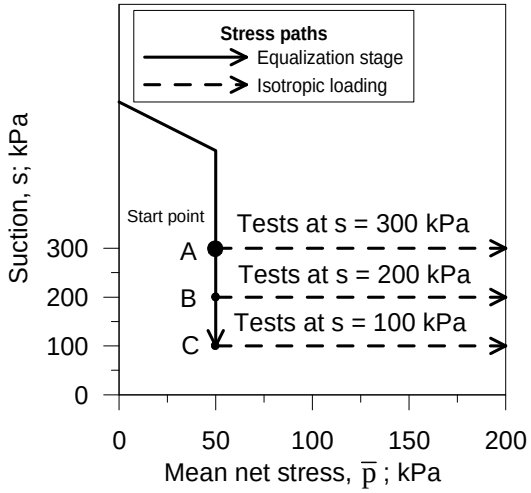

Figure 2- 31 Stress paths during equalisation and ramped isotropic consolidation stage for the tests analysed (after Wheeler and Sivakumar, 1995).

The initial values of void ratio and degree of saturation that have then been used in the analyses were therefore selected as an average of the initial values of e and S_r measured in the tests carried out at a suction of 300 kPa (see Sivakumar, 1993). The initial values of e_0 and S_{r0} obtained in this way are listed in Table 2.3 (which also includes the initial value of porosity n_0), together with the resulting initial values of mean Bishop's p^* stress and modified suction s^* (calculated from the values of e_0 and S_{r0} and the corresponding values of $\overline{p}$ and s).

Table 2. 3 Initial state.

$\overline{p}$ =50 kPa	s=300 kPa	p^*=229.1 kPa	p_0^*=271.1 kPa
e_0=1.210; n_0=0.547	S_{r0}=0.597	s^*=164.3 kPa	s_D^*=164.3 kPa

The initial values of the hardening parameters p_0^* and s_D^*, defining the initial locations of the *LC* and *SD* yield curves respectively, were determined by considering the behaviour observed during the equalisation stages. According to the model of Wheeler et al. (2003), at s=300 kPa the *SD* yield curve was already reached, because a significant increase of the degree of saturation was observed during the equalisation stages of the tests carried out at this value of suction (Sivakumar, 1993). Hence, the hardening parameter s_D^* defining the initial position of the *SD* yield curve coincides with the current value of modified suction (i.e. $s_D^*=s^*$=164.3 kPa; see Table 2.3). An estimation to determine the initial value of the remaining hardening parameter p_0^* was made by employing the information given in (2.43) and (2.44) which had not been used yet (i.e. N^*=2.768 and χ^*=0.755) in combination with the initial state previously described (see Table 2.3). Figure 2-32 illustrates the following description on how this information was used.

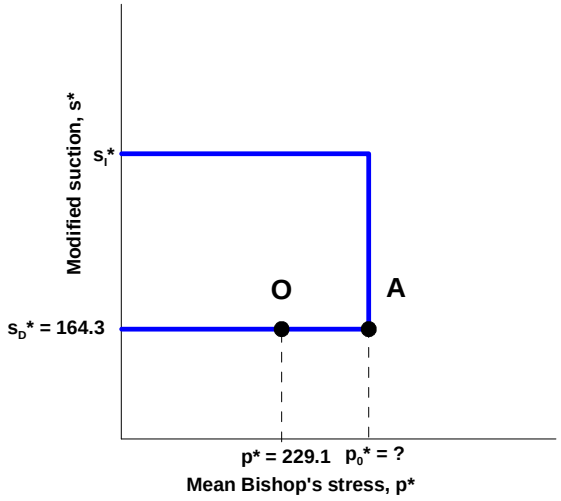

Figure 2- 32 Estimation of the initial value of the hardening parameter p_0^*.

Point *A* in Figure 2-32 is at the intersection between *LC* and *SD* yield curves and, therefore, lies on the planar surface given by (2.43):

$$v_A = 2.768 - 0.257 \ln p_0^* + 0.172 \ln 164.3 \qquad (2.49)$$

On the other hand, the increment of specific volume from *O* to *A* (Figure 2-32) is elastic and can be calculated (employing the value of the soil parameter κ from Table 2.2), so that a second independent expression for the value of v_A can be calculated by starting from the specific volume at the initial state *O* (v_0=2.210 from Table 2.3):

$$v_A = v_O - \kappa \ln \frac{p_0^*}{229.1} = 2.210 - 0.006 \ln \frac{p_0^*}{229.1} \qquad (2.50)$$

Combining (2.49) with (2.50), the calculated initial value of the hardening parameter is p_0^*=267.5 kPa.

Alternatively, point *A* in Figure 2-32 lies on the second planar surface given by (2.44):

$$S_{rA} = 0.755 - 0.206 \ln 164.3 + 0.159 \ln p_0^* \qquad (2.51)$$

Similarly, the increment of the degree of saturation from *O* to *A* (Figure 2-32) should be elastic and, therefore, zero (because no variations of modified suction take place from *A* to *O*).

$$S_{rA} = S_{rO} = 0.597 \qquad (2.52)$$

Combining (2.51) and (2.52) the obtained value of the hardening parameter is p_0^*=274.7 kPa.

The average of both estimations of the hardening parameter p_0^* gives the value included in Table 2.3

These initial values of the hardening parameters combined with the initial values of other state variables presented in Table 2.3 and the initial values of the model parameters summarised in Table 2.2 will be used in Chapter 5 to simulate the full experimental tests of Sivakumar (1993) and hence to partially validate the 3D generalised version of the constitutive model proposed by Wheeler et al. (2003) under isotropic stress paths and triaxial compression stress paths.

In summary this second part of this chapter has shown that the final states of the isotropic stages of the experiments carried out by Sivakumar (1993), when plotted in the spaces v:lnp^*:lns^* and S_r:lnp^*:lns^*, fall on two different planar surfaces (Figs. 2-25 and 2-26) as predicted by the model (i.e. (2.43) and (2.44)). This interesting result is further extended to critical states in Chapter 4.

Chapter 3

ELASTO-PLASTIC STRESS-STRAIN AND WATER RETENTION RELATIONSHIPS FOR ISOTROPIC STRESS CONDITIONS

3. Elasto-plastic stress-strain and water retention relationships for isotropic stress conditions

This chapter gives a very basic introduction to some of the most fundamental aspects of classical plasticity. Several of these aspects are subsequently applied in developing the elasto-plastic stress-strain and water retention relationships for isotropic stress conditions, employing the constitutive model described in Chapter 2. These relationships are then used to formulate a pair of stress-incremental subroutines. In one of them, the increments of Bishop's stress and the increments of modified suction are the inputs; while in the other, the inputs are increments of mean net stress and increments of matric suction. Both of these stress-driver algorithms are employed to analyse the computed response for elastic behaviour, elasto-plastic behaviour with only one plastic mechanism active and elasto-plastic behaviour with two plastic mechanisms acting simultaneously.

3.1. Introduction

Soils exhibit a range of characteristics, such as yield phenomena and/or shear-induced dilatancy, which suggest plasticity theory as a very adequate framework to be used for describing their behaviour (Gens and Potts, 1988). According to the Wheeler et al. (2003) model described in Chapter 2, two types of irreversible behaviour can be identified in unsaturated soils. One plastic mechanism is associated with slippage at inter-particle or inter-packet contacts, resulting in the occurrence of plastic volumetric strains. The other plastic mechanism is associated with flooding or emptying of voids with water, resulting in plastic changes of degree of saturation. Irreversible behaviour associated with these two phenomena can be mathematically approached within classical plasticity theory by defining a yield function f which characterise the limit between elastic ($f < 0$); and plastic behaviour ($f = 0$) and constrains (in stress space) the admissible states ($f \leq 0$). This function is formally introduced in the following section.

3.2. Classical plasticity fundamentals

This section is not intended to give an overview on the application of elasto-plasticity in geomaterials, but to provide the basic concepts of this theory to be employed in subsequent chapters of this document to numerically integrate the constitutive model presented in Chapter 2. Interesting discussions on the developments and use of elasto-plastic models in geomechanics can be found elsewhere (e.g. Gens and Potts,1988; and Potts and Zdravković, 1999) and detailed descriptions of classical plasticity theory are given, amongst others, in Prager (1949); Hill (1950) and Simo and Hughes (1998).

3.2.1. Elastic response and basic definitions

A basic principle in classical plasticity theory is the *additive decomposition of the strain tensor increments* $d\boldsymbol{\varepsilon}$ into elastic $d\boldsymbol{\varepsilon}^{\mathbf{e}}$ and plastic components $d\boldsymbol{\varepsilon}^{\mathbf{p}}$ (3.1). In general, the vectorial notation of tensors is adopted within this work, indicating them in bold.

$$\underbrace{d\boldsymbol{\varepsilon}}_{\text{Total}} = \underbrace{d\boldsymbol{\varepsilon}^{\mathbf{e}}}_{\text{Elastic/recoverable}} + \underbrace{d\boldsymbol{\varepsilon}^{\mathbf{p}}}_{\text{Plastic/irrecoverable}} \qquad (3.1)$$

The elastic part describes the recoverable fraction of the total strain after unloading and, therefore, has associated an energy notion of reversibility or, in other words, can be linked to an elastic energy quantity that is recoverable after unloading. On the other hand, the plastic component of the total strains describes that irrecoverable part of the strains that remains even after the load is removed. Equivalently to the elastic component, this plastic part has associated an energy notion of irreversibility that can be linked to an inelastic energy quantity.

In accordance to this, the process of loading/unloading can be described in terms of energy or, more precisely, in terms of work input per unit volume of material *dW* as:

$$dW = \boldsymbol{\sigma}^T d\boldsymbol{\varepsilon} \qquad (3.2)$$

where the subscript *T* in the vectorial form of the stress tensor $\boldsymbol{\sigma}$ indicates transposed.

Accounting for (3.1) and (3.2) the following expression relating the recoverable (irrecoverable) component of the total strains with an elastic energy quantity is obtained.

$$dW = \boldsymbol{\sigma}^T d\boldsymbol{\varepsilon}^{\mathbf{e}} + \boldsymbol{\sigma}^T d\boldsymbol{\varepsilon}^{\mathbf{p}} = dW^e + dW^p \qquad (3.3)$$

In general, for elastic materials, stresses are assumed to be related to strain increments by:

$$d\boldsymbol{\sigma} = \mathbf{D}^e d\boldsymbol{\varepsilon}^{\mathbf{e}} \qquad (3.4)$$

where $\boldsymbol{D}^{\mathbf{e}}$ is the elasticity tensor (see Appendix A.1). One particular case of elasticity is to consider linear and isotropic behaviour (Hooke's law). Under these circumstances the elasticity tensor can be expressed in terms of two constants. Lamé coefficients ($\bar{\lambda}$ and $\bar{\mu}$ in (3.5)) are typically used to evaluate the elasticity tensor.

$$d\boldsymbol{\sigma} = \bar{\lambda} Tr\left(d\boldsymbol{\varepsilon}\right)\mathbf{I} + 2\bar{\mu} d\boldsymbol{\varepsilon} \qquad (3.5)$$

where *Tr(.)* is the trace of a tensor (see Appendix A.1), $\boldsymbol{\sigma}$ and $d\boldsymbol{\varepsilon}$ are the stress and strain tensors and $\mathbf{I}$ is the identity matrix. Equation (3.5) can be written in terms of the Young's modulus E and the Poisson's ratio ν as follows (Appendix A.1):

$$d\boldsymbol{\sigma} = \frac{\nu E}{(1+\nu)(1-2\nu)} Tr\left(d\boldsymbol{\varepsilon}\right)\mathbf{I} + \frac{E}{1+\nu} d\boldsymbol{\varepsilon} = \frac{\nu E}{(1+\nu)(1-2\nu)} Tr\left(d\boldsymbol{\varepsilon}\right)\mathbf{I} + 2\bar{G} d\boldsymbol{\varepsilon} \qquad (3.6)$$

where $\bar{G}$ is the elastic shear modulus. Further details can be found in Oliver and Agelet (2000).

3.2.2. Plastic response

The essential feature characterising plastic flow is the notion of irreversibility (Simo and Hughes, 1998). This property can be mathematically described within classical plasticity theory as formally presented in the following.

3.2.2.1. Elastic domain and yield criterion

The definition of a yield function $f(\boldsymbol{\sigma}, \boldsymbol{\xi})$, in terms of stresses $\boldsymbol{\sigma}$ and internal variables $\boldsymbol{\xi}$ (3.7), identifies the elastic domain in stress space and constrains the admissible stress states (Figure 3-1).

$$f\left(\boldsymbol{\sigma}, \boldsymbol{\xi}\right) = 0 \qquad (3.7)$$

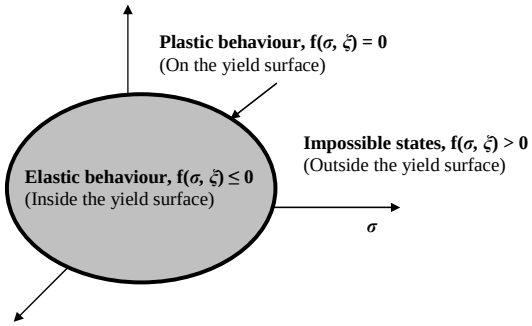

Figure 3- 1 Illustration of a yield surface in stress space defining the elastic and plastic domains and the admissible states.

As illustrated in Figure 3-1, elastic behaviour is restricted to those stress states falling inside the yield surface (i.e. $f < 0$) whereas plastic behaviour is restricted to those stress states lying on the yield surface (i.e. $f = 0$). Values of $\boldsymbol{\sigma}$ and $\boldsymbol{\xi}$ resulting in $f > 0$ are not admissible states.

3.2.2.2. Flow rule, hardening law and consistency condition

In classical plasticity theory, the way of mathematically characterising the evolution of the plastic strains and the internal variables is by defining a flow rule and a hardening law ((3.8) and (3.9) respectively).

$$d\boldsymbol{\varepsilon}^{\mathrm{p}} = d\chi \frac{\partial g\left(\boldsymbol{\sigma},\xi\right)}{\partial \boldsymbol{\sigma}} \qquad (3.\ 8)$$

where $d\chi$ is a non-negative scalar referred to as a plastic multiplier and g is a function called the plastic potential. The particular case of considering the plastic potential equal to the yield function (i.e. $g=f$) is known as *associated plasticity*.

Changes of the hardening internal variables $\boldsymbol{\xi}$ defining the evolution of the yield surface with stress variations are given by the hardening law (3.9).

$$d\xi = -d\chi\xi\left(\boldsymbol{\sigma},\xi\right) \qquad (3.\ 9)$$

The particular case of considering that the hardening is linked to plastic strains is known as *strain hardening* (3.10) and it is the one adopted in the subsequent development.

$$\xi = \xi\left(\boldsymbol{\varepsilon}^{\mathrm{p}}\right) \qquad (3.\ 10)$$

The plastic multiplier $d\chi$ is also known as a consistency parameter (Simo and Hughes, 1988) and is assumed to satisfy the following *Kuhn-Tucker complementary conditions*:

$$\begin{aligned} &d\chi \geq 0, \quad f\left(\boldsymbol{\sigma},\xi\right) \leq 0 \\ &\text{and} \\ &d\chi f\left(\boldsymbol{\sigma},\xi\right) = 0 \end{aligned} \qquad (3.\ 11)$$

In addition to (3.11) the parameter $d\chi$ obeys the *consistency condition*:

$$d\chi df\left(\boldsymbol{\sigma},\xi\right) = 0 \qquad (3.\ 12)$$

In classical plasticity, (3.11) and (3.12) are named *loading/unloading* and *consistency conditions* mathematically describing the intuitive notions of plastic loading and elastic unloading (Simo and Hughes, 1988).

3.2.2.3. Interpretation of the Kuhn-Tucker complementary conditions

If the stress state is inside the elastic domain defined by the yield surface (see Figure 3-1) $f(\boldsymbol{\sigma}, \boldsymbol{\xi})<0$ and, by considering (3.11):

$$d\chi f\left(\boldsymbol{\sigma},\xi\right)=0 \text{ and } f\left(\boldsymbol{\sigma},\xi\right)<0 \Rightarrow d\chi=0 \qquad (3.13)$$

Hence, according to (3.8) no plastic strains occur ($d\boldsymbol{\varepsilon}^p=0$) and the increment of the internal variables $d\boldsymbol{\xi}$ is also 0 (i.e. no movement of the yield surface). Then, from (3.1) it follows that $d\boldsymbol{\varepsilon}=d\boldsymbol{\varepsilon}^e$ and the stress variations are given by (3.4).

If now the stress state is considered to be on the yield surface $f(\boldsymbol{\sigma}, \boldsymbol{\xi})=0$, the Kuhn-Tucker complementary conditions are automatically satisfied. This stress state leads to two possible situations: $d\chi=0$ and $d\chi>0$. When $df(\boldsymbol{\sigma}, \boldsymbol{\xi})<0$:

$$d\chi df\left(\boldsymbol{\sigma},\xi\right)=0 \text{ and } df\left(\boldsymbol{\sigma},\xi\right)<0 \Rightarrow d\chi=0 \qquad (3.14)$$

Equivalently to the previous case described, (3.8) leads to no plastic strains ($d\boldsymbol{\varepsilon}^p=0$) and $d\boldsymbol{\xi}=0$, and Equation (3.4) gives the stress variations. This type of response is referred to as *unloading from a plastic state* (Simo and Hughes, 1988).

The second possible case, arises when $df(\boldsymbol{\sigma}, \boldsymbol{\xi})=0$. The consistency condition (3.12) is automatically satisfied. If $d\chi>0$, $d\boldsymbol{\varepsilon}^p\neq0$ and $d\boldsymbol{\xi}\neq0$ and the response is called *plastic loading* resulting in softening (when the yield surface reduces in size, $d\boldsymbol{\xi}<0$) or hardening (when the yield surface expands in size, $d\boldsymbol{\xi}>0$).

3.2.2.4. Elasto-plastic tangent modulus

It has been shown in previous sections that, under elastic response, the increments of stresses can be found by knowing the elastic increments of strains. This section is aimed at characterising stress variations under plastic loading conditions.

Applying the consistency condition (3.12) (with $d\chi>0$ because plastic loading is assumed within the remainder of this current section) yields to:

$$df\left(\boldsymbol{\sigma},\xi\right)=\left(\frac{\partial f}{\partial \boldsymbol{\sigma}}\right)^T d\boldsymbol{\sigma}+\left(\frac{\partial f}{\partial \xi}\right)^T d\xi=0 \qquad (3.15)$$

As pointed out in Simo and Huges (1988) the algorithmic elasto-plastic problem is typically regarded as a strain-driver problem and it is, therefore, useful to adopt the strain tensor as

the primary (driving) variable. In this sense, (3.15) can be expressed in terms of strains by using (3.4) in combination with (3.1):

$$\left(\frac{\partial f}{\partial \boldsymbol{\sigma}}\right)^T \mathbf{D}^e \left(d\boldsymbol{\varepsilon} - d\boldsymbol{\varepsilon}^{\mathbf{p}}\right) + \left(\frac{\partial f}{\partial \xi}\right)^T d\xi = 0 \qquad (3.16)$$

Using now the flow rule in combination with the hardening law (strain hardening) in (3.16):

$$\left(\frac{\partial f}{\partial \boldsymbol{\sigma}}\right)^T \mathbf{D}^e d\boldsymbol{\varepsilon} - d\chi \left(\frac{\partial f}{\partial \boldsymbol{\sigma}}\right)^T \mathbf{D}^e \frac{\partial g}{\partial \boldsymbol{\sigma}} + d\chi \left(\frac{\partial f}{\partial \boldsymbol{\varepsilon}^{\mathbf{p}}}\right)^T \frac{\partial g}{\partial \boldsymbol{\sigma}} = 0 \qquad (3.17)$$

From where it is possible to obtain an expression for the plastic multiplier in terms of the increments of strains:

$$d\chi = \frac{\left(\frac{\partial f}{\partial \boldsymbol{\sigma}}\right)^T \mathbf{D}^e d\boldsymbol{\varepsilon}}{\left(\frac{\partial f}{\partial \boldsymbol{\sigma}}\right)^T \mathbf{D}^e \frac{\partial g}{\partial \boldsymbol{\sigma}} - \left(\frac{\partial f}{\partial \boldsymbol{\varepsilon}^{\mathbf{p}}}\right)^T \frac{\partial g}{\partial \boldsymbol{\sigma}}} = \frac{\left(\frac{\partial f}{\partial \boldsymbol{\sigma}}\right)^T \mathbf{D}^e d\boldsymbol{\varepsilon}}{\left(\frac{\partial f}{\partial \boldsymbol{\sigma}}\right)^T \mathbf{D}^e \frac{\partial g}{\partial \boldsymbol{\sigma}} + H} \qquad (3.18)$$

where H is commonly referred to as the *plastic modulus* (e.g. Prat, 2003) and it gives the following information:

$H = 0$ Perfect plasticity (3.19)

$H > 0$ Hardening (3.20)

$H < 0$ Softening (3.21)

Equation (3.18) can be re-written as:

$$d\chi = \frac{\left(\frac{\partial f}{\partial \boldsymbol{\sigma}}\right)^T \mathbf{D}^e d\boldsymbol{\varepsilon}}{\left(\frac{\partial f}{\partial \boldsymbol{\sigma}}\right)^T \mathbf{D}^e \frac{\partial g}{\partial \boldsymbol{\sigma}} + H} = \frac{\mathbf{a}^T}{h} d\boldsymbol{\varepsilon} \qquad (3.22)$$

where the notation of h and $\boldsymbol{a}^T$ is introduced here in order to be consistent with the development presented in the remainder of this thesis.

It is now possible to obtain an expression for the *elasto-plastic tangent modulus*. Combining (3.4) with (3.1) and using the flow rule:

$$d\boldsymbol{\sigma} = \mathbf{D}^e \left(d\boldsymbol{\varepsilon} - d\chi \frac{\partial g}{\partial \boldsymbol{\sigma}} \right) \qquad (3.\ 23)$$

Substituting (3.22) into (3.23):

$$d\boldsymbol{\sigma} = \mathbf{D}^e \left(\mathbf{I} - \frac{\partial g}{\partial \boldsymbol{\sigma}} \frac{\mathbf{a}^T}{h} \right) d\boldsymbol{\varepsilon} = \mathbf{D}^{ep} d\boldsymbol{\varepsilon} \qquad (3.\ 24)$$

where $\boldsymbol{D^{ep}}$ is the elasto-plastic tangent modulus and $\boldsymbol{I}$ is the identity matrix.

Employing this classic elasto-plastic framework it is possible to build an equivalent development for the elasto-plastic constitutive model presented in Chapter 2. Obtaining, for this particular case, the relationships between mean Bishop's stress with volumetric strains (dp^*-$d\varepsilon_v$) and modified suction with degree of saturation (ds^*-dS_r), both required for the numerical integration of the model. This is explained in the next section.

3.3. Mathematical framework

This section is aimed at presenting a numerical approach to integrate the constitutive model proposed by Wheeler et al (2003) using elasto-plasticity as a framework to develop the stress-strain and water retention relationships for isotropic stress conditions (i.e. dp^*-$d\varepsilon_v$ and ds^*-dS_r). This model is characterised by the presence of multiple elasto-plastic mechanisms that can be active or not depending on the loading conditions. A procedure similar to the one presented in Sánchez et al. (2005) has been adopted here to take into account that different plastic mechanisms can induce plastic deformations and/or plastic changes of the degree of saturation.

3.3.1. Yield curves, flow rules and hardening laws

The yield curves under isotropic stress conditions were defined in Chapter 2 and are repeated here to facilitate the description of the mathematical development:

$$F_{LC} = p^* - p_0^* = 0$$

$$F_{SI} = s^* - s_I^* = 0$$

$$F_{SD} = s_D^* - s^* = 0$$

The intersection of the interior stress states defined by these three yield curves (i.e. $F_{LC} \leq 0 \cap F_{SI} \leq 0 \cap F_{SD} \leq 0$) in the s^*:p^* plane define the elastic domain of the model (see Figure 3-2).

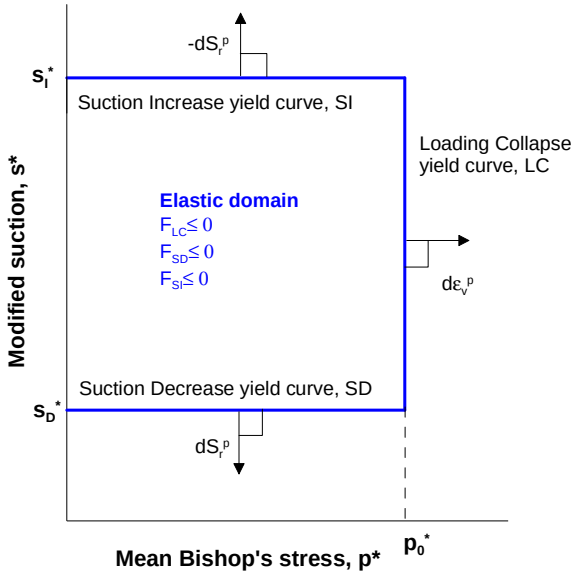

Figure 3- 2 Yield curves for isotropic stress states (Wheeler et al., 2003).

Two flow rules were proposed in the original model according to the two different plastic mechanisms (see (2.26) and (2.28) in Section 2.6). If yielding on the *LC* yield curve alone is taking place, the plastic volumetric deformations are given by:

$$d\varepsilon_v^p = d\chi_{LC} \frac{\partial G_{LC}}{\partial p^*} \qquad (3.\ 25)$$

where G_{LC} is the plastic potential associated with the *LC* curve and $d\chi_{LC}$ is the corresponding plastic multiplier.

Equivalently, if yielding on the *SD* yield curve alone takes place, the irrecoverable increments of the degree of saturation are given by:

$$-dS_r^p = d\chi_{SD} \frac{\partial G_{SD}}{\partial s^*} \qquad (3.\ 26)$$

where G_{SD} is the plastic potential associated with the *SD* curve and $d\chi_{SD}$ is the corresponding plastic multiplier.

If yielding on the *SI* yield curve alone takes place, the inelastic changes of S_r are computed by:

$$-dS_r^p = d\chi_{SI}\frac{\partial G_{SI}}{\partial s^*} \qquad (3.\ 27)$$

where G_{SI} is the plastic potential associated with the *SI* curve and $d\chi_{SI}$ is the corresponding plastic multiplier.

Two more elasto-plastic cases are also possible when yielding on two yield curves simultaneously (i.e. *LC+SD* or *LC+SI* respectively). The flow rules in those cases can be written as follows:

$$d\varepsilon_v^p = d\chi_{LC}^{LC+\beta}\frac{\partial G_{LC}}{\partial p^*} \qquad \text{with } \beta = SD/SI \qquad (3.\ 28)$$

$$-dS_r^p = d\chi_{\beta}^{LC+\beta}\frac{\partial G_{\beta}}{\partial s^*} \qquad \text{with } \beta = SD/SI \qquad (3.\ 29)$$

where $d\chi_{LC}{}^{LC+\beta}$ and $d\chi_{\beta}{}^{LC+\beta}$ are, respectively, the plastic multipliers associated with plastic changes of volumetric strains and plastic changes of the degree of saturation when simultaneous yielding is active.

Associated plasticity is adopted and, therefore, the plastic potential is equal to the corresponding yield surface (i.e. $G_{LC}=F_{LC}$ and $G_{\beta}=F_{\beta}$).

Finally, the hardening laws were presented in Chapter 2 by ((2.29) and (2.30)) and are also repeated here for completeness:

$$dp_0^* = p_0^*\left[\frac{v d\varepsilon_v^p}{\lambda-\kappa} - \frac{k_1 dS_r^p}{\lambda_s-\kappa_s}\right]$$

$$ds_{\beta}^* = s_{\beta}^*\left[-\frac{dS_r^p}{\lambda_s-\kappa_s} + k_2\frac{v d\varepsilon_v^p}{\lambda-\kappa}\right] \qquad \text{with } \beta = SD/SI$$

3.3.2. Additive decomposition of the volumetric strain and degree of saturation increments

The elastic relationships for volumetric strain increments with variations of mean Bishop's stress and degree of saturation with changes of modified suction were already introduced in Chapter 2 ((2.23) and (2.24)) respectively) but are repeated in this section because both are used within the mathematical framework presented hereafter.

$$d\varepsilon_v^e = \frac{\kappa dp^*}{vp^*} = \left(D^e\right)^{-1} dp^*$$

$$-dS_r^e = \frac{\kappa_s ds^*}{s^*} = \left(\gamma^e\right)^{-1} ds^*$$

where D^e and γ^e are two scalar quantities. Note that these scalars have an equivalent meaning to that shown by the components of the elasticity tensor introduced in Section 3.2.1. Under isotropic stress conditions, however, the elasticity tensor becomes a scalar.

The additive decomposition of strain tensor described in (3.1) is assumed to be valid in this approach to describe total volumetric strains and total degree of saturation variations. In the particular case of isotropic stress conditions, this assumption is written as:

$$d\varepsilon_v = d\varepsilon_v^e + d\varepsilon_v^p \qquad (3.30)$$

$$-dS_r = -dS_r^e - dS_r^p \qquad (3.31)$$

3.3.3. Consistency conditions and plastic multipliers

In order to describe the evolution of degree of saturation and volumetric strain when yielding takes place it is possible to follow an equivalent approach to that shown in 3.2.2.4 for the general elasto-plastic case presented. Using this constitutive model, however, it will be necessary to accommodate the mentioned development for each of the possible plastic mechanisms defined (see Section 2.6).

3.3.3.1. Yielding on the LC yield curve alone

It is possible to find an expression of the plastic multiplier $d\chi_{LC}$ (to give plastic variations of volumetric strains when yielding on the *LC* curve (3.25) alone) if applying the consistency condition and assuming that yielding on the *LC* yield curve alone takes place:

$$dF_{LC} = \frac{\partial F_{LC}}{\partial p^*} dp^* + \frac{\partial F_{LC}}{\partial p_0^*} dp_0^* = 0 \qquad (3.32)$$

Using (2.23) and (3.30) into (3.32) and employing the hardening law (2.29) with dS_r^p=0:

$$\frac{\partial F_{LC}}{\partial p^*} D^e \left(d\varepsilon_v - d\varepsilon_v^p\right) + \frac{\partial F_{LC}}{\partial p_0^*} \left(p_0^* \frac{v}{\lambda - \kappa} d\varepsilon_v^p \right) = 0 \qquad (3.33)$$

Using now the flow rule (3.25):

$$\frac{\partial F_{LC}}{\partial p^*} D^e \left(d\varepsilon_v - d\chi_{LC} \frac{\partial F_{LC}}{\partial p^*} \right) + \frac{\partial F_{LC}}{\partial p_0^*} \left(p_0^* \frac{v}{\lambda - \kappa} d\chi_{LC} \frac{\partial F_{LC}}{\partial p^*} \right) = 0 \qquad (3.\ 34)$$

From where it follows:

$$d\chi_{LC} = \frac{\frac{\partial F_{LC}}{\partial p^*} D^e d\varepsilon_v}{\frac{\partial F_{LC}}{\partial p^*} D^e \frac{\partial F_{LC}}{\partial p^*} - \frac{\partial F_{LC}}{\partial p_0^*} p_0^* \frac{v}{\lambda - \kappa} \frac{\partial F_{LC}}{\partial p^*}} = \frac{a_{LC}}{h_{LC}} d\varepsilon_v \qquad (3.\ 35)$$

where a_{LC} and h_{LC} are two scalar quantities with the subscript indicating which plastic mechanism is active (i.e. yielding on the *LC* yield curve alone).

It is now possible to obtain an expression of the elasto-plastic tangent modulus associated with yielding on the *LC* yield curve alone. Combining (2.23) with (3.30) and using the flow rule:

$$dp^* = D^e \left(d\varepsilon_v - d\chi_{LC} \frac{\partial F_{LC}}{\partial p^*} \right) \qquad (3.\ 36)$$

Finally, after inserting (3.35) into (3.36):

$$dp^* = D^e \left(1 - \frac{\partial F_{LC}}{\partial p^*} \frac{a_{LC}}{h_{LC}} \right) d\varepsilon_v = D_{LC}^{ep} d\varepsilon_v \qquad (3.\ 37)$$

where D_{LC}^{ep} is the corresponding elasto-plastic tangent modulus for yielding on the *LC* curve under isotropic stress conditions. Note that in this particular case (isotropic stress states) the elasto-plastic tangent modulus becomes a scalar quantity.

3.3.3.2. Yielding on the SD or SI yield curve alone

Applying the consistency condition on the *SD* (or *SI*) alone, it is possible to obtain an expression for the plastic multiplier $d\chi_\beta$ (giving plastic variations of degree of saturation when yielding on the *SD or SI* curve alone).

$$dF_\beta = \frac{\partial F_\beta}{\partial s^*} ds^* + \frac{\partial F_\beta}{\partial s_\beta^*} ds_\beta^* = 0 \qquad \text{with } \beta\text{=SD/SI} \qquad (3.\ 38)$$

Using (2.24) and (3.31) into (3.38) and employing the hardening law (2.30) with $d\varepsilon_v^p$=0:

$$\frac{\partial F_\beta}{\partial s^*}\gamma^e\left(-dS_r+dS_r^p\right)+\frac{\partial F_\beta}{\partial s_\beta^*}\left(-s_\beta^*\frac{1}{\lambda_s-\kappa_s}dS_r^p\right)=0 \qquad (3.\ 39)$$

Using now the flow rule for yielding on the *SD* or *SI* curve ((3.26) or (3.27) respectively):

$$\frac{\partial F_\beta}{\partial s^*}\gamma^e\left(-dS_r-d\chi_\beta\frac{\partial F_\beta}{\partial s^*}\right)+\frac{\partial F_\beta}{\partial s_\beta^*}\left(s_\beta^*\frac{1}{\lambda_s-\kappa_s}d\chi_\beta\frac{\partial F_\beta}{\partial s^*}\right)=0 \qquad (3.\ 40)$$

From where it follows:

$$d\chi_\beta=\frac{\frac{\partial F_\beta}{\partial s^*}\gamma^e dS_r}{-\frac{\partial F_\beta}{\partial s^*}\gamma^e\frac{\partial F_\beta}{\partial s^*}+\frac{\partial F_\beta}{\partial s_\beta^*}s_\beta^*\frac{1}{\lambda_s-\kappa_s}\frac{\partial F_\beta}{\partial s^*}}=\frac{d_\beta}{h_\beta}dS_r \qquad (3.\ 41)$$

where d_β and h_β are two scalar quantities with the subscript indicating which plastic mechanism is active (i.e. yielding on the *SD* or *SI* curve).

It is now possible to obtain an expression of the elasto-plastic tangent modulus associated with yielding on the *SD* or *SI* yield curve alone. Combining (2.24) with (3.31) and using the appropriate flow rule:

$$ds^*=\gamma^e\left(-dS_r-d\chi_\beta\frac{\partial F_\beta}{\partial s^*}\right) \qquad (3.\ 42)$$

Finally, after inserting (3.41) into (3.42):

$$ds^*=\gamma^e\left(1+\frac{\partial F_\beta}{\partial s^*}\frac{d_\beta}{h_\beta}\right)\left(-dS_r\right)=\gamma_\beta^{ep}\left(-dS_r\right) \qquad (3.\ 43)$$

where γ_β^{ep} is the corresponding elasto-plastic tangent modulus for yielding on the *SD* or *SI* curve alone under isotropic stress conditions.

3.3.3.3. Simultaneous yielding on LC and SD or SI

A more interesting case is when the stress path reaches the bottom (or top) corner illustrated in Figure 3-2 at the intersection between the *LC* and *SD* (or the *LC* and *SI*) yield curves and simultaneous yielding is activated. In such cases, the final expression of each plastic multiplier giving inelastic changes of volumetric strains $d\varepsilon_v^p$ and of degree of saturation dS_r^p is found by applying the consistency condition simultaneously at the two

yield curves reached. In other words, a system of two equations (in which the unknowns are both plastic multipliers) needs to be solved to give the expression for $d\chi_{LC}^{LC+\beta}$ and $d\chi_{\beta}^{LC+\beta}$. Applying the consistency condition on the *LC* curve and on the *β=SD* (or *SI*) curve simultaneously:

$$\begin{cases} dF_{LC} = \dfrac{\partial F_{LC}}{\partial p^*} dp^* + \dfrac{\partial F_{LC}}{\partial p_0^*} dp_0^* = 0 \\ dF_{\beta} = \dfrac{\partial F_{\beta}}{\partial s^*} ds^* + \dfrac{\partial F_{\beta}}{\partial s_{\beta}^*} ds_{\beta}^* = 0 \end{cases} \qquad (3.\ 44)$$

Following an equivalent development to that shown, separately, for yielding on the *LC* yield curve alone or for yielding on the *SD* (or *SI*) curve yield curve alone:

$$\begin{cases} \dfrac{\partial F_{LC}}{\partial p^*} D^e \left(d\varepsilon_v - d\varepsilon_v^p \right) + \dfrac{\partial F_{LC}}{\partial p_0^*} p_0^* \left[\dfrac{v d\varepsilon_v^p}{\lambda - \kappa} - \dfrac{k_1 dS_r^p}{\lambda_s - \kappa_s} \right] = 0 \\ \dfrac{\partial F_{\beta}}{\partial s^*} \gamma^e \left(-dS_r + dS_r^p \right) + \dfrac{\partial F_{\beta}}{\partial s_{\beta}^*} s_{\beta}^* \left[-\dfrac{dS_r^p}{\lambda_s - \kappa_s} + k_2 \dfrac{v d\varepsilon_v^p}{\lambda - \kappa} \right] = 0 \end{cases} \qquad (3.\ 45)$$

Using now the flow rules (3.28) and (3.29) for simultaneous yielding on the *LC* and *SD* (or *SI*) yield curves:

$$\begin{cases} \dfrac{\partial F_{LC}}{\partial p^*} D^e \left(d\varepsilon_v - d\chi_{LC}^{LC+\beta} \dfrac{\partial F_{LC}}{\partial p^*} \right) + \dfrac{\partial F_{LC}}{\partial p_0^*} p_0^* \left[\dfrac{v}{\lambda - \kappa} d\chi_{LC}^{LC+\beta} \dfrac{\partial F_{LC}}{\partial p^*} + \dfrac{k_1}{\lambda_s - \kappa_s} d\chi_{\beta}^{LC+\beta} \dfrac{\partial F_{\beta}}{\partial s^*} \right] = 0 \\ \dfrac{\partial F_{\beta}}{\partial s^*} \gamma^e \left(-dS_r - d\chi_{\beta}^{LC+\beta} \dfrac{\partial F_{\beta}}{\partial s^*} \right) + \dfrac{\partial F_{\beta}}{\partial s_{\beta}^*} s_{\beta}^* \left[\dfrac{1}{\lambda_s - \kappa_s} d\chi_{\beta}^{LC+\beta} \dfrac{\partial F_{\beta}}{\partial s^*} + \dfrac{k_2 v}{\lambda - \kappa} d\chi_{LC}^{LC+\beta} \dfrac{\partial F_{LC}}{\partial p^*} \right] = 0 \end{cases} \qquad (3.\ 46)$$

After some algebra (see Appendix A.2) one may obtain the following expression for each plastic multiplier when yielding on the *LC* and *SD* (or *LC* and *SI*) yield curves is active simultaneously:

$$\begin{cases} d\chi_{LC}^{LC+\beta} = \dfrac{a_{LC+\beta} d\varepsilon_v + b_{LC+\beta} dS_r}{h_{LC+\beta}} \\ d\chi_{\beta}^{LC+\beta} = \dfrac{c_{LC+\beta} d\varepsilon_v + d_{LC+\beta} dS_r}{h_{LC+\beta}} \end{cases} \qquad (3.\ 47)$$

where $a_{LC+\beta}$, $b_{LC+\beta}$, $c_{LC+\beta}$, $d_{LC+\beta}$, and $h_{LC+\beta}$ are scalar quantities with the subscript indicating the plastic mechanism active (see Appendix A.2 for further details).

Following a similar approach to that shown in Sections 3.3.3.1 and 3.3.3.2, it is possible to obtain the following expressions for dp^* and ds^* when simultaneous yielding is active:

$$dp^* = D^e\left(d\varepsilon_v - d\chi_{LC}^{LC+\beta}\frac{\partial F_{LC}}{\partial p^*}\right) \qquad (3.48)$$

$$\begin{aligned} dp^* &= D^e\left(1-\frac{\partial F_{LC}}{\partial p^*}\frac{a_{LC+\beta}}{h_{LC+\beta}}\right)d\varepsilon_v - D^e\frac{\partial F_{LC}}{\partial p^*}\frac{b_{LC+\beta}}{h_{LC+\beta}}dS_r \\ dp^* &= D_{LC+\beta}^{ep}d\varepsilon_v + D^e\frac{\partial F_{LC}}{\partial p^*}\frac{b_{LC+\beta}}{h_{LC+\beta}}\left(-dS_r\right) \end{aligned} \qquad (3.49)$$

And also,

$$ds^* = \gamma^e\left(-dS_r - d\chi_{\beta}^{LC+\beta}\frac{\partial F_{\beta}}{\partial s^*}\right) \qquad (3.50)$$

$$\begin{aligned} ds^* &= \gamma^e\left(1+\frac{\partial F_{\beta}}{\partial s^*}\frac{d_{LC+\beta}}{h_{LC+\beta}}\right)\left(-dS_r\right) - \gamma^e\frac{\partial F_{\beta}}{\partial s^*}\frac{c_{LC+\beta}}{h_{LC+\beta}}d\varepsilon_v \\ ds^* &= \gamma_{LC+\beta}^{ep}\left(-dS_r\right) - \gamma^e\frac{\partial F_{\beta}}{\partial s^*}\frac{c_{LC+\beta}}{h_{LC+\beta}}d\varepsilon_v \end{aligned} \qquad (3.51)$$

It is interesting to see here how the model describes the coupling between mechanical and water retention behaviour when simultaneous yielding is active. More precisely, it can be seen that the expressions accounting for the increments of mean Bishop's stress (3.49) and for the increments of modified suction (3.51) depend on both the volumetric strain changes and the variation of the degree of saturation.

3.3.4. Summary of mean Bishop's stress-volumetric strain and modified suction-degree of saturation relationships

In the previous section, the equations expressing the increments of mean Bishop's stress and modified suction in terms of volumetric strains and degree of saturation have been developed for each possible set of plastic mechanisms defined in the model of Wheeler et al. (2003). This way of expressing the variations of the stress state variables allows their automatic update by the formulation of an algorithm usually referred to as a *strain-driver* (because the assumed known or driving variables are volumetric strains and changes of degree of saturation).

It is shown later in Chapter 6, that the increments of degree of saturation can be expressed, for each type of mechanism, in terms of strain and suction increments which are the standard driving variables used in a Finite Element (FE) formulation. It is also possible, however, to express these relationships in a *stress-driver* manner. Indeed, it is equivalent to find the equations of the volumetric strain increments and of the degree of saturation increments in terms of increments of the stress variables (i.e. dp^* and ds^*). Furthermore, it is also possible to express these stress increments (i.e. dp^* and ds^*) in terms of mean net stress and suction changes. This alternative way of integrating the model is useful for validating the model before implementing it into a FE program as, typically, mean net stress and suction are the variables controlled in experiments. A more detailed description of both types of stress-driver algorithms is given in Section 3.5. Table 3.1 summarises both of these formulations (i.e. strain-driver and stress-driver) for the Wheeler et al. (2003) model.

3.4. Elasto-plastic domains associated with the Wheeler et al. (2003) model

A detailed overview of the fully coupled constitutive model proposed by Wheeler et al. (2003) was presented in Chapter 2. A particular feature of this constitutive model is that, in addition, to the three yield curves defined (i.e. Loading Collapse yield curve *LC*, Suction Decrease yield curve *SD* and Suction Increase yield curve *SI*) it is possible to identify different domains in stress space where different plastic mechanisms can be activated. As a consequence, the appropriate stress-strain relationships have to be used for each plastic mechanism (see Table 3.1). Essentially, the existence of these different domains is a consequence of the couplings defined within the model between the mechanical and the water retention behaviour and, therefore, the shape of these domains depend on the coupling parameters k_1 and k_2 as detailed below.

Based on the couplings presented in Section 2.6 and considering also the three yield curves defined (see Figure 3-2), one may identify six different domains in the $\ln s^*$:$\ln p^*$ plane. Indeed, if plotting the three yield curves defined in the model jointly with the trace of each corner (i.e. intersection between the *LC* and *SD* yield curves or intersection between the *LC* and *SI* yield curves, see Figure 3-2) when a single plastic mechanism is active (i.e. yielding on the *LC* yield curve alone as in Figure 3-3 or yielding on the *SD* yield curve alone as in Figure 3-4) five different regions can be defined (in addition to the elastic domain) identifying six different plastic mechanisms (including the elastic behaviour).

Figure 3-3 shows the trajectories, in the $\ln s^*$:$\ln p^*$ plane, traced by the bottom and top corners (i.e. intersection between the *LC* and *SD* yield curves and intersection between

the *LC* and *SI* yield curves, respectively) when yielding on the *LC* yield curve alone takes place. It can be seen that both traces are parallel straight lines having slope k_2 when plotted in this plane.

Figure 3-4 shows the trajectories, in the $\ln s^*$:$\ln p^*$ plane, traced by the bottom and top corners when yielding on the *SD* yield curve alone takes place. It can also be seen here that both traces are parallel straight lines having slope $1/k_1$ when plotted in this plane.

Table 3. 1 Incremental relationships of the integrated constitutive model.

	Strain-driver	***Stress-driver***
Elastic behaviour	$\begin{cases} dp^* = D^e d\varepsilon_v^e \\ ds^* = \gamma^e \left(-dS_r^e\right) \end{cases}$	$\begin{cases} d\varepsilon_v^e = \left(D^e\right)^{-1} dp^* \\ -dS_r^e = \left(\gamma^e\right)^{-1} ds^* \end{cases}$
Yielding on the LC yield curve alone	$\begin{cases} dp^* = D_{LC}^{ep} d\varepsilon_v \\ ds^* = \gamma^e \left(-dS_r^e\right) \end{cases}$	$\begin{cases} d\varepsilon_v = \left(D_{LC}^{ep}\right)^{-1} dp^* \\ -dS_r^e = \left(\gamma^e\right)^{-1} ds^* \end{cases}$
Yielding on the SD/SI yield curve alone	$\begin{cases} dp^* = D^e d\varepsilon_v^e \\ ds^* = \gamma_\beta^{ep} \left(-dS_r\right) \end{cases}$	$\begin{cases} d\varepsilon_v^e = \left(D^e\right)^{-1} dp^* \\ -dS_r = \left(\gamma_\beta^{ep}\right)^{-1} ds^* \end{cases}$
Simultaneous yielding on the LC and SD/SI yield curves (strain-driver)	$\begin{cases} dp^* = D_{LC+\beta}^{ep} d\varepsilon_v + D^e \dfrac{\partial G_{LC}}{\partial p^*} \dfrac{b_{LC+\beta}}{h_{LC+\beta}} \left(-dS_r\right) \\ ds^* = \gamma_{LC+\beta}^{ep} \left(-dS_r\right) - \gamma^e \dfrac{\partial G_\beta}{\partial s^*} \dfrac{c_{LC+\beta}}{h_{LC+\beta}} d\varepsilon_v \end{cases}$	
Simultaneous yielding on the LC and SD/SI yield curves (stress-driver)	$\begin{cases} d\varepsilon_v = \left[dp^* - D^e \dfrac{\partial G_{LC}}{\partial p^*} \dfrac{b_{LC+\beta}}{h_{LC+\beta}} \left(\gamma_{LC+\beta}^{ep}\right)^{-1} ds^* \right] \left[D_{LC+\beta}^{ep} + D^e \dfrac{\partial G_{LC}}{\partial p^*} \dfrac{b_{LC+\beta}}{h_{LC+\beta}} \left(\gamma_{LC+\beta}^{ep}\right)^{-1} \gamma^e \dfrac{\partial G_\beta}{\partial s^*} \dfrac{c_{LC+\beta}}{h_{LC+\beta}} \right]^{-1} \\ -dS_r = \left[ds^* + \gamma^e \dfrac{\partial G_\beta}{\partial s^*} \dfrac{c_{LC+\beta}}{h_{LC+\beta}} \left(D_{LC+\beta}^{ep}\right)^{-1} dp^* \right] \left[\gamma_{LC+\beta}^{ep} + \gamma^e \dfrac{\partial G_\beta}{\partial s^*} \dfrac{c_{LC+\beta}}{h_{LC+\beta}} \left(D_{LC+\beta}^{ep}\right)^{-1} D^e \dfrac{\partial G_{LC}}{\partial p^*} \dfrac{b_{LC+\beta}}{h_{LC+\beta}} \right]^{-1} \end{cases}$	

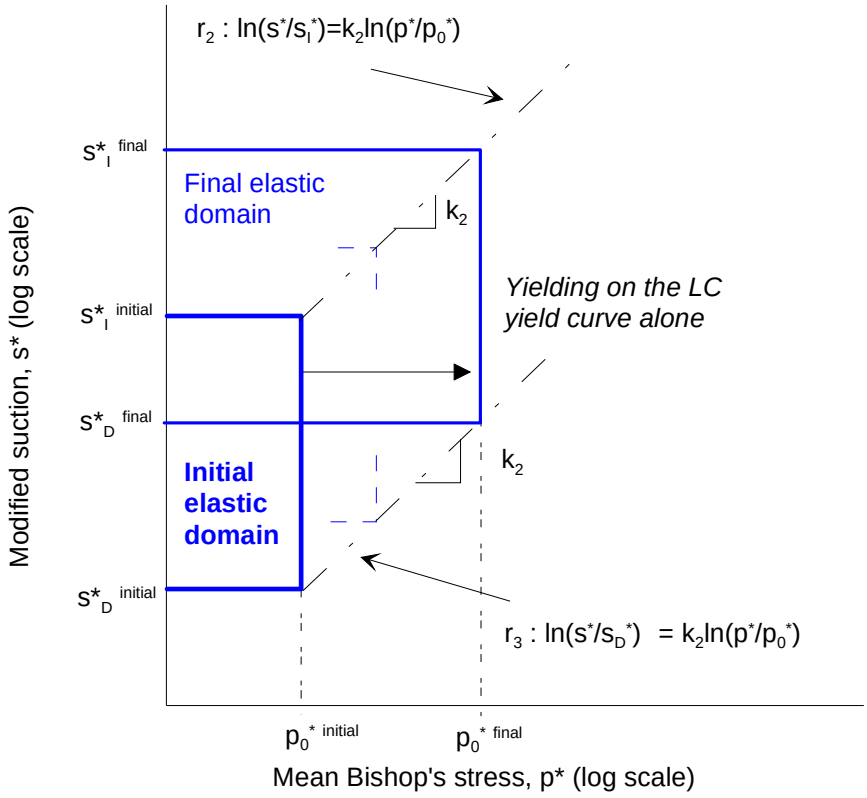

Figure 3- 3 Illustration of the coupled movements associated with yielding on the LC yield curve alone (after Wheeler et al., 2003).

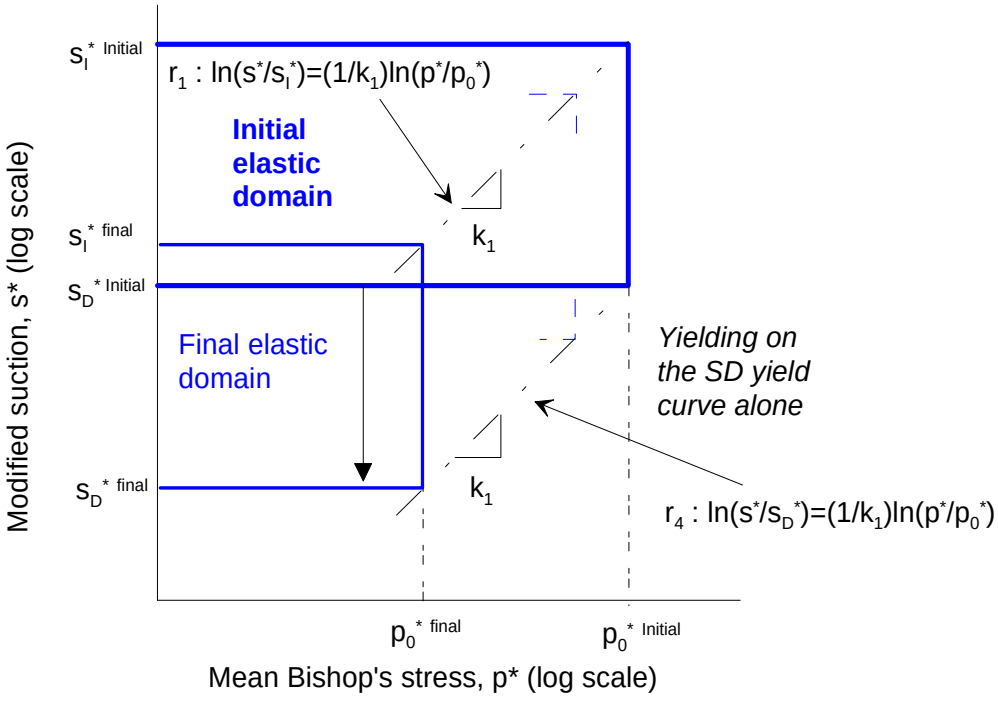

Figure 3- 4 Illustration of the coupled movements associated with yielding on the SD yield curve alone (after Wheeler et al., 2003).

The mathematical expression of the straight lines plotted in Figures 3-3 and 3-4 are given by the following expressions:

$$r_1 : \ln\left(\frac{p^*}{p_0^*}\right) = k_1 \ln\left(\frac{s^*}{s_I^*}\right) \qquad (3.\ 52)$$

$$r_2 : \ln\left(\frac{s^*}{s_I^*}\right) = k_2 \ln\left(\frac{p^*}{p_0^*}\right) \qquad (3.\ 53)$$

$$r_3 : \ln\left(\frac{s^*}{s_D^*}\right) = k_2 \ln\left(\frac{p^*}{p_0^*}\right) \qquad (3.\ 54)$$

$$r_4 : \ln\left(\frac{p^*}{p_0^*}\right) = k_2 \ln\left(\frac{s^*}{s_D^*}\right) \qquad (3.\ 55)$$

It is useful to express all previous equations in the s^*:p^* plane (rather than the lns^*:lnp^* plane) as this is the common plane used in the algorithm formulation:

$$f_1 : s^* - s_I^* \left(\frac{p^*}{p_0^*}\right)^{\frac{1}{k_1}} = 0 \qquad (3.\ 56)$$

$$f_2 : s^* - s_I^* \left(\frac{p^*}{p_0^*}\right)^{k_2} = 0 \qquad (3.\ 57)$$

$$f_3 : s^* - s_D^* \left(\frac{p^*}{p_0^*}\right)^{k_2} = 0 \qquad (3.\ 58)$$

$$f_4 : s^* - s_D^* \left(\frac{p^*}{p_0^*}\right)^{\frac{1}{k_1}} = 0 \qquad (3.\ 59)$$

Using these mathematical expressions, the important aspect of determining how the algorithm distinguishes and establishes if a plastic mechanism has been activated can be addressed. Without going into details of the algorithm adopted to integrate the model (discussion delayed to Chapter 6) a possible methodology to differentiate which plastic mechanism, if any, is active, is to define five different regions in the isotropic stress p^*:s^* plane (see Figure 3-5) by plotting the four lines f_1, f_2, f_3, and f_4 in combination with the three yield curves .

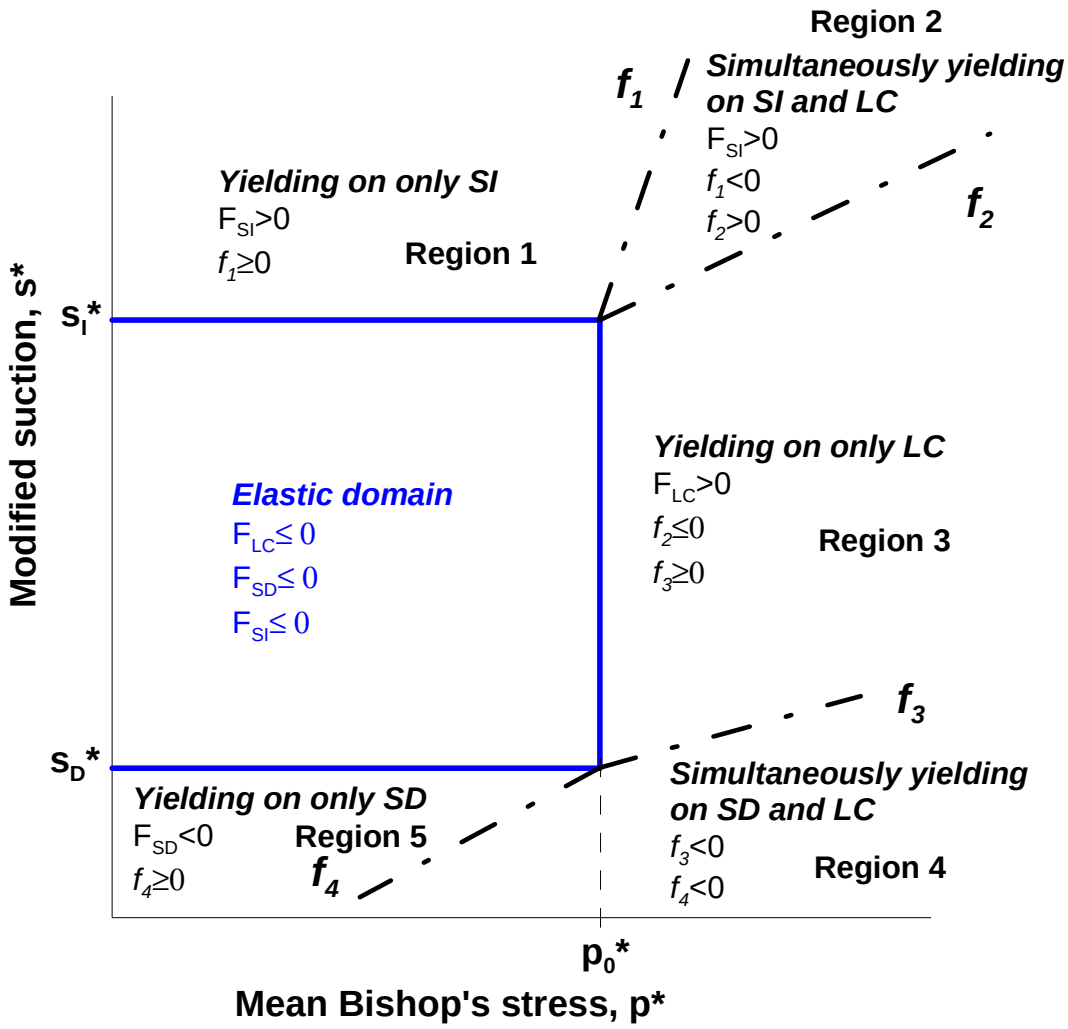

Figure 3- 5 Idealised representation of the different elasto-plastic domains.

As illustrated in Figure 3-5, for a given initial position of the yield curves (p_0^*, s_I^* and s_D^*) the lines presented above define the boundaries between the different elasto-plastic domains (in addition to the elastic domain) defining five different types of behaviour (i.e. yielding on the *SI* yield curve alone; yielding on the *LC* yield curve alone; yielding on the *SD* yield curve alone; and simultaneous yielding on *SI* and *LC* or on *LC* and *SD*). In this way, any stress state falling, for instance, in Region 3 (see Figure 3-5) activates the plastic mechanism associated with yielding on the *LC* yield curve alone, and equivalent concepts apply in regions 1, 2, 4 and 5 for yielding on the *SI* yield curve alone, simultaneous yielding on *SI*+*LC*, simultaneous yielding on *LC*+*SD* and yielding on the *SD* yield curve alone respectively.

3.5. Stress-driver algorithm formulation for isotropic stress conditions

In this work, the constitutive model of Wheeler et al. (2003) was initially integrated using a stress-driver algorithm. This algorithm was then used as a way to partially verify that the mathematical formulation presented above correctly reproduces the model response for a prescribed stress path. This is a useful check, considering the complexity of the mathematical expressions previously presented. For instance, complexity arises because there is a strong link between the two stress state variables in the model, with both the mean Bishop's stress p^* and the modified suction s^* depending on a state variable influenced by the other. That is p^* includes the degree of saturation (see Equation (2.15)), changes of which are governed by the water retention behaviour; and s^* includes the porosity (see Equation (2.16)) which is affected by the mechanical response. This strong interrelation adds significant complexity to the classical plasticity problem (see also Lloret et al. (2008a)).

In general, a stress-driver algorithm is used when stress changes are known and these are used to compute strain changes. For this particular case, volumetric strains increments $\Delta\varepsilon_v$ and degree of saturation increments ΔS_r are computed by knowing increments of modified suction Δs^* and increments of mean Bishop's stress Δp^* as in the first stress-driver algorithm presented (see Section 3.5.1); or increments of suction Δs and increments of mean net stress $\Delta\bar{p}$ as in the second stress-driver algorithm presented (see Section 3.5.2). In general, from an initial stress state inside the elastic domain and by knowing the increments of stresses (inputs), a stress-driver algorithm calculates an elastic trial stress state to decide which plastic mechanism (if any) is active and then to update the state variables correspondingly (see Table 3.1). When the stress path is found to fall outside the elastic domain, yielding will take place and it will be necessary to find the intersection of the stress path with the corresponding yield curve. The algorithms used in this thesis employ the classical bisection method to find the intersection point. This method requires the specification of a tolerance which will be referred to as *TOL1* in the remainder of this work. When yielding takes place, it is also necessary to specify a second tolerance referred to as *TOL2*. This is to ensure that the final stress state lies on the pertinent yield curve during yielding. Due to the tendency to drift, it is commonly needed to project back the stress state to the corresponding yield curve using a drift correction method (Potts and Gens, 1985). A more detailed description of these issues is given when presenting the complete algorithmic formulation of the 3D extended version of the Wheeler et al. (2003) model in Chapter 6.

Two types of stress-driver algorithms are presented in this section. The first one requires the increments of modified suction Δs^* and mean Bishop's stress Δp^* as inputs. By knowing these increments the algorithm computes increments of volumetric strain $\Delta\varepsilon_v$ and increments of degree of saturation ΔS_r (see Table 3.1). The second scheme uses the increments of suction Δs and the increments of mean net stress $\Delta\bar{p}$ as inputs, from where increments of volumetric strain $\Delta\varepsilon_v$ and increments of degree of saturation ΔS_r are calculated. Further details of both stress-driver subroutines are given as follows.

3.5.1. Stress-driver algorithm based on mean Bishop's stress and modified suction

This algorithm is used to analyse the computed response for two different prescribed stress paths. The first one is an isotropic loading at constant modified suction, and the second one is an isotropic wetting at constant mean Bishop's stress. Both of these stress paths require the increments of Δs^* and Δp^* (inputs) to calculate ΔS_r and $\Delta\varepsilon_v$ (outputs). Table 3.1 presents the equations to compute changes of ΔS_r and $\Delta\varepsilon_v$ in terms of Δs^* and Δp^* for each of the possible cases defined in the model (i.e. elastic; yielding on the *LC* yield curve alone; yielding on the *SD* or *SI* yield curve alone; simultaneous yielding on the *SD* or *SI* and *LC* yield curves). The algorithm used is summarised as follows.

i. *Initial stress state*

The initial state should be inside the elastic domain (see Figure 3.2) and it is defined by giving the initial mean Bishop's stress p^*, the initial modified suction s^*, the initial void ratio e, the initial degree of saturation S_r and the initial values of the hardening parameters.

ii. *Elastic trial*

Assume that the given Δp^* and Δs^* are purely elastic and compute the elastic trial increments of the volumetric strain and degree of saturation by integrating (2.23) and (2.24).

Update p_{k+1}^* and s_{k+1}^* with the given increments and evaluate the new stress point. If the trial stress state is inside or on each of the yield curves defined (i.e. $F_{LC}(p^*_{k+1},p_0^*)\leq 0$ ***and*** $F_{SD}(s^*_{k+1},s_D^*)\leq 0$ ***and*** $F_{SI}(s^*_{k+1},s_I^*)\leq 0$) update variables with the elastic trial and exit.

iii. *Identification of the elasto-plastic mechanism active and update*

Otherwise, determine the elasto-plastic mechanism active (Section 3.4), find the corresponding intersection/s and update variables accordingly (see Table 3.1). A number of schemes are available in the literature to find the intersection of the stress path with the yield curve. A detailed description of the approach used in this work is given in Chapter 6

when describing the algorithm used to implement this model in the FE program CODE_BRIGHT (Olivella et al., 1996).

iv. *Yield surface drift correction*

Each time the final state lies outside the updated yield curves, the current state should be projected back to the pertinent yield curve/s using a drift correction method. Section 6.5 describes in detail the scheme used in this research to correct this drift based on the work presented by Potts and Gens (1985).

3.5.1.1. Model response under isotropic loading paths at constant modified suction

An isotropic loading stress path at a constant modified suction of 250 kPa is considered in this section to explore the performance of the mathematical approach described in Section 3.3. This stress path involves elastic behaviour, then yielding on the *LC* yield curve alone and finally simultaneous yielding on the *LC* and *SD* yield curves. Under this type of stress path, it is possible to study the error in the computed results by comparing them with the predicted model response for the following model parameters: κ (associated with volumetric elastic response), λ (associated with the volumetric behaviour when yielding on the *LC* curve) and k_2 (coupling parameter associated with the influence of the mechanical behaviour on the water retention behaviour, see Section 2.6). Also, as the stress path reaches the bottom corner defined at the intersection between the *LC* and *SD* yield curves, simultaneous yielding occurs and the parameters λ^* and k_2^* (introduced in Section 2.7) can be also studied.

Table 3.2 contains the values of the model parameters (κ, λ, κ_s, λ_s, k_1 and k_2) used in the analysis; the initial state (in terms of the initial values of e, S_r, p^*, s^* and the hardening parameters p_0^* and s_D^*); the input increments for the prescribed stress path (i.e. $\Delta s^*=0$ and $\Delta p^*=0.1$ kPa) and the tolerances adopted for intersection and drift correction subroutines (i.e. *TOL1* and *TOL2* respectively). The values of the gradients of the isotropic normal compression surfaces λ^*, λ_s^*, k_1^* and k_2^* calculated from the original soil parameters λ, κ, λ_s, κ_s, k_1 and k_2 (see Section 2.7) have been also included.

Table 3. 2 Model parameters and initial state used in the computations.

$\kappa=0.006$	$\lambda=0.118$	$\lambda_s=0.0971$	$\kappa_s=0.009$	$k_1=0.7$	$k_2=0.8$
$p_0^*=200$kPa	$s_D^*=150$kPa	$e=1.2$	$S_r=0.6$	$p^*=100$kPa	$s^*=250$kPa
$\Delta s^*=0$	$\Delta p^*=0.1$kPa	$TOL1<10^{-07}$	$TOL2<10^{-07}$		
$\lambda^*=0.260$	$\lambda^*_s=0.209$	$k^*_1=0.178$	$k^*_2=0.160$		

Figure 3-6a shows the stress path (in the $\ln s^*$:$\ln p^*$ plane) and Figures 3-6b and 3-6c show the computed variations of v and S_r respectively (both plotted against $\ln p^*$). Table 3.3 includes the values of the model parameters back-calculated from the gradients in Figure 3-6. These values have been estimated using the least-square method implemented in GRAPHER software (www.goldensoftware) from the computed response and the coefficient of determination R^2 has been also included in Table 3.3. Inspection of Figure 3-6 in combination with the information summarised in Table 3.3 indicates that the computed results for this particular stress path are indistinguishable from the predicted model response. A first elastic compression controlled by κ is observed from *A* to *B*. At *B* the *LC* curve is reached and yielding on this yield curve alone occurs. As a consequence, the evolution of the specific volume with p^* is controlled by the parameter λ (Figure 3-6b). This type of behaviour lasts until the bottom corner *LC*-*SD* is reached at *C* from where simultaneous yielding on the *LC* and *SD* curves begins. From *C* to the end of the test *D*, the specific volume changes with p^* are controlled by λ^*. Also the degree of saturation changes with p^* are illustrated in the bottom plot of this figure (Figure 3-6c) showing that the only variations observed in S_r occur when simultaneous yielding on the *LC* and *SD* curves is active and those changes are controlled by k_2^*. In accordance to this, three cases are checked to coincide with the predicted response, comprising: elastic behaviour (*A*-*B)*, yielding on the *LC* curve alone *(B*-*C)* and simultaneous yielding on the *LC* and *SD* curves (*C*-*D*).

Table 3. 3 Comparison between the theoretical and estimated soil parameters values (mechanical behaviour).

Soil parameter	***Theoretical value***	***Back-calculated value***	***Coefficient of determination R^2***
κ	*0.006*	*0.006002*	*1.000000*
λ	*0.118*	*0.118021*	*1.000000*
λ^*	*0.260*	*0.260577*	*1.000000*
k_2^*	*0.160*	*0.160019*	*1.000000*

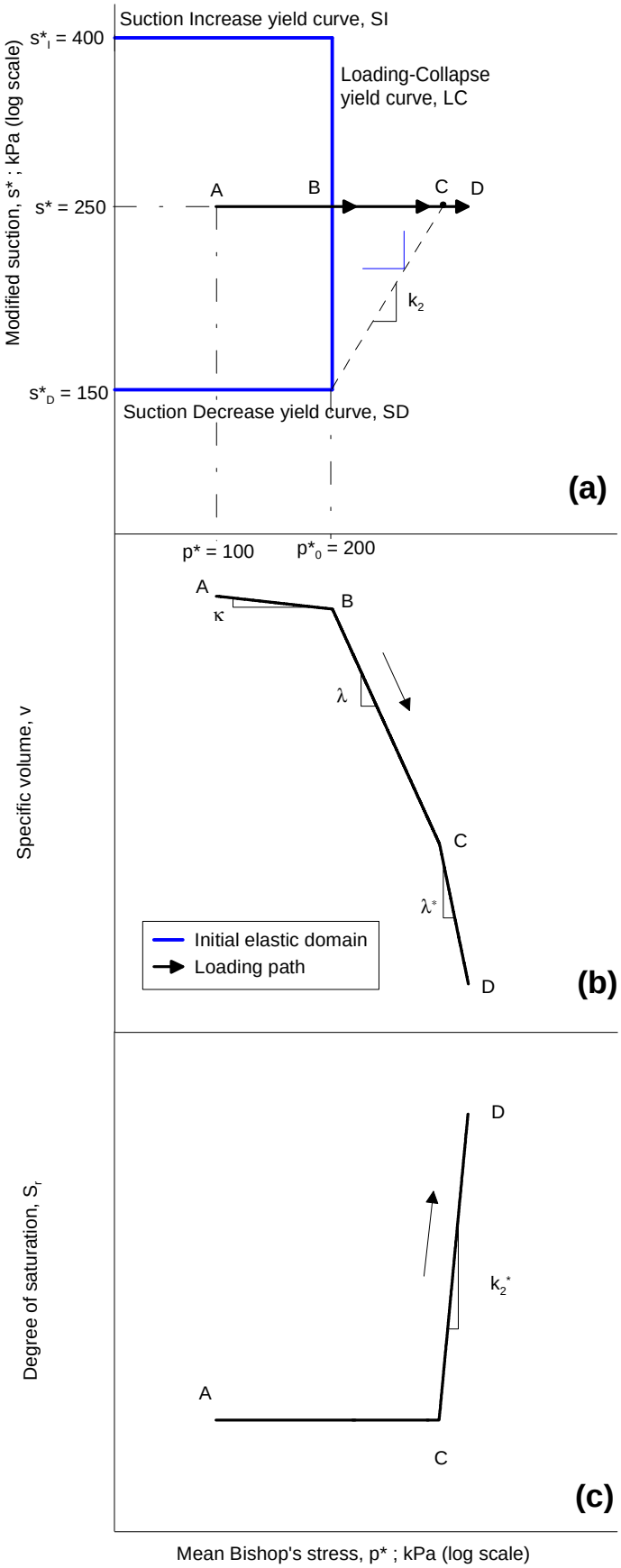

Figure 3- 6 Model response under an isotropic loading stress path at constant modified suction.

3.5.1.2. Model response under isotropic wetting paths at constant mean Bishop's stress

An isotropic wetting path at a constant mean Bishop's stress of 100kPa is studied in this section to analyse the formulation proposed in Section 3.3. This stress path involves elastic behaviour, yielding on the *SD* yield curve alone and simultaneous yielding on the *LC* and *SD* curves. In this way, it is possible to carry out a first analysis on the following model parameters employed in the model: κ_s (associated with the elastic water retention response), λ_s (associated with the water retention behaviour when yielding on the *SD/SI* yield curve alone) and k_1 (coupling parameter associated with of the water retention behaviour on the mechanical behaviour, see Section 2.6). Also, as the stress path reaches the bottom corner defined at the intersection between the *LC* and *SD* yield curves, simultaneous yielding occurs and the parameters λ_s^* and k_1^* (also calculated from the original set of parameters defined in the model) introduced in Section 2.7 can be also analysed. The same values for the initial state and model parameters summarised in Table 3.2 are used in this analysis.

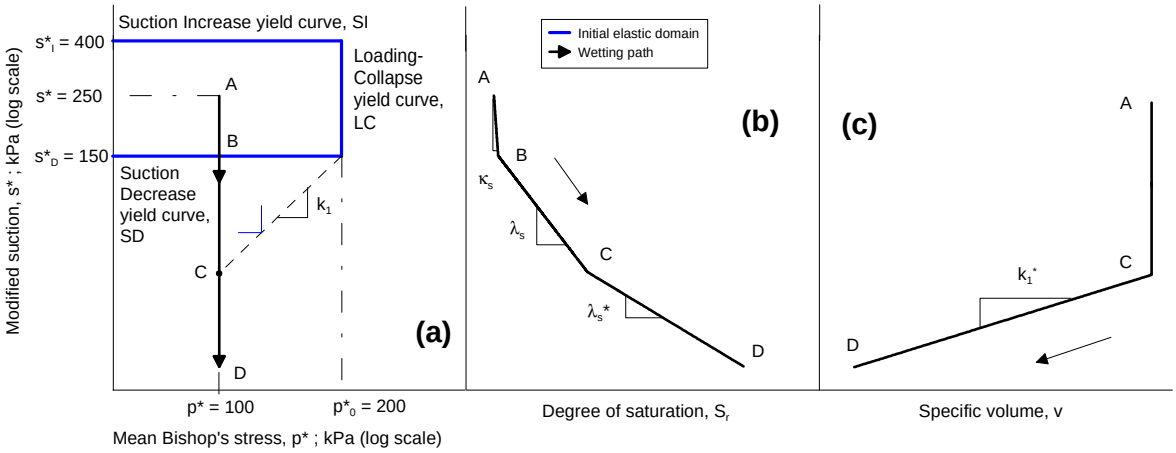

Figure 3- 7 Model response under an isotropic wetting stress path at constant mean Bishop's stress.

Figure 3-7a shows the stress path (in the lns^*:lnp^* plane) and Figures 3-7b and 3-7c show the computed variations of S_r and v respectively (both plotted against lns^*). A first elastic increase of S_r controlled by the soil parameter κ_s is observed from *A* to *B*. At *B* the *SD* yield curve is reached and yielding on this curve alone takes place. Consequently, the evolution of the degree of saturation with s^* is controlled by the parameter λ_s (see Figure 3-7b). This type of behaviour lasts until the bottom corner *LC-SD* is reached at *C* from where simultaneous yielding on *LC* and *SD* begins. From *C* to the end of the test *D*, changes of the degree of saturation with s^* are controlled by λ_s^*. Changes of specific volume (see Figure 3-7c) show no variation of v until simultaneous yielding on *SD* and *LC* is occurring (from *C*), with subsequent changes governed by k_1^*.

Table 3. 4 Comparison between theoretical and estimated soil parameters values (water retention behaviour).

Soil parameter	***Theoretical value***	***Back-calculated value***	***Coefficient of determination R^2***
κ_s	*0.0009*	*0.0008998*	*1.000000*
λ_s	*0.0971*	*0.096947*	*1.000000*
λ_s^*	*0.209*	*0.208721*	*1.000000*
k_1^*	*0.178*	*0.177944*	*1.000000*

Table 3.4 shows that the accuracy achieved in the computations for this second type of isotropic stress path, involving first elastic water retention behaviour, then yielding on only *SD* yield curve and finally simultaneous yielding on *LC* and *SD*, is very satisfactory, which suggests also that the model has been correctly implemented in the algorithm.

3.5.2. Stress-driver algorithm based on mean net stress and suction

This second type of stress-driver algorithm employs as inputs the increments of mean net stress and matric suction. These variations are commonly controlled in isotropic stress tests and it is, therefore, interesting to present an algorithm using them as driving or known variables. In particular, in this work, this second type of stress-driver approach is used to compare the computed results with the predicted normal compression relationships presented in Chapter 2.

i. *Initial stress state*

Given the initial values of mean net stress, matric suction, void ratio and degree of saturation, compute the initial mean Bishop's stress and modified suction. Define the initial elastic domain (see Figure 3-2) with the initial values of the hardening parameters

ii. *Elastic trial*

Assuming that the given $\Delta\bar{p}$ and Δs are purely elastic, compute an elastic trial increment of Δp^* and Δs^*. In order to do that is necessary to find expressions for these increments in terms of the input increments $\Delta\bar{p}$ and Δs by assuming elastic behaviour (see Appendix A.3).

$$\Delta p^{*trial} = f\left(\Delta\bar{p}, \Delta s\right) \qquad (3.\ 60)$$

$$\Delta s^{*trial} = f\left(\Delta\bar{p}, \Delta s\right) \qquad (3.\ 61)$$

Update p_{k+1}^* and s_{k+1}^* with the computed increments and evaluate the new stress point. If the trial stress state is inside or on each of the yield surfaces defined (i.e. $F_{LC}(p^*_{k+1},p_0^*)\leq 0$ ***and*** $F_{SD}(s^*_{k+1},s_D^*)\leq 0$ ***and*** $F_{SI}(s^*_{k+1},s_I^*)\leq 0$) update variables with the elastic trial and exit.

iii. *Identification of the elasto-plastic mechanism active and update*

Determine the elasto-plastic mechanism active (Section 3.4), find the corresponding intersection/s and update variables accordingly. As further detailed in Appendix A.3 it is possible to find different expressions for Δp^* and Δs^* in terms of the input increments $\Delta \overline{p}$ and Δs for each possible mechanism defined in the model.

iv. *Yield surface drift correction*

If the final state lies outside the updated yield surfaces, project the current state back to the pertinent yield surface/s using a drift correction method (see Section 6.5).

3.5.2.1. Computed and predicted normal compression relationships during simultaneous yielding on LC and SD

A final analysis is included in this section to explore if the numerical scheme reproduces the predicted model response when simultaneous yielding on the *LC* and *SD* curves is active. In other words, this analysis is aimed at checking if the final states of the computed isotropic normal compression stress paths fall on an isotropic planar normal compression surface (of gradients λ^* and k_2^*) in v:lnp^*:lns^* space and also on a second isotropic planar surface (of gradients λ_s^* and k_1^*) in S_r:lnp^*:lns^* space (see Chapter 2). A possible way to check this is by using the mathematical scheme presented previously to reproduce the isotropic normal compression tests at constant suction on samples of speswhite kaolin (Sivakumar, 1993) presented in Section 2.7.3. Then, by plotting the final states of these isotropic normal compression tests in the v:lnp^*:lns^* and S_r:lnp^*:lns^* spaces (Figures 3-8 and 3-9) it is possible to see whether the values of λ^*, k_2^*, λ_s^* and k_1^* estimated from these computed final states are as those summarised in Table 3.5.

Table 3.5 shows the model parameters and initial state used in the computations. These values are taken from the analysis presented in Section 2.7.4 on the tests of Sivakumar (1993) when describing the methodology to determine the soil parameters defined in the model but any other set of values would be also possible. Table 3.5 also includes the values of the parameters defining the gradients of the planar surfaces introduced in Chapter 2 and that can be used to study the performance of the mathematical scheme employed.

Table 3. 5 Model parameters and initial state used in the computations.

κ=0.006	λ=0.124	λ_s=0.0971	κ_s=0.0004	k_1=0.685	k_2=0.773
p^*=229 kPa	s^*=164 kPa	p_0^*=271 kPa	s_D^*=164 kPa	e=1.210	S_r=0.597
λ^*=0.257	λ^*_s=0.206	k^*_1=0.172	k^*_2=0.159		

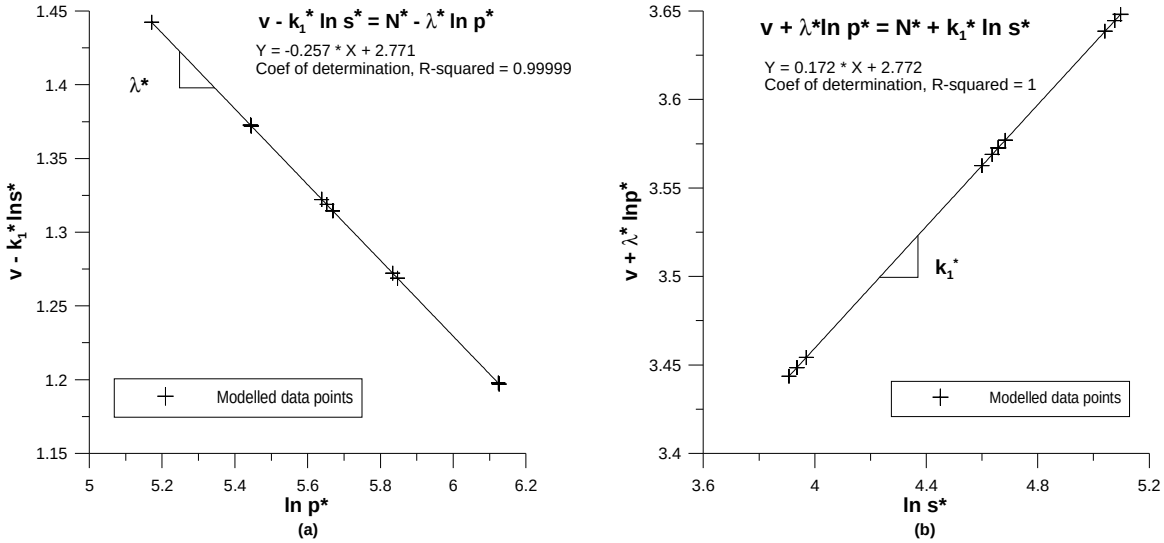

Figure 3- 8 Orthogonal two-dimensional views of planar surface for v with computed results.

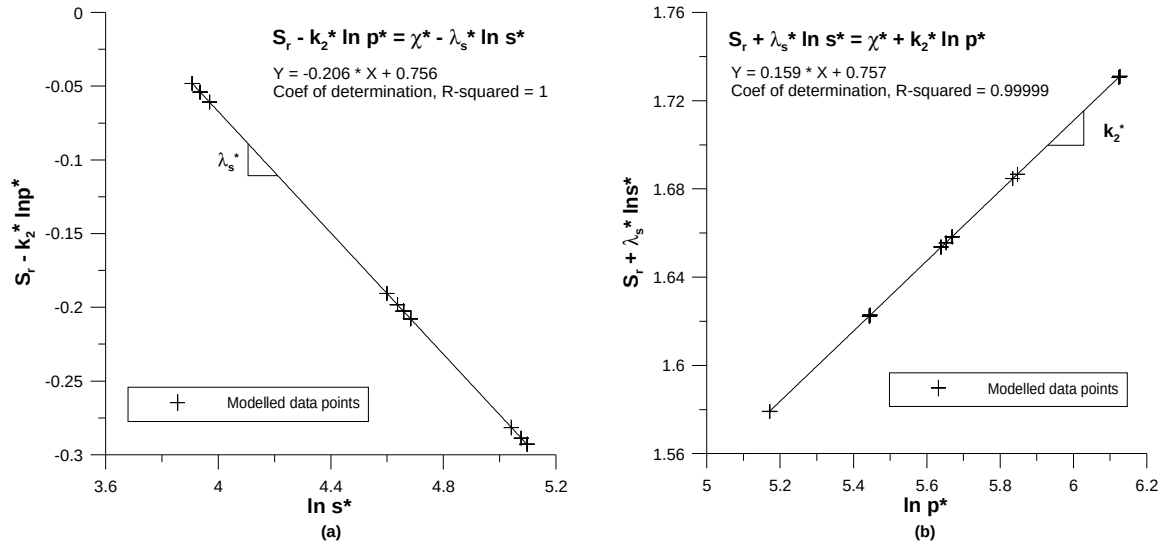

Figure 3- 9 Orthogonal two-dimensional views of planar surface for S_r with computed results.

Figures 3-8 and 3-9 represent a pair of orthogonal two-dimensional views of each isotropic normal compression planar surface (one for *v* and one for S_r) estimated from the modelled final states of the normal compression tests of Sivakumar (1993). For example, (Figure 3-8a) shows $(v-k_1^* ln s^*)$ plotted against lnp^* and (Figure 3-8b) shows $(v+\lambda^* lnp^*)$ plotted against lns^*. In both of these plots presented in Figure 3-8, the planar surface for *v*

has been reduced in each case to a single straight line (of gradients λ^* and k_1^* respectively), and it is easy to check that all final states of the test modelled lie on this planar surface (as the estimated gradients from the computed results are practically the same as those calculated from the original set of model parameters, see Table 3.6). Similarly, Figure 3-9 illustrates the computed results of the water retention response also showing that, as predicted by the model, all the final states of the normal compression tests modelled lie on a straight line of slope λ_s^* when plotting such states in the $(S_r - k_2^* lnp^*):lns^*$ plane (Figure 3-9a) and on a second straight line of slope k_2^* when plotting the same results in the $(S_r+\lambda_s^* lns^*):lnp^*$ plane (Figure 3-9b).

The fact that in both figures (Figure 3-8 and Figure 3-9) all final states of the tests modelled fall on both planar surfaces presented in Section 2.7.2 is a significant component of verification of the mathematical expressions implemented in the algorithm.

Table 3.6 summarises the relevant information of the accuracy achieved in the computations analysed in this final section. The estimated values in Table 3.6 have been calculated using the least-square method implemented in the GRAPHER software applied to the seventeen final states computed. These values can be compared with the actual (theoretical) parameter values and estimate the error made in the computations. It is observed that the theoretical values of the parameters and those values back-calculated from the final states of the computed isotropic normal compression tests are, as expected, practically the same, with a coefficient of determination R^2 very close to one in all cases. This reinforces again the conclusion that the Wheeler et al. (2003) model is being correctly integrated.

Table 3. 6 Comparison between theoretical and estimated gradients of the normal compression planar surfaces.

Soil parameter	***Theoretical value***	***Back-calculated value***	***Coefficient of determination R^2***
λ^*	*0.257*	*0.257*	*0.99999*
k_1^*	*0.172*	*0.172*	*1.00000*
λ_s^*	*0.206*	*0.206*	*1.00000*
k_2^*	*0.159*	*0.159*	*0.99999*
N^*	*2.768*	*2.771*	-
χ^*	*0.755*	*0.756*	-

Chapter 4

CRITICAL STATE RELATIONSHIPS FOR UNSATURATED COMPACTED SOILS

4. Critical state relationships for unsaturated compacted soils

The constitutive model for isotropic stress states of Wheeler et al. (2003) was presented in Chapter 2 and a possible mathematical approach to numerically integrating it has been proposed in Chapter 3. Based on this constitutive model, two normal compression relationships assuming simultaneous yielding on *LC* and *SD* were developed in Chapter 2 showing a very satisfactory agreement with the experimental results of Sivakumar (1993). It was also showed that both relationships form unique planar surfaces: one in v:lnp^*:lns^* space and a second in S_r:lnp^*:lns^* space. When presenting the final states of the isotropic normal compression stages of Sivakumar (1993) in these spaces it was found that such states fall on two planar surfaces, as predicted by the model.

This chapter presents an extension of the model of Wheeler et al. (2003) to the stress states applicable to triaxial tests, by including the role of deviator stress q. Following the ideas developed in Wheeler (2009), this chapter then develops for ultimate (critical) states equivalent relationships to those previously proposed for isotropic normal compression cases. Assuming again simultaneous yielding on *LC* and *SD* surfaces, and that the soil remains under unsaturated conditions (i.e. $0<S_r<1$), a pair of critical state relationships expressing the ultimate values of specific volume and of degree of saturation in terms of mean Bishop's stress and modified suction variations, are developed in this current chapter. The representation of these critical state relationships in the v:lnp^*:lns^* and S_r:lnp^*:lns^* spaces show a second pair of unique planar surfaces. Equivalent to the work presented in Section 2.7, when developing the isotropic normal compression relationships, the experimental critical state data of Sivakumar (1993) have been plotted in these spaces and the results obtained are presented and discussed.

4.1. Critical state models for saturated soils

The first critical state models were the series of Cam Clay formulations for saturated soils developed at the University of Cambridge by Roscoe and his co-workers. Two main versions of this family of models were proposed. In the original Cam Clay formulation of Roscoe et al. (1958) the yield curve was given by a logarithmic curve, whereas in the modified version of Roscoe and Burland (1968) the yield curve was an ellipse (see Figure 4-1). This modification was included in order to avoid non-zero shear strains for q=0 as a consequence of the use of an associated flow rule (see Roscoe and Burland, 1968). The basic aspects of the Modified Cam Clay (*MCC*) version are briefly introduced in this section, as the proposed extension of the Wheeler et al. (2003) model to triaxial stress conditions (presented in Section 4.2) uses *MCC* as the saturated base model. A more

complete description of the Cam Clay family of models can be found in the original works of Roscoe et al. (1958) and Roscoe and Burland (1968) or, more recently, in Muir Wood (1990).

4.1.1. Modified Cam Clay model

The yield surface of the *MCC* model, illustrated in the *q:p'* plane in Figure 4.1, is given by the following mathematical expression:

$$q^2 = M^2 p'\left(p_0^{'} - p'\right) \qquad (4.1)$$

where q is the deviatoric stress ($q=\sigma_1-\sigma_3$), M is the aspect ratio of the elliptical yield curve, p' is the mean effective stress ($p'=(\sigma'_1+\sigma'_2+\sigma'_3)/3$) and $p_0^{'}$ is the hardening parameter defining the size of the yield surface. σ'_1, σ'_2, and σ'_3 are principal effective stresses.

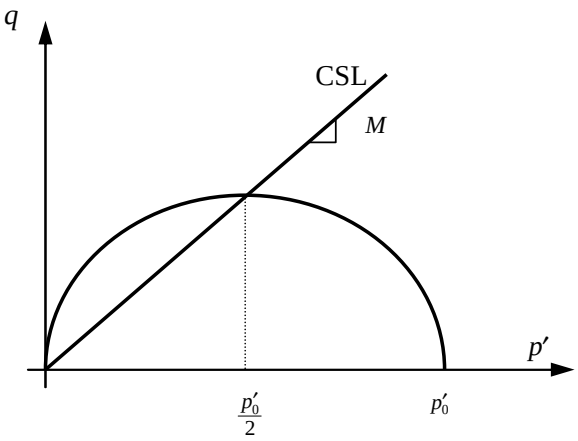

Figure 4- 1 Representation of the yield surface of the Modified Cam Clay model in the q:p' plane.

The hardening law depends on the plastic volumetric strain and is given by:

$$\frac{dp_0'}{p_0'} = d\varepsilon_v^p \frac{v}{(\lambda-\kappa)} \qquad (4.2)$$

where $d\varepsilon_v^p$ is the increment of plastic volumetric strain, v is the specific volume, and λ and κ are the gradient of the isotropic normal compression line and the gradient of swelling lines respectively in the v:lnp' plane. An associated flow rule is employed:

$$\frac{d\varepsilon_q^p}{d\varepsilon_v^p} = \frac{2\eta}{M^2-\eta^2} \qquad (4.3)$$

where $d\varepsilon_q^p$ is the increment of plastic deviatoric strain and $\eta=q/p'$.

Elastic volumetric strains are given by:

$$d\varepsilon_v^e = \frac{\kappa}{v}\frac{dp'}{p'} \qquad (4.4)$$

The model predicts the occurrence of a unique normal compression line (*NCL*), for isotropic loading to virgin states, defined by:

$$v = N - \lambda \ln p' \qquad (4.5)$$

where *N* is a soil parameter.

The model also predicts the occurrence of critical states (shear strains increasing indefinitely with no further change of *q*, *p'* or *v*), with all critical states falling on a unique critical state line (*CSL*) defined in *q:p':v* space by:

$$q = Mp' \qquad (4.6)$$

$$v = \Gamma - \lambda \ln p' \qquad (4.7)$$

Γ is a soil parameter and, according to *MCC*, the vertical spacing between the *NCL* and the *CSL* in the *v*:ln*p'* plane is given by:

$$\Gamma = N - (\lambda - \kappa)\ln 2 \qquad (4.8)$$

An illustration of the critical state relationship (4.5) along with the normal compression line (4.2) and swelling lines (4.3) is represented in Figure 4-2.

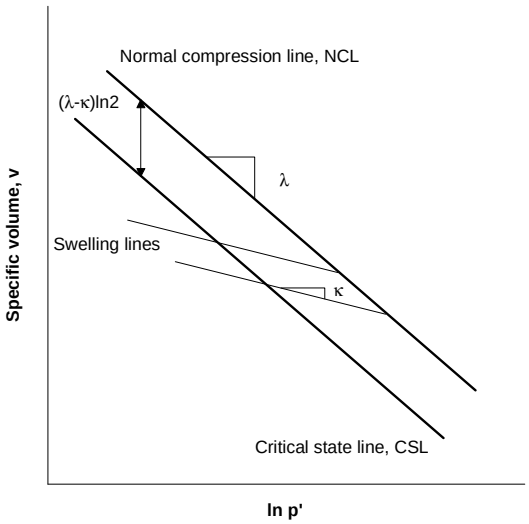

Figure 4- 2 Normal compression line, swelling lines and critical state line in the v:lnp' plane according to MCC.

4.2. Extension of the Wheeler et al. (2003) model to triaxial stress conditions

Lloret et al. (2008b) and Raveendiraraj (2009) proposed a simple extension of the Wheeler et al. (2003) model to the stress conditions of the triaxial test, by incorporating the role of the deviator stress q (and including the shear strength behaviour). This extended version of the model is presented here.

Two important assumptions are made in the formulation of the extended model. The first is to assume *MCC* as the underlying model for saturated conditions and the second is to assume a unique Critical State Line (*CSL*) in the q:p^* plane (where p^* is the mean Bishop's stress) as expressed by:

$$q = Mp^* \qquad (4.\ 9)$$

where M is the gradient of the *CSL* in the q:p^* plane.

The second assumption is based on experimental observations. Figure 4-3 plots the critical states of the experimental data of Sivakumar (1993) in the q:p^* plane. It can be seen that, for this set of results covering three different values of suction (i.e. 100 kPa, 200 kPa and 300 kPa), the approximation of a unique *CSL* in the q:p^* plane gives a reasonably good estimation, giving a slope of the *CSL* M=0.716. Similar results were obtained by other authors (e.g. Gallipoli et al., 2008; Raveendiraraj, 2009). In the work of Gallipoli et al. (2008) and Raveendiraraj (2009), in addition to the experimental data plotted in Figure 4-3, they also considered the experimental results on compacted speswhite kaolin presented in Wheeler and Sivakumar (2000) and, moreover, they also included tests at saturated conditions. Raveendiraraj (2009) argued that a deeper inspection of the results plotted in this plane suggested that the critical state relationship between q and p^* may not be entirely unique. A small trend with variation of suction was observed when analysing the critical states in the q:p^* plane, with the saturated critical state data points lying at the top of the range and the data points at the highest suction lying at the bottom of the range. In the work presented here, however, the simplest possible extension of the Wheeler et al. (2003) model to include the role of deviator stress has been adopted and a unique critical state line in the q:p^* plane has been adopted.

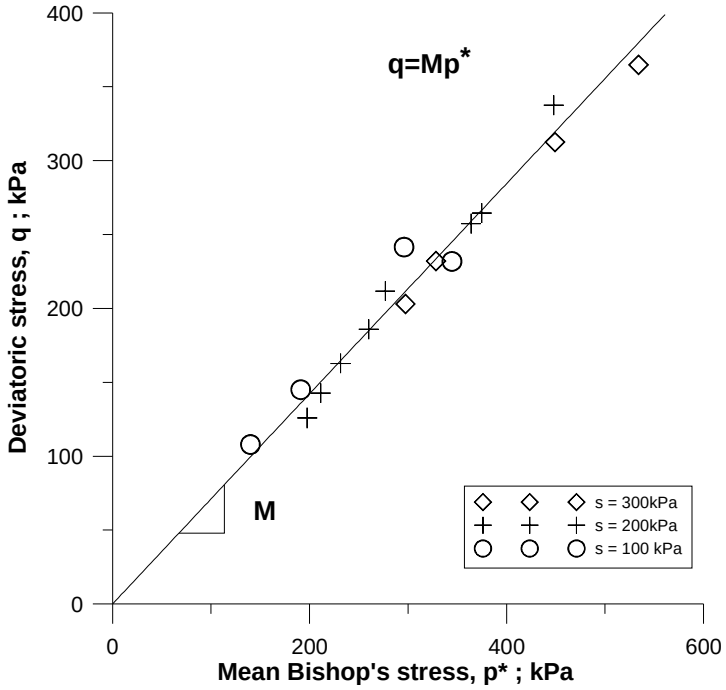

Figure 4- 3 Representation of the critical states of the experimental results of Sivakumar (1993) in the q:p plane.*

Lloret et al. (2008b) and Raveendiraraj (2009) extended the model of Wheeler et al. (2003) to triaxial stress states, to include the role of deviator stress *q*, by extending the *LC*, *SD* and *SI* yield curves from the isotropic p^*:s^* plane to form yield surfaces in *q*:p^*:s^* space (see Figure 4-4). Based on the assumptions of a unique critical state line in the *q*:p^* plane (defined by Equation (4.9)), and the assumption of *MCC* as the saturated base model, constant s^* cross-sections of the *LC* yield surface were assumed to be elliptical in shape, with aspect ratio *M* and the left hand boundary falling on the s^* axis (see Figure 4-4). The equation of the *LC* yield surface is therefore:

$$q^2 - M^2 p^* \left(p_0^* - p^* \right) = 0 \qquad (4.10)$$

The *SI* and *SD* yield surfaces were assumed to be vertical planes in *q*:p^*:s^* space (see Figure 4-4), given by:

$$s^* = s_I^* \qquad (4.11)$$

$$s^* = s_D^* \qquad (4.12)$$

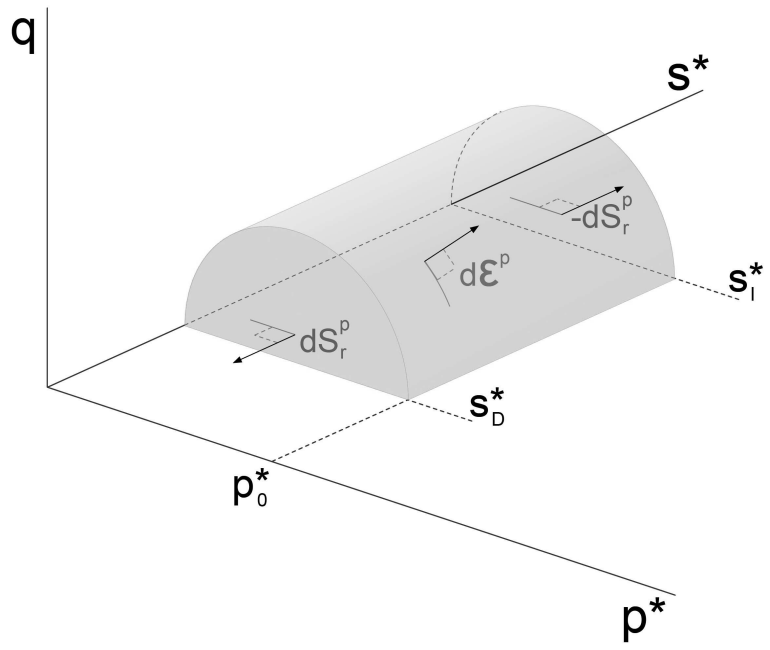

Figure 4- 4 Extension of the Wheeler et al. (2003) model to triaxial stress states.

The hardening laws assumed in the model are unchanged from the equations presented for the model under isotropic stress states (see Chapter 2). Associated flow rules are assumed on all three yield surfaces. Remembering that plastic volumetric strain increment $d\varepsilon_v^p$, plastic deviatoric strain increment $d\varepsilon_q^p$ and plastic decrement of degree of saturation $-dS_r^p$ are work-conjugate to p^*, q and s^* respectively, this results in the following flow rules:

$$\frac{d\varepsilon_q^p}{d\varepsilon_v^p} = \frac{2\eta^*}{M^2 - \left(\eta^*\right)^2} \qquad \text{and} \qquad dS_r^p = 0 \tag{4. 13}$$

on the *LC* yield surface (where $\eta^* = q/p^*$), and

$$d\varepsilon_q^p = d\varepsilon_v^p = 0 \tag{4. 14}$$

on the *SI* and *SD* surfaces.

Elastic deviatoric strains are given by:

$$d\varepsilon_q^p = \frac{dq}{3G'} \tag{4. 15}$$

where *G'* is the elastic shear modulus (see Appendix A.1).

4.3. Occurrence of critical states

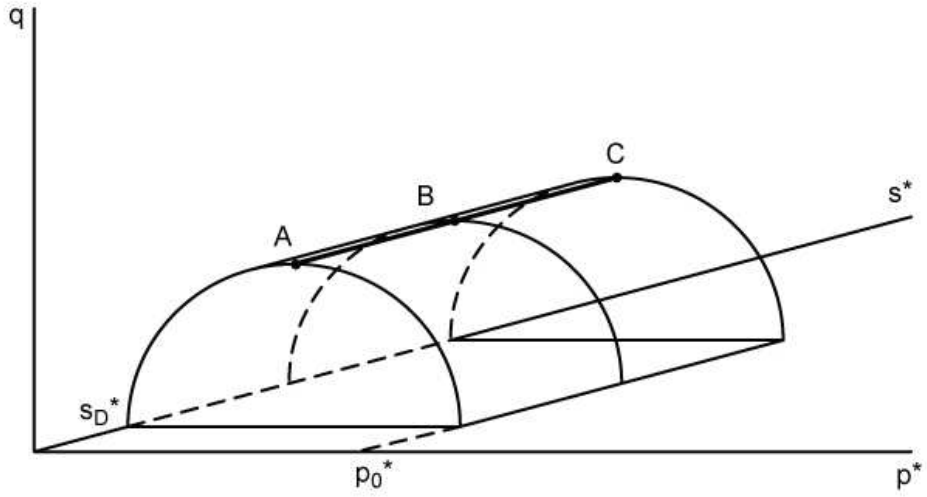

Figure 4- 5 Representation of critical states in the q:p^*:s^* space.

According to the extended model, critical states will correspond to points such as *A*, *B* and *C* in Figure 4-5, each of which lies at the top of the *LC* yield surface (i.e. at the apex of an elliptical constant s^* cross-section of the *LC* surface). At any such point, the associated flow rule of Equation (4.13) will imply that plastic shear strains can occur without any occurrence of plastic volumetric strains. The absence of plastic volumetric strains will imply no hardening of the *LC* yield surface and also no coupled movements of the *SD* or *SI* yield surfaces. Points such as *A*, *B* and *C* in Figure 4-5 therefore correspond to states where plastic shear straining can continue indefinitely without further change of q, p^*, s^*, v or S_r (i.e. without change of state), thus fulfilling the definition of critical state.

As all points such as *A*, *B* and *C* in Figure 4-5 fall on a line defined by Equation (4.9), critical states predicted by the model lie on a unique line in the q:p^* plane, defined by Equation (4.9) (as intended).

In general, however, critical state values of v for a given value of s^* will not lie on a unique line in the v:lnp^* plane (i.e. in general, there is no unique critical state surface in v:p^*:s^* space), because the value of v will also depend upon the current positions of the *SD* and *SI* yield surfaces. For example, consider the two different situations illustrated in Figure 4-6. Points A_1 and A_2 in Figure 4-6a and Figure 4-6b respectively, represent two critical states at identical values of q, p^* and s^*, and with the *LC* yield surface in identical positions in the two cases. The only difference in the two cases is a difference in the positions of the *SD* and *SI* surfaces. As a consequence, the predicted values of v will be different at points A_1 and A_2. This is because the differences in positions of the *SD* and *SI* yield surfaces

imply different amounts of coupled movement of the *LC* yield surface, which means that there must have been different amounts of yielding on the *LC* surface in the two cases (to produce the overall result that the *LC* surface is the same size in the two cases).

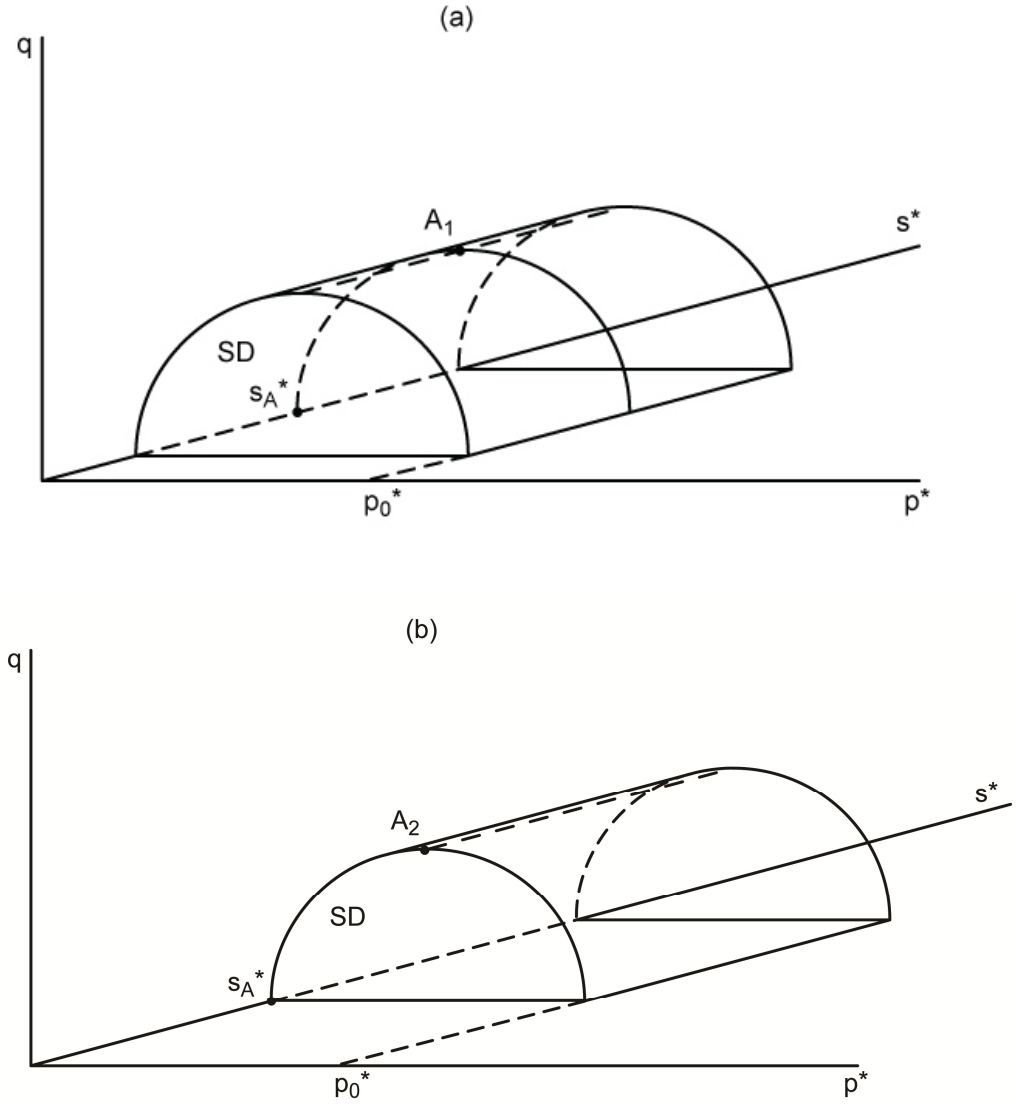

Figure 4- 6 Representation of critical states in in the q:p:s* space: (a) lying on the LC yield surface alone; (b) lying on both LC and SD yield surfaces.*

Although, critical states will not all lie on a unique surface in *v*:*p*:*s** space, it is shown in the next section that a unique surface does exist if consideration is restricted to critical states that lie on both *LC* and *SD* yield surfaces (i.e. points such as *A* in Figure 4-5 and A_2 in Figure 4-6b). As discussed in Chapter 2 (for isotropic states), it is surprisingly common for stress paths to arrive at the intersection between *LC* and *SD* surfaces, because of the coupling between the two surfaces. This is even more true for critical states. It will be very common (although not universal) that plastic volumetric straining (caused by yielding on the *LC* surface) during shearing or during prior isotropic loading will produce sufficient

coupled movement of the *SD* yield surface to bring the *SD* surface to the stress point prior to arrival at a critical state.

The special case of critical states which lie on both the *LC* yield surface and the *SD* yield surface is therefore considered in the next section.

4.4. Critical state relationships for simultaneous yielding on LC and SD surfaces

In Chapter 2 a pair of relationships expressing the variation of specific volume v and degree of saturation S_r in terms of mean Bishop's stress p^* and modified suction s^*, were presented for isotropic stress conditions and assuming simultaneous yielding on *LC* and *SD* yield curves. The equations were developed assuming also that the soil remained under unsaturated conditions (i.e. $0<S_r<1$). Each of these relationships, (2.37) and (2.40), when represented in the v:lnp^*:lns^* and S_r:lnp^*:lns^* spaces respectively, forms a unique planar surface having slopes λ^* and k_1^* (2.37) and k_2^* and λ_s^* (2.40). When the experimental results of Sivakumar (1993) from constant suction isotropic loading of compacted speswhite kaolin were presented in these spaces, they were found to lie on planar surfaces, as predicted by the model (see Section 2.7.2).

This section presents an equivalent analysis for critical states, resulting in the prediction of a second pair of unique planar surfaces in the v:lnp^*:lns^* and S_r:lnp^*:lns^* spaces. In Section 4.5 the results of Sivakumar (1993) are plotted in these spaces and compared with the model predictions

Figure 4-7 shows the stress path adopted in the development of the critical state relationships for v and S_r. Note that isotropic stress state *A* is at the intersection between the *LC* and *SD* yield surfaces and, therefore, lies on both planar surfaces defined for the isotropic normal compression relationships (2.37) and (2.40). An isotropic unloading stress path at constant modified suction (i.e. $s^*=s_D^*$) is considered from *A* to *B*. As a result, an elastic swelling controlled by κ is observed (see Figure 4-8) but no change of degree of saturation is computed because s^* remains constant and no yielding on *SD/SI* takes place (Figure 4-9). Shearing at constant modified suction and constant mean Bishop's stress is considered afterwards to reach a critical state at *C* (see Figure 4-7). As the path from *B* to *C* is elastic, and there is no change of either p^* or s^*, the values of v and S_r at *C* are identical to the corresponding values at *B* (see Figures 4-7 and 4-8). Note that stress state *C* is on both *LC* and *SD* yield surfaces.

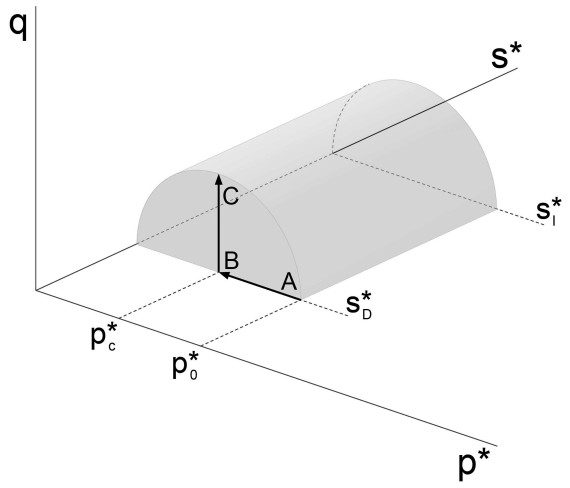

Figure 4- 7 Stress path ABC considered in the development of the critical state relationships.

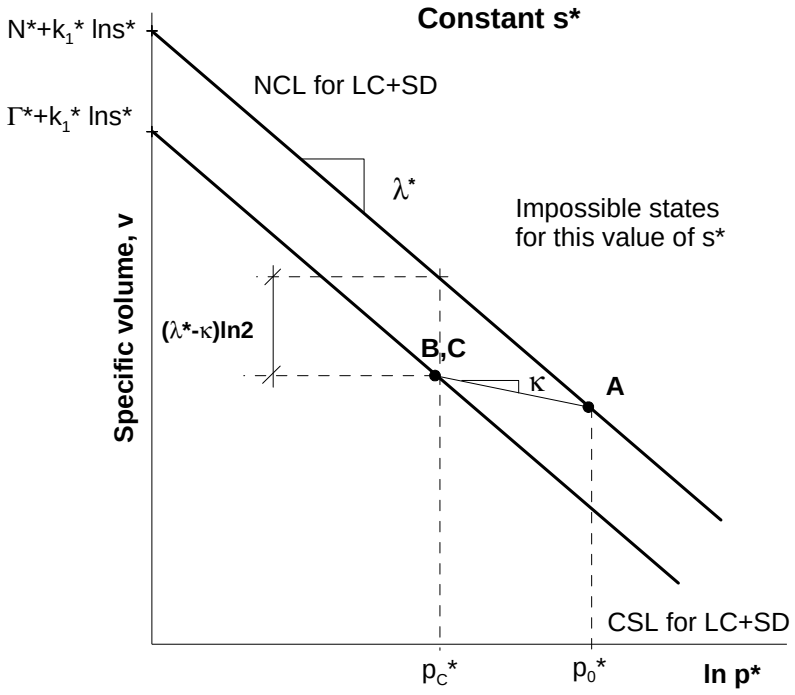

Figure 4- 8 Representation of stress path ABC in the v:lnp^* plane.

Figure 4-8 illustrates the stress path *ABC* at constant modified suction (see Figure 4-7) in the *v*:lnp^* plane. From this figure it can be seen that the specific volume v_c at the critical state *C* is related to the specific volume v_A at *A* by:

$$v_C = v_A + \kappa \ln \frac{p_0^*}{p_C^*} \qquad (4.16)$$

However, the elliptical shape of the constant s^* cross-sections of the *LC* yield surface implies $p_0^*=2p_C^*$ (see Figure 4-7), and the value of v_A can be related to p_0^* by the isotropic

normal compression planar surface of Equation (2.37) to give the following expression for the specific volume at critical states:

$$v = N^* - \left(\lambda^* - \kappa\right)\ln 2 - \lambda^* \ln p^* + k_1^* \ln s^* \qquad (4.\ 17)$$

This can also be written as:

$$v = \Gamma^* - \lambda^* \ln p^* + k_1^* \ln s^* \qquad (4.\ 18)$$

where:

$$\Gamma^* = N^* - \left(\lambda^* - \kappa\right)\ln 2 \qquad (4.\ 19)$$

Equation (4.18) defines a unique planar surface in v:lnp^*:lns^* space for critical states corresponding to simultaneous yielding on *LC* and *SD* surfaces. Comparison with Equation (2.37) shows that the predicted critical state surface for v is parallel to the isotropic normal compression surface for v. Equation (4.19) shows that the vertical spacing between the two planar surfaces is predicted to be (λ^*-κ)ln2 (see Figure 4-8).

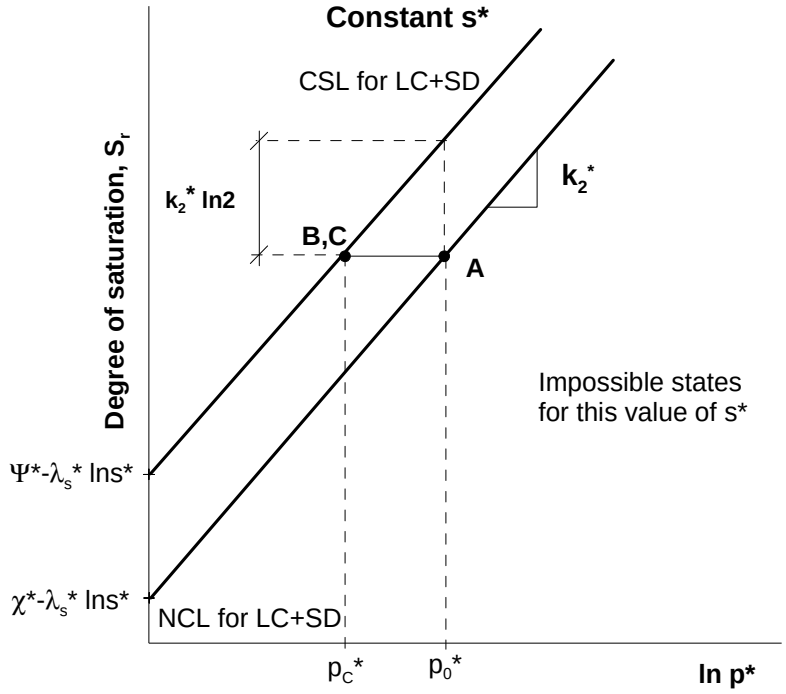

Figure 4- 9 Representation of stress path ABC in the S_r:lnp^* plane.

Figure 4-9 illustrates the stress path *ABC* at constant modified suction (see Figure 4-7) in the S_r:lnp^* plane. From this figure it is clear that:

$$S_{rC} = S_{rA} \qquad (4.\ 20)$$

Noting that S_{rA} can be related to p_0^* by the isotropic normal compression planar surface expression of Equation (2.40), and then noting again that $p_0^*=2p_C^*$, this results in the following expression for degree of saturation at critical states:

$$S_r = \chi^* + k_2^* \ln 2 - \lambda_s^* \ln s^* + k_2^* \ln p^* \qquad (4.\ 21)$$

This can be re-written as:

$$S_r = \Psi^* - \lambda_s^* \ln s^* + k_2^* \ln p^* \qquad (4.\ 22)$$

where:

$$\Psi^* = \chi^* + k_2^* \ln 2 \qquad (4.\ 23)$$

Equation (4.21) defines a unique planar surface in S_r:lnp^*:lns^* space for critical states corresponding to simultaneous yielding on *LC* and *SD* surfaces. Comparison with Equation (2.40) shows that the predicted critical state surface for S_r is parallel to the isotropic normal compression surface for S_r. Equation (4.23) shows that the vertical spacing between the two planar surfaces is predicted to be k_2^*ln2 (see Figure 4-9).

4.5. Experimental validation

The experimental tests of Sivakumar (1993) on compacted speswhite kaolin involved shearing to failure after the isotropic loading stages analysed in Chapter 2. The final critical states from these tests are employed in this section to investigate the validity of the pair of proposed critical states relationships. Shearing was applied in only sixteen of the seventeen tests used in Chapter 2. It is important to note that all the final states of the preceding isotropic normal compression stages had arrived at the corner between *LC* and *SD* yield surfaces (see Section 2.7.2.1) and, therefore, simultaneous yielding on the two surfaces would be expected to occur throughout the subsequent shearing stage. It is also important to emphasise that in none of these tests did the sample reach a fully saturated condition.

Equivalently to the analysis of the isotropic normal compression relationships, the least-square multi-regression method implemented in MATLAB has been used to best fit the final critical states of the experiments to a pair of planar surfaces in the v:lnp^*:lns^* and S_r:lnp^*:lns^* spaces. The fitted planar surfaces and the experimental data points for v and S_r

are shown in Figures 4-10 and 4-11 respectively. The fitted planar surfaces are summarised in the following pair of equations:

$$v = 2.709 - 0.258 \ln p^* + 0.166 \ln p^* \qquad (4.\ 24)$$

$$S_r = 0.714 - 0.229 \ln s^* + 0.203 \ln p^* \qquad (4.\ 25)$$

From where, by comparison with (4.18) and (4.22), the values of the parameters Γ^*, Ψ^*, λ^*, λ_s^*, k_1^* and k_2^* are:

Table 4. 1 Best fit parameters from the critical states of the experimental results of Sivakumar (1993).

Γ^*=2.709	λ^*=0.258	k_1^*=0.166
Ψ^*=0.714	λ_s^*=0.229	k_2^*=0.203

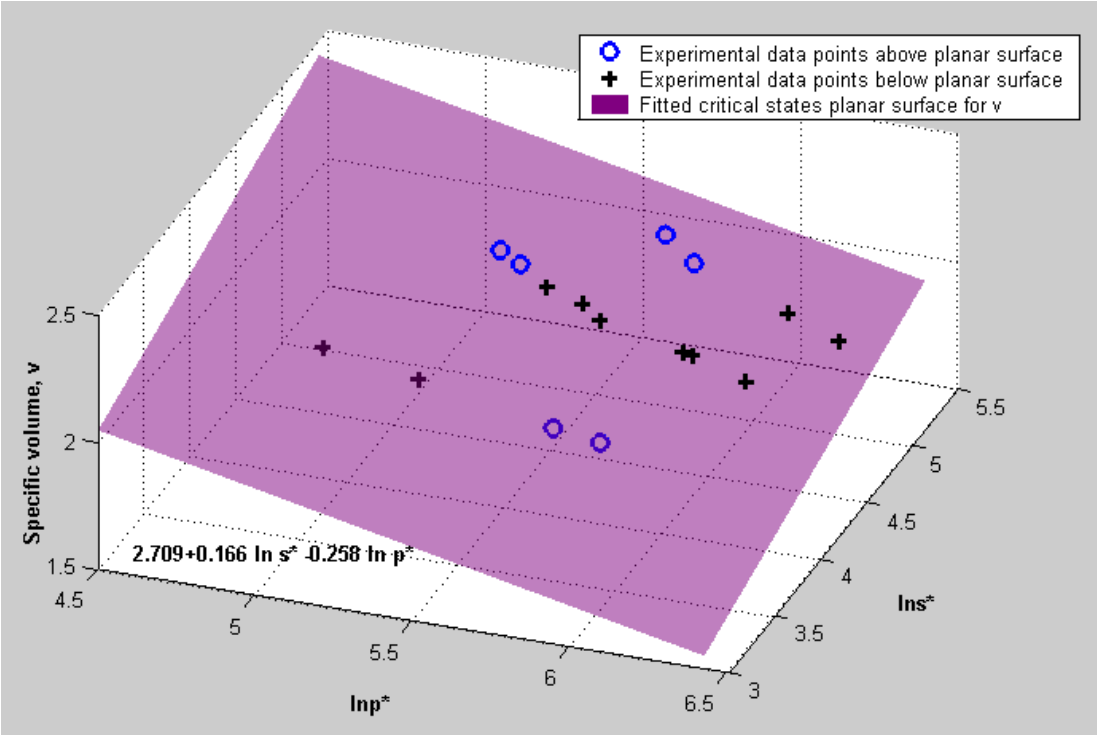

Figure 4- 10 Planar surface for v fitted to experimental results of Sivakumar (1993) at critical states.

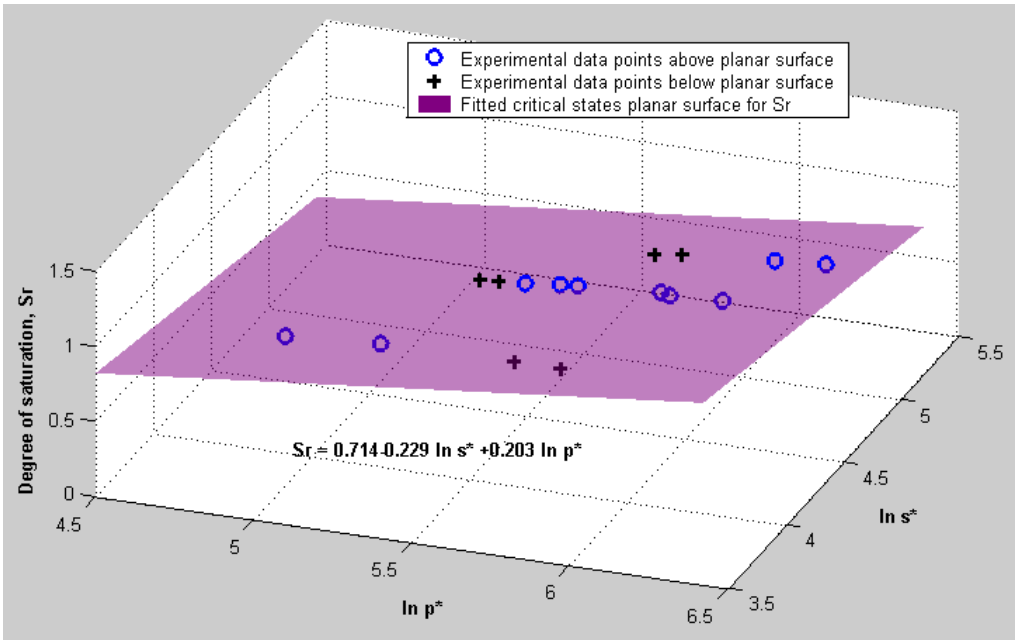

Figure 4- 11 Planar surface for S_r fitted to experimental results of Sivakumar (1993) at critical states.

To better illustrate the quality of fit of the two planar relationships of Equations (4.24) and (4.25) to the experimental data, Figures 4-12 and 4-13 show pairs of orthogonal two-dimensional views of the results, presented in suitable form so that, in each view, the fitted planar surface is reduced to a single straight line. Inspection of Figure 4-12 shows that the experimental critical state results for *v* are reasonably well matched by a planar surface in *v*:lnp^*:lns^* space. Similarly, inspection of Figure 4-13 shows that the experimental critical state results for S_r are well matched by a planar surface in S_r:lnp^*:lns^* space.

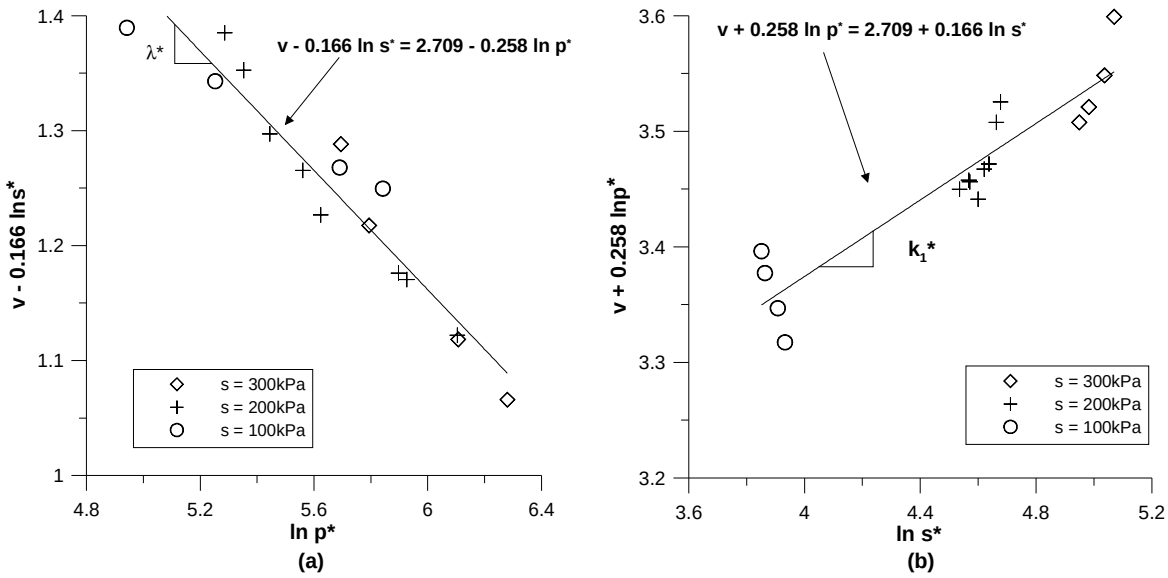

Figure 4- 12 Orthogonal two-dimensional views of planar surface for v compared with experimental results.

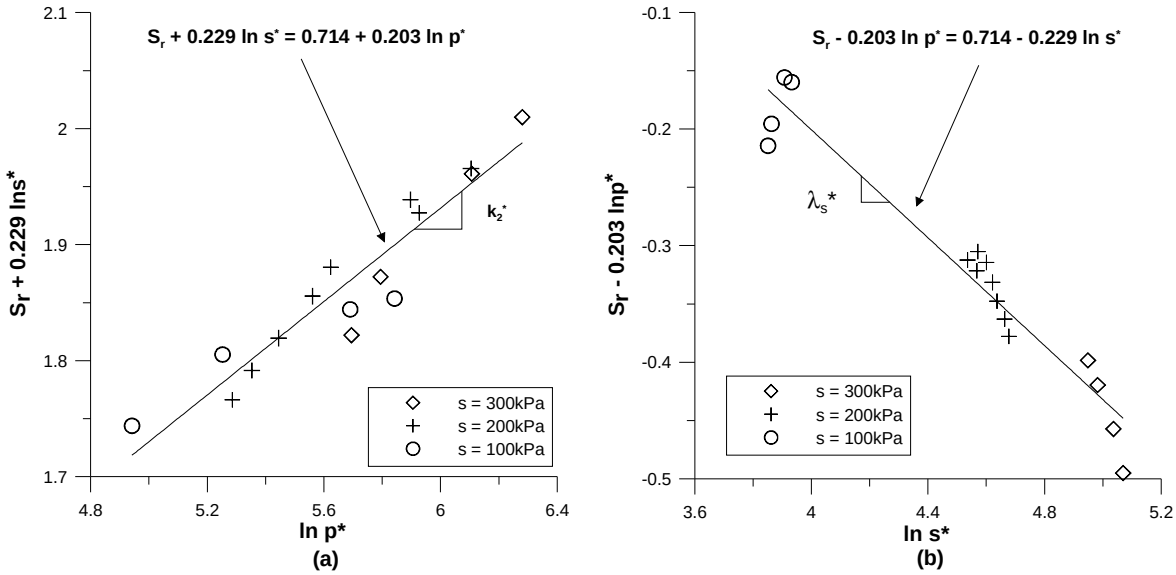

Figure 4- 13 Orthogonal two-dimensional views of planar surface for S_r compared with experimental results.

The next steps are to see whether the planar surfaces for v and S_r fitted to the experimental critical state data are parallel to the corresponding planar surfaces fitted to the experimental isotropic normal compression data (as predicted by the model) and whether the vertical spacings between the experimental normal compression and critical state surfaces are well predicted by the model. Figures 4-14 and 4-15 show the two fitted surfaces for v and the two fitted surfaces for S_r respectively.

Table 4.2 shows the two sets of experimentally determined values of λ^*, k_1^*, λ_s^*, and k_2^*; one set from the planar surfaces fitted to the isotropic normal compression data and the second set from the planar surfaces fitted to the critical state data. Inspection of Table 4.2 shows that the two different sets of values of λ^* and k_1^* (giving the gradients of the planar surfaces for v) are remarkably consistent. The values of λ_s^* and k_2^* (giving the gradients of the planar surfaces for S_r) show bigger differences between the two sets, but still a reasonably level of consistency.

Table 4. 2 Gradients of the planar surfaces fitted to the experimental isotropic normal compression data and critical state data of Sivakumar (1993).

	λ^*	k_1^*	λ_s^*	k_2^*
Normal Compression	*0.257*	*0.172*	*0.206*	*0.159*
Critical states	*0.258*	*0.166*	*0.229*	*0.203*

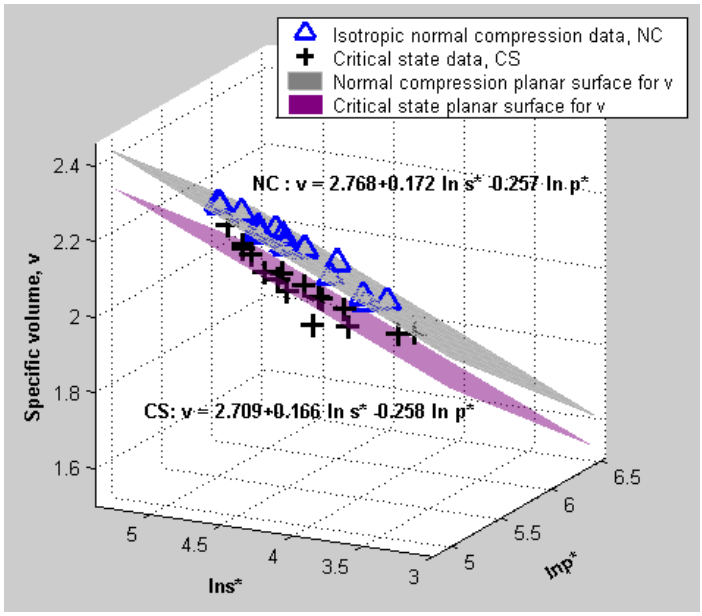

Figure 4- 14 Two planar surfaces for v fitted to experimental results of Sivakumar (1993) at final states of isotropic compression and at critical states.

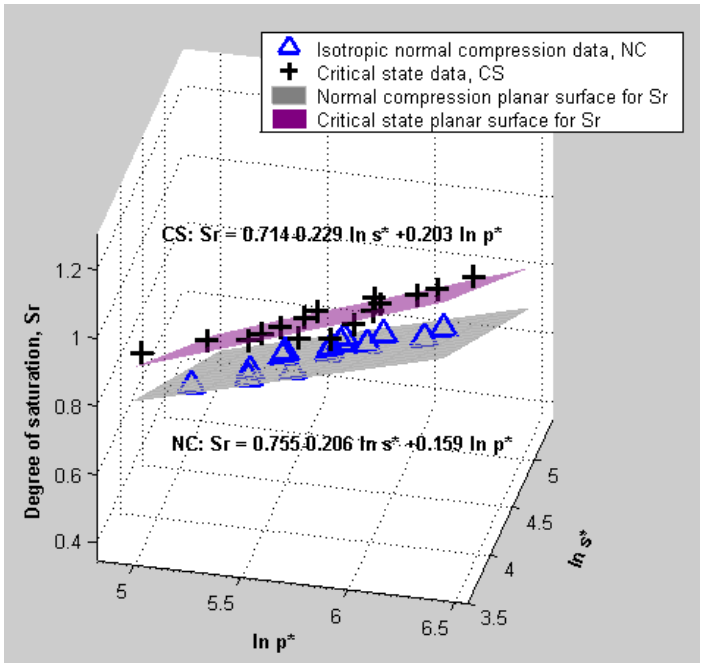

Figure 4- 15 Two planar surfaces for S_r fitted to experimental results of Sivakumar (1993) at final states of isotropic compression and at critical states.

Figure 4-16 shows a pair of orthogonal two-dimensional representations of the isotropic normal compression data and critical state data for *v*, presented in suitable form. The continuous lines in Figure 4-16a and 4-16b represent the best fit planar surface to the experimental isotropic normal compression data. The dashed lines in Figure 4-16a and 4-16b represent the form of the critical state surface predicted by the model (4.18), if values

of N^*, λ^*, and k_1^* determined from the isotropic normal compression planar surface are employed. Inspection of Figure 4-16 shows that the two planar surfaces for v are parallel, as predicted by the model, but that the vertical spacing between the critical state and isotropic normal compression surfaces for v is significantly overpredicted by the model (by a factor of approximately 2). This is a common observation when the predictions of *MCC* are compared with experimental data for saturated soils. It can therefore be viewed as a weakness of *MCC* that has been transferred through to the extended version of the Wheeler et al. (2003) model, by the assumption of *MCC* as the saturated base model.

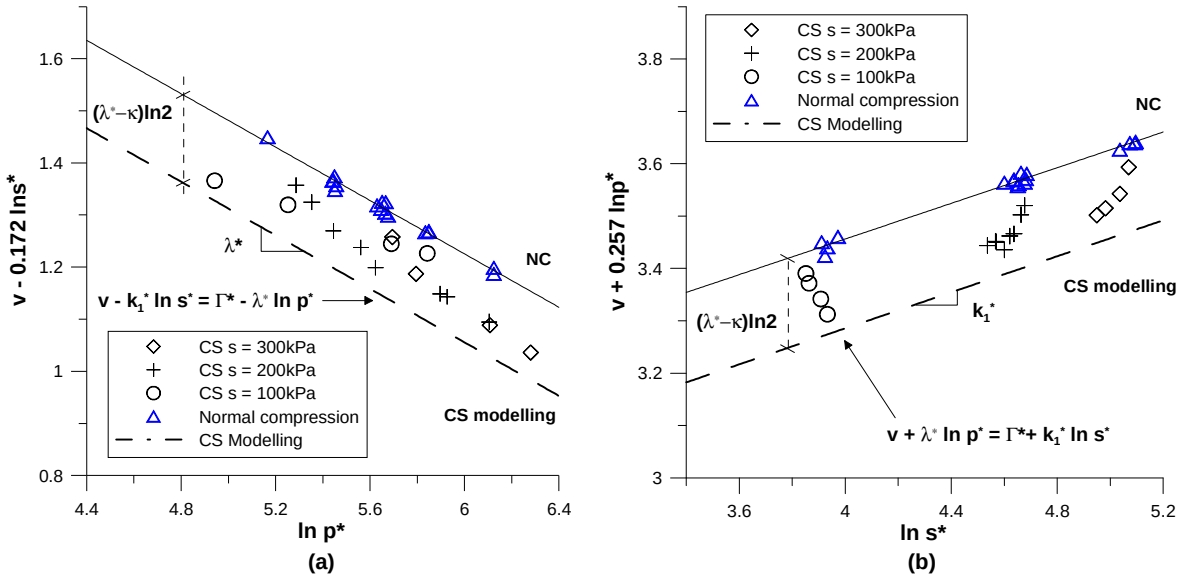

Figure 4- 16 Orthogonal two-dimensional views of planar surfaces for v compared with experimental results.

Figure 4-17 shows a pair of orthogonal two-dimensional representations of the isotropic normal compression data and critical state data for S_r, presented in suitable form. The continuous lines in Figure 4-17a and 4-17b represent the best fit planar surface to the experimental isotropic normal compression data. The dashed lines in Figure 4-17a and 4-17b represent the form of the critical state surface predicted by the model (4.22), if values of χ^*, λ^*, and k_1^* determined from the isotropic normal compression planar surface are employed. Inspection of Figure 4-17 shows that the two planar surfaces for S_r are parallel, as predicted by the model. It is also observed in Figure 4-17 that the vertical spacing between the critical state and isotropic normal compression surfaces for S_r predicted by the model provides an excellent match to the experimental results of Sivakumar (1993).

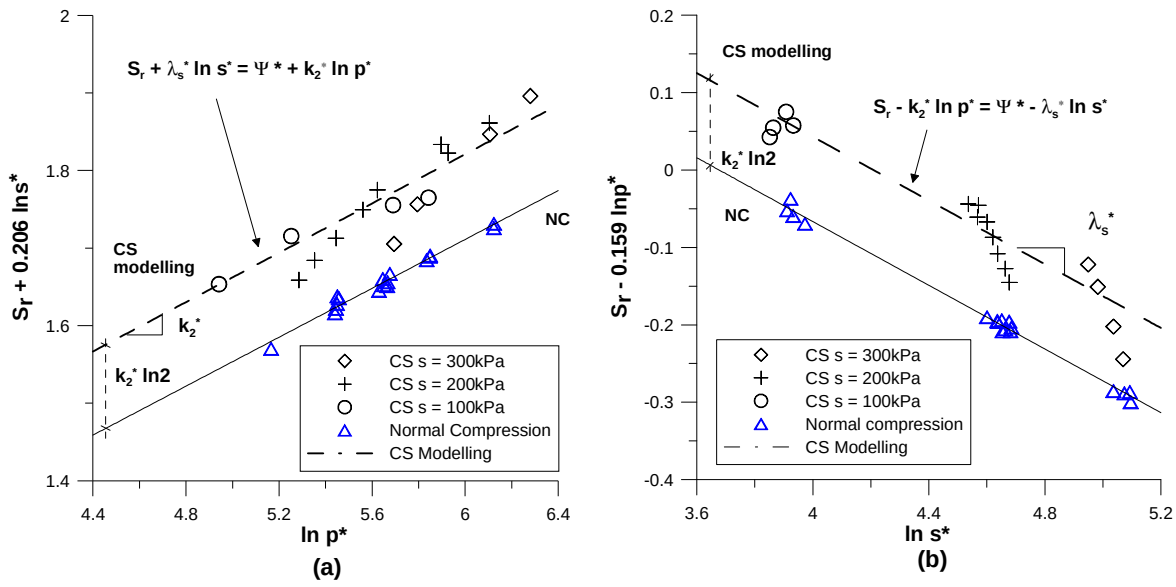

Figure 4- 17 Orthogonal two-dimensional views of planar surfaces for S_r compared with experimental results.

Chapter 5

3D FULLY COUPLED MECHANICAL-WATER RETENTION MODEL FOR UNSATURATED SOILS

5. 3D fully coupled mechanical-water retention model for unsaturated soils

5.1. Introduction

An extension of the Wheeler et al. (2003) model to the particular stress conditions of the triaxial test has been presented and discussed within Chapter 4. In order to implement the model in a finite element program, a generalisation to the general case of 3D stress conditions is proposed in this Chapter 5. The extended version of the model is afterwards used to simulate the experimental results of Sivakumar (1993) involving isotropic and triaxial stress paths at three different constant values of suction (i.e. 100 kPa, 200 kPa and 300 kPa). This modelling provide verification of the correct implementation of the 3D version of the model (by checking that the predicted final states after isotropic loading and then after shearing to critical states lie on the unique planar surfaces derived in Sections 2.7.2 and 4.4 respectively). Comparison of the full model simulations with the experimental results of Sivakumar (1993) then provides partial validation of the extended version of the model (although limited to the stress conditions of the triaxial test).

Even though all the results presented in previous chapters are very promising, the full formulation of the model for 3D conditions and its subsequent validation, are crucial steps that have to be done before implementing the constitutive model in a finite element code and using it to solve problems of practical interest. This current chapter focuses on this aspect.

5.2. Extension of the Wheeler et al. (2003) model to 3D conditions

The generalised version of the model is formulated in terms of the three invariants (p^*, J, θ) (where: p^* is the first invariant of the Bishop's stress tensor: $p^*=1/3(\sigma_1^*+\sigma_2^*+\sigma_3^*)$; J is the second invariant of the deviatoric Bishop's stress tensor: $s_{ij}^*=\sigma_{ij}^*-\delta_{ij}p^*$ and θ is the Lode angle) and the modified suction (s^*) (see also Appendix A.1 for more details). An illustration of the yield surfaces is shown in Figure 5-1.

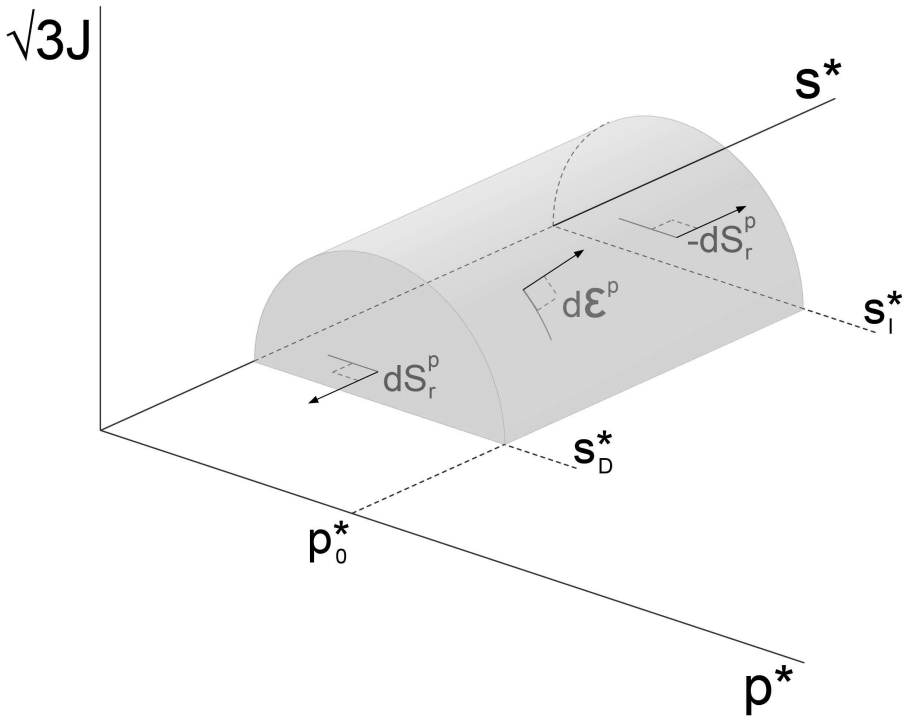

Figure 5- 1 Yield surfaces of the 3D generalised model.

5.2.1. Yield surfaces

Equivalent to the original model described in Chapter 2, the plastic mechanisms of this generalised version are described by three different yield surfaces (Figure 5-1): the Loading Collapse yield surface (*LC*); the Suction Increase yield surface (*SI*); and the Suction Decrease yield surface (*SD*). In order to describe the different inelastic behaviour observed in unsaturated soils, Wheeler and co-workers proposed the following plastic mechanisms and couplings: 1) yielding on the *LC* surface causes plastic volumetric strain, which produces coupled upwards movements of *SI* and *SD* surfaces; 2) yielding on the *SI* surface causes plastic decrease of S_r, which produces coupled upward movement of the *SD* surface and outward movement of the *LC* surface; and 3) yielding on the *SD* surface causes plastic increments of S_r, which produces coupled downward movement of the *SI* surface and inward movement of the *LC* surface. Further details can be found in Chapter 2.

As discussed in Chapter 4, experimental evidences suggest that a reasonable first approximation is to assume a unique critical state line (*CSL*) in the p^*:q plane (see Section 4.2). With this assumption, the elastic domain of the extended constitutive model is defined by the three yield surfaces (previously introduced) illustrated in Figure 5-1. As in

Chapter 4, the Modified Cam Clay (*MCC*) model has been adopted as the boundary condition for the saturated case, therefore:

$$F_{LC} = 3J - \left[\frac{g(\theta)}{g(\theta)\big|_{\theta=-\frac{\pi}{6}}} \right]^2 M^2 p^* \left(p_0^* - p^* \right) = 0 \qquad (5.\ 1)$$

$$F_{SI} = s^* - s_I^* = 0 \qquad (5.\ 2)$$

$$F_{SD} = s_D^* - s^* = 0 \qquad (5.\ 3)$$

where p_0^* is the hardening parameter defining the position of the *LC* yield surface, s_I^* and s_D^* are the hardening parameters defining the locations of *SI* and *SD* yield surfaces respectively, *J* is the second invariant of the Bishop's deviatoric stress tensor (see Appendix A.1) and $g(\theta)$ is a function of the Lode angle (equivalent to *M* in p^*:q plane). Different expressions for $g(\theta)$ are given for different failure criteria in Appendix A.1. Note also, that θ=-(π/6) corresponds to the triaxial stress conditions and (5.1) recovers the form of the *LC* yield surface for the particular case of triaxial stress conditions presented in Chapter 4 (see Equation (4.10)).

To express the equations in a more compact way, the following notation of generalised stress and strain increment vectors is adopted:

$$\tilde{\boldsymbol{\sigma}}^* = \left(\sigma_{xx}^* \quad \sigma_{yy}^* \quad \sigma_{zz}^* \quad \tau_{xy} \quad \tau_{yz} \quad \tau_{xz} \quad s^* \right)^T \qquad (5.\ 4)$$

$$d\tilde{\boldsymbol{\varepsilon}} = \left(d\varepsilon_{xx} \quad d\varepsilon_{yy} \quad d\varepsilon_{zz} \quad d\gamma_{xy} \quad d\gamma_{yz} \quad d\gamma_{xz} \quad -dS_r \right)^T \qquad (5.\ 5)$$

5.2.2. Flow rules

During yielding one or more plastic mechanisms are activated and the irreversible changes of the generalised strain increments are calculated through the flow rule. Associated flow rules are assumed within this framework to evaluate the direction of the plastic strain increments. Therefore, it is possible to express these plastic strain increments according to the following general expression:

$$d\tilde{\boldsymbol{\varepsilon}}_j^p = d\chi_l^j \frac{\partial F_l}{\partial \tilde{\boldsymbol{\sigma}}^*} \qquad \text{where} \qquad \begin{matrix} l = LC, \beta; \\ j = LC, \beta, LC + \beta \text{ with } \beta = SD \text{ or } SI \end{matrix} \qquad (5.\ 6)$$

where $d\chi_l^j$ is the plastic multiplier with *j* related to the plastic mechanism active and *l* associated with plastic changes of degree of saturation or volumetric strains. In particular, this means that $dS_r^p=0$ when yielding on the *LC* yield surface alone (5.7); whereas dS_r^p is the only non-zero term of $d\tilde{\boldsymbol{\varepsilon}}^p$ when yielding on the *SD* or *SI* yield surface alone (5.8). All terms of $d\tilde{\boldsymbol{\varepsilon}}^p$ can be non-zero when two plastic mechanisms are active simultaneously (5.9).

$$d\tilde{\boldsymbol{\varepsilon}}_{LC}^p = \begin{pmatrix} d\varepsilon_{xx}^p & d\varepsilon_{yy}^p & d\varepsilon_{zz}^p & d\gamma_{xy}^p & d\gamma_{yz}^p & d\gamma_{xz}^p & 0 \end{pmatrix}^T \quad (5.7)$$

$$d\tilde{\boldsymbol{\varepsilon}}_{\beta}^p = \begin{pmatrix} 0 & 0 & 0 & 0 & 0 & 0 & -dS_r^p \end{pmatrix}^T \quad (5.8)$$

$$d\tilde{\boldsymbol{\varepsilon}}_{LC+\beta}^p = \begin{pmatrix} d\varepsilon_{xx}^p & d\varepsilon_{yy}^p & d\varepsilon_{zz}^p & d\gamma_{xy}^p & d\gamma_{yz}^p & d\gamma_{xz}^p & -dS_r^p \end{pmatrix}^T \quad (5.9)$$

Combining with (5.6), the flow rule can be written as (5.10) when yielding on the *LC* yield surface alone; (5.12) when yielding on the *SD* or *SI* yield surface alone and (5.14) when yielding simultaneous on both *LC* and *SD* or *SI* yield surfaces.

$$d\tilde{\boldsymbol{\varepsilon}}_{LC}^p = d\chi_{LC}^{LC} \quad \frac{\partial f_{LC}}{\partial \tilde{\boldsymbol{\sigma}}^*} = d\chi_{LC}^{LC}\mathbf{m}_{LC} \quad (5.10)$$

where

$$\mathbf{m}_{LC}^T = \begin{pmatrix} \frac{\partial F_{LC}}{\partial \sigma_{xx}^*} & \frac{\partial F_{LC}}{\partial \sigma_{yy}^*} & \frac{\partial F_{LC}}{\partial \sigma_{zz}^*} & \frac{\partial F_{LC}}{\partial \tau_{xy}} & \frac{\partial F_{LC}}{\partial \tau_{yz}} & \frac{\partial F_{LC}}{\partial \tau_{xz}} & 0 \end{pmatrix} \quad (5.11)$$

$$d\tilde{\boldsymbol{\varepsilon}}_{\beta}^p = d\chi_{\beta}^{\beta} \quad \frac{\partial f_{\beta}}{\partial \tilde{\boldsymbol{\sigma}}^*} = d\chi_{\beta}^{\beta}\mathbf{m}_{\beta} \quad (5.12)$$

where

$$\mathbf{m}_{\beta}^T = \begin{pmatrix} 0 & 0 & 0 & 0 & 0 & 0 & \frac{\partial F_{\beta}}{\partial s^*} \end{pmatrix} \quad (5.13)$$

$$d\tilde{\boldsymbol{\varepsilon}}_{LC+\beta}^p = d\chi_{LC}^{LC+\beta} \quad \frac{\partial f_{LC}}{\partial \tilde{\boldsymbol{\sigma}}^*} + d\chi_{\beta}^{LC+\beta} \quad \frac{\partial f_{\beta}}{\partial \tilde{\boldsymbol{\sigma}}^*} = d\chi_{LC}^{LC+\beta}\mathbf{m}_{LC} + d\chi_{\beta}^{LC+\beta}\mathbf{m}_{\beta} \quad (5.14)$$

5.2.3. Hardening laws and couplings between plastic mechanisms

The hardening laws are expressed as relations between plastic increments of volumetric strain $d\varepsilon_v^p$, plastic increments of degree of saturation dS_r^p and the increments of the hardening variables dp_0^*, ds_D^* and ds_I^*. The hardening laws in the generalised version of the model are identical to the ones proposed by Wheeler el al. (2003), as presented in Chapter 2 (i.e. (2.29) and (2.30)). Their expressions are repeated here in order to facilitate the description of this development.

$$dp_0^* = p_0^* \left[\frac{v d\varepsilon_v^p}{\lambda - \kappa} - \frac{k_1 dS_r^p}{\lambda_s - \kappa_s} \right]$$

$$ds_\beta^* = s_\beta^* \left[-\frac{dS_r^p}{\lambda_s - \kappa_s} + k_2 \frac{v d\varepsilon_v^p}{\lambda - \kappa} \right] \qquad \beta = SI \text{ or } SD$$

where k_1 and k_2 are the coupling parameters, λ_s and κ_s are soil parameters characterising the water retention behaviour, κ is the slope of an elastic swelling line for saturated conditions and λ is the slope of the normal compression line for saturated conditions. More details can be found in Section 2.6.

5.3. Generalised incremental stress-strain relationships

A procedure similar to the one presented in Sánchez et al. (2005) has been adopted here to take into account that different plastic mechanisms can act simultaneously and induce generalised plastic deformations. A first step is the assumption of an additive decomposition of the generalised strains into elastic and plastic components; so the increment of total generalised strains can be expressed as:

$$d\tilde{\boldsymbol{\varepsilon}} = d\tilde{\boldsymbol{\varepsilon}}^e + d\tilde{\boldsymbol{\varepsilon}}_j^p \qquad (5.15)$$

The plastic mechanisms that are active are not known in advance and a possible approach to develop the governing equations is to assume which plastic mechanism(s) is (are) initially active. A full description of the procedure followed to express the generalised stress-strain relationships for each plastic process is shown in detail in Appendix A.2 and only the main equations are presented in this chapter.

When the stress path remains inside the elastic domain, the increment of generalised stress can be expressed in terms of the elastic operator and the generalised strain increment according to:

$$d\tilde{\boldsymbol{\sigma}}^{*} = \mathbf{D}_{e}^{*} d\tilde{\boldsymbol{\varepsilon}} \qquad (5.16)$$

where $\boldsymbol{D}_e^{*}$ is the generalised elastic matrix (see Appendix A.2).

When a plastic mechanism is active, it is also possible to obtain a general expression to compute the increments of generalised stresses:

$$d\tilde{\boldsymbol{\sigma}}^{*} = \mathbf{D}_{ep}^{*} d\tilde{\boldsymbol{\varepsilon}} \qquad (5.17)$$

The form of $\boldsymbol{D}_{ep}^{*}$ will depend on which plastic mechanism(s) is (are) active (i.e. the *LC* plastic mechanism alone, the *SD* or *SI* mechanism alone, or both *LC* and *SD* or *SI* plastic mechanisms active simultaneously). The particular forms for $\boldsymbol{D}_{ep}^{*}$ for each of these different cases are derived in the following sections.

5.3.1. Yielding on the LC surface alone

When yielding on the *LC* surface alone is taking place:

$$d\tilde{\boldsymbol{\sigma}}^{*} = \mathbf{D}_{e}^{*} d\tilde{\boldsymbol{\varepsilon}}^{e} = \mathbf{D}_{e}^{*} \left(d\tilde{\boldsymbol{\varepsilon}} - d\tilde{\boldsymbol{\varepsilon}}_{LC}^{p} \right) \qquad (5.18)$$

where the subscript *LC* indicates the plastic mechanism that is active.

Using now the flow rule (5.10) for this case considered:

$$d\tilde{\boldsymbol{\sigma}}^{*} = \mathbf{D}_{e}^{*} \left(d\tilde{\boldsymbol{\varepsilon}} - d\chi_{LC}^{LC} \mathbf{m}_{LC} \right) \qquad (5.19)$$

The plastic multiplier associated with yielding on the *LC* surface alone $d\chi^{LC}{}_{LC}$ can be determined by imposing the consistency condition on the *LC* yield surface:

$$dF_{LC} = \left(\frac{\partial F_{LC}}{\partial \boldsymbol{\sigma}^{*}} \right)^{T} d\boldsymbol{\sigma}^{*} + \frac{\partial F_{LC}}{\partial p_{0}^{*}} dp_{0}^{*} = 0 \qquad (5.20)$$

After some algebra and using (5.19) combined with the hardening law (2.29) with dS_r^p set to zero (see Section 2.6.4 in Chapter 2), the following expression for this plastic multiplier can be obtained:

$$d\chi_{LC}^{LC} = \frac{\mathbf{a}_{LC}^{T} d\boldsymbol{\varepsilon}}{h_{LC}} \qquad (5.21)$$

where

$$\mathbf{a}_{LC}^{T} = \left(\frac{\partial F_{LC}}{\partial \boldsymbol{\sigma}^{*}} \right)^{T} \mathbf{D}_{e} \qquad (5.\ 22)$$

$$h_{LC} = \left(\frac{\partial F_{LC}}{\partial \boldsymbol{\sigma}^{*}} \right)^{T} \mathbf{D}_{e} \frac{\partial F_{LC}}{\partial \boldsymbol{\sigma}^{*}} - \frac{\partial F_{LC}}{\partial p_{0}^{*}} \frac{v}{\lambda - \kappa} p_{0}^{*} \mathbf{m}^{T} \frac{\partial F_{LC}}{\partial \boldsymbol{\sigma}^{*}} \qquad (5.\ 23)$$

where the subscript *LC* indicates that the *LC* mechanism is active and $\boldsymbol{m}^{T}=(1,1,1,0,0,0)$ is an auxiliary vector. Substituting (5.21) into (5.19) and after some algebra (see Appendix A.2) the following expression for the generalised elasto-plastic matrix can be obtained:

$$\mathbf{D}_{ep}^{*\ LC} = \begin{pmatrix} \mathbf{A}_{LC} & \mathbf{0} \\ \mathbf{0} & D_{LC} \end{pmatrix} \qquad (5.\ 24)$$

where

$$\left(\mathbf{A}_{LC} \right)_{6x6} = \mathbf{D}_{e} \left(\mathbf{Id}_{6x6} - \frac{\partial F_{LC}}{\partial \boldsymbol{\sigma}^{*}} \frac{\mathbf{a}_{LC}^{T}}{h_{LC}} \right) \qquad (5.\ 25)$$

$$\left(D_{LC} \right)_{1x1} = \gamma_{e} = \left(1/\kappa_{s} \right) s^{*} \qquad (5.\ 26)$$

5.3.2. Yielding on SD or SI yield surface alone

When yielding on only *β=SD* or *SI* is taking place:

$$d\tilde{\boldsymbol{\sigma}}^{*} = \mathbf{D}_{e}^{*} d\tilde{\boldsymbol{\varepsilon}}^{e} = \mathbf{D}_{e}^{*} \left(d\tilde{\boldsymbol{\varepsilon}} - d\tilde{\boldsymbol{\varepsilon}}_{\beta}^{p} \right) \qquad (5.\ 27)$$

where the subscript *β* indicates that the only plastic mechanism active is yielding on the *SD* or *SI* surface.

Employing now the flow rule (5.12) for yielding on only *SD* or *SI*:

$$d\tilde{\boldsymbol{\sigma}}^{*} = \mathbf{D}_{e}^{*} \left(d\tilde{\boldsymbol{\varepsilon}} - d\chi_{\beta}^{\beta} \mathbf{m}_{\beta} \right) \qquad (5.\ 28)$$

The plastic multiplier associated with yielding on the *SD* or *SI* surface alone $d\chi^{\beta}{}_{\beta}$ can be determined by imposing the consistency condition on the *β=SD* or *SI*:

$$dF_{\beta} = \frac{\partial F_{\beta}}{\partial s^{*}} ds^{*} + \frac{\partial F_{\beta}}{\partial s_{\beta}^{*}} ds_{\beta}^{*} = 0 \qquad (5.\ 29)$$

After some algebra and using (5.28) in combination with the hardening law (2.30) with $d\varepsilon_v^p$ set to zero (see Section 2.6.4), the following expression for this plastic multiplier can be obtained:

$$d\chi_{\beta}^{\beta} = \frac{d_{\beta} dS_r}{h_{\beta}} \tag{5. 30}$$

$$d_{\beta} = \frac{\partial F_{\beta}}{\partial s^*} \gamma_e \tag{5. 31}$$

$$h_{\beta} = -\frac{\partial F_{\beta}}{\partial s^*} \gamma_e \frac{\partial F_{\beta}}{\partial s^*} + \frac{\partial F_{\beta}}{\partial s_{\beta}^*} s_{\beta}^* \frac{1}{\lambda_s - \kappa_s} \frac{\partial F_{\beta}}{\partial s^*} \tag{5. 32}$$

where the subscript β indicates that the *SD* or *SI* mechanism is active. Substituting (5.30) into (5.28) and after some algebra (see Appendix A.2) the following expression for the generalised elasto-plastic matrix can be obtained:

$$\mathbf{D}_{ep}^{*\,\beta} = \begin{pmatrix} \mathbf{A}_{\beta} & \mathbf{0} \\ \mathbf{0} & D_{\beta} \end{pmatrix} \tag{5. 33}$$

where

$$\left(\mathbf{A}_{\beta}\right)_{6x6} = \mathbf{D}_e \tag{5. 34}$$

$$\left(D_{\beta}\right)_{1x1} = \gamma_e \left(1 + \frac{\partial F_{\beta}}{\partial s^*} \frac{d_{\beta}}{h_{\beta}}\right) \tag{5. 35}$$

5.3.3. Simultaneous yielding on SI and LC or SD and LC

The most general case is when two plastic mechanisms are active simultaneously and this is the case detailed in this section. When simultaneous yielding is taking place:

$$d\tilde{\boldsymbol{\sigma}}^* = \mathbf{D}_e^* d\tilde{\boldsymbol{\varepsilon}}^e = \mathbf{D}_e^* \left(d\tilde{\boldsymbol{\varepsilon}} - d\tilde{\boldsymbol{\varepsilon}}_{LC+\beta}^p\right) \tag{5. 36}$$

where the subscript β indicates that yielding on the *SD* or *SI* surface is active while the subscript *LC* indicates that yielding on the *LC* surface is also active.

Considering now the flow rule (5.14):

$$d\tilde{\boldsymbol{\sigma}}^{*} = \mathbf{D}_{e}^{*}\left(d\tilde{\boldsymbol{\varepsilon}} - d\chi_{\beta}^{LC+\beta}\mathbf{m}_{\beta} - d\chi_{LC}^{LC+\beta}\mathbf{m}_{LC}\right) \quad (5.37)$$

The plastic multiplier $d\chi_{\beta}^{LC+\beta}$ associated with yielding on β and the one $d\chi_{LC}^{LC+\beta}$ associated with yielding on *LC* when simultaneous yielding on two surfaces is occurring can be determined by imposing the consistency condition on the *LC* and on the β yield surfaces at the same time:

$$dF_{LC} = \left(\frac{\partial F_{LC}}{\partial \boldsymbol{\sigma}^{*}}\right)^{T} d\boldsymbol{\sigma}^{*} + \frac{\partial F_{LC}}{\partial p_{0}^{*}} dp_{0}^{*} = 0 \quad (5.38)$$

$$dF_{\beta} = \frac{\partial F_{\beta}}{\partial s^{*}} ds^{*} + \frac{\partial F_{\beta}}{\partial s_{\beta}^{*}} ds_{\beta}^{*} = 0 \quad (5.39)$$

After some algebra (see Appendix A.2) and using (5.37) combined with the hardening laws (2.29) and (2.30) the following expression for each plastic multiplier can be obtained:

$$d\chi_{LC}^{LC+\beta} = \frac{\mathbf{a}_{LC+\beta}^{T} d\boldsymbol{\varepsilon} + b_{LC+\beta} dS_{r}}{h_{LC+\beta}} \quad (5.40)$$

$$d\chi_{\beta}^{LC+\beta} = \frac{\mathbf{c}_{LC+\beta}^{T} d\boldsymbol{\varepsilon} + d_{LC+\beta} dS_{r}}{h_{LC+\beta}} \quad (5.41)$$

where the subscript $LC+\beta$ indicates that the *LC* and β mechanisms are both active; $\boldsymbol{a}_{LC+\beta}^{T}$, and $\boldsymbol{c}_{LC+\beta}^{T}$ are vectors associated with strain changes; and $b_{LC+\beta}$ and $d_{LC+\beta}$ are scalars related to degree of saturation changes. Their complete expression is given in Appendix A.2. Substituting (5.40) and (5.41) into (5.37) and after some algebra (see Appendix A.2) the following expression for the generalised elasto-plastic matrix can be obtained:

$$\mathbf{D}_{ep}^{*\,LC+\beta} = \begin{pmatrix} \mathbf{A}_{LC+\beta} & \mathbf{B}_{LC+\beta} \\ \mathbf{C}^{T}{}_{LC+\beta} & D_{LC+\beta} \end{pmatrix} \quad (5.42)$$

where

$$\left(\mathbf{A}_{LC+\beta}\right)_{6x6} = \mathbf{D}_{e}\left(\mathbf{Id}_{6x6} - \frac{\partial F_{LC}}{\partial \boldsymbol{\sigma}^{*}} \frac{\mathbf{a}_{LC+\beta}^{T}}{h_{LC+\beta}}\right) \quad (5.43)$$

$$\left(\mathbf{B}_{LC+\beta}\right)_{6x1} = \mathbf{D}_{e}\left(\frac{\partial F_{LC}}{\partial \boldsymbol{\sigma}^{*}} \frac{b_{LC+\beta}}{h_{LC+\beta}}\right) \quad (5.44)$$

$$\left(\mathbf{C}_{LC+\beta}\right)^{T}_{1x6} = -\gamma_e \left(\frac{\partial F_\beta}{\partial s^*} \frac{\mathbf{c}^{T}_{LC+\beta}}{h_{LC+\beta}} \right) \qquad (5.\ 45)$$

$$\left(D_{LC+\beta}\right)_{1x1} = \gamma_e \left(1 + \frac{\partial F_\beta}{\partial s^*} \frac{d_{LC+\beta}}{h_{LC+\beta}} \right) \qquad (5.\ 46)$$

It is interesting to highlight here that $\boldsymbol{C}_j^T$ and $\boldsymbol{B}_j$ (with the subscript *j* indicating the plastic mechanism active) become zero when only one plastic mechanism is activated (i.e. yielding on the *SD* or *SI* yield surface alone; or yielding on the *LC* yield surface alone) and, in such cases, only the components of $\boldsymbol{A}_j$ and D_j of the elasto-plastic matrix $\boldsymbol{D}_{ep,\,j}^{\,*}$ account for the increments of the generalised stress vector (more details in Appendix A.2).

5.4. Identification of the generalised elasto-plastic domains

In Chapter 3 a possible methodology to identify which plastic mechanism(s) is (are) active was formally proposed for isotropic stress conditions. The mathematical expressions of four straight lines in the lns^*:lnp^* plane were presented identifying five different elasto-plastic domains that, in addition to the elastic case, characterised the different possible behaviours defined within the model for isotropic stress conditions (see Section 3.4). A simple extension of these expressions is presented in this section for generalised 3D conditions. The resulting extended expressions define four different surfaces in J:p^*:s^* space which describe the boundaries between five different elasto-plastic domains (in addition to the elastic domain) defining five different types of behaviour (i.e. yielding on the *LC* surface alone; yielding on the *SD* or *SI* surface alone; or simultaneous yielding on the *LC* and *SD* or *SI*). The development of these four expressions is detailed as follows.

Each of the mathematical expressions used to define the boundaries between the different elasto-plastic mechanisms is essentially developed by combining the expression of the extended *LC* yield surface in the J:p^*:s^* space (5.1) with the expression of the appropriate straight line used in Section 3.4 to define the limits of each elasto-plastic mechanism under isotropic stress conditions (i.e. (3.56), (3.57), (3.58) and (3.59)). The *LC* yield surface (5.1) can be also expressed as as:

$$\frac{3J}{\left[\dfrac{g(\theta)}{g(\theta)\big|_{\theta=-\frac{\pi}{6}}}\right]^2} - M^2 p^* \left(p_0^* - p^* \right) = 0 \qquad (5.\ 47)$$

and (3.56), (3.57), (3.58) and (3.59) can be re-written as:

$$p^* = p_0^* \left(\frac{s^*}{s_I^*} \right)^{k_1} \quad (5.48)$$

$$p^* = p_0^* \left(\frac{s^*}{s_I^*} \right)^{\frac{1}{k_2}} \quad (5.49)$$

$$p^* = p_0^* \left(\frac{s^*}{s_D^*} \right)^{\frac{1}{k_2}} \quad (5.50)$$

$$p^* = p_0^* \left(\frac{s^*}{s_D^*} \right)^{k_1} \quad (5.51)$$

Substituting appropriately each of these expressions into (5.47):

$$f_1 : \frac{3J}{\left[\frac{g(\theta)}{g(\theta)\big|_{\theta=-\frac{\pi}{6}}} \right]^2} - M^2 p^* \left(p_0^* \left(\frac{s^*}{s_I^*} \right)^{k_1} - p^* \right) = 0 \quad (5.52)$$

$$f_2 : \frac{3J}{\left[\frac{g(\theta)}{g(\theta)\big|_{\theta=-\frac{\pi}{6}}} \right]^2} - M^2 p^* \left(p_0^* \left(\frac{s^*}{s_I^*} \right)^{\frac{1}{k_2}} - p^* \right) = 0 \quad (5.53)$$

$$f_3 : \frac{3J}{\left[\frac{g(\theta)}{g(\theta)\big|_{\theta=-\frac{\pi}{6}}} \right]^2} - M^2 p^* \left(p_0^* \left(\frac{s^*}{s_D^*} \right)^{\frac{1}{k_2}} - p^* \right) = 0 \quad (5.54)$$

$$f_4 : \frac{3J}{\left[\frac{g(\theta)}{g(\theta)\big|_{\theta=-\frac{\pi}{6}}} \right]^2} - M^2 p^* \left(p_0^* \left(\frac{s^*}{s_D^*} \right)^{k_1} - p^* \right) = 0 \quad (5.55)$$

Similarly to the isotropic stress case described in Chapter 3, it is now possible to combine these equations with the yield surfaces defined (i.e. (5.1), (5.2) and (5.3)) and identify five

domains in the $J{:}p^*{:}s^*$ space describing the boundaries between each elasto-plastic mechanism of the model. Note that if J=0 the previous equations (5.52), (5.53), (5.54) and (5.55) recover the expression of the equations presented for isotropic stress conditions (5.48), (5.49), (5.50) and (5.51), which is a necessary condition that should be verified.

In particular, f_1 forms a conical surface extending out from the junction between *LC* and *SI* yield surfaces and delimits the boundary between stress paths involving yielding on the *SI* yield surface alone and those involving simultaneous yielding on both *SI* and *LC* yield surfaces. Similarly, f_2 forms a separate conical surface also extending out from the junction between *LC* and *SI* yield surfaces and delimits the boundary between stress paths involving yielding on the *LC* yield surface alone and those involving simultaneous yielding on both *SI* and *LC* yield surfaces.

An equivalent situation occurs on the bottom corner with f_3 and f_4 which has been illustrated in Figure 5-2. In this case, f_3 forms a conical surface extending out from the junction between the *LC* and *SD* yield surfaces and delimits the boundary between stress paths involving yielding on the *LC* yield surface alone and those involving simultaneously yielding on both *SD* and *LC*. f_4 also forms a conical surface delimiting the boundary between the stress paths involving yielding on the *SD* yield surface alone and those involving simultaneously yielding on both *SD* and *LC*. For example, if a stress path goes from the elastic domain defined by the three yield surfaces *LC*, *SD* and *SI* (see Figure 5-1) to the inner domain defined by f_4 (see also Figure 5-2) the plastic mechanism associated with yielding on the *SD* yield surface alone will be activated. If, otherwise, a different stress path moves from the elastic domain to the domain outside of f_3 (and also outside of f_4), the plastic mechanism activated will correspond to yielding on the *SD* and *LC* yield surfaces simultaneously (see Figure 5-2). An equivalent situation occurs for the junction between *LC* and *SI* yield surfaces (top corner).

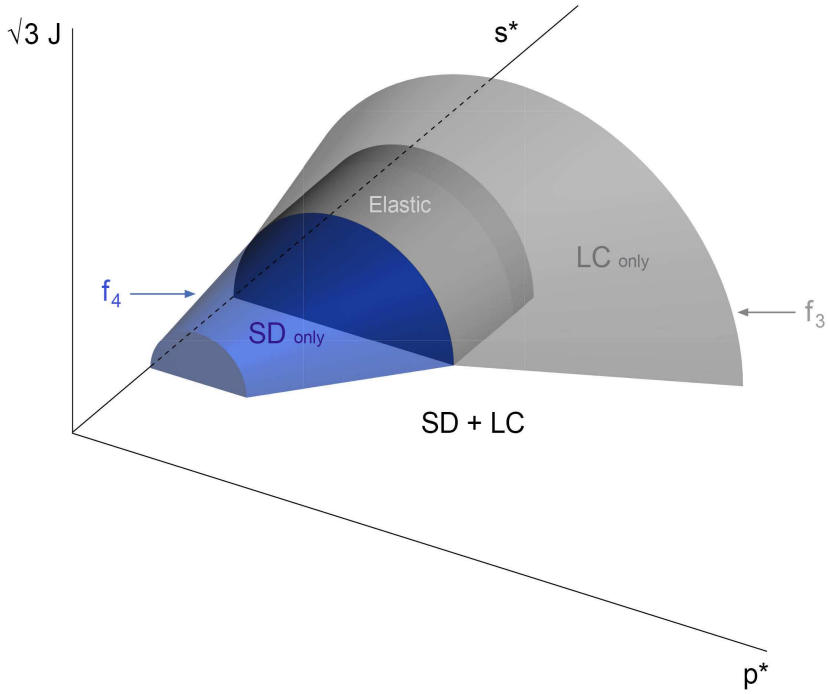

Figure 5- 2 Illustration of the elastic domain and the f_3 and f_4 surfaces.

5.5. Model application and partial validation

This partial validation of the constitutive model involves a set of experimental tests comprising conventional isotropic and triaxial compression stress paths at three different values of suction (Figure 5-3). Tests carried out by Sivakumar (1993) have been adopted in this section to explore the capabilities of the model introduced in this chapter to describe the behaviour of unsaturated soils. The tests selected for this (partial) validation of the model were carried out on statically compacted samples of speswhite kaolin using a suction controlled triaxial cell. Each of the tests involved first isotropic compression to a virgin state. Shearing in triaxial compression was applied afterwards to critical state under three types of conditions: Type A (Tests 2A, 3A, 4A, 5A, 10A and 15A) in which deviator stress was applied at constant suction and constant volume, Type B (6B, 7B, 11B, 12B and 16B) which involved application of deviator stress at constant suction and at constant mean net stress; and Type C (8C, 9C, 17C and 18C), which involved application of deviator stress at constant suction and constant radial net stress (Sivakumar, 1993). Test 1A is only analysed for isotropic stress conditions because no shearing stage was conducted. Problems occurred during shearing in Test 13C (i.e. buckling failure) and it is therefore not considered in the shearing analysis (Sivakumar, 1993). Test 9C is only analysed during shearing as no experimental data was available for the isotropic stress conditions. Finally, neither Test 8C nor Test 14A is considered in this study because the

complete set of the experimental data was not available when performing this analysis. In summary, 15 tests are employed to analyse isotropic stress conditions (i.e. 1A, 2A, 3A, 4A, 5A, 6B, 7B, 10A, 11B, 12B, 13C, 15A, 16B, 17C and 18C) while 14 tests are used to study the response during shearing (2A, 3A, 4A, 5A, 6B, 7B, 9C, 10A, 11B, 12B, 15A, 16B, 17C and 18C). Finally, it is also important to mention that only unsaturated soil samples (i.e. $0<S_r<1$) are analysed and, hence, the saturated tests have been not included in this validation (see Section 2.6.3).

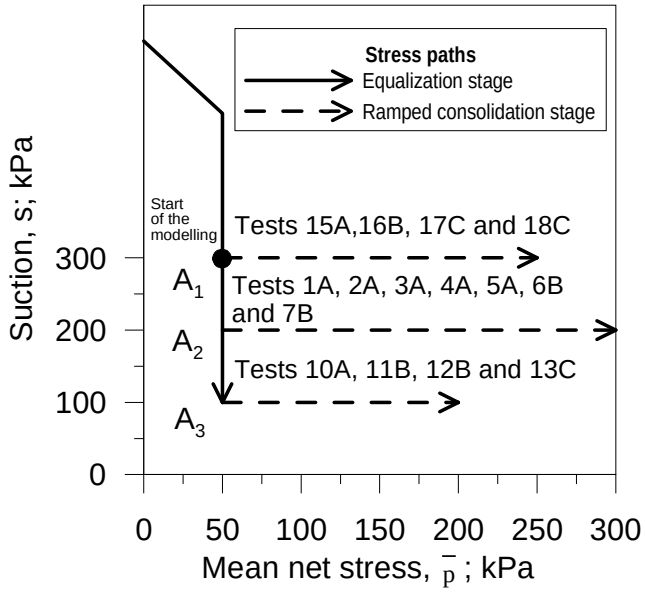

Figure 5- 3 Stress paths during equalization and ramped consolidation stage (Wheeler and Sivakumar, 1995)

The same set of constitutive parameters estimated in Chapter 2 when describing a methodology for their determination (see Section 2.7.4), is adopted herein. Table 5.1 presents all of them.

Table 5. 1 Constitutive model parameters

λ=0.124	λ_s=0.0971	κ_s=0.0004	M=0.716
κ=0.006	k_1=0.685	k_2=0.773	υ^1=0.3

[1]*Poisson's ratio*

The initial state presented in Table 5.2 corresponds to the state of soil after the compaction and then equalization under an isotropic stress state with a suction of 300 kPa and a mean net stress of 50 kPa (point A_1 in Figure 5-3). The initial values of e and S_r employed are those corresponding to the average of tests at s=300 kPa (i.e. 15A, 16B, 17C and 18C; Sivakumar, 1993). From this initial state a wetting path at constant mean net stress of 50 kPa has been modelled to reach the value of suction of 200 kPa for tests

1A, 2A, 3A, 4A, 5A, 6B, 7B and 9C and of 100 kPa for tests 10A, 11B, 12B and 13C (see Figure 5-3). Also the initial values of the hardening parameters (p_0^* and s_D^*) used in this validation are included in Table 5-2. A detailed description on how these parameter values have been estimated is given in Chapter 2 when describing the methodology to determine the model parameters (see Section 2.7.4 for further details).

Drying paths have not been analysed in this work and therefore the initial value of the hardening parameter s_I^* defining the position of the *SI* yield surface has not been determined.

Table 5. 2 Initial state at the start of the modelling.

$\overline{p}$ =50 kPa	s=300 kPa	p^*=229kPa	p_0^*=271 kPa
e_0=1.210	S_{r0}=0.597	s^*=164 kPa	s_D^*=164 kPa

Once the pertinent value of suction was reached at the end of the equalization stage (300, 200 or 100 kPa), an isotropic loading at constant suction was applied to the relevant value of mean net stress $\overline{p}$ for each test. This was followed by shearing under one of the three different types of conditions previously defined (i.e. Type A, B and C). All samples were sheared until critical state was reached.

5.5.1. Behaviour under isotropic stress paths

Figures 5-4, 5-5 and 5-6 illustrate the performance of the model in simulating the constant suction isotropic loading stages. Experimental results and model simulations for the tests at a suction of 300 kPa are shown in Figure 5-4, with corresponding results at suctions of 200 kPa and 100 kPa shown in Figures 5-5 and 5-6 respectively. In each of the three figures, the experimental results are indicated by symbols joined by fine lines, whereas the model simulation is indicated by a heavier continuous line.

The model simulations shown in Figures 5-5 and 5-6 involve only the constant suction isotropic loading stages (in order to correspond to the experimental results). The starting points of the model simulations in Figures 5-5 and 5-6 therefore correspond to points A_2 and A_3 in Figure 5-3, and the model simulations of the prior wetting from point A_1 have been omitted.

Each of Figures 5-4, 5-5 and 5-6 is in five parts. Parts (a) and (b) show the variation of void ratio e and degree of saturation S_r plotted against mean net stress $\overline{p}$ (the conventional stress variable). Part (c) shows the stress path in terms of the new stress

variables of modified suction s^* and mean Bishop's stress p^*. It is important to note that, whereas suction s remains constant during the isotropic loading stages, modified suction s^* decreases, because of the reduction of porosity during isotropic loading. Parts (d) and (e) of Figures 5-4, 5-5 and 5-6 show the variation of void ratio e and degree of saturation S_r plotted against mean Bishop's stress p^*.

The various tests shown in Figures 5-4, 5-5 and 5-6 were taken to different final values of mean net stress $\overline{p}$ during isotropic loading. For example, in Figure 5-4, Tests 16B and 17C involved isotropic loading to $\overline{p} = 100$ kPa, Test 18C involved isotropic loading to $\overline{p} = 150$ kPa and Test 15A involved isotropic loading to $\overline{p} = 250$ kPa. The single model simulation shown in each of the three figures is for isotropic loading to the highest appropriate value of $\overline{p}$ (e.g. $\overline{p} = 250$ kPa in Figure 5-4). Obviously, the model simulations for the tests loaded isotropically to lower values of $\overline{p}$ simply correspond to truncated versions of the model simulation shown in the figure.

The model simulation stress paths shown in Figures 5-4 (c), 5-5(c) and 5-6(c) show an initial stress point (A_1, A_2 or A_3) that is on the *SD* yield surface (because of wetting during the previous equalization stage) but inside the *LC* yield surface. The predicted initial positions of *SD* and *LC* yield curves are shown in the figures by dashed lines labelled SD_0 and LC_0 respectively. The initial part of the predicted stress path during isotropic loading involves yielding on the *SD* yield surface, because of the reduction of s^* caused by a reduction of porosity (which is, in turn, the result of elastic volumetric strain caused by the increase of p^*). However, the decrease of s^* during this early part of the loading stage is very small (hardly noticeable in the model simulations in Figures 5-4(c), 5-5(c) and 5-6(c)) and as a consequence the predicted elastic and plastic increases of S_r are extremely small (hardly noticeable in the model simulations in Figures 5-4(b) and (e), 5-5(b) and (e) and 5-6(b) and (e).

At a point during the isotropic loading, the stress path in the model simulation reaches the *LC* yield surface. This is indicated by points Y_1, Y_2 and Y_3 in Figures 5-4, 5-5 and 5-6. From this point onwards simultaneous yielding on both *SD* and *LC* surfaces is predicted. Yielding on the *LC* surface results in predictions of large plastic decreases of specific volume v from the yield point onwards (see Figures 5-4(a) and (d), 5-5(a) and (d) and 5-6(a) and (d)). This yielding on the *LC* surface and the resulting plastic volumetric strain also produces both a significant reduction of s^*, (see Figures 5-4(c), 5-5(c) and 5-6(c)), as the porosity reduces, and coupled upward movement of the *SD* yield surface. Together these result in predictions of significant yielding on the *SD* surface, and hence large

plastic increases of S_r after the yield point (see Figures 5-4(b) and (e), 5-5(b) and (e) and 5-6(b) and (e)). The predicted final positions of the *SD* and *LC* yield curves are shown in Figures 5-4(c), 5-5(c) and 5-6(c) by dashed lines labelled SD_f and LC_f respectively.

Inspection of all the model simulations shown in Figures 5-4 to 5-6 confirms that during the latter part of the isotropic loading stages, once yielding is occurring on both *LC* and *SD* yield surfaces (i.e. after point Y_1, Y_2 or Y_3), the values of v and S_r lie on the unique normal compression planar surfaces in v:lnp^*:lns^* and S_r:lnp^*:lns^* spaces predicted by the model in Equations (2.37) and (2.40) (see also Section 6.6.1). This provides verification that the numerical implementation of the model has been performed correctly for isotropic stress states.

Inspection of Figures 5-4, 5-5 and 5-6 shows that the model simulations provide an excellent match to the experimental results. Not only is the variation of the void ratio e well predicted in all cases, but the variation of degree of saturation S_r is also predicted with a high degree of accuracy (correctly representing the significant increase of S_r during these constant suction isotropic loading stages). As a consequence, the model accurately captures the stress path in the s^*:p^* plane (see Figures 5-4(c), 5-5(c) and 5-6(c)). Obviously, the model simulations of the variations of both e and S_r with $\overline{p}$ or p^* show a sharp discontinuity of gradient at the yield point where the *LC* yield surface is reached (point Y_1, Y_2 or Y_3), whereas this feature is more rounded in the experimental results. However, this mild weakness is a natural consequence of the use of classical elasto-plasticity for the modelling framework, and this type of minor mis-match would also be observed in corresponding classical elasto-plastic models for saturated soils (such as Modified Cam Clay).

The excellent match between model predictions and experimental results for the isotropic loading stages is partly a consequence of the fact that the experimental results from isotropic loading of these unsaturated samples were used in the selection of values for the model parameters λ_s, κ_s, k_1 and k_2 (see Section 2.7.4). However, the excellent match would not be possible unless it was also true that the model equations (particularly the hardening laws of Equations (2.29) and (2.30)) provided a good representation of the soil behaviour during isotropic loading at different values of constant suction. The comparisons presented in Figures 5-4, 5-5 and 5-6 therefore provide a good validation of this aspect of the model.

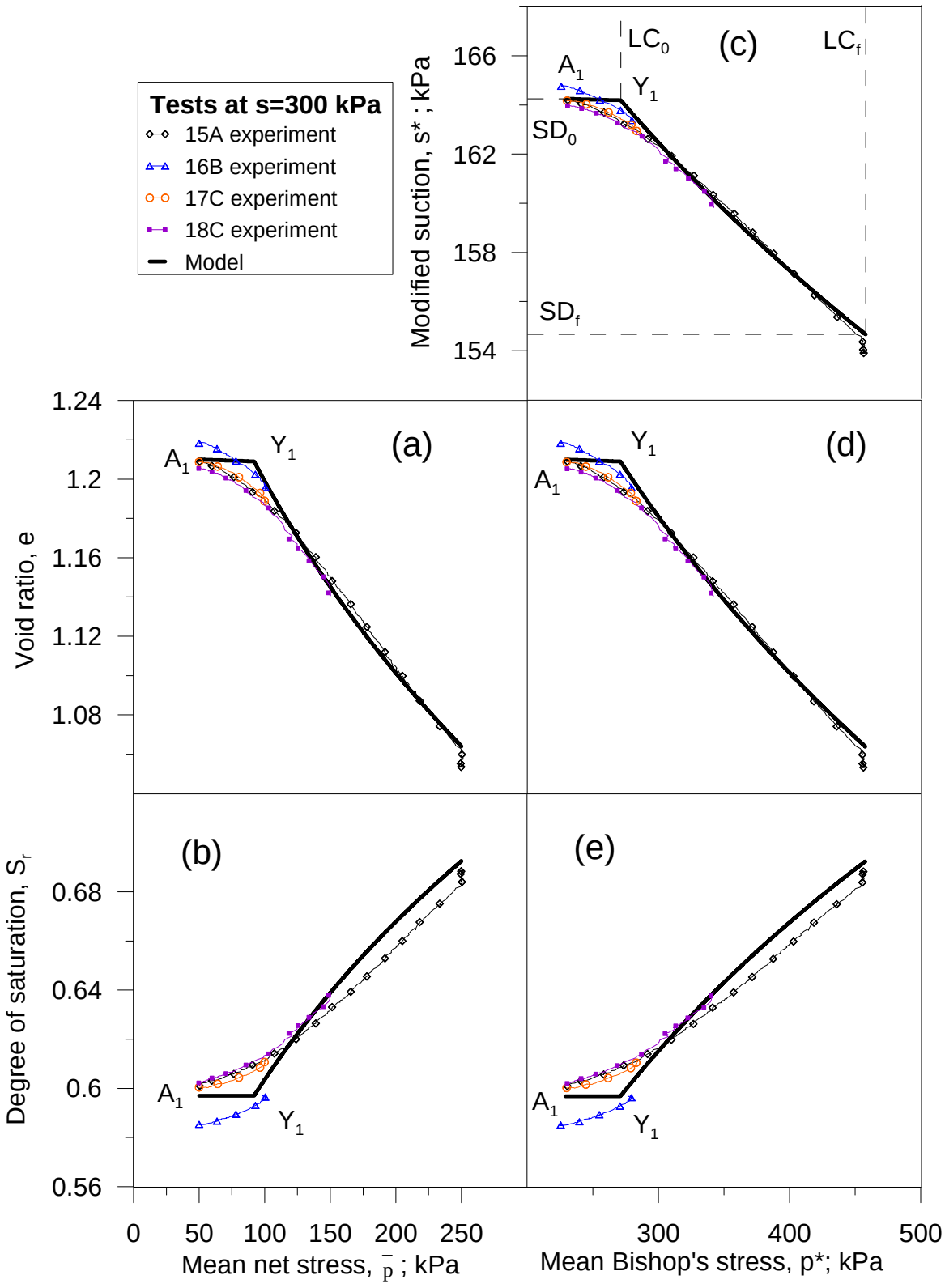

Figure 5- 4 Comparison between model simulations and experimental results (Sivakumar,1993) for isotropic loading at s=300 kPa.

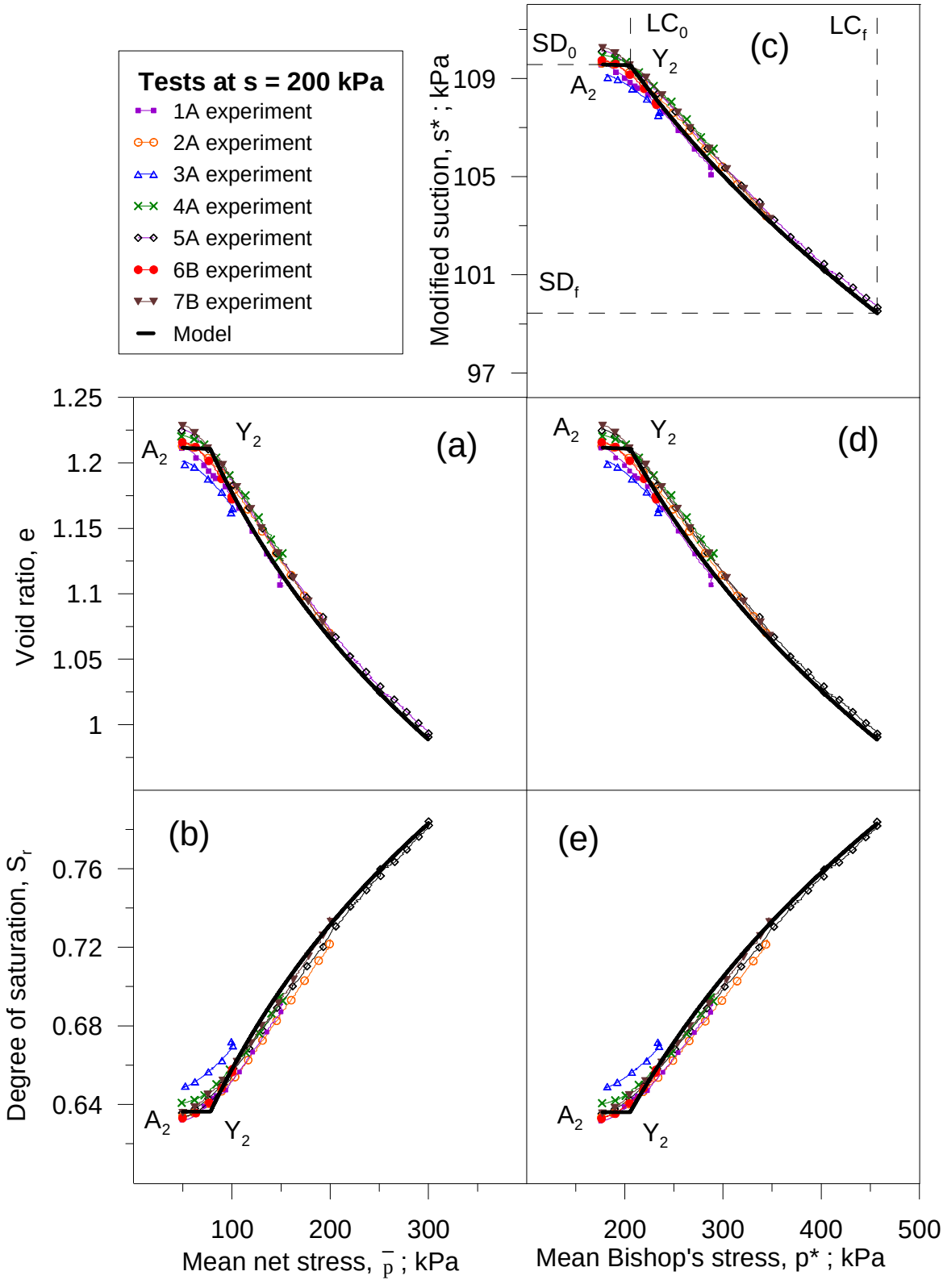

Figure 5- 5 Comparison between model simulations and experimental results (Sivakumar,1993) for isotropic loading at s=200 kPa.

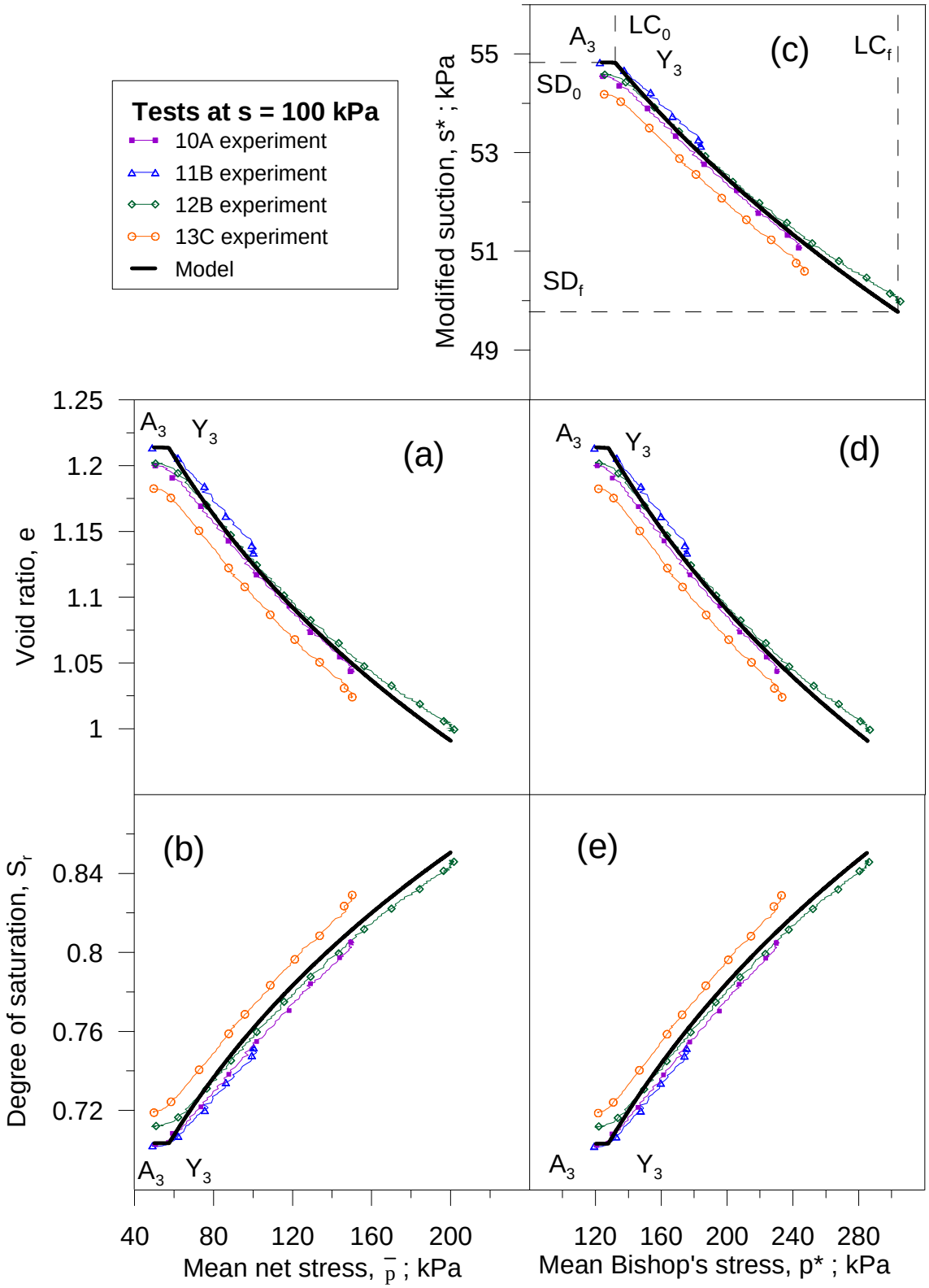

Figure 5- 6 Comparison between model simulations and experimental results (Sivakumar,1993) for isotropic loading at s=100 kPa.

5.5.2. Behaviour under shearing stress paths

Figures 5-7 to 5-12 show the performance of the model in simulating the various constant suction shearing stages. Figure 5-7 and 5-8 show the tests conducted at a suction of 300 kPa, Figures 5-9 and 5-10 show the tests at s=200 kPa and Figures 5-11 and 5-12 show the tests at s=100 kPa. Again, experimental results are indicated by symbols joined by fine lines, whereas model simulations are indicated by heavier continuous lines (for shearing stages there is a separate model simulation for each test).

All model simulations show the stress point at the corner between *LC* and *SD* curves at the start of the shearing (following the preceding equalization (wetting) and constant suction isotropic loading stages) and then simultaneous yielding on *LC* and *SD* surfaces occurring throughout the shearing process. As a consequence, all the final critical states in the simulations are on both *LC* and *SD* yield surfaces (on the vertex between the two surfaces). Inspection of the final critical state values of q, p^*, s^*, v and S_r in the simulations (see Figures 5-7 to 5-12) confirms that all points lie on the unique critical state line in the q:p^* plane assumed in the model in Equation (4.9) and on the two unique critical state planar surfaces in v:lnp^*:lns^* and S_r: lnp^*:lns^* spaces predicted by the model in Equations (4.17) and (4.21) (see also Section 6.6.1). This provides verification that the numerical implementation of the model has been performed correctly.

Figure 5-7(a) shows the test results and model simulations in the q:p^* plane for the four tests conducted at a suction of 300 kPa (Tests 15A, 16B, 17C and 18C). Inspection of Figure 5-7(a) shows that the stress path for the test involving shearing at constant mean net stress $\overline{p}$ (Test 16B) is not a vertical line in the q:p^* plane, because the variation of S_r during shearing means that p^* does not remain constant (this is true for both experimental results and model predictions). Similarly, the stress paths for the two tests conducted at constant radial net stress (Tests 17C and 18C) do not rise at a gradient of 3 in the q:p^* plane, because the variation of S_r means that the radial Bishop's stress does not remain constant during shearing (again this is true for both experimental results and model predictions). As the variations of degree of saturation in Tests 17C and 18C were well-predicted (see later), the stress paths in the q:p^* plane for these two tests were accurately predicted (see Figure 5-7(a)). The model prediction of the variation of S_r during Test 16B was rather less accurate (see later) and hence the predicted stress path in the q:p^* plane was less accurate (see Figure 5-7(a)), although the mis-match was still relatively minor. With the stress paths in the q:p^* plane for Tests 17C, 18C and 16B predicted with acceptable accuracy and the location of the critical state line in the q:p^* plane selected to match the experimental results (see Section 4.2), the model predictions of critical state

values of deviatoric stress q are a good match to the experimental results for these three tests. In contrast, for the single constant suction constant v shear test shown in Figure 5-7 (Test 15A) the model predictions of the stress path in the q:p^* plane and the critical state value of q are not good matches to the experimental results. The reasons for this are discussed in the next paragraph.

Figure 5-7(b) shows the model predictions and experimental results for the variation of void ratio e with mean Bishop's stress p^* during the shear stages of the four tests conducted at a suction of 300 kPa. All four model simulations involve simultaneous yielding on *LC* and *SD* yield surfaces throughout the shearing stages. The simulations of Tests 16B, 17C and 18C involve large amounts of yielding on the *LC* surface, producing large plastic volumetric strains and hence predictions of large reductions of void ratio e. In contrast, the simulation of the single constant v shear test (Test 15A) involves only a small amount of yielding on the *LC* surface, sufficient to cause enough positive plastic volumetric strain to cancel out the negative elastic volumetric strain predicted from the decrease of mean Bishop's stress p^*. Although, the predictions of large reductions of void ratio in Tests 16B, 17C and 18C and a significant decrease of p^* during Test 15A are qualitatively correct, the magnitudes of the reductions of v or decrease of p^* are significantly over-predicted in all cases. This is a consequence of the fact that the position of the critical state surface in v:p^*:s^* space is poorly predicted, with the model predicting too large spacing between the critical state planar surface and the normal compression planar surface in v:lnp^*:lns^* space (see Section 4.5). This weakness of the model is analogous to the situation of the Modified Cam Clay model for saturated soils, which is commonly reported to over-predict the spacing between normal compression line and critical state line in the v:lnp' plane. One consequence of the fact that the model poorly predicts the locations of critical states in the v:p^* plane in Figure 5-7(b) is that the reduction of p^* during the shearing stage of Test 15A (the constant v shear test) is over-predicted, and hence the stress path for Test 15A is poorly predicted in the q:p^* plane (see Figure 5-7(a)) and the critical state value of q is significantly under-predicted in this test.

Figure 5-7(c) shows the model predictions and experimental results for the variation of deviatoric stress q with axial strain ε_a during the shearing stages of the four tests conducted at a suction of 300 kPa. Although the critical state values of q are accurately predicted in Tests 16B, 17C and 18C, Figure 5-7(c) shows that the development of shear strain (and hence axial strain) is over-predicted in these tests, with critical states only being reached in the model simulations at excessively large values of axial strain. For Test 15A (the constant v shear test), not only is the critical state value of deviatoric stress

under-predicted (as discussed in the previous paragraph), but also the development of shear strain (and hence axial strain) is under-predicted, with the critical state being reached in the model simulation at an axial strain that is much lower than that observed in the experimental results. This pattern of behaviour is very similar to commonly reported observations on the use of the Modified Cam Clay model for saturated soils, which generally over-predicts the shear strain required to reach a critical state during drained shearing of normally consolidated samples and under-predicts the shear strain required to reach a critical state during undrained (constant v) shearing of normally consolidated samples. This can be attributed to the use of an associated flow rule in combination with an elliptical yield curve shape in Modified Cam Clay. A similar choice of an associated flow rule on the *LC* yield surface and elliptical cross-sections of the *LC* surface in the q:p^* plane has been made in the extension of the Wheeler et al. (2003) model to triaxial stress conditions (see Section 4.2), and hence it is not surprising that similar faults are observed when comparing model simulations with experimental results.

Figure 5-7(d) shows the model predictions and experimental results for the variation of void ratio e with axial strain ε_a during the shearing stages of the four tests conducted at a suction of 300 kPa. The model predictions for Tests 17C and 18C appear to be a good match to the experimental results, but this is a rather fortuitous result, as it is the consequence of two poor predictions cancelling out: the model over-predicting the final reductions of v in reaching critical states but also over-predicting the development of shear strain (and hence axial strain) prior to achieving critical states. For Test 16B the mis-match is clearer, because the over-prediction in the final reduction of v in reaching critical state is more severe and over-prediction of the shear strains prior to achieving a critical state is less severe.

Figure 5-8 shows the model predictions and experimental results for the variation of degree of saturation S_r (plotted against deviatoric stress q) during the shearing stages of the four tests conducted at a suction of 300 kPa. In all four cases both elastic and plastic increases of S_r are predicted throughout shearing. The former are a consequence of the predicted reduction of modified suction s^* (as a result of the reduction of porosity) and the latter are a consequence of yielding on the *SD* surface. Inspection of Figure 5-8 shows that for Tests 17C and 18C the model predictions provide reasonably accurate predictions of the increase of S_r during shearing. A small disparity is that the experimental results for Tests 17C and 18C show only relatively small increases of S_r in the early part of shearing (until the deviatoric stress exceeds about 100 kPa), whereas the model simulations show large increases of S_r from the start of shearing. This minor disparity between model

simulations and experimental results is more marked for Test 16B, with the result that the final increase of S_r (when a critical state is reached) is over-predicted in this case. Finally, Figure 5-8 shows that the model correctly predicts only a very small increase of S_r during the constant suction, constant v shearing of Test 15A.

Figures 5-9 and 5-10 show the corresponding results for tests conducted at a suction of 200 kPa and Figures 5-11 and 5-12 show the results for tests at s=100 kPa. Comparison of model predictions and experimental results in these figures leads to the same conclusions as the previous discussion around Figures 5-7 and 5-8. In particular, the model predictions generally provide a reasonable match to experimental results. For tests involving shearing at constant mean net stress $\overline{p}$ or constant radial net stress, the variations of S_r during shearing are predicted reasonably well, and as a consequence the stress paths in the q:p^* plane and the critical state values of q are well predicted. However, in these tests, the reductions of void ratio e during shearing are over-predicted, as a consequence of the over-prediction of the spacing between the normal compression planar surface and critical state planar surface in v:lnp^*:lns^* space. For tests involving shearing at constant v, the reductions of p^* during shearing are over-predicted (as a consequence of the over-prediction of the spacing between normal compression planar surface and critical state planar surface in v:lnp^*:lns^* space) and hence the critical state values of q are under-predicted. Development of shear strain (and hence axial strain) is over-predicted during constant $\overline{p}$ or constant radial net stress shearing and under-predicted during constant v shearing. This can be attributed to the choice of an associated flow rule in combination with elliptical cross-sections of the *LC* yield surface.

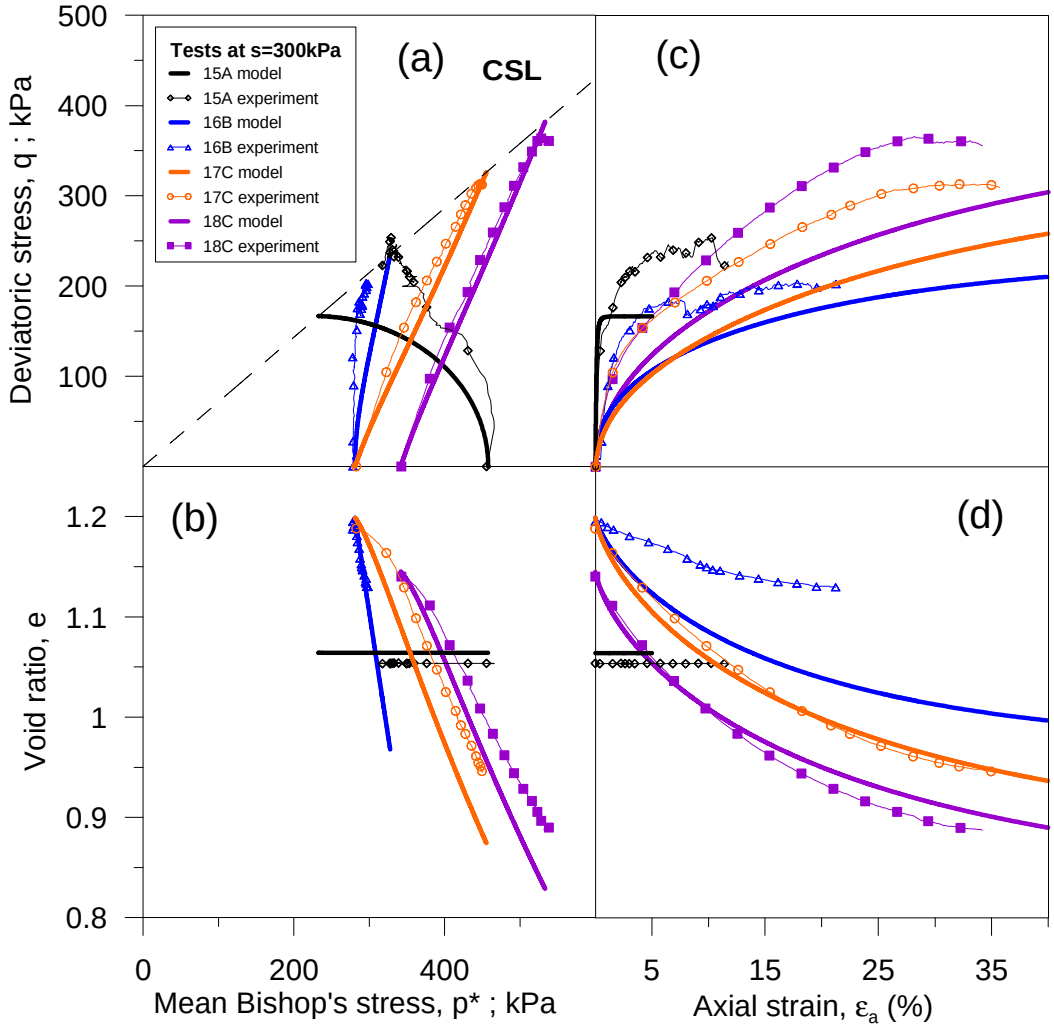

Figure 5- 7 Comparisons between model simulations and experimental results (Sivakumar,1993) for shearing at s=300 kPa.

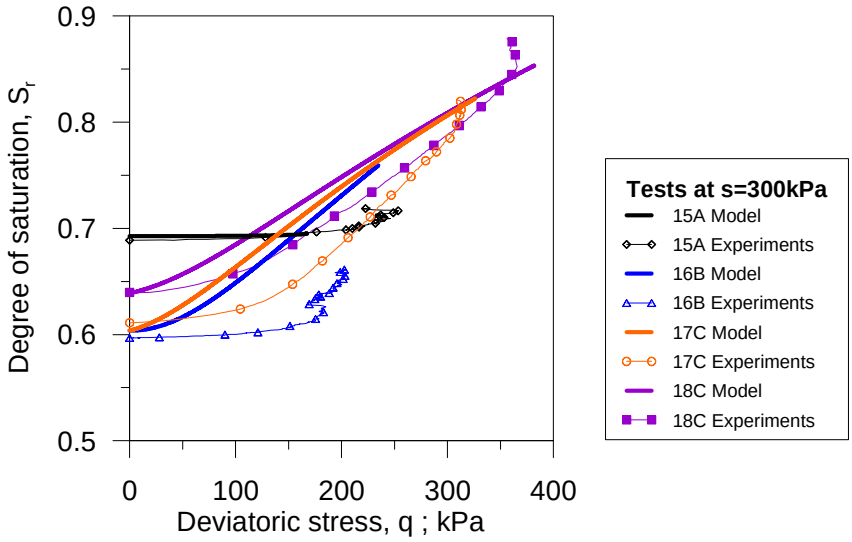

Figure 5- 8 Comparisons between model simulations and experimental results (Sivakumar,1993) for shearing at s=300 kPa: variation of degree of saturation.

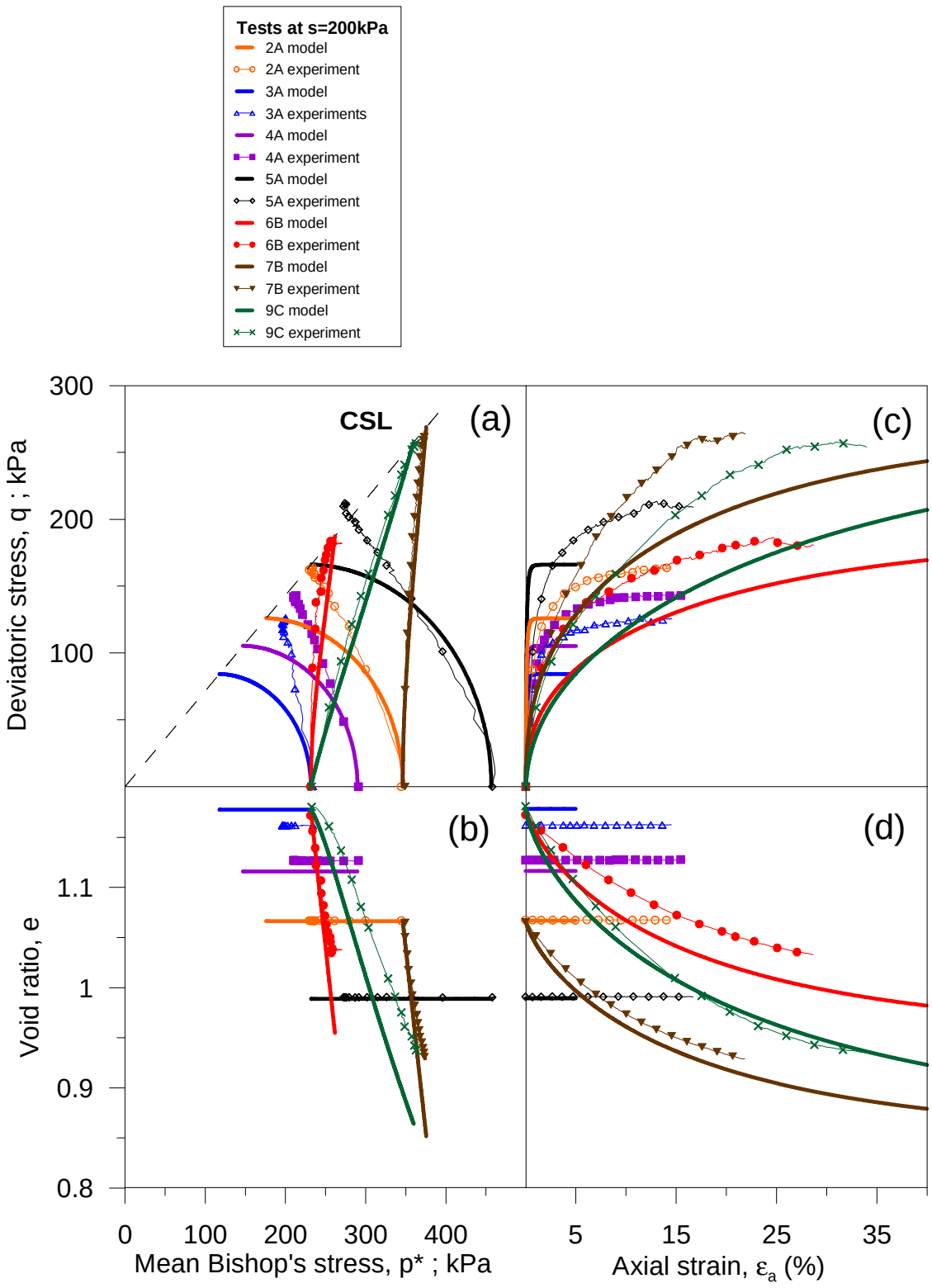

Figure 5- 9 Comparisons between model simulations and experimental results (Sivakumar,1993) for shearing at s=200 kPa.

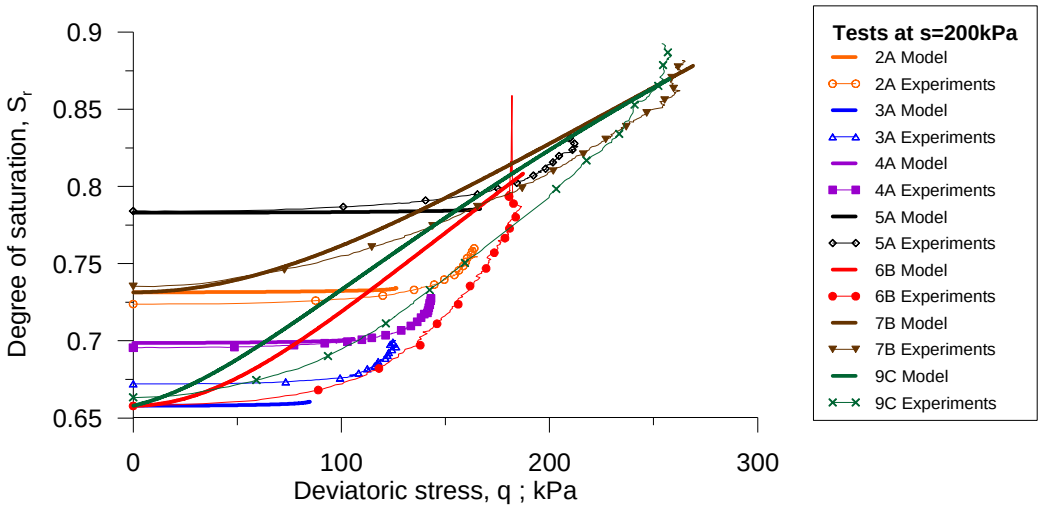

Figure 5- 10 Comparisons between model simulations and experimental results (Sivakumar,1993) for shearing at s=200 kPa: variation of degree of saturation.

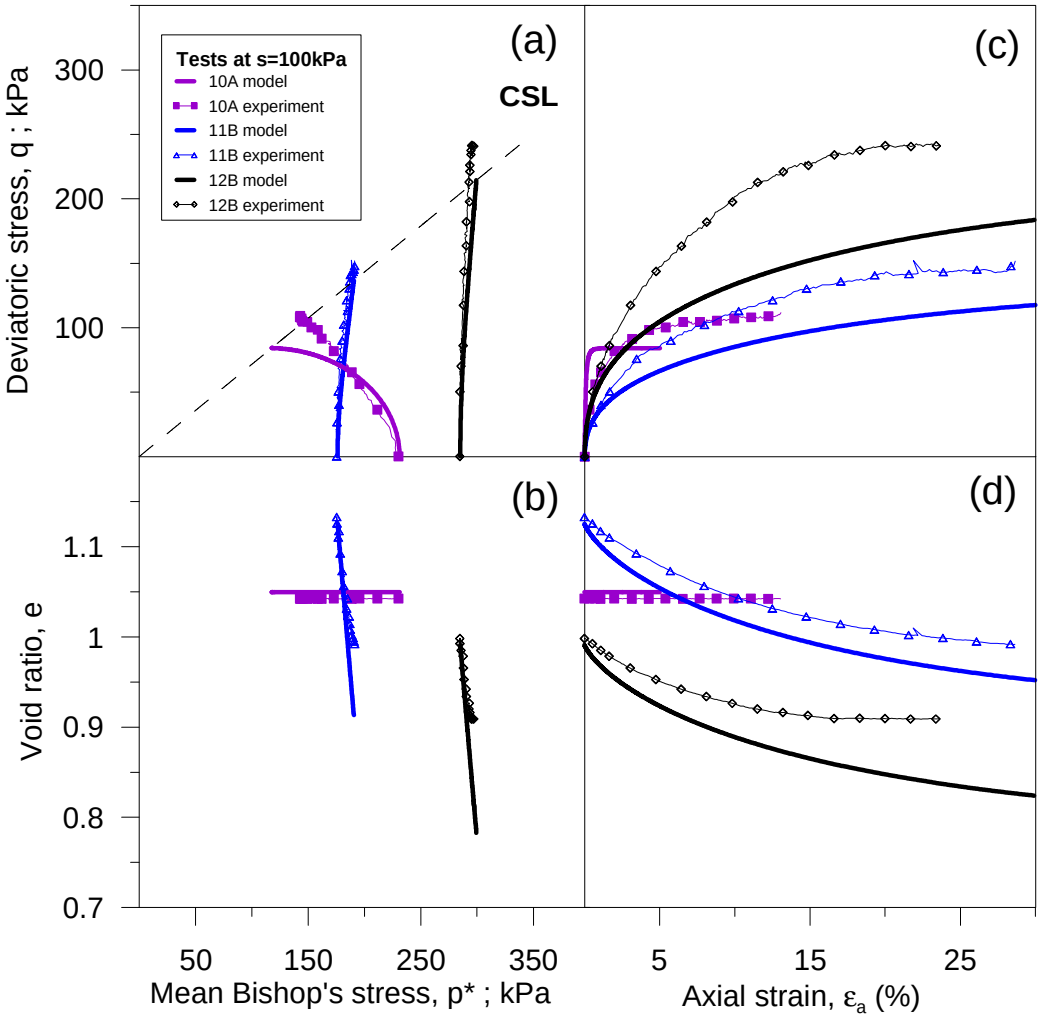

Figure 5- 11 Comparisons between model simulations and experimental results (Sivakumar,1993) for shearing at s=100 kPa.

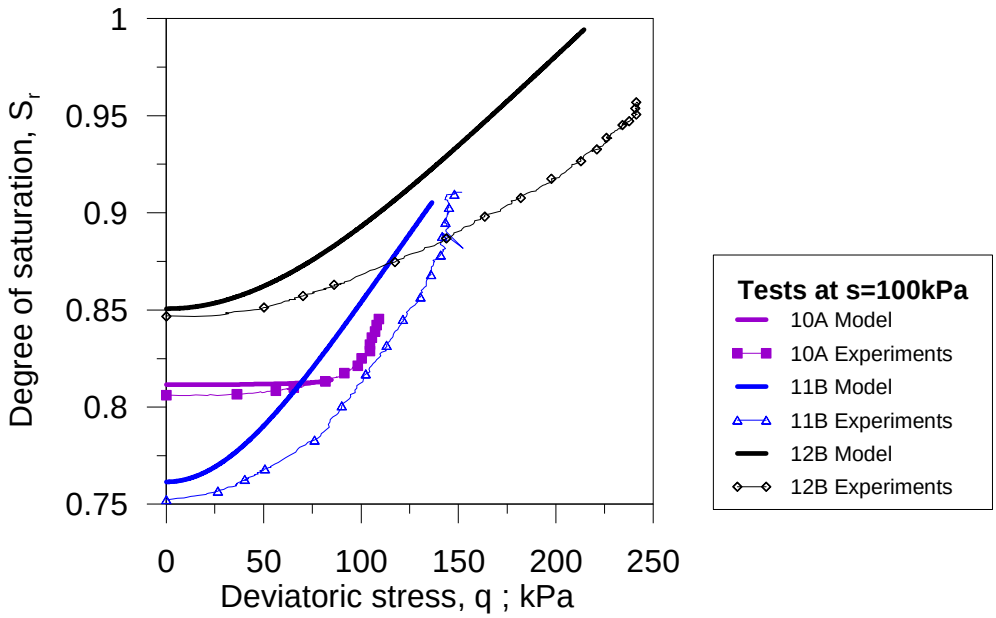

Figure 5- 12 Comparisons between model simulations and experimental results (Sivakumar,1993) for shearing at s=100 kPa: variation of degree of saturation.

5.5.3. Final discussion

Overall, the model predictions provide a reasonable match to the mechanical and water retention behaviour observed in the experimental tests of Sivakumar (1993). The significant mis-matches between model predictions and experimental results arise because the spacing between normal compression planar surface and critical state planar surface in v:lnp^*:lns^* space is over-predicted and because the development of shear strain during plastic straining is not accurately predicted. These weaknesses are also apparent in the Modified Cam Clay model for saturated soils which has been used as the saturated base model in the extension of the Wheeler et al. (2003) model to triaxial stress states. The weaknesses seem to arise because of the choice of elliptical cross-sections of the *LC* yield surface and the use of an associated flow rule on this surface.

From the comparison of model simulations with the experimental results of Sivakumar (1993) it appears that the extended model of Wheeler et al (2003) is able to represent the mechanical and water retention behaviour of unsaturated soils with the same level of success as can be achieved by Modified Cam Clay in representing the mechanical behaviour of saturated soils. If this is true, it represents a major success on the part of the Wheeler et al. (2003) model.

It should, however, be appreciated that the comparison of model predictions with the experimental results of Sivakumar (1993), presented here, represents only a partial

validation of the extended model of Wheeler et al. (2003). In particular, the results of Sivakumar (1993) do not show directly the effects of hydraulic hysteresis on water retention and mechanical behaviour, because Sivakumar's tests did not generally involve reversals of suction (the tests shown here involved wetting during the initial equalization stage and then constant suction during the remainder of each test). This absence of the effects of hydraulic hysteresis on the soil behaviour reported in the tests of Sivakumar (1993) means that the mechanical behaviour in these tests could be adequately represented by a more conventional unsaturated elasto-plastic mechanical constitutive model expressed in terms of net stresses and suction (see, for example, Wheeler and Sivakumar, 1995). The additional achievement of the extended Wheeler et al. (2003) model in simulating these tests is that it is also able to accurately predict the variation of degree of saturation S_r.

Full validation of the extended model of Wheeler et al. (2003) will require comparison with experimental results involving strong reversals of suction, where the impact of hydraulic hysteresis on water retention and mechanical behaviour is crucial. Inability to model properly this type of situation was identified by Wheeler et al. (2003) as a weakness of existing mechanical constitutive models expressed in terms of net stresses and suction, and was the motivation behind their development of a new model. However, it is reassuring to see, in the partial validation of the extended Wheeler et al. (2003) model against the experimental results of Sivakumar (1993) presented here, that in developing a model capable of dealing with the complexities of the effects of hydraulic hysteresis on mechanical behaviour it has not been necessary to sacrifice any accuracy in the modelling of unsaturated soil behaviour when hydraulic hysteresis is not involved.

Chapter 6

STRAIN-DRIVER ALGORITHMS FOR THE INTEGRATION OF THE GENERALISED STRESS-STRAIN RELATIONSHIPS

6. Strain-driver algorithms for the integration of the generalised stress-strain relationships (*Local Equations*)

An extended version of the Wheeler et al. (2003) model, for 3D stress conditions, was presented in Chapter 5 along with a comparative analysis between model simulations and the experimental results of Sivakumar (1993). Some fundamental tools (i.e. expressions for flow rules, hardening laws, extended yield functions, plastic multipliers and elastic and elasto-plastic generalised matrices) to numerically integrate this model were also presented in this Chapter 5 and a methodology to identify which elasto-plastic mechanisms are active was proposed. All these ideas are combined within this current Chapter 6 to present a complete strain-driver algorithmic formulation that enables the update of the stress variables (i.e. Bishop's stress tensor, modified suction, net stress tensor and matric suction); updating also degree of saturation and void ratio. This is achieved by expressing the equations of the problem in terms of strain and suction increments, which are the driving or known inputs of the algorithmic scheme described. Two different numerical approaches are presented (i.e. first order error forward Euler and second order error modified Euler) and several aspects of their computational response are discussed at the end of the chapter. The following Chapter 7 includes this algorithmic formulation into the finite element program CODE_BRIGHT to provide a tool for the solution of boundary value problems.

6.1. Introduction

In general, in each *iteration* of an elasto-plastic finite element analysis involving unsaturated soils (under isothermal conditions and neglecting any chemical or biological coupled effects), the increments of displacements and the increments of pore fluid pressures (i.e. air and water pressures) can be found from the *global* or *balance equations* (i.e. momentum balance for the medium, mass balance of air and mass balance of water, see Chapter 7 for further details). Once the nodal displacement increments ($\Delta\boldsymbol{u}$) are known, the strain increments ($\Delta\boldsymbol{\varepsilon}$) at a discrete number of integration points within each element can be determined (i.e. employing the compatibility equation, see Chapter 7). Also the increments of pore water pressure (Δu_w) and pore air pressure (Δu_a) can be used to determine the increments of matric suction (i.e. $\Delta s=\Delta u_a-\Delta u_w$). In general, both of these increments (strains and matric suction) are afterwards used at the integration or *Gauss* points to update the stress variables (i.e. typically computing the increments of net stresses, $\Delta\overline{\boldsymbol{\sigma}}=\boldsymbol{\sigma}-\mathbf{I}u_a$ where $\boldsymbol{\sigma}$ is the total stress tensor and $\boldsymbol{I}$ the identity matrix) and the internal variables. In order to do this it is necessary to formulate an algorithm that numerically integrates the elasto-plastic model (Sheng et al., 2003a). A wide range of

solution strategies is available in the literature to solve or *integrate* standard stress-strain equations. However, the constitutive model employed in this research presents some particular features that make the integration of this model particularly challenging, with several differences from classical approaches. The main aim of this current Chapter 6 is to give a detailed description of a formulation to integrate the 3D version of this advanced constitutive model, highlighting the main differences with respect to the integration of more standard models.

6.2. Formulation of the generalised stress-strain problem

The elasto-plastic integration presented in the following, employs the generalised strain vector increments ($\Delta\tilde{\boldsymbol{\varepsilon}}$) to update the generalised stress increments ($\Delta\tilde{\boldsymbol{\sigma}}^*$), where $\tilde{\boldsymbol{\sigma}}^*$ and $d\tilde{\boldsymbol{\varepsilon}}$ were introduced in Chapter 5 (Equations (5.4) and (5.5)):

$$\tilde{\boldsymbol{\sigma}}^* = \left(\sigma^*_{xx} \quad \sigma^*_{yy} \quad \sigma^*_{zz} \quad \tau_{xy} \quad \tau_{yz} \quad \tau_{xz} \quad s^*\right)^T$$

$$d\tilde{\boldsymbol{\varepsilon}} = \left(d\,\varepsilon_{xx} \quad d\varepsilon_{yy} \quad d\varepsilon_{zz} \quad d\gamma_{xy} \quad d\gamma_{yz} \quad d\gamma_{xz} \quad -dS_r\right)^T$$

This requires building up first the generalised strain increment from the information at the nodes (i.e. displacements and pore fluid pressures). The first six components of the generalised strain vector are found from the compatibility equation in the same way as explained for the standard strain increment vector ($\Delta\boldsymbol{\varepsilon}$) in Section 6.1. The last component of the generalised strain vector is the degree of saturation decrement and this requires a bit more work, as this incremental quantity is not known in advance. It is possible, however, using the extended version of the constitutive model of Wheeler et al. (2003) (see Chapter 5), to express the decrement of degree of saturation in terms of strain and suction increments as presented later in Section 6.3.

If the generalised stress increments ($d\tilde{\boldsymbol{\sigma}}^*$) associated with $d\tilde{\boldsymbol{\varepsilon}}$ activate an elasto-plastic mechanism causing plastic yielding, it is necessary to solve the following system of ordinary differential equations:

$$d\tilde{\boldsymbol{\sigma}}^* = \mathbf{D}^{*\,j}_{ep}\, d\tilde{\boldsymbol{\varepsilon}} \qquad \text{with} \quad \mathrm{j} = LC, \beta, LC+\beta \ \text{ and } \ \beta = SD/SI \qquad (6.1)$$

$$d\mathbf{h}^T = d\boldsymbol{\chi}^T \overline{\mathbf{B}} \qquad (6.2)$$

where,

$$\mathbf{D}_{ep}^{*\ j}=\begin{pmatrix}\mathbf{A}_{6x6}^{j} & \mathbf{B}_{6x1}^{j}\\ \mathbf{C}_{1x6}^{j} & D_{1x1}^{j}\end{pmatrix}_{7x7} \qquad \text{with} \quad \mathrm{j}=LC,\beta,LC+\beta \ \text{ and } \ \beta=SD/SI \tag{6. 3}$$

$$d\mathbf{h}^{T}=\begin{pmatrix}dp_0^{*} & ds_{\beta}^{*}\end{pmatrix} \qquad \text{with} \quad \beta=SD/SI \tag{6. 4}$$

$$d\boldsymbol{\chi}^{T}=\begin{pmatrix}d\chi_{LC}^{j} & d\chi_{\beta}^{j}\end{pmatrix} \qquad \text{with} \quad \mathrm{j}=LC,\beta,LC+\beta \ \text{ and } \ \beta=SD/SI \tag{6. 5}$$

$$\bar{\mathbf{B}}=\begin{pmatrix}\bar{B}_1 & \bar{B}_2\\ \bar{B}_3 & \bar{B}_4\end{pmatrix}=\begin{pmatrix}p_0^{*}\dfrac{v}{\lambda-\kappa}\mathbf{m}_{\varepsilon}^{T}\mathbf{m}_{LC} & k_2 s_{\beta}^{*}\dfrac{v}{\lambda-\kappa}\mathbf{m}_{\varepsilon}^{T}\mathbf{m}_{LC}\\ k_1 p_0^{*}\dfrac{1}{\lambda_s-\kappa_s}\mathbf{m}_{s}^{T}\mathbf{m}_{\beta} & s_{\beta}^{*}\dfrac{1}{\lambda_s-\kappa_s}\mathbf{m}_{s}^{T}\mathbf{m}_{\beta}\end{pmatrix} \tag{6. 6}$$

where the superscript *T* indicates transposed, ***β*** indicates that yielding on the *SD* yield surface or yielding on the *SI* yield surface is active, $\boldsymbol{D_{ep}}^{*j}$ is the elasto-plastic matrix which takes different forms depending on the plastic mechanism activated *j* (see Chapter 5 and Appendix A.2), $\boldsymbol{m}_{LC}$ and $\boldsymbol{m}_{\beta}$ are the same vectors introduced in Chapter 5 when presenting the formulation of the 3D extended model (Equations (5.11) and (5.13), respectively):

$$\mathbf{m}_{LC}^{T}=\begin{pmatrix}\dfrac{\partial F_{LC}}{\partial\tilde{\sigma}_1^{*}} & \dfrac{\partial F_{LC}}{\partial\tilde{\sigma}_2^{*}} & \dfrac{\partial F_{LC}}{\partial\tilde{\sigma}_3^{*}} & \dfrac{\partial F_{LC}}{\partial\tilde{\sigma}_4^{*}} & \dfrac{\partial F_{LC}}{\partial\tilde{\sigma}_5^{*}} & \dfrac{\partial F_{LC}}{\partial\tilde{\sigma}_6^{*}} & 0\end{pmatrix}$$

$$\mathbf{m}_{\beta}^{T}=\begin{pmatrix}0 & 0 & 0 & 0 & 0 & 0 & \dfrac{\partial F_{\beta}}{\partial\tilde{\sigma}_7^{*}}\end{pmatrix}$$

and the remaining auxiliary vectors are $\boldsymbol{m}^{T}_{\varepsilon}$=(1,1,1,0,0,0,0) and $\boldsymbol{m}^{T}_{s}$=(0,0,0,0,0,0,1). It should be note that (6.2) also accounts for the couplings defined in the model (see Section 2.6.2) when only one plastic mechanism is active (i.e. *LC* only with $d\chi_{\beta}^{LC}$=0, as dS_r^{p}=0; and *SD/SI* only with $d\chi_{LC}^{\beta}$=0, as $d\varepsilon_v^{p}$=0).

The system of equations formed by (6.1) and (6.2), expresses changes of the generalised stresses (i.e. containing increments of Bishop's stress tensor and modified suction) as a function of the generalised strain variations (i.e. containing strain increments and degree of saturation changes). This way of expressing the (generalised) stress is very convenient as it can be easily adapted to the conventional finite element formulations, where the displacements/pore pressures changes are found first to calculate strain and suction variations, which in turn are used to update the stresses (Sheng et al., 2003a).

The evolution of the yield surfaces defined in this problem (6.4) is also expressed in terms of the generalised strain variations (see the expressions developed for each plastic multiplier in Chapter 5 and Appendix A.2). Therefore, the system of equations formed by (6.1) and (6.2) enables the generalised stresses and the hardening parameters to be updated by knowing changes of the generalised strains and the initial state. This is achieved with the formulation of the generalised stress-strain algorithm discussed and presented in the following sections.

Note that the elastic case is equivalent to (6.1) employing the elastic matrix instead of the elasto-plastic matrix (6.3) and with hardening parameters remaining constant.

6.3. Variations of degree of saturation in terms of strain and suction changes

It is important to stress again that the expression for the generalised strain changes, $d\tilde{\boldsymbol{\varepsilon}}$, (5.5) includes the variation of the degree of saturation. The degree of saturation is a fundamental variable in the model presented and it is interesting to demonstrate that it is possible to express dS_r in terms of the known or driving variables (i.e. $\Delta\boldsymbol{\varepsilon}$ and Δs). This section is aimed at developing an expression of the degree of saturation changes in terms of strain and matric suction variations for the fully coupled model of Wheeler et al. (2003). In order to do this it is necessary to first express the increments of the stress state variables employed in the constitutive model (i.e. Bishop's stress tensor and modified suction) in the following terms:

$$d\boldsymbol{\sigma}^* = d\overline{\boldsymbol{\sigma}} + \mathbf{m}\left(S_r ds + s dS_r\right) \qquad (6.7)$$

$$ds^* = \frac{e}{1+e} ds - \frac{s}{1+e} \mathbf{m}^T d\boldsymbol{\varepsilon} \qquad (6.8)$$

where $\boldsymbol{m}^T$=(1,1,1,0,0,0).

On the other hand, expansion of (6.1) leads to two more equations:

$$d\boldsymbol{\sigma}^* = \mathbf{A}^j_{6x6} d\boldsymbol{\varepsilon} + \mathbf{B}^j_{6x1}\left(-dS_r\right) \qquad (6.9)$$

$$ds^* = \mathbf{C}^j_{1x6} d\boldsymbol{\varepsilon} + D^j_{1x1}\left(-dS_r\right) \qquad (6.10)$$

where the superscript *j* indicates the plastic mechanism that is active (yielding on the *LC* yield surface alone; yielding on the *SD* or *SI* yield surface alone; or simultaneous yielding

on the *LC* and *SD* or *SI* yield surfaces) including the elastic case. The expressions for $\boldsymbol{A}$, $\boldsymbol{B}$, $\boldsymbol{C}$ and D take the forms shown in Appendix A.2.

Expressions (6.7), (6.8), (6.9) and (6.10) define a system of equations with six unknowns: increment of Bishop's stress $d\boldsymbol{\sigma}^*$ (which, in turn, has six components), increment of net stress $d\overline{\boldsymbol{\sigma}}$ (which, in turn, has six components), strain increment $d\boldsymbol{\varepsilon}$ (which, in turn, has six components), increment of matric suction ds (scalar), increment of modified suction ds^* (scalar) and increment of degree of saturation dS_r (scalar). If a pair of these six unknowns is assumed to be known, it should be then possible to express these equations as functions of these pair of known variables. For instance, if it is assumed that $d\boldsymbol{\varepsilon}$ and ds are known, the remaining four unknowns can be expressed (by employing these four equations) in terms of $d\boldsymbol{\varepsilon}$ and ds. In fact, when strains and matric suction changes are known (these are typically the driving variables of strain-driver algorithms used in finite element formulations), one may find, after some algebra, the following expression for the decrement of the degree of saturation:

$$-dS_r = \left(D^j\right)^{-1}\left[\frac{e}{1+e}ds + \left(\frac{-s}{1+e}\mathbf{m}^T - \mathbf{C}^j\right)d\boldsymbol{\varepsilon}\right] \qquad (6.11)$$

where the superscript j indicates elastic; yielding on the *LC* yield surface alone; yielding on only the *SD* or *SI* yield surface alone; or simultaneous yielding on the *LC* and *SD* or *SI* yield surfaces; and C and D take the forms shown in Appendix A.2.

6.4. Explicit strain-driver algorithms

A large variety of methods are available in the literature to solve or *integrate* stress-strain equations numerically. Typically, integration algorithms are classified into two different groups: *explicit* and *implicit*. In the former, the updated stress is obtained by integrating the strain increments with the elasto-plastic matrix evaluated at the start of each integration step; whereas *implicit* algorithms calculate the stress increment employing the elasto-plastic matrix evaluated at the end of the integration step. With implicit algorithms it is necessary to solve first an iterative scheme because the values at the end of the step are not initially known (Solowsky, 2008).

As pointed out by several authors, the integration process of an elasto-plastic model is crucial when using finite element analysis (see, for instance, Tamaginini et al., 2002 or Solowsky and Gallipoli, 2010a,b). It is, therefore, important to build an efficient algorithm minimising the associated computational costs and optimising the accuracy of the solution. In this direction, the following sections present the general formulation to

integrate, in an explicit way, the extended version of the Wheeler et al. (2003) model. Two different explicit algorithms are described: first order Euler method (also known as forward Euler algorithm) and second order modified Euler. A comparison between the computed results obtained from both schemes is given at the end of this chapter. An interesting future line research would be to extend this comparison to other numerical schemes such as the family of explicit algorithms with automatic error control developed by Sloan and co-workers (Sloan, 1987; Abbo, 1997; Sloan et al., 2001; Sheng et al., 2003a,b and subsequent papers); or equivalent implicit algorithm formulations to those presented in Simo and Hughes (1998) or Crisfield (1991) (see also Chapter 8).

6.4.1. Forward Euler formulation

Given the initial state (i.e. void ratio e, degree of saturation S_r, net stress tensor $\overline{\boldsymbol{\sigma}}$ and matric suction s) the algorithm calculates the initial values of the Bishop's stress tensor $\boldsymbol{\sigma}^*$ and modified suction s^* to build the initial generalised stress vector $\tilde{\boldsymbol{\sigma}}^*$. Then, given the increments of strains $\Delta\boldsymbol{\varepsilon}$ and suction Δs (calculated from the increments of displacements and increments of pore pressures, respectively), an initial elastic trial increment of the degree of saturation is calculated employing (6.11). Combining this information it is possible to construct the generalised strain increment $\Delta\tilde{\boldsymbol{\varepsilon}}$ which will be used (combined with the generalised elastic matrix $\boldsymbol{D}_e^*$) to calculate an elastic generalised stress trial. Given also the initial values of the hardening parameters defining the initial elastic domain, the explicit algorithm presented below updates the stress state variables and the hardening parameters according to the following steps. The formulation adopted here follows a similar scheme to the one presented in Abbo (1997).

i. *Computation of the initial stress state*

Given the initial net stress tensor $d\overline{\boldsymbol{\sigma}}_{k=0}$, the initial matric suction $s_{k=0}$, the initial void ratio $e_{k=0}$ and the initial degree of saturation $S_{r\,k=0}$, compute first the initial Bishop's stress tensor $\boldsymbol{\sigma}^*_{k=0}$ and the initial modified suction $s^*_{k=0}$ at $k=0$. Build afterwards the initial generalised stress tensor as:

$$\tilde{\boldsymbol{\sigma}}^*_{k=0} = \left(\sigma_1^* \quad \sigma_2^* \quad \sigma_3^* \quad \sigma_4^* \quad \sigma_5^* \quad \sigma_6^* \quad s^*\right)_{k=0} \qquad (6.12)$$

Given the initial values of the hardening parameters at $k=0$ $\boldsymbol{h}_{k=0}=(p_0^*, s_\beta^*)_{k=0}$ (where $\beta=SD/SI$) and the initial generalised stress tensor (6.12), compute the initial elastic domain defined by the three yield surfaces evaluated at $k=0$ (5.1), (5.2) and (5.3) according to:

$$F_{LC}\left(\tilde{\boldsymbol{\sigma}}^{*}_{k=0},\mathbf{h}_{k=0}\right)\leq 0 \qquad (6.\ 13)$$

$$F_{SD}\left(\tilde{\boldsymbol{\sigma}}^{*}_{k=0},\mathbf{h}_{k=0}\right)\leq 0 \qquad (6.\ 14)$$

$$F_{SI}\left(\tilde{\boldsymbol{\sigma}}^{*}_{k=0},\mathbf{h}_{k=0}\right)\leq 0 \qquad (6.\ 15)$$

If the resulting stress point lies outside the elastic domain (i.e. $F_{LC}(\tilde{\boldsymbol{\sigma}}^{*}_{k=0},\boldsymbol{h}_{k=0})>0$ ***or*** $F_{SD}(\tilde{\boldsymbol{\sigma}}^{*}_{k=0},\boldsymbol{h}_{k=0})>0$ ***or*** $F_{SI}(\tilde{\boldsymbol{\sigma}}^{*}_{k=0},\boldsymbol{h}_{k=0})>0$) the stress state is impossible, exit.

ii. *Computation of an elastic trial of the degree of saturation*

Assume that the given increments of strains $\Delta\boldsymbol{\varepsilon}$ and suction Δs are purely elastic and compute an elastic trial increment of the degree of saturation ΔS_r^{trial} using (6.11) with elastic behaviour.

iii. *Construction of the generalised strain vector*

Once the elastic trial of the degree of saturation has been computed $\Delta S_r^{trial}(\Delta\boldsymbol{\varepsilon}, \Delta s)$, build the generalised strain vector:

$$\Delta\tilde{\boldsymbol{\varepsilon}}=\begin{pmatrix}\Delta\varepsilon_1 & \Delta\varepsilon_2 & \Delta\varepsilon_3 & \Delta\varepsilon_4 & \Delta\varepsilon_5 & \Delta\varepsilon_6 & -\Delta S_r^{trial}\end{pmatrix} \qquad (6.\ 16)$$

iv. *Elastic trial of the generalised stresses*

Assuming that $\Delta\tilde{\boldsymbol{\varepsilon}}$ is purely elastic, compute a trial generalised stress increment $\Delta\tilde{\boldsymbol{\sigma}}^{*trial}$ and update the generalised stresses according to:

$$\Delta\tilde{\boldsymbol{\sigma}}^{*trial}=\mathbf{D}_{\mathbf{e}}^{*}\Delta\tilde{\boldsymbol{\varepsilon}} \qquad (6.\ 17)$$

$$\tilde{\boldsymbol{\sigma}}^{*trial}=\tilde{\boldsymbol{\sigma}}^{*}_{k=0}+\Delta\tilde{\boldsymbol{\sigma}}^{*trial} \qquad (6.\ 18)$$

Determine if the trial generalised stress state is outside of the elastic domain defined in (*i.*). If the trial (generalised) stress state is inside or on all of the yield surfaces defined (i.e. $F_{LC}(\tilde{\boldsymbol{\sigma}}^{*trial},\boldsymbol{h}_{k=0})\leq 0$ ***and*** $F_{SD}(\tilde{\boldsymbol{\sigma}}^{*trial},\boldsymbol{h}_{k=0})\leq 0$ ***and*** $F_{SI}(\tilde{\boldsymbol{\sigma}}^{*trial},\boldsymbol{h}_{k=0})\leq 0$) update (generalised) stresses and internal variables with the elastic trial and exit.

v. *Identification of the elasto-plastic mechanism active*

Given $\tilde{\boldsymbol{\sigma}}^{*trial}$ and $\boldsymbol{h}_{k=0}$ evaluate the functions proposed in Section 5.4 at *k=0* to identify which is the elasto-plastic mechanism that should be activated:

$$F_1^{trial} = F_1\left(\tilde{\boldsymbol{\sigma}}^{*trial}, \mathbf{h}_{k=0}\right) \quad (6.19)$$

$$F_2^{trial} = F_2\left(\tilde{\boldsymbol{\sigma}}^{*trial}, \mathbf{h}_{k=0}\right) \quad (6.20)$$

$$F_3^{trial} = F_3\left(\tilde{\boldsymbol{\sigma}}^{*trial}, \mathbf{h}_{k=0}\right) \quad (6.21)$$

$$F_4^{trial} = F_4\left(\tilde{\boldsymbol{\sigma}}^{*trial}, \mathbf{h}_{k=0}\right) \quad (6.22)$$

Combining these functions with the three yield surfaces also evaluated at *k=0* (i.e. (6.13), (6.14) and (6.15)), define the five domains to identify the five different elasto-plastic mechanisms according to (see also Section 5.4):

$$\text{Domain 1: } \left\{F_1\left(\tilde{\boldsymbol{\sigma}}^{*trial}, \mathbf{h}_{k=0}\right) \le 0\right\} \cap \left\{F_{SI}\left(\tilde{\boldsymbol{\sigma}}^{*trial}, \mathbf{h}_{k=0}\right) > 0\right\} \quad (6.23)$$

$$\text{Domain 2: } \left\{F_1\left(\tilde{\boldsymbol{\sigma}}^{*trial}, \mathbf{h}_{k=0}\right) > 0\right\} \cap \left\{F_{SI}\left(\tilde{\boldsymbol{\sigma}}^{*trial}, \mathbf{h}_{k=0}\right) > 0\right\} \cap \left\{F_2\left(\tilde{\boldsymbol{\sigma}}^{*trial}, \mathbf{h}_{k=0}\right) < 0\right\} \quad (6.24)$$

$$\text{Domain 3: } \left\{F_2\left(\tilde{\boldsymbol{\sigma}}^{*trial}, \mathbf{h}_{k=0}\right) \ge 0\right\} \cap \left\{F_{LC}\left(\tilde{\boldsymbol{\sigma}}^{*trial}, \mathbf{h}_{k=0}\right) > 0\right\} \cap \left\{F_3\left(\tilde{\boldsymbol{\sigma}}^{*trial}, \mathbf{h}_{k=0}\right) \le 0\right\} \quad (6.25)$$

$$\text{Domain 4: } \left\{F_3\left(\tilde{\boldsymbol{\sigma}}^{*trial}, \mathbf{h}_{k=0}\right) > 0\right\} \cap \left\{F_4\left(\tilde{\boldsymbol{\sigma}}^{*trial}, \mathbf{h}_{k=0}\right) > 0\right\} \quad (6.26)$$

$$\text{Domain 5: } \left\{F_4\left(\tilde{\boldsymbol{\sigma}}^{*trial}, \mathbf{h}_{k=0}\right) \le 0\right\} \cap \left\{F_{SD}\left(\tilde{\boldsymbol{\sigma}}^{*trial}, \mathbf{h}_{k=0}\right) > 0\right\} \quad (6.27)$$

where $\cap$ indicates intersection between surfaces.

If the trial is found to fall in any of these five domains defined (i.e. (6.23)-(6.27)), yielding will take place according to the elasto-plastic mechanism activated (i.e. Domain 1: yielding on the *SI* yield surface alone, Domain 2: simultaneous yielding on the *SI* and *LC* yield surfaces, Domain 3: yielding on the *LC* yield surface alone, Domain 4: simultaneous yielding on the *LC* and *SD* yield surfaces, Domain 5: yielding on the *SD* yield surface alone).

vi. *Intersection(s)*

Two separate sets of alternatives arise when the stress trial is found to fall outside the elastic domain. If the trial is found to activate just one plastic mechanism (i.e. Domain 1, Domain 3 or Domain 5) only one intersection point is required to update the stresses (see Figure 6-1). However, when two plastic mechanisms are activated simultaneously (i.e.

Domain 2 and Domain 4) two intersection points are generally required, as described below.

Figure 6-1 is intended to illustrate yield surface intersection when only one plastic mechanism is activated. This figure shows an ideal trial path that, from the elastic domain, falls in Domain 5, causing yielding on the *SD* yield surface alone. Therefore, it is necessary to find the fraction (α_1) of $\Delta\tilde{\boldsymbol{\varepsilon}}$ that changes the generalised stresses from $\tilde{\boldsymbol{\sigma}}^*_{k=0}$ to $\tilde{\boldsymbol{\sigma}}^*_{\text{intersection1}}$ on the yield surface (i.e. *SD*). This classical problem of non-linear elasticity can be solved by using a wide range of numerical methods (see Sheng, 2003a) and it is formulated as follows:

$$F\left(\tilde{\boldsymbol{\sigma}}^*_{k=0} + \alpha_1 \mathbf{D}^*_{\boldsymbol{\epsilon}} \Delta\tilde{\boldsymbol{\varepsilon}}, \mathbf{h}_{k=0}\right) = F\left(\tilde{\boldsymbol{\sigma}}^*_{\text{intersection1}}, \mathbf{h}_{k=0}\right) \qquad \textit{(6. 28)}$$

where α_1 is the root searched.

The algorithm presented in this section employs the classical bisection method to find the intersection between the stress path and the pertinent surface. This method, although being robust, has, in general, an expensive computational cost. However, this alternative has been considered appropriate for the purposes discussed here, where the primary aim is to develop and propose an algorithmic formulation capable of integrating this advanced constitutive model. A future step would be to analyse the influence on the solution (and on relevant computational aspects) of employing other intersection schemes (such as the 'Pegasus algorithm' suggested in Sloan et al., 2001). In order to approximate the solution α_1 to the desired accuracy, the bisection method requires the specification of a tolerance (indicated as *TOL1* in this work).

It may be important to mention that the sketch shown in Figure 6-1 is an idealised plot to illustrate the intersection of an idealised stress path with the *SD* yield surface. In particular, due to the non-linearity of the problem, the intersection point plotted would not be, in general, on the same trial path (see Sloan et al., 2001), as $\Delta\tilde{\boldsymbol{\sigma}}^{*trial}$ and $\alpha_1\Delta\tilde{\boldsymbol{\sigma}}^{*trial}$ are nonlinear.

Equivalent results would be found for yielding on the *LC* yield surface alone and for yielding on the *SI* yield surface alone and, therefore, are not repeated here.

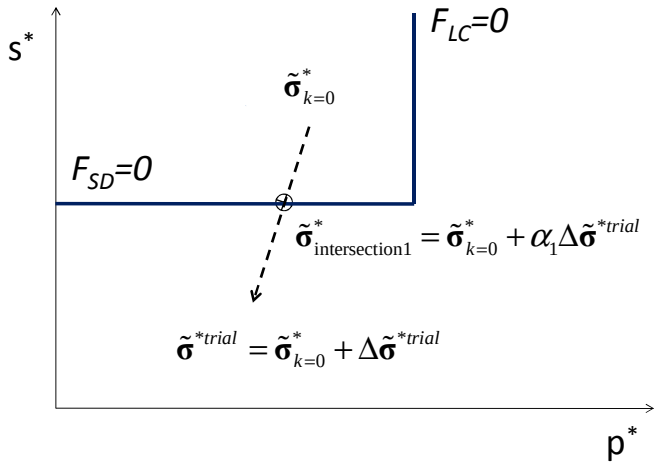

Figure 6- 1 Idealisation of yield surface intersection for yielding on the SD yield surface alone.

Following a similar approach to the one presented above for one plastic mechanism active, Figure 6-2 illustrates the two intersections points solved when two plastic mechanisms are activated simultaneously. In particular, this figure shows an ideal trial stress path that, from the elastic domain, falls in Domain 4 causing simultaneous yielding on the *LC* and *SD* yield surfaces. For this particular case, it is necessary to solve the previously presented intersection problem twice. The first one is equivalent to that described in Figure 6-1. Then, changing the stress state from the initial point $\tilde{\boldsymbol{\sigma}}^*_{k=0}$ to $\tilde{\boldsymbol{\sigma}}^*_{\text{intersection1}}$ on the *SD* yield surface, it is necessary to find a second intersection between the stress path and the surface F_4 (see Figure 6-2). The difference is, however, that the part of the remaining fraction of $\Delta\tilde{\boldsymbol{\varepsilon}}$ not yet integrated will cause yielding on the *SD* yield surface alone. In this way, a new problem is defined according to:

$$F\left(\tilde{\boldsymbol{\sigma}}^*_{\text{intersection1}} + \alpha_2 \mathbf{D}^{*j}_{\mathbf{ep}} \Delta\tilde{\boldsymbol{\varepsilon}}_2, \mathbf{h}\right) = F\left(\tilde{\boldsymbol{\sigma}}^*_{\text{intersection2}}, \mathbf{h}\right) = 0 \qquad (6.\ 29)$$

with

$$\Delta\tilde{\boldsymbol{\varepsilon}}_2 = (1-\alpha_1)\Delta\tilde{\boldsymbol{\varepsilon}}_1 \qquad (6.\ 30)$$

where α_1 is the solution from the first intersection problem (6.28), α_2 is the current unknown root and the superscript *j* indicates the plastic mechanism active (i.e. in this particular case: yielding on the *SD* yield surface alone).

An implicit assumption in (6.29) is that the hardening parameters (***h***) do not change. This is not true as yielding on the *SD* surface is taking place from $\tilde{\boldsymbol{\sigma}}^*_{\text{intersection1}}$ to $\tilde{\boldsymbol{\sigma}}^*_{\text{intersection2}}$. However, as F_4 gives the trace of the corner while yielding on the *SD* yield curve alone

takes place (see Section 3.3.5), the stress state $\tilde{\boldsymbol{\sigma}}^*_{\text{intersection2}}$ (see Figure 6-2) will be on the corner between *LC* and *SD* yield surfaces by definition of F_4 (see Chapter 3 for more details). Or, in other words, yielding on the *SD* yield surface alone from $\tilde{\boldsymbol{\sigma}}^*_{\text{intersection1}}$ to $\tilde{\boldsymbol{\sigma}}^*_{\text{intersection2}}$ will bring both yield surfaces (i.e. *LC* and *SD*) to the second intersection point (bottom corner) where the values of the hardening parameters are known. It is important to emphasise here that F_4 remains in the same position while yielding on the *SD* yield surface alone is taking place. All these observations, which are equivalent to those found for simultaneous yielding on the *LC* and *SI* surfaces, are further illustrated below when describing how the algorithm updates the generalised stresses.

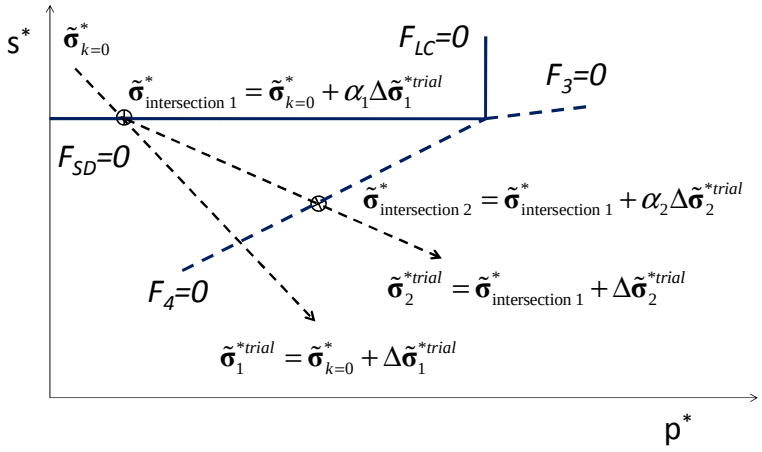

Figure 6- 2 Idealisation of yield surface intersection for the simultaneous yielding on the LC and SD yield surfaces.

Other cases than that illustrated in Figure 6-2 are also possible. Indeed, Figure 6-3 shows three separate possibilities arising when simultaneous yielding on the *LC* and *SD* yield surfaces is activated. The first and the third cases are equivalent, with two intersections points required. The second case presented in Figure 6-3 considers an ideal path intersecting exactly the corner between the *LC* and *SD* yield curves. This case, although being very rare, would involve the solution of only one intersection problem.

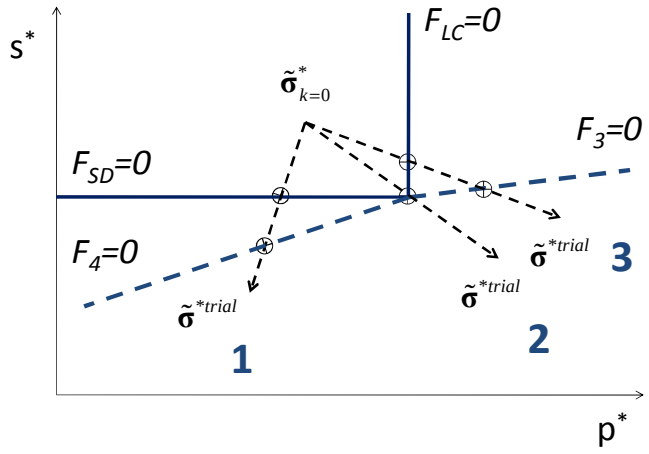

Figure 6- 3 Diagram illustrating three possible ways to activate simultaneous yielding on the LC and SD surfaces.

All prior discussions are illustrated under isotropic stress conditions because it is clearer and easier to represent the results in the isotropic stress plane. Equivalent comments, however, are also valid for the 3D generalised case.

vii. *Generalised stress integration and update of the hardening parameters*

Following the description given above, the update of generalised stresses and yield surfaces also shows two different situations: when only one elasto-plastic mechanism is active or when yielding simultaneously on two yield surfaces. The discussion below is subdivided into these two cases.

Note that, as described below, the strategy used to solve the problem when only one mechanism is activated by the elastic trial (for example yielding on the *SD* yield surface alone see Figure 6-1) is very similar to that used when solving the standard classical problem (see, for instance, Márquez, 1984 and Lloret and Ledesma, 1993). Once the intersection point has been identified (see Figure 6-1), the generalised stresses are elastically updated from the initial state to the intersection of the pertinent yield surface:

$$\tilde{\boldsymbol{\sigma}}^*_{\text{intersection1}} = \tilde{\boldsymbol{\sigma}}^*_{k=0} + \alpha_1 \Delta\tilde{\boldsymbol{\sigma}}^{*trial} = \tilde{\boldsymbol{\sigma}}^*_{k=0} + \mathbf{D}^*_{\mathbf{e}} \left(\alpha_1 \Delta\tilde{\boldsymbol{\varepsilon}}_1\right) \qquad (6.\ 31)$$

where the scalar quantity α_1 identifies the portion of $\Delta\tilde{\boldsymbol{\varepsilon}}_1$ that should be integrated as elastic. The remaining part (i.e. $(1\text{-}\alpha_1)\,\Delta\tilde{\boldsymbol{\varepsilon}}_1$) accounts for the elasto-plastic update of the generalised stress (for example, as represented in Figure 6-1, yielding on the *SD* yield surface alone). It is then necessary to rebuild the increment of generalised strains by computing first the increment of degree of saturation for the plastic mechanism active (i.e.

yielding on the *SD* yield surface alone for the case plotted in Figure 6-1). This involves employing (6.11) with the plastic mechanism activated and considering only the non integrated part of $\Delta\tilde{\boldsymbol{\varepsilon}}_1$ (this is to calculate ΔS_r using $(1-\alpha_1)\Delta\boldsymbol{\varepsilon}$ and $(1-\alpha_1)\Delta s$). As a result, the generalised strain vector becomes:

$$\Delta\tilde{\boldsymbol{\varepsilon}}_2 = \left((1-\alpha_1)\Delta\boldsymbol{\varepsilon}, \Delta S_r^j\left((1-\alpha_1)\Delta\boldsymbol{\varepsilon}, (1-\alpha_1)\Delta s\right)\right) \qquad (6.\ 32)$$

where the superscript *j* indicates the plastic mechanism active.

The following step is to calculate the increment of generalised stress (by computing first the elasto-plastic matrix associated with the plastic mechanism active) and update the generalised stress tensor:

$$\tilde{\boldsymbol{\sigma}}_{k+1}^{*} = \tilde{\boldsymbol{\sigma}}_{\text{intersection}}^{*} + \Delta\tilde{\boldsymbol{\sigma}}^{*j} = \tilde{\boldsymbol{\sigma}}_{\text{intersection}}^{*} + \mathbf{D}_{ep}^{*j}\left(\Delta\tilde{\boldsymbol{\varepsilon}}_2\right) \qquad (6.\ 33)$$

where, again, the superscript *j* indicates the plastic mechanism active.

Finally it is necessary to update the position of the yield surfaces according to:

$$\mathbf{h}_{k+1} = \mathbf{h}_{k=0} + \Delta\mathbf{h} \qquad (6.\ 34)$$

where $\Delta\boldsymbol{h}$ has been calculated using (6.2) and accounting only for the plastic mechanism activated.

This scheme is equivalent to that required for yielding on the *LC* yield surface alone or yielding on the *SI* yield surface alone. However, a different procedure is necessary when two elasto-plastic mechanisms are active simultaneously. When two elasto-plastic mechanisms are active simultaneously, the first step needed is to integrate the elastic part in the same manner as presented for the previous example (6.31). This is to change the stress state from the prior elastic stress state to the first intersection point (for example, the intersection point between the stress path and the *SD* yield surface shown in Figure 6-2)

The non integrated part of $\Delta\boldsymbol{\varepsilon}$ and Δs will now be used to calculate the second generalised stress trial (see Figure 6-2):

$$\Delta\tilde{\boldsymbol{\sigma}}_2^{*trial} = \mathbf{D}_{ep}^{*j}\left(1-\alpha_1\right)\Delta\tilde{\boldsymbol{\varepsilon}}_1 = \mathbf{D}_{ep}^{*j}\Delta\tilde{\boldsymbol{\varepsilon}}_2 \qquad (6.\ 35)$$

where $\Delta\tilde{\boldsymbol{\varepsilon}}_2$ has been calculated according to (6.32) with the pertinent plastic mechanism. Now the second scalar quantity α_2 identifying the portion of $\Delta\tilde{\boldsymbol{\varepsilon}}_2$ that should be elasto-plastically integrated can be found using (6.29). This value is used to move the generalised stress state from the first intersection point to the second one (see Figure 6-2) according to:

$$\tilde{\boldsymbol{\sigma}}^*_{\text{intersection2}} = \tilde{\boldsymbol{\sigma}}^*_{\text{intersection1}} + \alpha_2 \Delta\tilde{\boldsymbol{\sigma}}_2^{*trial} \qquad (6.\ 36)$$

Looking at Figure 6-2, one should note that in this second update of the generalised stress vector, the plastic mechanism considered to change the stress state from the first intersection (i.e. intersection of the stress path with the *SD* yield surface, indicated as *intersection1* in Figure 6-2) to the second intersection (i.e. intersection of the stress path with the surface F_4, indicated as *intersection2* in Figure 6-2) has been yielding on the *SD* yield surface alone. Also the hardening parameters should be updated using (6.34) but now considering only the part integrated as elasto-plastic (i.e. $(1-\alpha_1)\Delta\tilde{\boldsymbol{\varepsilon}}_1 = \Delta\tilde{\boldsymbol{\varepsilon}}_2$) with the appropriate plastic mechanism (i.e. yielding on the *SD* surface for the case illustrated in Figure 6-2).

Finally, the remaining part of $\Delta\tilde{\boldsymbol{\varepsilon}}_2$ should be integrated considering, for this particular case (see Figure 6-2), simultaneous yielding on the *LC* and *SD* yield surfaces. To do this it is first necessary to compute the pertinent increment of degree of saturation, along with the generalised strain vector, according to:

$$\Delta\tilde{\boldsymbol{\varepsilon}}_3 = \left((1-\alpha_2)\Delta\boldsymbol{\varepsilon}, \Delta S_r^j \left((1-\alpha_2)\Delta\boldsymbol{\varepsilon}, (1-\alpha_2)\Delta s\right)\right) \qquad (6.\ 37)$$

where the superscript *j* indicates the plastic mechanism activated.

Note that for the case illustrated in Figure 6-2, the increment of degree of saturation ΔS_r^j appearing in (6.37) is calculated employing (6.11) with simultaneous yielding on the *LC* and *SD* yield surfaces, and considering only the not yet integrated part of $\Delta\tilde{\boldsymbol{\varepsilon}}_2$ (i.e. calculated using $(1-\alpha_2)\Delta\boldsymbol{\varepsilon}$ and $(1-\alpha_2)\Delta s$).

The next step is to calculate the increment of generalised stress by computing first the corresponding elasto-plastic matrix (which, for the case illustrated in Figure 6-2, corresponds to yielding on *LC*+*SD*, see Section 5.3).This information is then used to update the generalised stress tensor as:

$$\tilde{\boldsymbol{\sigma}}^{*}_{k+1} = \tilde{\boldsymbol{\sigma}}^{*}_{\text{intersection2}} + \Delta\tilde{\boldsymbol{\sigma}}^{*j} = \tilde{\boldsymbol{\sigma}}^{*}_{\text{intersection2}} + \mathbf{D}^{*j}_{ep}\left(\Delta\tilde{\boldsymbol{\varepsilon}}_3\right) \qquad (6.\ 38)$$

Finally, also the hardening parameters should be updated using (6.34) with the current plastic mechanism considering only the part of yielding caused by the last remaining integrated part (i.e. $\Delta\tilde{\boldsymbol{\varepsilon}}_3$).

viii. *Yield surface drift correction*

Each time the final generalised stress lies outside the updated yield surface/s currently yielding, the current state should be projected back to the pertinent yield surface/s using a drift correction method. Section 6.5 describes a possible scheme to correct this drift based on the work presented by Potts and Gens (1985).

6.4.2. Modified Euler formulation

The modified Euler formulation essentially uses the same scheme presented above and will not be fully repeated here. Only the significant differences are discussed. The main significant difference between both numerical schemes lies in how each algorithm updates the state variables. For the modified Euler method, the elastic/elasto-plastic matrix needs to be evaluated also at the end of the interval, once all the state variables have been updated with the first order Euler method. Then, employing this new calculated elastic/elasto-plastic matrix, a second increment of the state variables is obtained and is used, in combination with the first order increments previously found, to update each state variable. A more detailed mathematical description on how each variable is updated is given as follows.

The first order algorithm is employed to update all variables in the same manner as described in Section 6.4.1. This is, at *k+1*:

$$\tilde{\boldsymbol{\sigma}}^{*\,\text{FE}}_{k+1} = \tilde{\boldsymbol{\sigma}}^{*}_{k} + \Delta\tilde{\boldsymbol{\sigma}}^{*}1 = \tilde{\boldsymbol{\sigma}}^{*}_{k} + \mathbf{D}^{*}_{e\,k}\left(\Delta\tilde{\boldsymbol{\varepsilon}}\right) \qquad (6.\ 39)$$

$$\mathbf{h}^{\text{FE}}_{k+1} = \mathbf{h}_k + \Delta\mathbf{h}1 = \mathbf{h}_k + \left(\Delta\boldsymbol{\chi}^{T}\bar{\mathbf{B}}\right)_k \qquad (6.\ 40)$$

$$e^{\text{FE}}_{k+1} = e_k + \Delta e1 \qquad (6.\ 41)$$

$$S^{\text{FE}}_{r\,k+1} = S_{r\,k} + \Delta S_r 1 \qquad (6.\ 42)$$

with *FE* indicating the current numerical scheme employed (i.e. Forward Euler method).

Now the elasto-plastic matrix can be evaluated at *k+1*:

$$\mathbf{D}^{*\ j}_{ep\ k+1} = \begin{pmatrix} \mathbf{A}^{j}_{6x6} & \mathbf{B}^{j}_{6x1} \\ \mathbf{C}^{j}_{1x6} & D^{j}_{1x1} \end{pmatrix}_{k+1} \quad \text{with} \quad \mathrm{j} = LC, \beta, LC+\beta \ \text{ and } \ \beta = SD/SI \tag{6. 43}$$

Also the matrix containing the information from the hardening laws:

$$\bar{\mathbf{B}}_{k+1} = \begin{pmatrix} \bar{B}_1 & \bar{B}_2 \\ \bar{B}_3 & \bar{B}_4 \end{pmatrix}_{k+1} \tag{6. 44}$$

Each of these matrices can now be employed to update the generalised stresses and the hardening parameters as:

$$\tilde{\boldsymbol{\sigma}}^{*\,\mathrm{ME}}_{k+1} = \tilde{\boldsymbol{\sigma}}^{*}_{k} + \frac{1}{2}\left(\Delta\tilde{\boldsymbol{\sigma}}^{*}1 + \Delta\tilde{\boldsymbol{\sigma}}^{*}2\right) = \tilde{\boldsymbol{\sigma}}^{*}_{k} + \frac{1}{2}\left(\mathbf{D}^{*\,j}_{ep\ k}\left(\Delta\tilde{\boldsymbol{\varepsilon}}1\right) + \mathbf{D}^{*\,j}_{ep\ k+1}\left(\Delta\tilde{\boldsymbol{\varepsilon}}2\right)\right) \tag{6. 45}$$

$$\mathbf{h}^{\mathrm{ME}}_{k+1} = \mathbf{h}_{k} + \frac{1}{2}\left(\Delta\mathbf{h}1 + \Delta\mathbf{h}2\right) = \mathbf{h}_{k} + \frac{1}{2}\left(\left(\Delta\boldsymbol{\chi}^{T}\bar{\mathbf{B}}\right)_{k} + \left(\Delta\boldsymbol{\chi}^{T}\bar{\mathbf{B}}\right)_{k+1}\right) \tag{6. 46}$$

Note that vectors $\Delta\tilde{\boldsymbol{\varepsilon}}1$ and $\Delta\tilde{\boldsymbol{\varepsilon}}2$ are essentially the same except for the last component containing the information of the degree of saturation changes (6.11). In fact:

$$-\Delta S_r 1 = \left\{\left(D^{j}\right)^{-1}\left[\frac{e}{1+e}\Delta s + \left(\frac{-s}{1+e}\mathbf{m}^{T} - \mathbf{C}^{j}\right)\Delta\boldsymbol{\varepsilon}\right]\right\}_{k} \tag{6. 47}$$

$$-\Delta S_r 2 = \left\{\left(D^{j}\right)^{-1}\left[\frac{e}{1+e}\Delta s + \left(\frac{-s}{1+e}\mathbf{m}^{T} - \mathbf{C}^{j}\right)\Delta\boldsymbol{\varepsilon}\right]\right\}_{k+1} \tag{6. 48}$$

Then, the void ratio and degree of saturation are updated as:

$$e^{\mathrm{ME}}_{k+1} = e_{k} + \frac{1}{2}\left(\Delta e1 + \Delta e2\right) \tag{6. 49}$$

$$S^{\mathrm{ME}}_{r\ k+1} = S_{r\ k} + \frac{1}{2}\left(\Delta S_r\ 1 + \Delta S_r\ 2\right) \tag{6. 50}$$

with *ME* indicating the current numerical scheme employed in updating the state variables (i.e. Modified Euler method).

Note, finally, that for the elastic case, the update of the state variables employing the modified Euler method is practically the same as that just shown for the elasto-plastic cases and it is not repeated here.

6.5. Drift correction

In general, when integrating the stress-strain relationships of standard elasto-plastic models, the stresses may diverge from the imposed yield condition (i.e. *F=0*). Several approaches are possible to address this problem, typically known as yield surface drift correction. The alternative adopted here is based on the work presented by Potts and Gens (1985) who after analysing different methods to project back the stress state to the yield surface, recommended an optimal drift correction approach assuming no changes of the total strains.

6.5.1. Problem under consideration

Figure 6-4 illustrates the problem under consideration. From a given initial state *A* lying on the yield surface, an increment of load is considered causing elasto-plastic yielding from *A* to *B*. As yielding takes place, the position of the yield surface changes from F_A to F_B (Figure 6-4). Due to the tendency to drift, the predicted (generalised) stress state at *B* does not necessarily lie on this new yield surface (Potts and Gens, 1985). The stress state should then be corrected to effectively be on the yield surface (*C* in Figure 6-4).

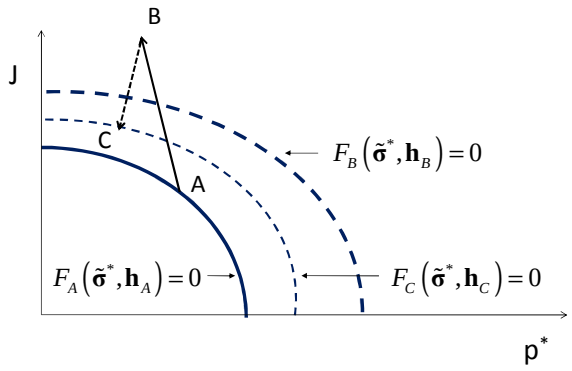

Figure 6- 4 Illustration of the yield surface drift correction (after Potts and Gens, 1985).

As described within previous chapters, the constitutive model employed in this research uses two separate elasto-plastic mechanisms. One is related to yielding on the *LC* yield surface and accounts for elasto-plastic changes of strains, and the other one, is associated with yielding on the *SD/SI* and accounts for irreversible changes of the degree of saturation. There is also the possibility to have both types of plastic behaviour occurring simultaneously. The following description of application of the optimal drift correction method proposed in Potts and Gens (1985) is subdivided into these possible cases.

6.5.2. Yielding on only one yield surface

This section is intended to describe the application of the drift correction method of Potts and Gens (1985) to the elasto-plastic model presented in Chapter 5, when yielding on only one yield surface is taking place.

A key issue of the proposed method is to consider that during the projection back of the (generalised) stresses to the yield surface, an associated change in the elastic (generalised) strains takes place. This leads to:

$$\Delta\tilde{\boldsymbol{\varepsilon}}^{e} = \left(\mathbf{D}_{\mathbf{e}}^{*}\right)^{-1}\left(\tilde{\boldsymbol{\sigma}}_{C}^{*} - \tilde{\boldsymbol{\sigma}}_{B}^{*}\right) \qquad (6.\ 51)$$

where $\tilde{\boldsymbol{\sigma}}_{B}^{*}$ and $\tilde{\boldsymbol{\sigma}}_{C}^{*}$ are, respectively, the generalised stress to be corrected and the corrected generalised stress (see Figure 6-4). The assumption of no changes in the total generalised strains during the correction process implies that the elastic (generalised) strain change must be balanced by an equal and opposite change in the plastic (generalised) strains (Potts and Gens, 1985). Assuming that the elasto-plastic mechanism active is yielding on the *LC* yield surface alone:

$$\Delta\tilde{\boldsymbol{\varepsilon}}_{LC}^{total} = 0 \Rightarrow \Delta\tilde{\boldsymbol{\varepsilon}}_{LC}^{e} = -\Delta\tilde{\boldsymbol{\varepsilon}}_{LC}^{p} \qquad (6.\ 52)$$

where the subscript *LC* indicates the plastic mechanism considered. This is important because the last component of the generalised strain increment vector is the decrement of degree of saturation which is zero for this particular case. Indeed, as yielding on the *LC* yield surface alone is assumed, no plastic variations of S_r are possible in applying (6.52) there will be no changes of S_r from *B* to *C* (see Figure 6.4). This leads to no changes of the modified suction during the projection back, as discussed later.

The (generalised) plastic strain increments are proportional to the gradient of the plastic potential. In particular, for the case analysed here (associated plasticity), the plastic strain increments are proportional to the gradient of the *LC* yield surface (see flow rule definition in Section 5.2.).

$$\Delta\tilde{\boldsymbol{\varepsilon}}_{LC}^{p} = \alpha^{LC}\mathbf{m}_{LC} \qquad (6.\ 53)$$

where α^{LC} is the unknown scalar quantity and $\boldsymbol{m}_{\mathrm{LC}}$ is the same generalised vector introduced in (5.12) when defining the flow rules (see also Section 6.2). Combining (6.51) with (6.52) and (6.53) the following equation expressing the corrected generalised stress is obtained:

$$\tilde{\boldsymbol{\sigma}}_C^* = \tilde{\boldsymbol{\sigma}}_B^* - \alpha^{LC}\mathbf{D}_e^*\mathbf{m}_{LC} \qquad (6.54)$$

It is important to emphasise that in (6.54) only the terms of the generalised stress tensor related to Bishop's stresses are corrected, with no changes of the modified suction term. As a result, the increments of degree of saturation are not modified during this drift correction scheme when yielding on the *LC* yield surface alone.

As a consequence of the occurrence of plastic generalised strains, the position of the yield surfaces changes. This can be written as:

$$\mathbf{h}_C = \mathbf{h}_B + \Delta\mathbf{h} = \mathbf{h}_B + \Delta\boldsymbol{\alpha}_j^T\bar{\mathbf{B}} \quad \text{with} \quad \mathrm{j} = LC, \beta, LC+\beta \text{ where } \beta = SD/SI \qquad (6.55)$$

Considering now that yielding on the *LC* yield surface takes place (i.e. *j=LC*):

$$\Delta\boldsymbol{\alpha}_{LC}^T = \begin{pmatrix} \alpha^{LC} & 0 \end{pmatrix} \qquad (6.56)$$

Imposing that the corrected (generalised) stress state is on the *LC* yield surface:

$$F_{LC}\left(\tilde{\boldsymbol{\sigma}}_C^*, \mathbf{h}_C\right) = 0 \qquad (6.57)$$

Finally, expanding Taylor's series and neglecting second order terms, the following expression for the scalar quantity α^{LC} can be found:

$$\alpha^{LC} = \frac{F_{LC}\left(\tilde{\boldsymbol{\sigma}}_B^*, \mathbf{h}_B\right)}{h_{LC}} \qquad (6.58)$$

where the scalar quantity h_{LC} was already introduced in Chapter 5 when finding an expression for the plastic multiplier for yielding on the *LC* yield surface alone and it takes the form shown in Appendix A.2.

The formulation of this method requires the specification of a tolerance (indicated as *TOL2*). This value is used to control the accuracy of the given solution after the drift correction. In other words, *TOL2* indicates the proximity of the stress state to the yield surface.

Drift correction during yielding on the *SD* or *SI* yield surface alone has an equivalent formulation to the one just presented (except from the fact that yielding is taking place on F_β instead of F_{LC} where *β=SD* or *SI*) and the procedure will not be repeated here. However, simultaneous yielding on the *LC* and *SD* yield surfaces leads to some

substantial differences in the drift correction procedure and it has been considered appropriate to include this latter case in a separate section.

6.5.3. Simultaneous yielding on the LC and SD or SI yield surfaces

The same assumption given by (6.51) is applied here, combined with:

$$\Delta\tilde{\boldsymbol{\varepsilon}}^{total} = 0 \Rightarrow \Delta\tilde{\boldsymbol{\varepsilon}}^{e} = -\Delta\tilde{\boldsymbol{\varepsilon}}^{p} \qquad (6.59)$$

Note that now the expression for the generalised strain increments (6.59) includes both plastic strain increments and plastic decrements of the degree of saturation. This is because the case analysed involves simultaneous yielding on two yield surfaces.

The (generalised) plastic strain increments are proportional to the gradient of the pertinent yield surface according to:

$$\Delta\tilde{\boldsymbol{\varepsilon}}^{p}_{LC} = \alpha_{LC}^{LC+\beta}\mathbf{m}_{LC} \qquad (6.60)$$

$$\Delta\tilde{\boldsymbol{\varepsilon}}^{p}_{\beta} = \alpha_{\beta}^{LC+\beta}\mathbf{m}_{\beta} \qquad (6.61)$$

where $\alpha_{LC}{}^{LC+\beta}$ and $\alpha_{\beta}{}^{LC+\beta}$ are the two unknown scalar quantities. Combining (6.51) and (6.59) with (6.60) and (6.61) the following equation expressing the corrected generalised stress is obtained:

$$\tilde{\boldsymbol{\sigma}}^{*}_{C} = \tilde{\boldsymbol{\sigma}}^{*}_{B} - \mathbf{D}^{*}_{\mathbf{e}}\left(\alpha_{LC}^{LC+\beta}\mathbf{m}_{LC} + \alpha_{\beta}^{LC+\beta}\mathbf{m}_{\beta}\right) \qquad (6.62)$$

Note that in here, all terms of the generalised stress tensor are corrected. This involves, those terms related to the Bishop's stress tensor and those associated with modified suction (because of the occurrence of irreversible changes of both strains and degree of saturation).

As in the previous case described, there will be also a variation of the position of the yield surfaces during drift correction, given by the same equation (6.55) with:

$$\Delta\boldsymbol{\alpha}^{T}_{LC+\beta} = \begin{pmatrix} \alpha_{LC}^{LC+\beta} & \alpha_{\beta}^{LC+\beta} \end{pmatrix} \qquad (6.63)$$

Imposing that the corrected (generalised) stress state is on the *LC* yield surface and also on the *SD/SI* yield surface:

$$F_{LC}\left(\tilde{\boldsymbol{\sigma}}^{*}_{C}, \mathbf{h}_{C}\right) = 0 \qquad (6.64)$$

$$F_\beta\left(\tilde{\boldsymbol{\sigma}}_C^*, \mathbf{h}_C\right) = 0 \qquad (6.\ 65)$$

Expanding Taylor's series in both yield surfaces and neglecting second order terms, the following system of equations is obtained:

$$F_{LC}\left(\tilde{\boldsymbol{\sigma}}_C^*, \mathbf{h}_C\right) \approx F_{LC}\left(\tilde{\boldsymbol{\sigma}}_B^*, \mathbf{h}_B\right) + \mathbf{m}_{LC}^T \delta\tilde{\boldsymbol{\sigma}}^* + \frac{\partial F_{LC}}{\partial p_0^*}\delta p_0^* \qquad (6.\ 66)$$

$$F_\beta\left(\tilde{\boldsymbol{\sigma}}_C^*, \mathbf{h}_C\right) \approx F_\beta\left(\tilde{\boldsymbol{\sigma}}_B^*, \mathbf{h}_B\right) + \mathbf{m}_\beta^T \delta\tilde{\boldsymbol{\sigma}}^* + \frac{\partial F_\beta}{\partial s_\beta^*}\delta s_\beta^* \qquad (6.\ 67)$$

From where, after some algebra, it is possible to find an expression for each scalar quantity:

$$\alpha_{LC}^{LC+\beta} = \frac{a_1 F_{LC}\left(\tilde{\boldsymbol{\sigma}}_B^*, \mathbf{h}_B\right) + a_2 F_\beta\left(\tilde{\boldsymbol{\sigma}}_B^*, \mathbf{h}_B\right)}{h_{LC+\beta}} \qquad (6.\ 68)$$

$$\alpha_\beta^{LC+\beta} = \frac{a_3 F_{LC}\left(\tilde{\boldsymbol{\sigma}}_B^*, \mathbf{h}_B\right) + a_4 F_\beta\left(\tilde{\boldsymbol{\sigma}}_B^*, \mathbf{h}_B\right)}{h_{LC+\beta}} \qquad (6.\ 69)$$

where the scalar quantity $h_{LC+\beta}$ was already introduced in Chapter 5 when finding an expression for the plastic multiplier for simultaneous yielding on the *LC* and *SD* yield surfaces and it takes the form shown in Appendix A.2. Also the complete expressions for the scalar quantities a_1, a_2, a_3 and a_4 are detailed in Appendix A.2.

6.6. Analysis and verification

Because of the complexity on the mathematical expressions associated with the 3D extended version of the Wheeler et al. (2003) constitutive model, it has been considered appropriate to check if the predicted model response was obtained when using the strain-driver algorithmic formulation presented in Section 6.4. In order to do this, two complementary analyses are presented in this final part of the chapter. Both of them were intended to study the response of the algorithmic formulation. The first analysis is a very basic check on the computed response at critical states. This is to confirm whether the computed solution shows the results predicted by the model for critical states involving simultaneous yielding on *LC* and *SD* surfaces, with the final states falling on the two planar surfaces in v:lnp^*:lns^* and S_r: lnp^*:lns^* spaces presented in Section 4.4. The second part of this analysis focuses on the comparison between the two explicit strain-driver algorithms presented (i.e. forward Euler and modified Euler). The plots shown within this

second part satisfactorily illustrate that, when using the algorithms presented in this chapter, the forward Euler method gives a first order error approximation and the modified Euler gives a second order approximation for the computed values of e and S_r.

6.6.1. Computed and predicted critical state relationships during simultaneous yielding on the LC and SD yield surfaces

The predicted normal compression relationships developed in Chapter 2, were used in the second part of Chapter 3 to see whether the model computations under isotropic stress conditions reproduced the predicted behaviour of the constitutive model when yielding simultaneously on the *LC* and *SD* yield surfaces. Following that analysis, a possible way to partially verify that the equations presented in Chapter 6 have been correctly implemented within the algorithm is to extend the analysis from isotropic stress conditions to critical states. This extension of the analysis to critical states is presented in this section and it is essentially aimed at checking if the computed critical states fall on a planar critical state surface (of gradients λ^* and k_2^*) in v:lnp^*:lns^* space and on a second planar surface (of gradients λ_s^* and k_1^*) in S_r:lnp^*:lns^* space (see Chapter 4). Using the strain-driver algorithms presented in Section 6.4, the tests sheared at constant volume on samples of speswhite kaolin (Sivakumar, 1993) described in Section 2.7.3 are simulated in this current Section 6.6.1. Then, by plotting the critical states of these modelled tests in the v:lnp^*:lns^* and S_r:lnp^*:lns^* spaces it is easy to see whether the values of λ^*, k_2^*, λ_s^* and k_1^* estimated from these computed critical states are as those expected.

Note that from the sixteen tests used in Chapter 4 to validate the critical state relationships proposed, only those involving shearing under constant volume (i.e. noted as Type A) are used here. This is because tests sheared at constant volume can be easily modelled employing the strain-driver algorithm presented in the previous sections (as they can be simulated directly using increments of strains $\Delta\boldsymbol{\varepsilon}$ and increments of matric suction Δs as known inputs). Figure 6-5 shows the stress paths of the tests simulated. The six tests employed are: 2A, 3A, 4A and 5A (all at a constant suction of 200 kPa), 10A (at a constant suction of 100 kPa) and 15A (at a suction of 300 kPa). The same initial state and model parameters as used for the computations under isotropic stress conditions are also adopted here (see also Table 6.1). Shearing starts at the final stages of the normal compression tests as illustrated in Figure 6-5.

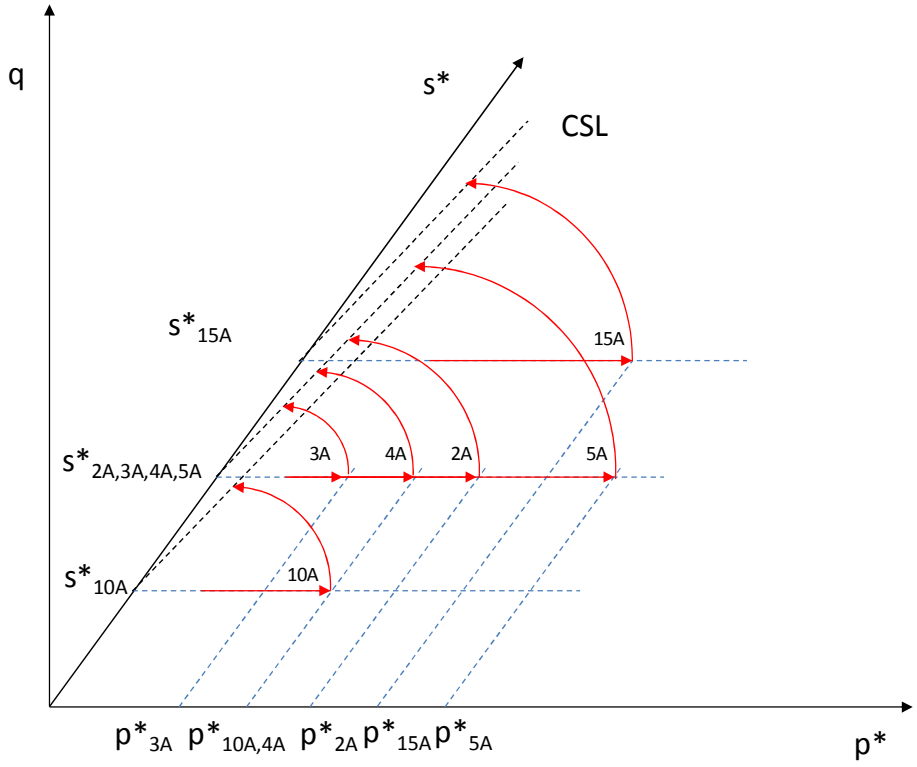

Figure 6- 5 Stress paths analysed in the computations.

Table 6. 1 Parameters, initial state and strain and suction increments used in the computations.

κ=0.006	λ=0.124	λ_s=0.0971	κ_s=0.0004	k_1=0.685	k_2=0.773	M=0.72	υ^1=0.3
p^*=229kPa	s^*=164kPa	p_0^*=271kPa	s_D^*=164kPa	e=1.210	S_r=0.597		
$\Delta\varepsilon_1=10^{-05}$	$\Delta\varepsilon_2$= -5·10^{-06}	$\Delta\varepsilon_3$= -5·10^{-06}	$\Delta\varepsilon_4=\Delta\varepsilon_5=\Delta\varepsilon_6$=0	Δs=0.0	TOL1<10^{-07};TOL2<10^{-07}		
λ^*=0.257	k^*_1=0.172	λ^*_s=0.206	k^*_2=0.159				

[1]*Poisson's ratio*

Figures 6-6 and 6-7 represent a pair of orthogonal two-dimensional views of the two planar surfaces at critical states presented in Chapter 4. For example, (Figure 6-6a) shows $(v-k_1^* lns^*)$ plotted against lnp^* and (Figure 6-6b) shows $(v+\lambda^* lnp^*)$ plotted against lns^*. In both of these plots presented in Figure 6-6, the planar surface for v has been reduced to a single straight line (of gradients λ^* and k_1^* respectively), and it is easy to check that, as expected, the computed critical states lie on this planar surface. Similarly, Figure 6-7 illustrates the computed critical states results of the water retention response. It is also observed that, as predicted by the model, all critical states computed lie on a straight line of slope λ_s^* when plotting such states in the $(S_r-k_2^* lnp^*):lns^*$ plane (Figure 6-7a) and on a second straight line of slope k_2^* when plotting the same results in the $(S_r+\lambda_s^* lns^*):lnp^*$ plane (Figure 6-7b). Similarly to the comments made on Figure 6-6, the

straight lines observed in Figure 6-7, represent a pair of orthogonal two-dimensional views of the planar surface at critical states for S_r (see Chapter 4 for further details).

The fact that in both figures (Figure 6-6 and Figure 6-7) all critical states of the tests modelled (represented as symbols in the plotts) fall on both planar surfaces presented in Section 4.4 is a significant component of verification of the mathematical expressions implemented in the algorithm.

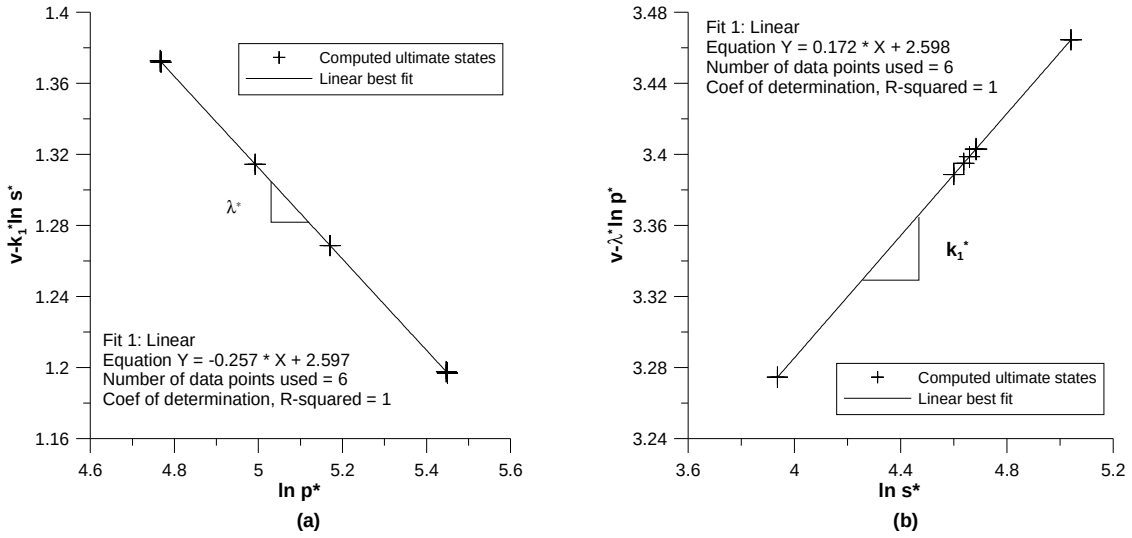

Figure 6- 6 Orthogonal two-dimensional views of planar surface for v at critical states with computed results.

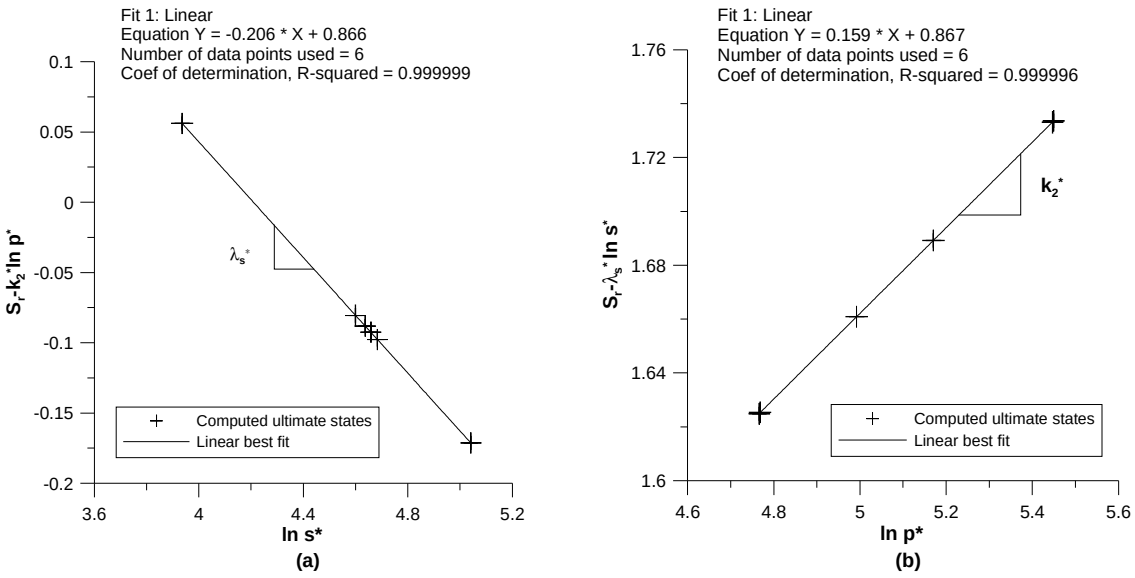

Figure 6- 7 Orthogonal two-dimensional views planar surface for S_r at critical states with computed results.

The following table is intended to summarise some relevant information of the computed solution. The estimated values of the gradients for the two critical state surfaces shown (see Table 6.2) have been calculated using the least-squares method implemented in the

software GRAPHER (www.goldensoftware) for the critical states of the six tests analysed. These values can be then compared with the theoretical ones (calculated from the input parameter values, see Section 2.7.2) to have an estimation of the error made in the computations. Also the coefficient of determination R^2 is included in this table.

Table 6. 2 Comparison between theoretical an estimated gradients of the critical state planar surfaces.

Soil parameter	***Theoretical value***	***Back-calculated value***	***Coefficient of determination R^2***
λ^*	*0.257*	*0.257*	*1.00000*
k_1^*	*0.172*	*0.172*	*1.00000*
λ_s^*	*0.206*	*0.206*	*0.99999*
k_2^*	*0.159*	*0.159*	*0.99996*

All the information illustrated and discussed above, consistently suggests that the mathematical equations of the constitutive model presented in this Chapter 6 have been correctly implemented within the strain-driver algorithm. The next step is to study and compare the computed response when using the forward Euler and the modified Euler algorithms presented. This discussion is given in the following sections.

6.6.2. Comparison between forward Euler and modified Euler methods

This section shows that, when using the forward Euler scheme with the constitutive model introduced in Chapter 5, the error achieved in the computations for e and S_r corresponds to a first order approximation; whereas the approximated solution when employing the modified Euler scheme, gives a second order error. This is illustrated when plotting the error of the approximated solution (on a logarithmic scale) against the number of steps (again on a logarithmic scale). When presenting the results in this way (i.e. a log-log plot of relative error *vs.* number of steps) a straight line of gradient -1 is observed for the first order algorithm and a second straight line of gradient -2 is observed for the second order algorithm.

Figure 6-8 illustrates the stress paths considered in the analysis. *ABCDEF* in Figure 6-8 is an isotropic loading stress path at constant suction. From *F* shearing at constant volume (and constant suction) is applied until *G* (Figure 6-8b). In the analysis presented below, the relative errors presented are those for void ratio e and degree of saturation S_r at *B, D, F* and *G* (see Figures 6-8).

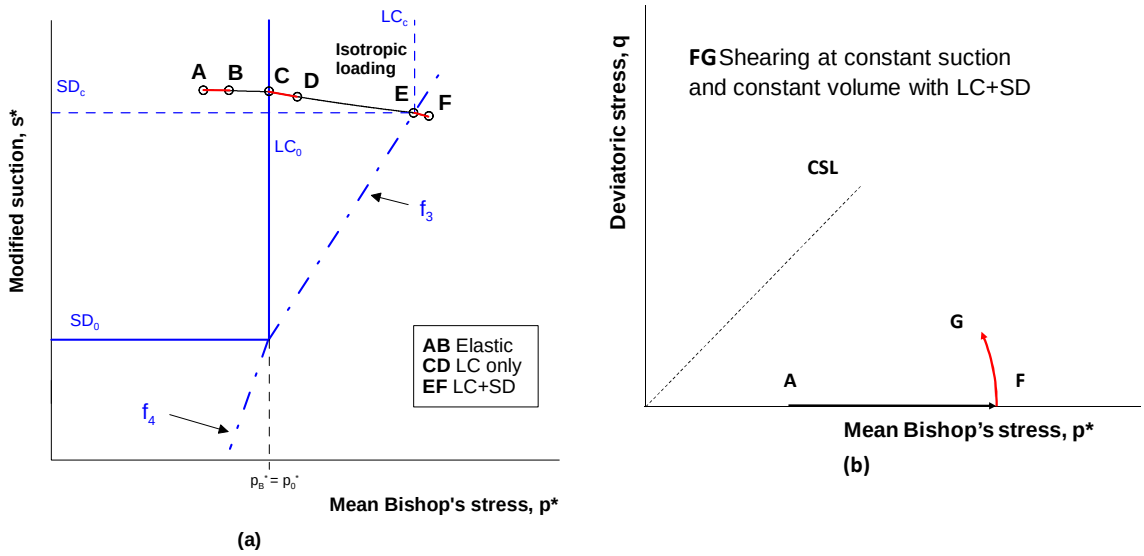

Figure 6- 8 Constant suction isotropic loading followed by shearing at constant suction and constant volume.

The following table summarises the model parameter values and the initial state used in the computations. *TOL1* is the tolerance used in the algorithm for the intersection/s of the stress path with the appropriate surface(s) and *TOL2* is the tolerance used in the drift correction scheme (see Sections 6.4 and 6.5).

Table 6. 3 Model parameters and initial state used in the computations.

κ=0.02	λ=0.15	λ_s=0.12	κ_s=0.02	k_1=0.7	k_2=0.8	M=0.77	ν^1=0.3
$\overline{p}$ =10kPa	s=200kPa	p_0^*=200kPa	s_D^*=70kPa	e=1.2	S_r=0.65		
TOL1<10^{-10}; TOL2<10^{-10}							
λ^*=0.315	k_1^*=0.206	λ_s^*=0.247	k_2^*=0.181				

[1] *Poisson's ratio*

Using the strain-driver formulations presented in Section 6.4 (i.e. forward Euler and modified Euler) with a particular step size for Δs and $\Delta\boldsymbol{\varepsilon}$ it is possible to study the relative error for void ratio e and degree of saturation S_r made in the computations when changing the initial state from *A* to *B*, *D*, *F* and *G* (see Figure 6-8). In the analysis presented here, this particular strain step size (suction remains constant) is used for a specified number of times (i.e. number of steps) to reproduce the correct length of the stress path analysed (i.e. *AB*, *CD*, *EF* and *FG* all starting at *A*, see Figure 6-8). This procedure can be employed using a higher number of steps while decreasing, appropriately, the size of the strain step (in order to keep the same length of the stress path analysed).

The corresponding computed values of void ratio *e* and degree of saturation S_r at *B*, *D*, *F* and *G* can then be compared with an appropriate reference value (see Equation (6.70)) to quantify the error made in *e* and S_r. As further detailed below, this information can be combined with different number of steps to study the error variations with the number of steps used.

There are several ways to calculate the error made in the computations. Here, however, only the relative error is used, defined as:

$$\text{Relative error}=\frac{\left|\text{computed value-analytical or reference value}\right|}{\text{analytical or reference value}} \qquad (6.70)$$

In many cases it is difficult to find analytical values of the variables being considered. A standard alternative procedure is to consider, as a sufficiently accurate reference value, the computed result obtained when employing a very small step size (i.e. very high number of steps). This methodology has been used here and is extended below organising the discussion according to the model response, covering (under isotropic stress states): elastic (*AB* in Figure 6-8a), yielding on the *LC* yield surface alone (*CD* in Figure 6-8a), and simultaneous yielding on the *LC* and *SD* yield surfaces (*EF* in Figure 6-8a). Also simultaneous yielding on the *LC* and *SD* yield surfaces during shearing at constant suction and constant volume has been analysed (*FG* in Figure 6-8b).

6.6.2.1. Elastic case

As mentioned above, the result from a very smooth computed approximation of the void ratio and degree of saturation at *B* (see Figure 6-8a) has been used as the reference value in (6.70). This reference value has been calculated using a very small strain step of 10^{-09}. A possible way to ensure that the step size is sufficiently small is to consider the following. As from *A* to *B* only elastic behaviour takes place, these initial and final states should satisfy (see Section 2.6 for more details):

$$e_B - e_A + \kappa \ln\left(\frac{p_B^*}{p_A^*}\right) = 0 \qquad (6.71)$$

$$S_{rB} - S_{rA} + \kappa_s \ln\left(\frac{s_B^*}{s_A^*}\right) = 0 \qquad (6.72)$$

where the values of the variables at *A* correspond to the initial state and the values at *B* are those calculated from the second order error strain-driver algorithm using the very

small step size. With a strain step size of 10^{-09}, the resulting values in equations (6.71) and (6.72) were at least an order of magnitude less than the smallest value obtained using the other step sizes used in the analysis and this justified the use of 10^{-09} for computing reference values of e and S_r at point B.

6.6.2.2. Yielding on the LC yield surface alone

As in the previous case, it was not possible to easily calculate exact analytical values of void ratio and degree of saturation at D (see Figure 6-8). The same methodology is used here to give reference values of void ratio and degree of saturation at D by using the second order error strain-driver algorithm with very small strain increments. From C to D (see Figure 6-8) only yielding on the LC surface takes place, and therefore these states should satisfy (see Section 2.6 for more details):

$$e_D - e_C + \lambda \ln\left(\frac{p_D^*}{p_C^*}\right) = 0 \qquad (6.73)$$

$$S_{rD} - S_{rC} + \kappa_s \ln\left(\frac{s_D^*}{s_C^*}\right) = 0 \qquad (6.74)$$

where the values of the variables at C are taken from the previous section (i.e. elastic case) and the values at D are those calculated from the appropriate strain-driver algorithm using the very small step size. With a strain increment size of 10^{-09}, the resulting values in equations (6.73) and (6.74) was at least an order of magnitude less than the smallest value obtained using the other step sizes used in the analyses, and this justified the use of a strain increment size of 10^{-09} for computing reference values of e and S_r at point D.

6.6.2.3. Simultaneous yielding on the LC and SD yield surfaces

Equivalently to the previous two cases presented, it was not possible to calculate exact analytical values of void ratio and degree of saturation at F (see Figure 6-8). The same approach was also used in this section to give a sufficiently precise approximation of the state variables at F in order to use as reference values. From E to F simultaneous yielding on the SD and LC yield surfaces takes place, and therefore these states should satisfy (see Section 2.7 for further details):

$$e_F - e_E + \lambda^* \ln\left(\frac{p_F^*}{p_E^*}\right) - k_1^* \ln\left(\frac{s_F^*}{s_E^*}\right) = 0 \qquad (6.75)$$

$$S_{rF} - S_{rE} - \lambda_s^* \ln\left(\frac{s_F^*}{s_E^*}\right) + k_2^* \ln\left(\frac{p_F^*}{p_E^*}\right) = 0 \qquad (6.\ 76)$$

where the values of the variables at *E* and *F* are those calculated with the second order error strain-driver algorithm using the very small step size. For this particular case, when using a strain step size of 10^{-09} equations (6.75) and (6.76) give, in both cases, values that were at least an order of magnitude smaller than the equivalent values obtained when using the other step sizes employed in the analyses.

Note that simultaneous yielding on the *LC* and *SD* yield surfaces is also active during shearing at constant suction and constant volume (*FG* in Figure 6-8b) the same methodology described in this section can be used to estimate the relative error of the degree of saturation (void ratio changes are zero from *F* to *G* and, therefore, the relative error obtained for *e* at *G* would be the same as the relative error of *e* approximated at *F*).

6.6.2.4. Discussion of the error for each plastic mechanism including the elastic case

Figures 6-9 and 6-10 show the relative error associated with both numerical schemes when considering the computed values of void ratio and degree of saturation at *B*, *D*, *F* and *G*. As the length of the strain path is previously specified (by fixing the final state analysed *B*, *D*, *F* and *G*) and sizes of strain steps are fixed for all cases (see Tables 6.4 and 6.5), it is possible to make a direct comparison between the different model responses. The following paragraphs describe how the data points plotted in these figures are obtained while highlighting the main results observed in both Figures 6-9 and 6-10.

For example, for the elastic isotropic loading analysed (*AB* in Figure 6-8) the length of the strain path is specified by fixing the final state *B*. When using the strain-driver algorithms presented in Section 6.4, ten steps are necessary to change the initial state from *A* to *B* if employing a fixed strain increment size of 10^{-04} (i.e. $\Delta\varepsilon_1=\Delta\varepsilon_2=\Delta\varepsilon_3=10^{-04}$). When using a smaller strain increment size of 10^{-05}, 100 steps are needed to reach *B*, and 1000 steps with a strain increment size of 10^{-06}. Thus, using the strain-driver algorithms for each of these three strain increment sizes (with their corresponding number of steps 10, 100 and 1000) gave three values of the void ratio and degree of saturation at *B*. Then, combining these three values of void ratio (and degree of saturation) with (6.70) and the appropriate reference value (see Section 6.2.2.1), three different values of the relative error for *e* and three different values of the relative error for S_r (involving elastic behaviour under isotropic stress states) were obtained. These three different values of relative error for *e* and for S_r, along with their corresponding number of steps, gave the three data points plotted in

Figure 6-9 when using the forward Euler scheme. Another three data points of the relative error for *e* were obtained (see Figure 6-9) when using the modified Euler scheme. An equivalent procedure was used for S_r (see Figure 6-10).

As expected, the relative error for *e* and S_r is lower when using the modified Euler scheme than when using the forward Euler algorithm (see Figures 6-9 and 6-10). It is also illustrated in these figures that the decrease of the relative error for *e* and S_r when increasing the number of steps is also faster when using the second order error scheme (showing a gradient of -2) than when employing the first order scheme (showing a gradient of -1). This general behaviour is observed for all cases (see Figures 6-9 and 6-10). For this particular (elastic) case, it is important to ensure that the model response is elastic during all strain path analysed. This implies ensuring that along the stress path *AB* no yield surface is reached.

An equivalent analysis has been used for the rest of the cases. For instance, when yielding on the *LC* yield surface alone is active 10, 100 and 1000 steps were considered from *C* to *D* (see Figure 6-8); employing, respectively, an isotropic strain step size (i.e. $\Delta\varepsilon_1=\Delta\varepsilon_2=\Delta\varepsilon_3$) of 10^{-04}, 10^{-05} and 10^{-06} (see Tables 6.4 and 6.5). Ensuring, previously, that these step sizes (with their corresponding number of steps 10, 100 and 1000 respectively) were not sufficient to reach the corner at *E* (i.e. only yielding on the *LC* yield surface was active during the isotropic loading stress path *CD* shown in Figure 6-8a). Similarly for simultaneous yielding on the *SD* and *LC* yield surfaces under isotropic stress conditions (*EF*, see Figure 6-8a) and simultaneous yielding on the *SD* and *LC* yield surfaces under shearing at constant suction and constant volume (*FG* in Figure 6-8b). For the latter case of simultaneous yielding under shearing, however, different strain input increments were used. In order to get zero volumetric strain variations, the strain increments used were $\Delta\varepsilon_2=\Delta\varepsilon_3=(-\Delta\varepsilon_1/2)$ where $\Delta\varepsilon_1$ took different values (i.e. 10^{-04}, 10^{-05} and 10^{-06}) corresponding to each number of steps employed (i.e. 10, 100 and 1000, respectively). More details of the information illustrated in Figures 6-9 and 6-10 is summarised in Tables 6.4 and 6.5.

Overall, the variations of the relative errors with number of steps for the two strain-driver algorithms used, followed the expected patterns when plotting the results in the log-log plot of relative error *vs*. number of steps. For all cases presented, Figures 6-9 and 6-10 show a gradient of approximately -1 when using the first order error forward Euler method and -2 when employing the second order error modified Euler scheme. Also as expected, the results plotted in these figures showed an increase of the relative errors for a given step size when also increasing the complexity of the equations being integrated; giving lower values of the error for elastic behaviour than for elasto-plastic behaviour. This was

also due to the fact that points *D*, *F* and *G* already included all the other preceding relative errors as all the computations started at point *A*; and it was, therefore, highly likely to observe largest relative errors after *B*. Moreover, the increase of complexity observed when solving the Bishop's stress-strain and modified suction-degree of saturation relationships for simultaneous yielding on the *LC* and *SD* yield surfaces (see also Section 5.3), is also reflected when comparing the relative errors obtained with those involving only one plastic mechanism active. In general, then, these figures showed that the relative error for *e* and S_r, for a given step size, are smallest for the elastic case, then for the case of yielding on one yield surface alone and largest for the case involving yielding on two yield surfaces (confirming expected behaviour that relative errors increase as the complexity of the problem increases). All this information suggests that both strain-driver algorithms have been correctly implemented.

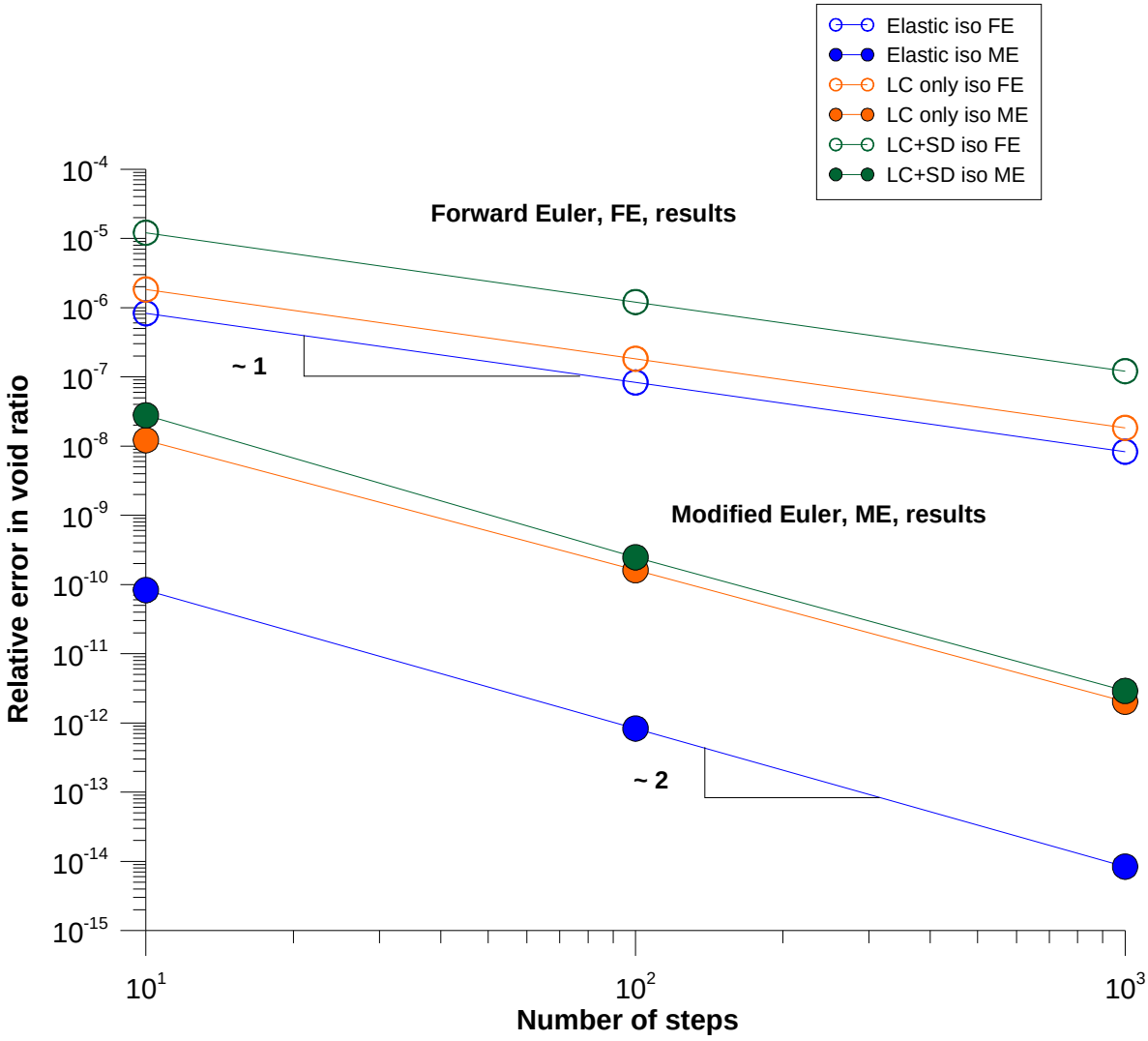

Figure 6- 9 Comparison of the relative error in void ratio associated with different model responses.

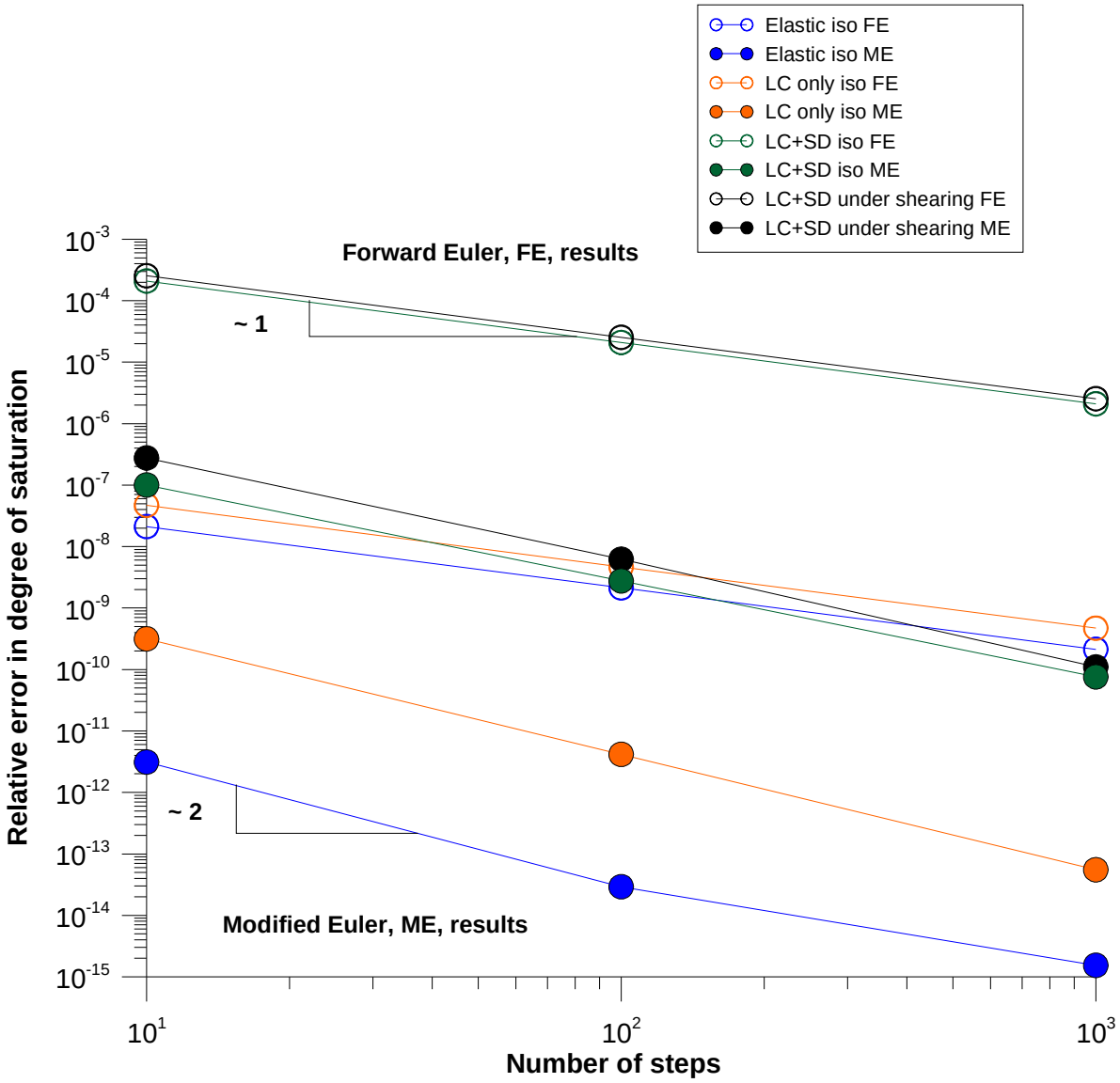

Figure 6- 10 Comparison of the relative error in degree of saturation associated with different model responses.

Table 6. 4 Forward Euler results for isotropic loading and shearing at constant suction and constant volume.

		Elastic		***LC only***		***LC and SD under isotropic stress***		***LC and SD under shearing***
Strain increment ($\Delta\varepsilon_1$)	***Num. of steps***	***Relative error e***	***Relative error S_r***	***Relative error e***	***Relative error S_r***	***Relative error e***	***Relative error S_r***	***Relative error S_r***
10^{-04}	10	$8{\cdot}10^{-07}$	$2{\cdot}10^{-08}$	$2{\cdot}10^{-06}$	$5{\cdot}10^{-08}$	$1{\cdot}10^{-05}$	$2{\cdot}10^{-04}$	$2.5{\cdot}10^{-04}$
10^{-05}	100	$8{\cdot}10^{-08}$	$2{\cdot}10^{-09}$	$2{\cdot}10^{-07}$	$5{\cdot}10^{-09}$	$1{\cdot}10^{-06}$	$2{\cdot}10^{-05}$	$2.5{\cdot}10^{-05}$
10^{-06}	1000	$8{\cdot}10^{-09}$	$2{\cdot}10^{-10}$	$2{\cdot}10^{-08}$	$5{\cdot}10^{-10}$	$1{\cdot}10^{-07}$	$2{\cdot}10^{-06}$	$2.5{\cdot}10^{-06}$

Table 6. 5 Modified Euler results for isotropic loading and shearing at constant suction and constant volume.

		Elastic		**LC only**		**LC and SD under isotropic stress**		**LC and SD under shearing**
Strain increment ($\Delta\varepsilon_1$)	**Num. of steps**	**Relative error e**	**Relative error S_r**	**Relative error e**	**Relative error S_r**	**Relative error e**	**Relative error S_r**	**Relative error S_r**
10^{-04}	10	$8{\cdot}10^{-11}$	$3{\cdot}10^{-12}$	$1{\cdot}10^{-08}$	$3{\cdot}10^{-10}$	$3{\cdot}10^{-08}$	$3{\cdot}10^{-07}$	$1{\cdot}10^{-07}$
10^{-05}	100	$8{\cdot}10^{-13}$	$3{\cdot}10^{-14}$	$2{\cdot}10^{-10}$	$4{\cdot}10^{-12}$	$2{\cdot}10^{-10}$	$6{\cdot}10^{-09}$	$3{\cdot}10^{-09}$
10^{-06}	1000	$8{\cdot}10^{-15}$	$1.5{\cdot}10^{-15}$	$2{\cdot}10^{-12}$	$5.5{\cdot}10^{-14}$	$3{\cdot}10^{-12}$	$1{\cdot}10^{-10}$	$8{\cdot}10^{-11}$

Chapter 7

NUMERICAL IMPLEMENTATION OF THE COUPLED CONSTITUTIVE MODEL INTO CODE_BRIGHT

7. Numerical implementation of the coupled constitutive model into CODE_BRIGHT

Two strain-driver algorithms to integrate the generalised stress-strain relationships of the 3D extended constitutive model of Wheeler et al. (2003) were proposed in Chapter 6. Several computational aspects were discussed at the end of the chapter, concluding that the results obtained using the algorithmic formulation were satisfactory. This current Chapter 7 is aimed at including this strain-driver formulation into the existing finite element program CODE_BRIGHT (Olivella et al., 1996). A brief introduction of this computer code is given first, including a general description of the main governing equations considered in the mathematical formulation adopted to develop the code (Olivella et al., 1994). In order to implement the strain-driver algorithm, some aspects of the finite element program have been extended to adapt the new strain-driver scheme. This extension is also detailed when describing the governing equations. The final part of the chapter analyses the performance of this implementation first on a test case that could be compared with equivalent results obtained directly from the strain-driver algorithm and then on a simple boundary value problem.

7.1. Introduction to the finite element program CODE_BRIGHT

CODE_BRIGHT is an existing finite element program designed to analyse Thermo-Hydro-Mechanical (*THM*) coupled problems in porous media (Olivella, 1995). The theoretical formulation adopted considers a macroscopic approach based on continuum theory for porous media. In particular, it assumes that the porous medium comprises three phases: solid, liquid and gas. The liquid phase is composed of water and dissolved air, while the gas phase comprises dry air (assumed as a single species) and water vapour. The formulation incorporates basic thermal phenomena (accounting for heat conduction, heat advection and latent heat associated with phase changes), flow (liquid flow and gas flow, including movements of water vapour and dissolved air, and phase changes due to water evaporation/condensation and air dissolution/exsolution) and mechanical effects (describing the dependence of material deformations on stresses, suction/fluid pressures and temperatures) in a coupled way (Sánchez, 2005). The mathematics of this macroscopic approach is expressed in terms of a set of balance equations, a set of constitutive equations and a set of equilibrium restrictions. Table 7.1 summarises these equations. Note that each of them is associated with one variable, as proposed in the original work of Olivella et al. (1994). This association is not unique as each equation is related to several variables. Hence, the variable shown in Table 7.1 should be understood

as the one employed in subsequent derivations. The superior dot indicates temporal variations.

Table 7. 1 Constitutive equations and equilibrium restrictions (Olivella et al.,1994 and 1996).

Equation name		
Balance equations	***Variable name***	***Variable***
Solid mass balance	*Porosity*	n
Water mass balance	*Liquid pressure*	u_l
Air mass balance	*Gas pressure*	u_g
Energy balance	*Temperature*	T
Momentum balance	*Displacements*	$\dot{\mathbf{u}}$
Constitutive equations		
Fick's law (vapour and air)	*Vapour and air non-advective flux*	
Darcy's law (liquid and gas)	*Liquid and gas advective fluxes*	$\mathbf{q_l}$, $\mathbf{q_g}$
Retention curve	*Liquid phase degree of saturation*	S_l^*, S_g
Fourier's law	*Conductive heat flux*	$\mathbf{i_c}$
Mechanical constitutive model	*Stress tensor*	$\boldsymbol{\sigma}$
Liquid density	*Liquid density*	ρ_l
Gas law	*Gas density*	ρ_g
Equilibrium restrictions		
Henry's law	*Air dissolved mass fraction*	w_l^a
Psychrometric law	*Vapour mass fraction*	w_g^w
Constraints		
$\dot{\boldsymbol{\varepsilon}} = \frac{1}{2}\left(\nabla\dot{\mathbf{u}} + \nabla\dot{\mathbf{u}}^{T}\right)$	*Strains (compatibility equation)*	$\dot{\boldsymbol{\varepsilon}}$
$w_l^w + w_l^a = 1$	*Mass fraction of water in the liquid phase*	w_l^w
$w_g^w + w_g^a = 1$	*Mass fraction of air in the gas phase*	w_g^a
$S_l^* + S_g = 1$	*Volumetric fraction of pore volume occupied by gas*	S_g
$\mathbf{i}_l^w + \mathbf{i}_l^a = 0$	*Non-advective mass flux of water in the liquid phase*	$\mathbf{i}_l^w$
$\mathbf{i}_g^w + \mathbf{i}_g^a = 0$	*Non-advective mass flux of air in the gas phase*	$\mathbf{i}_g^a$

*Both notations of liquid phase degree of saturation (i.e. S_r and S_l) are used within the document.

Related to the last paragraph above, an important issue is the choice of state (independent) variables from which all other variables are derived using the constitutive or equilibrium constraints. In particular, the state or independent variables considered within this mathematical framework are: solid velocity $\dot{\mathbf{u}}$, liquid pressure u_l, gas pressure u_g and temperature T (see Olivella et al., 1994 for further details).

As described in Chapter 2, unsaturated soils can be modelled as a three phase porous system composed of gas phase (typically air), liquid phase (typically water) and solid phase (soil grains). Consequently, this macroscopic approach is an adequate framework to study boundary value problems involving the unsaturated soil condition. In particular, it is possible to use CODE_BRIGHT as a framework to include the fully coupled mechanical-water retention constitutive model described in previous chapters of this work. Essentially this required two major inputs in the computer formulation. Firstly, it was necessary to adapt the update of the stresses accordingly with the extended version of the Wheeler et al. (2003) constitutive model (see Chapter 6). Secondly, the water retention behaviour adopted to update the degree of saturation had to be the one proposed within the constitutive model (see Figure 7.1). A major challenge of this implementation is related to the fully coupled Hydro-Mechanical (*HM*) character of the constitutive stresses adopted by this model (see Equations (2.15) and (2.16) in Section 2.6). The following sections are intended to describe the implementation of this advanced constitutive model into CODE_BRIGHT assuming isothermal conditions.

7.2. Balance equations

The compositional approach has been adopted to establish the mass balance equations and it consists of balancing the species (mineral, water and air) instead of balancing phases (solid, liquid and gas). The subscript is used, in the remainder of this chapter, to identify the phase (*s* for solid, *l* for liquid and *g* for gas) and the superscript indicates the species: *w* for water and *a* for air. No symbol is attributed to the mineral species, because it has been assumed that it coincides with the solid phase. The main balance equations are presented below and a more detailed description can be found elsewhere (i.e. Olivella et al., 1994).

7.2.1. Water mass balance equation

$$\frac{\partial}{\partial t}\left(\theta_l^w S_l \mathrm{n} + \theta_g^w S_g \mathrm{n}\right) + \nabla.\left(\mathbf{j}_l^w + \mathbf{j}_g^w\right) = f^w \qquad (7.1)$$

where, n is the porosity, θ^w_l and θ^w_g are the masses of water per unit volume of liquid and gas phase respectively, $\mathbf{j}^w_l$ and $\mathbf{j}^w_g$ denote the total mass fluxes of water in the liquid and gas phases with respect to a fixed reference system, f^w is the external mass supply of water per unit volume of medium and S_α is the volumetric fraction of pore volume occupied by the alpha phase (α=*l,g*). Note that the degree of saturation of the liquid phase is also termed S_r in this work.

7.2.2. Air mass balance equation

$$\frac{\partial}{\partial t}\left(\theta^a_l S_l \mathrm{n} + \theta^a_g S_g \mathrm{n}\right) + \nabla.\left(\mathbf{j}^a_l + \mathbf{j}^a_g\right) = f^a \qquad (7.\ 2)$$

where n is the porosity, θ^a_l and θ^a_g are the masses of air per unit volume of liquid and gas phase respectively, $\mathbf{j}^a_l$ and $\mathbf{j}^a_g$ denote the total mass fluxes of air in the liquid and gas phases with respect to a fixed reference system and f^a is the external mass supply of air per unit volume of medium. Note that dry air is considered as a single species in spite of the fact that it is a mixture of gasses. The gaseous phase is assumed as a mixture of air and water vapour. Air is also dissolved in the liquid phase.

7.2.3. Solid mass balance equation

$$\frac{\partial}{\partial t}\left(\rho_s\left(1-\mathrm{n}\right)\right) + \nabla\cdot\left(\rho_s\left(1-\mathrm{n}\right)\dot{\mathbf{u}}\right) = 0 \qquad (7.\ 3)$$

where n is the porosity and $\dot{\mathbf{u}}$ is the solid velocity vector. The variation of porosities in terms of changes in solid density and volumetric deformation of the soil skeleton is obtained from (7.3) (Olivella et al., 1994).

7.2.4. Momentum balance equation (equilibrium)

Assuming equilibrium of the medium, the momentum balance equation becomes:

$$\nabla.\boldsymbol{\sigma} + \mathbf{b} = 0 \qquad (7.\ 4)$$

where $\boldsymbol{\sigma}$ is the total stress tensor and $\boldsymbol{b}$ the vector of body forces.

In (7.4) inertial terms have been neglected. This assumption is commonly accepted because both velocities and accelerations are small (yielding terms are negligible in comparison with the stress terms, Gens and Olivella, 2001). The assumption of small strain rate is also made.

As introduced in Chapter 3, a basic principle in classical plasticity theory is the *additive decomposition of the strain tensor increments* $\dot{\boldsymbol{\varepsilon}}$ into elastic component $\dot{\boldsymbol{\varepsilon}}^e$ and plastic component $\dot{\boldsymbol{\varepsilon}}^p$:

$$\dot{\boldsymbol{\varepsilon}} = \dot{\boldsymbol{\varepsilon}}^e + \dot{\boldsymbol{\varepsilon}}^p \qquad (7.\ 5)$$

In turn, the total strains are related to the solid velocities $\dot{\mathbf{u}}$ through the compatibility equation:

$$\dot{\boldsymbol{\varepsilon}} = \frac{1}{2}\left(\nabla\dot{\mathbf{u}} + \nabla\dot{\mathbf{u}}^T\right) \qquad (7.\ 6)$$

7.3. Constitutive equations

The constitutive equations establish the link between the unknowns and the dependent variables. There are several categories of dependent variables depending on the complexity with which they are related to the unknowns. The governing equations are finally written in terms of the unknowns when the constitutive equations are substituted in the balance equations. Here, some of the basic constitutive laws are presented, divided into hydraulic and mechanical types. This distinction between the two basic components of the problem is only in order to facilitate its description, as both, mechanical and hydraulic constitutive relationships are in general coupled. For instance, the *HM* constitutive model employed within this research couples mechanical (stress-strain) relationships with water retention (fluid pressures-degree of saturation) relationships.

7.3.1. Hydraulic problem

Advective fluxes are computed using generalized Darcy's law, expressed as (Gens and Olivella, 2001):

$$\mathbf{q}_\alpha = -\mathbf{K}_\alpha\left(\nabla u_\alpha - \rho_\alpha \mathbf{g}\right); \qquad \alpha = l, g \qquad (7.\ 7)$$

where u_α is the phase pressure, $\boldsymbol{K}_\alpha$ is the permeability tensor of the α phase and $\boldsymbol{g}$ is the gravity vector. The permeability tensor is not constant but, in turn, it depends on other variables:

$$\mathbf{K}_\alpha = \mathbf{k}\frac{k_{r\alpha}}{\mu_\alpha}; \qquad \alpha = l, g \qquad (7.\ 8)$$

where μ_α is the dynamic viscosity of the α phase, $k_{r\alpha}$ is the α phase relative permeability and $\boldsymbol{k}$ is the intrinsic permeability tensor that depends on pore structure. Several laws are available in the program to describe this dependence (see CODE_BRIGHT User's Manual 2011 for further details). Also for the dependence of the relative permeabilities of liquid and gaseous phases on the degree of saturation, different laws are available to be employed when using CODE_BRIGHT (CODE_BRIGHT User's Manual 2011).

The retention behaviour relates degree of saturation with matric suction. CODE_BRIGHT allows for the possibility of choosing different water retention constitutive laws (see CODE_BRIGHT User's Manual 2011). An illustration of the water retention relationships implemented herein is given in Figure 7-1 and it corresponds to the model proposed by Wheeler et al. (2003). Note that the model employs two hardening parameters to define the locations of the *SD* and *SI* yield surfaces (i.e. s_D^* and s_I^*, respectively) and another two soil parameters to define the gradients of the modified suction-degree of saturation relationships. One defines the gradient of the main drying/wetting curves λ_s and the other one κ_s defines the gradient of the scanning curves (see Chapter 2 for more details).

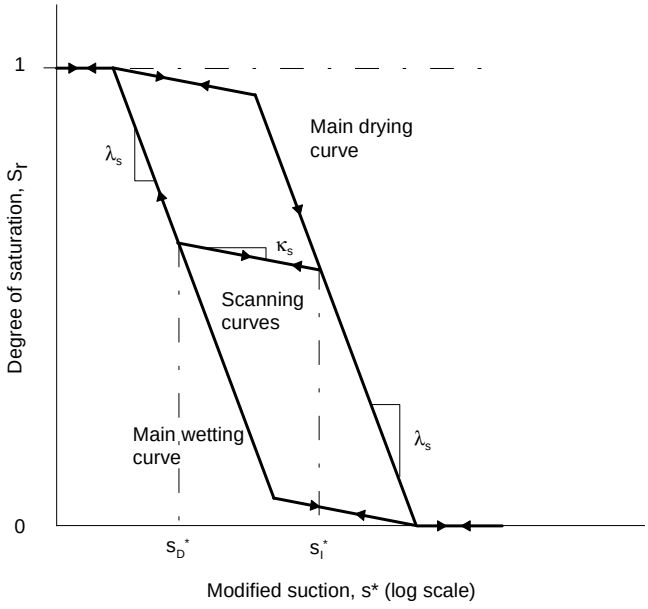

Figure 7- 1 Water retention model in Wheeler et al. (2003).

Non-advective fluxes of species inside the fluid phases are computed with Fick's law, which expresses these fluxes in terms of gradients of mass fraction of species through a hydrodynamic dispersion tensor that includes both molecular diffusion and mechanical dispersion (Olivella et al., 1994; Gens and Olivella, 2001):

$$\mathbf{i}_\alpha^i = -\mathbf{D}_\alpha^i \nabla \mathrm{w}_\alpha^i; \qquad i = w, a; \quad \alpha = l, g \qquad (7.\ 9)$$

where $\boldsymbol{D}^{j}_{\alpha}$ is the dispersion tensor of the medium and *w* the mass fraction of *i* species in α phase (Olivella et al., 1994; CODE_BRIGHT User's Manual 2011).

7.3.2. Mechanical problem

In order to implement the Wheeler et al. (2003) constitutive model into CODE_BRIGHT it is useful to express some of the equations of this constitutive model in such a way that make them compatible with the existing formulation of CODE_BRIGHT. In particular, it is convenient to express the total stress tensor variations in terms of strain and fluid pressure changes using the relationships proposed within the constitutive model. The mathematical development to find these expressions is detailed in Appendix A.4 and the main equations are summarised below.

Using the definition of Bishop's stresses given in Chapter 2, temporal variations of total stresses can be expressed as:

$$\dot{\boldsymbol{\sigma}} = \dot{\boldsymbol{\sigma}}^{*} + \mathbf{m}\dot{u}_g - \mathbf{m}\dot{S}_r\left(u_g - u_l\right) - \mathbf{m}S_r\left(\dot{u}_g - \dot{u}_l\right) \qquad (7.\ 10)$$

where $\boldsymbol{m}$ is the auxiliary vector (1,1,1,0,0,0), $\boldsymbol{\sigma}$ is the total stress tensor, $\boldsymbol{\sigma}^{*}$ is the Bishop's stress tensor, u_l and u_g are the liquid and gas pressures, respectively, and the upper dot indicates temporal variations.

Employing also the expression of the generalised constitutive stiffness matrix introduced in Chapter 5, the Bishop's stress changes can be expressed as:

$$\dot{\boldsymbol{\sigma}}^{*} = \mathbf{A}^{j}_{6x6}\dot{\boldsymbol{\varepsilon}} + \mathbf{B}^{j}_{1x6}\left(-\dot{S}_r\right) \qquad (7.\ 11)$$

where *j* indicates the elasto-plastic mechanism active, and $\boldsymbol{A}$ and $\boldsymbol{B}$ take different forms depending on the elasto-plastic mechanism as shown in Appendix A.2.

On the other hand, temporal variations of degree of saturation can be expressed in terms of temporal variations of pore fluid pressures and strains as (see also Section 6.3):

$$-\dot{S}_r = \left(D^{j}\right)^{-1}\left[\frac{e}{1+e}\left(\dot{u}_g - \dot{u}_l\right) + \left(\frac{-\left(u_g - u_l\right)}{1+e}\mathbf{m}^{T} - \mathbf{C}^{j}\right)\dot{\boldsymbol{\varepsilon}}\right] \qquad (7.\ 12)$$

where *T* indicates transposed, *j* indicates the elasto-plastic mechanism active, and *D* and $\boldsymbol{C}$ take different forms depending on the elasto-plastic mechanism as shown in Appendix

A.2. Note that (7.12) is already expressed in terms of the main unknowns (i.e. $\boldsymbol{\varepsilon}$, u_l and u_g variations).

Combining (7.10), (7.11) and (7.12) it is possible, after some algebra (see Appendix A.4), to find the following expression for the total stress temporal variations in terms of the temporal variations of strains and fluid pressures:

$$\dot{\boldsymbol{\sigma}} = \boldsymbol{\Lambda}_1 \dot{\boldsymbol{\varepsilon}} + \boldsymbol{\gamma}_1 \dot{u}_g + \boldsymbol{\gamma}_2 \dot{u}_l \qquad (7.13)$$

where the 6x6 matrix $\boldsymbol{\Lambda_1}$ and the 6x1 vectors $\boldsymbol{\gamma_1}$ and $\boldsymbol{\gamma_2}$ take the forms shown in Appendix A.4.

In order to update the degree of saturation (7.12) and the total stresses (7.13) it is necessary to know the previous values of stress variables (i.e. total stresses, degree of saturation and water and air pressures); previous values of history variables (i.e. void ratio and hardening variables related to plastic mechanisms); and the increment of the generalised strains, given by the strain rates (determined from solid velocities) and matric suction rates (determined from the fluid pressure rates i.e. $\dot{s} = \dot{u}_g - \dot{u}_l$). Then, by means of the strain-driver algorithm introduced in Chapter 6, Bishop's stresses and degree of saturation are updated. As explained in Chapter 6, this algorithm identifies the active elastic or elasto-plastic mechanism (i.e. elastic, yielding on the *SD* or *SI* yield surface alone, yielding on the *LC* yield surface alone; or simultaneous yielding on the *LC* and *SD* or *SI* yield surfaces) and updates the state variables accordingly. Finally, using the Bishop's stress changes in combination with the degree of saturation and fluid pressures variations, the total stress changes are calculated.

7.4. Equilibrium restrictions

It is assumed that phase changes are rapid in relation to the characteristic times typically employed when solving a boundary value problem. Consequently, phase changes can be considered in local equilibrium, which leads to a set of equilibrium restrictions that must be satisfied at all times (Olivella, 1995 and Gens and Olivella, 2001).

7.4.1. Psychometric law

The vapour concentration in the gaseous phase is governed by the psychometric law, which can be expressed as (Gens and Olivella, 2001):

$$\theta_g^w = \left(\theta_g^w\right)^0 \exp\left(\frac{\Psi M_w}{R\left(273.15+T\right)\rho_l}\right) \qquad (7.\ 14)$$

where θ_g^w is the vapour concentration in the gas phase, $(\theta_g^w)^0$ is the vapour concentration in the gas phase in equilibrium with a liquid across a flat interface (at the sample temperature), Ψ is the total water potential of water (excluding gravity terms), in this case it is related to suction ($\Psi=u_l-u_g$); M_w is the molecular mass of the water (0.018 kg/mol); R is the gas constant (8.314 J/mol/ºK) and T is the temperature in ℃. The gas law relates vapour density and vapour pressure (Olivella, 1995):

$$\left(\theta_g^w\right)^0 = \frac{M_w u_{v(T)}}{R\left(273.15+T\right)} \qquad (7.\ 15)$$

For pure water the vapour pressure has been approximated as (Olivella, 1995):

$$u_{v(T)} = 136075 \exp\left(\frac{-5239.7}{273.15+T}\right) \qquad (7.\ 16)$$

7.4.2. Henry's law

Henry's law is adopted to define the amount of air dissolved in water. This law expresses a linear relationship between the concentration of air in solution and the partial pressure of air (u_a) in the gaseous phase:

$$\theta_l^a = w_l^a \rho_l = \frac{u_a}{H}\frac{M_a}{M_w}\rho_l \qquad (7.\ 17)$$

where M_a is the molecular mass of the air (0.02895 kg/mol), and H is Henry's constant (1000 MPa).

7.5. Phase physical properties

The properties of the fluid phases appear in the balance equations and in the constitutive laws. In general, they depend on the composition of the phase and on the state variables (temperatures and pressures). Some of them are introduced below.

The density of the liquid phase can be expressed as (Olivella, 1995; Gens and Olivella, 2001):

$$\rho_l = 1002.6 \exp\left(4.5\cdot 10^{-04}\left(u_l - 0.1\right) - 3.4\cdot 10^{-4} T\right) \qquad (7.\ 18)$$

where T is expressed in ºC, u_l in MPa and in ρ_l kg/m^3. This expression must have a cut-off for large negative liquid pressures; if not, unrealisticly low liquid density is obtained.

The air density is obtained from the law of ideal gases:

$$\theta_g^a = \frac{M_a u_a}{R\left(273.15+T\right)} \qquad (7.\ 19)$$

The density of the gas phase is obtained adding the partial densities of the two species:

$$\rho_g = \theta_g^w + \theta_g^a \qquad (7.\ 20)$$

Finally, the viscosities of the liquid and gas phases are, respectively (Olivella, 1995):

$$\mu_l = 2.1\cdot 10^{-12} \exp\left(\frac{1808.5}{273.15+T}\right) \qquad (7.\ 21)$$

$$\mu_g = 1.48\cdot 10^{-12} \exp\left(\frac{\left(273.15+T\right)^{1/2}}{1+\frac{119}{\left(273.15+T\right)}}\right) \qquad (7.\ 22)$$

where T is expressed in ºC and μ_α in MPa.s.

7.6. Computer code and numerical implementation

The system of *PDE's* (Partial Differential Equations) is solved numerically and simultaneously in terms of the state variables of the problem: solid velocity $\dot{\mathbf{u}}$; liquid pressure u_l; and gas pressure u_g. Note that temperature effects are not considered in this research. From these variables, the dependent ones are calculated using the constitutive equations or equilibrium restrictions (see Table 7.1).

The complete formulation related to the discretization of the problem and the numerical approach employed can be found in Olivella et al. (1996) and only some of the main features have been summarised here. The numerical approach uses the Galerkin finite element method for the spatial discretization and finite differences for the temporal discretization. An implicit scheme is adopted for time integration and the Newton-Raphson method is used as an iterative scheme to solve the nonlinear system. The program has an automatic discretization of time, increasing or decreasing the time increment according to

convergence conditions or output requirements (more details can be found in CODE_BRIGHT User's Manual, 2011).

Another important aspect of the numerical approach is that different elements types can be adopted, including segments, triangles, quadrilaterals, tetrahedrons and triangular prisms. Linear interpolation functions and quadratic interpolation functions for some elements are also available. Analytical integration or numerical integration is employed depending on element type (see Olivella, 1995 and Olivella et al., 1996 for further details).

7.7. Computational aspects of the implementation

As described above, several modifications of the finite element program CODE_BRIGHT were necessary for the implementation of the Wheeler et al. (2003) constitutive model. Also some changes were required to the strain-driver algorithm (see Chapter 6) to adapt the subroutine for the finite element framework. Despite these minor changes, the final algorithm implemented within CODE_BRIGHT is essentially the one described in Chapter 6. The main modification to the algorithm was the inclusion of a *substepping* strategy for the subdivision of strain and suction increments. The implemented subroutine allows the subdivision of the strain and suction increments into a specified number of steps (referred to as *Nsubs*) in order to provide smoother computations to the non-linear solution. The number of steps *Nsubs* should be defined along with the parameters used in the model.

Some re-arrangements were also necessary to be introduced in CODE_BRIGHT, essentially associated with updating of the degree of saturation. CODE_BRIGHT, as originally formulated, uses two separate constitutive models to update the stresses and degree of saturation (a mechanical model and a water retention model respectively). In here, however, both types of variable (stresses and degree of saturation) are updated using a single constitutive model (i.e. the 3D constitutive model presented in Chapter 5).

Because of these minor modifications to the strain-driver subroutine and to the main finite element program, it was considered appropriate to extend the analysis of computational aspects presented in Chapter 6, studying the performance of the new implemented constitutive model. This analysis is essentially aimed at checking that the algorithm has been correctly implemented within the finite element program. This section, then, continues and complements prior discussions on computational aspects by including other important variables such as CPU time (amount of time that the computer's Central Processing Unit (CPU) uses to solve the proposed problem), which is mainly associated (in these analyses) with the number of *substeps* (*Nsubs*) adopted. All CPU times

presented in this section are for an Intel Xeon E5405 Quad Core 2.00GHz processor with 12MB of cache and 16GB of RAM.

The computed results from a given stress path involving isotropic loading and shearing of a cylindrical sample, are analysed following an equivalent approach to the one presented in Section 6.6.2 when investigating the relative error made in the computations. A 2D axisymmetric regular finite element mesh comprised of 10x10 four-node quadrilateral elements was used. Matric suction was imposed constant and equal to 0.11MPa in the whole sample. The same value of pore liquid pressure (u_l=-0.01 MPa) was applied at all nodes and the pore air pressure was assumed constant (u_a=0.1 MPa) during all the test simulated. Null water flux was imposed on the bottom and lateral sides of the sample. No vertical displacements were allowed on the bottom of the sample. The test was analysed as axisymmetric (with a vertical axis of symmetry) and the information presented below is aimed at studying the computed response at a Gauss point level. All the results presented in the remainder of this chapter use GiD (http://gid.cimne.upc.es) in the pre- and post-processing analysis.

Two stages are considered during this simulation. An initial isotropic loading at constant matric suction (0.11 MPa) is applied first; changing the mean total stress from 0.11 MPa to 0.21 MPa (*A* to *B* in Figure 7-2). Shearing at a constant axial strain rate is applied, afterwards, by applying vertical displacements to the top of the sample at constant rate. This shearing stage *BC* was performed at constant suction and constant radial net stress to a final deviator stress of 155 kPa. The complete loading stress path is illustrated in Figure 7-2. Different numbers of substeps have been considered to compute the values of the void ratio and degree of saturation at *B* and *C*. These computed values of the void ratio and degree of saturation at *B* and *C* are afterwards compared with a solution computed using a very high number of substeps (*Nsubs*=10.000), to estimate the relative error made in the computations. The solution obtained with *Nsubs*=10.000 is used in Equation (6.70) as a *reference value*, and solutions obtained using smaller numbers of substeps (i.e. 1, 10, 100 and 1.000) are compared with this in an equivalent manner to that described in Chapter 6 (further details in Section 6.6.2).

Table 7.2 summarises the soil parameter values of the coupled water retention-mechanical model used in the computations along with the initial state. The values used for *TOL1* (tolerance used in the algorithm for the intersection/s of the stress path with the appropriate surface) and *TOL2* (tolerance used in the drift correction method), see Sections 6.4 and 6.5, are also included in this table. Without going into further details, the convergence criteria imposed in the Newton-Raphson (*N-R*) method when solving the

global non-linear system of *PDE's* introduced in Section 7.6 is in all cases lower than $5 \cdot 10^{-06}$ (more details on these convergence criteria used in CODE BRIGHT can be found in CODE_BRIGHT User's Manual, 2011).

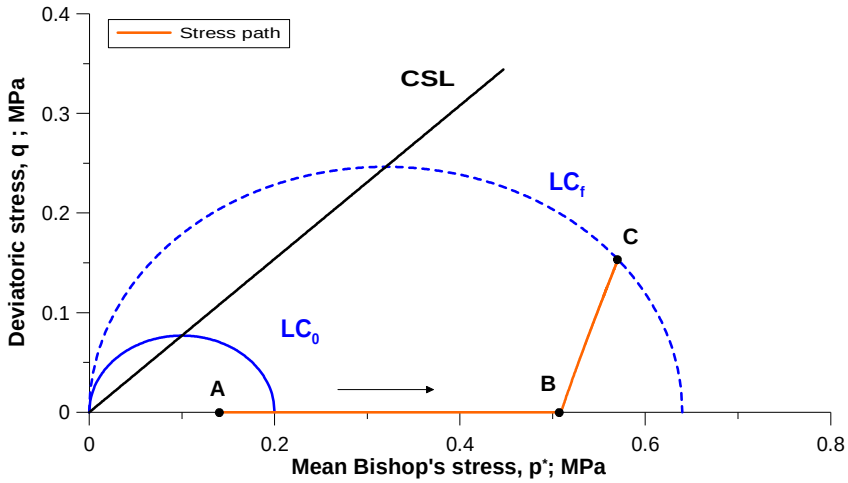

Figure 7- 2 Stress path used in the computations.

Table 7. 2 Soil parameters and initial state used in the computations.

κ=0.02	λ=0.15	λ_s=0.12	κ_s=0.02	k_1=0.7	k_2=0.8
ν^1=0.3	M=0.77				
p_0^*=0.2 MPa	s_D^*=0.07 MPa	e=1.2	S_r=0.65	s=0.2 MPa	$\overline{p}$ =0.01 MPa
TOL1=10^{-07}		TOL2=10^{-07}			

[1] *Poisson's ratio.*

Four different values of substeps (*NSubs*) were used to compute the values of the void ratio and degree of saturation at *B* and *C* (see Figure 7-2). To estimate the errors at *B* and *C*, as previously described, these values are compared with a reference value computed using *NSubs*=10.000 and (6.70). The total accumulated CPU time, the total number of time increments and the total number of Newton-Raphson (*N-R*) iterations used in the computations, were also analysed for *B* and *C*. A summary of the results obtained is given in Tables 7.3 and 7.4, and it is illustrated in Figure 7-3. The ratio between the number of *N-R* iterations and the number of time intervals is included in these two tables to give information on the convergence within the *N-R* scheme.

An increase of the CPU time when *NSubs* increases is clearly observed in all cases plotted. It is also observed that the estimated relative error is lower than $5 \cdot 10^{-04}$ in all cases (see Tables 7.3 and 7.4). As expected, the highest error is obtained when employing the lowest number of substeps (i.e. *NSubs*=1). In this case, the implemented

subroutine uses directly the increments of strains calculated from the *N-R* scheme and the results obtained, in terms of error, are still quite satisfactory. When using a higher number of *NSubs* (*Nsubs*=10, 100 and 1.000) the error observed decreases and it is, in all cases, smaller than $1 \cdot 10^{-04}$, which has been considered sufficient for the purposes of this work. It is surprising that the errors in *e* at *B* and in *e* and S_r at *C* show an increase between *Nsubs*=10 and *Nsubs*=100 (see Figure 7.3a), but the overall trends in all cases are for errors to decrease as *Nsubs* increases.

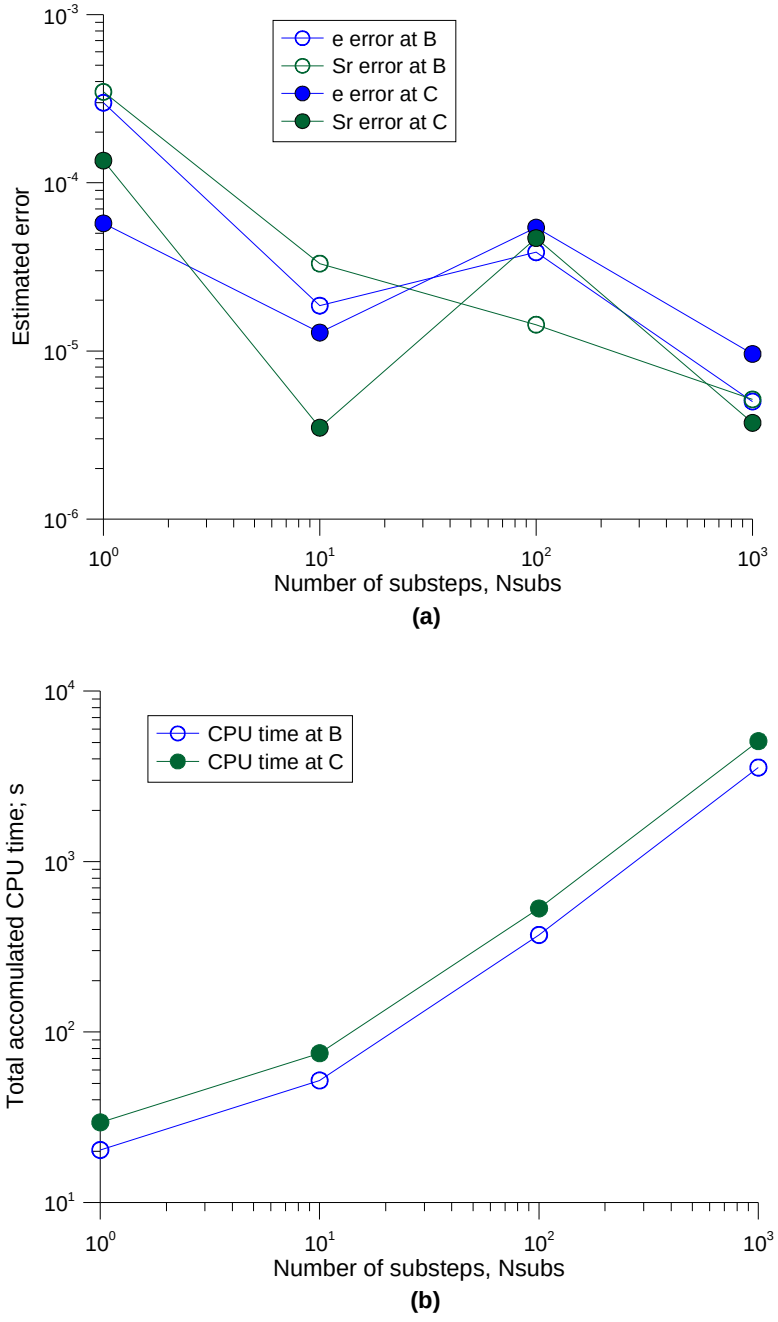

Figure 7- 3 Analysis of computational aspects: (a) Error against number of substeps; (b) Total accumulated CPU time against number of substeps.

Table 7. 3 Results at end of isotropic loading (B in Figure 7-2) for different numbers of substeps (NSubs).

					Relative error	
Nsubs	**Total number of time intervals**	**Total number of N-R iterations**	**Ratio**	**CPU time (seconds)**	**Void ratio at B**	**Degree of saturation at B**
1	1019	1084	1.06	$2.03 \cdot 10^{+01}$	$2.99 \cdot 10^{-04}$	$3.47 \cdot 10^{-04}$
10	1019	1031	1.01	$5.20 \cdot 10^{+01}$	$1.86 \cdot 10^{-05}$	$3.30 \cdot 10^{-05}$
100	1019	1029	1.01	$3.71 \cdot 10^{+02}$	$3.86 \cdot 10^{-05}$	$1.43 \cdot 10^{-05}$
1000	1019	1030	1.01	$3.56 \cdot 10^{+03}$	$5.00 \cdot 10^{-06}$	$5.15 \cdot 10^{-06}$

Table 7. 4 Results at end of shearing (C in Figure 7-2) for different number of substeps (NSubs).

					Relative error	
Nsubs	**Total number of time intervals**	**Total number of N-R iterations**	**Ratio**	**CPU time (seconds)**	**Void ratio at C**	**Degree of saturation at C**
1	1436	1505	1.05	$2.95 \cdot 10^{+01}$	$5.73 \cdot 10^{-05}$	$1.35 \cdot 10^{-04}$
10	1436	1448	1.01	$7.51 \cdot 10^{+01}$	$1.29 \cdot 10^{-05}$	$3.49 \cdot 10^{-05}$
100	1436	1448	1.01	$5.31 \cdot 10^{+02}$	$5.41 \cdot 10^{-05}$	$4.69 \cdot 10^{-05}$
1000	1436	1447	1.01	$5.09 \cdot 10^{+03}$	$9.60 \cdot 10^{-06}$	$3.73 \cdot 10^{-06}$

7.8. Partial verification of FE implementation

This section is intended to provide (partial) verification that the generalized 3D version of the Wheeler et al. (2003) model has been correctly implemented within the FE code. This is achieved by performing a finite element simulation of a problem where the results can be compared with corresponding results produced directly with the strain-driver algorithm. The output from the driver algorithm has itself been previously verified by checking that isotropic loading states and critical states involving simultaneous yielding on *LC* and *SD* surfaces are correctly predicted to fall on the appropriate planar surfaces in v:lnp^*:lns^* and S_r:lnp^*:lns^* spaces (see Sections 5.5 and 6.6). Of course, using the output from the strain-driver algorithm as the reference against which the FE simulations are to be compared placed considerable restriction on the type of problem that could be analysed. In particular, the boundary value problem studied with the FE code had to be one where there was no spatial variation of suction or of other variables, so that it was essentially the same as a single element simulation (rather than a true boundary problem). This fact that

the problem analysed involved no spatial variation of any variable means that this exercise can only be considered as partial verification of the correct FE implementation of the constitutive model.

The problem that was analysed was the simulation of the suction-controlled triaxial test 18C of Sivakumar (1993), where the corresponding strain-driver algorithm simulations were presented in Section 5.5. The same 2D axisymmetric finite element mesh of 10x10 four-node quadrilateral elements described in Section 7.7 was used for the FE simulation. The imposed stress path involved isotropic loading from a mean net stress of 50 kPa to 150 kPa at constant suction of 300 kPa, followed by shearing at the same constant suction and at constant radial net stress until failure. Throughout the simulation constant (and uniform) values of suction were imposed at all nodes, with the result that there was no spatial variation of any variables across the mesh. The parameters of the implemented *HM* constitutive model and initial state used are those defined in Chapter 5 to validate the 3D extended version of the Wheeler et al. (2003) model when using the Sivakumar (1993) experimental data. These values are summarised in Table 7.5 (see also Chapter 5).

Table 7. 5 Model parameters and initial state used in the computations.

$\lambda=0.124$	$\lambda_s=0.097$	$\kappa_s=0.0004$	$M=0.716$
$\kappa=0.006$	$k_1=0.685$	$k_2=0.773$	$\upsilon^1=0.3$
$\overline{p}=0.05$ MPa	$s=0.3$ MPa	$p^*=0.229$ MPa	$p_0^*=0.271$ MPa
$e_0=1.210$	$S_{r0}=0.597$	$s^*=0.164$ MPa	$s_D^*=0.164$ MPa
$TOL1=1\cdot10^{-04}$	$TOL2=1\cdot10^{-04}$		

[1]*Poisson's ratio*

Figures 7-4 and 7-5 show the results of the strain driver and FE simulations of Test 18C. Figure 7-4 includes both the constant suction isotropic loading stage (*AB*) and the constant suction, constant radial net stress shearing stage (*BC*), whereas Figure 7-5 shows only the shearing stage. Yielding on the *SD* yield surface is occurring throughout the full simulations, whereas yielding on the *LC* surface commences at point *Y* (see Figure 7-4) within the isotropic loading stage (see Section 5.5 for further details).

Inspection of Figures 7-4 and 7-5 shows that the FE simulations are indistinguishable from the strain-driver simulations in all respects, including the predicted stress path in the q:p^* plane, the predicted variations of void ratio e and degree of saturation S_r and the development of shear strain (and hence axial strain). Given that the results of the strain driver algorithm have already been verified, this comparison provides verification (at least

for the limited condition of a boundary value problem involving no spatial variation of variables) of correct implementation in the finite element code.

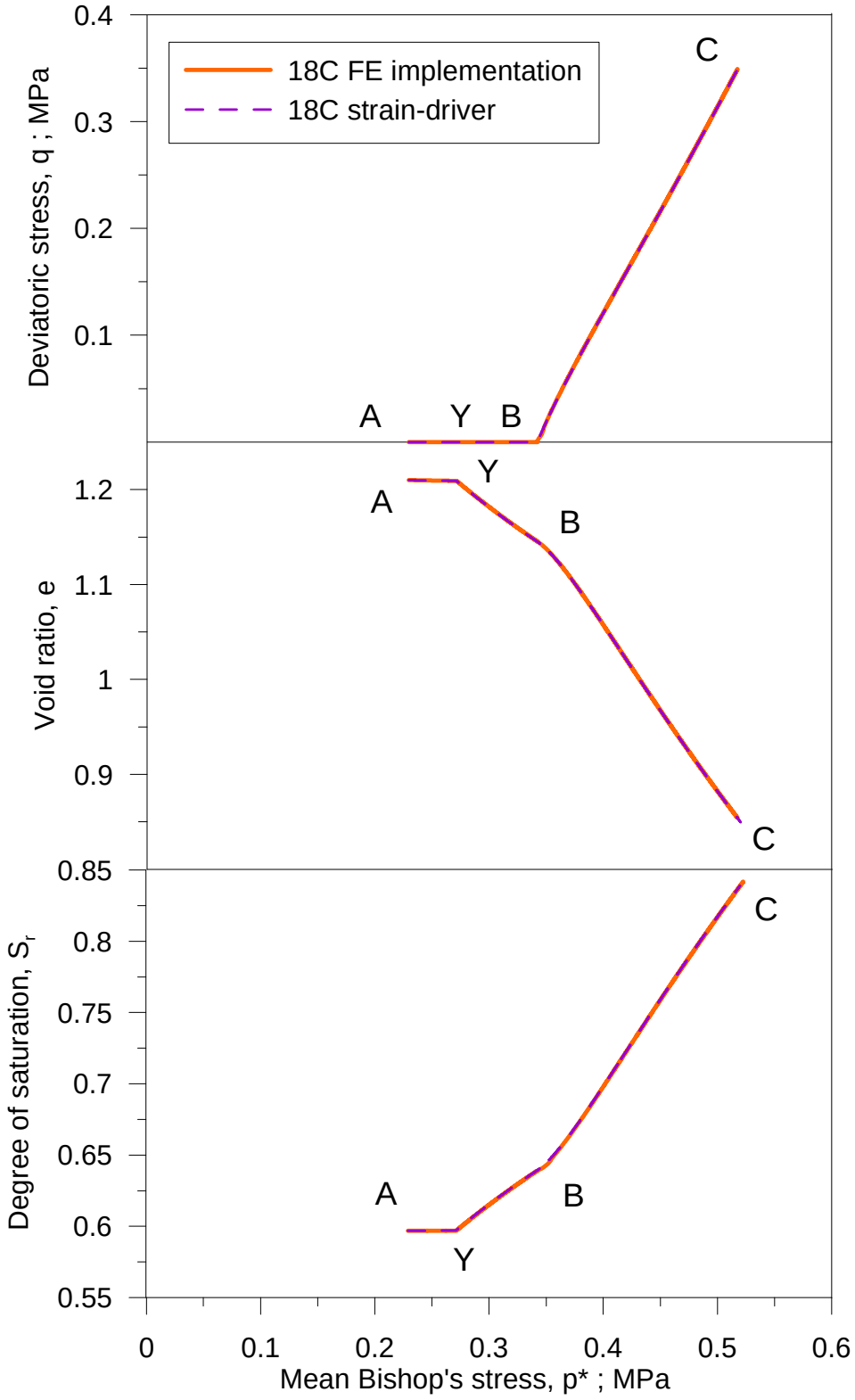

Figure 7- 4 Comparison of strain driver simulation and FE simulation for Test 18C of Sivakumar (1993).

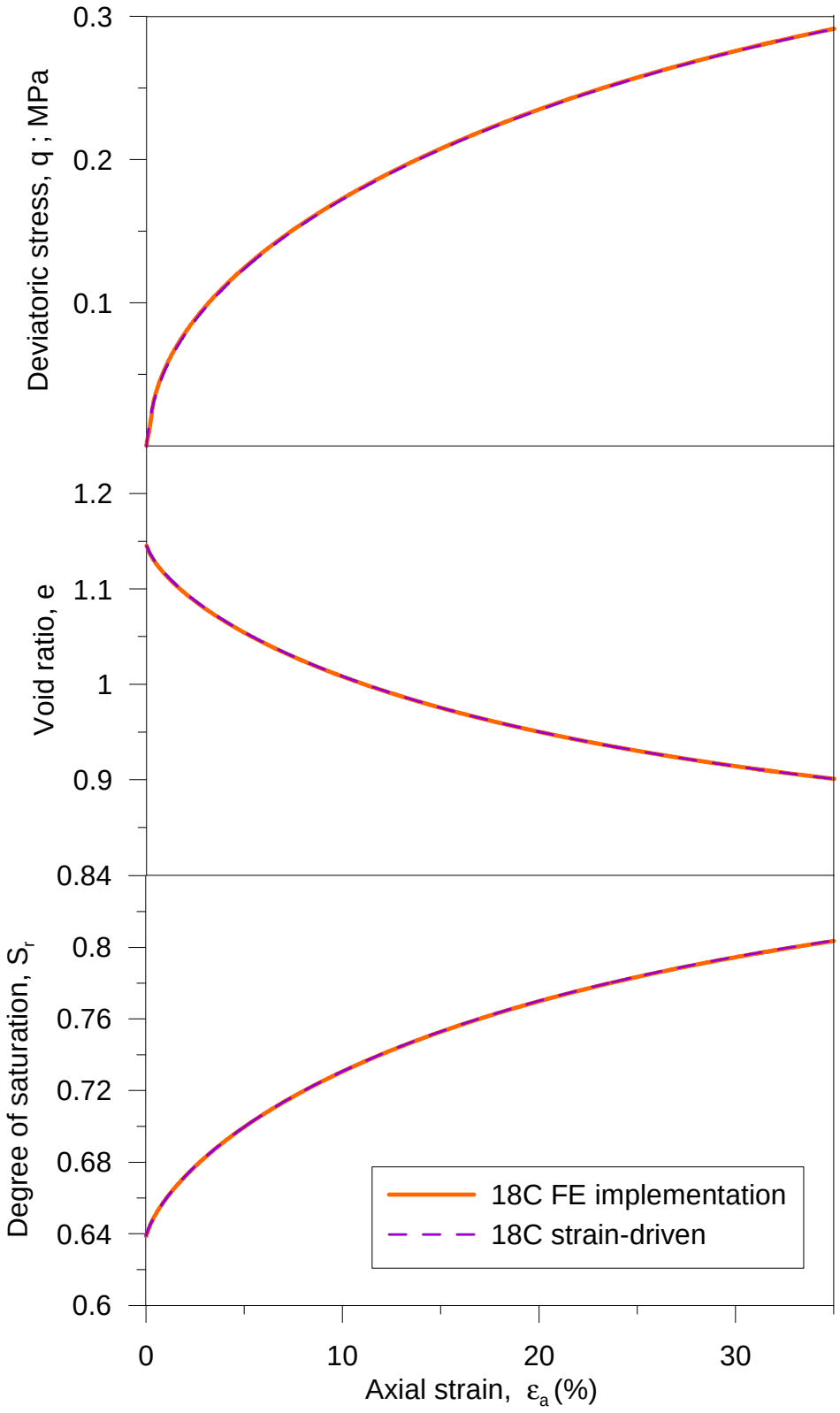

Figure 7- 5 Comparison of strain driver simulation and FE simulation for shearing stage of Test 18C of Sivakumar (1993).

7.9. Modelling of a boundary value problem: wetting of a cylindrical soil sample

This section presents the FE simulation of a simple boundary value problem, incorporating spatial variation of suction and other variables and therefore full solution of the coupled hydro-mechanical governing equations. The objective is simply to demonstrate the FE code, incorporating the extended 3D version of the Wheeler et al. (2003) constitutive model, working on a full boundary value problem. As this is a full boundary value problem involving highly complex non-linear constitutive relations there is no analytical solution against which the FE results can be compared. Neither is there an alternative numerical solution against which the results can be compared. This exercise does not, therefore, constitute a formal verification of the correct implementation of the new constitutive model with the FE code. All that can be checked is that the FE code runs satisfactorily and that the results are qualitatively sensible. This will provide increased confidence, but not formal verification, that the constitutive model has been correctly implemented in the FE code.

7.9.1. Problem description

A very simple boundary value problem has been analysed. The problem consists of wetting of a cylindrical sample from top and bottom, with the wetting carried out with constant isotropic stress conditions applied on the boundaries. For this problem, pore air pressure is assumed perfectly mobile and, therefore, mass balance of air (7.2) is not considered (air pressure u_a is assumed constant and equal to 0.1 MPa in all the simulation).

The adopted geometry of the problem is shown in Figure 7-13. The soil specimen has a total height of L=0.076m and a radius of R=0.019m. Because of symmetry conditions of the sample an axisymmetric (vertical axis) analysis has been performed based on the top half of the sample, as illustrated in Figure 7-13. Therefore, the dimensions of the 2D axisymmetric mesh analysed are L/2=0.038m and R=0.019. The adopted finite element mesh consists of 38x19 four-node quadrilateral elements as illustrated in Figure 7-14.

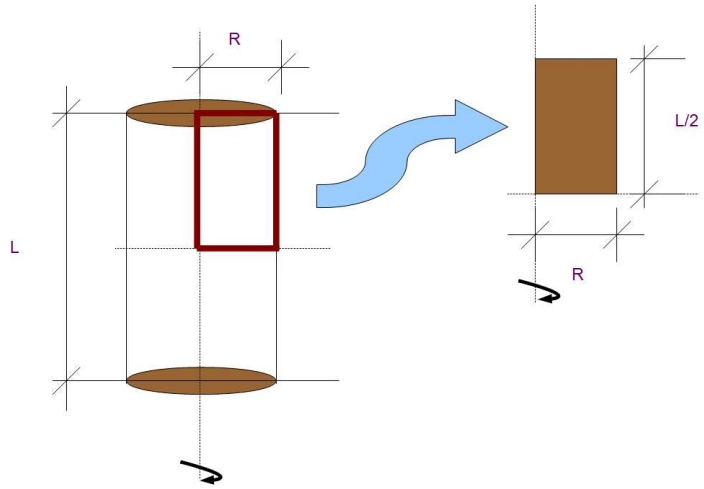

Figure 7- 6 Graphical representation of the axisymmetric problem analysed.

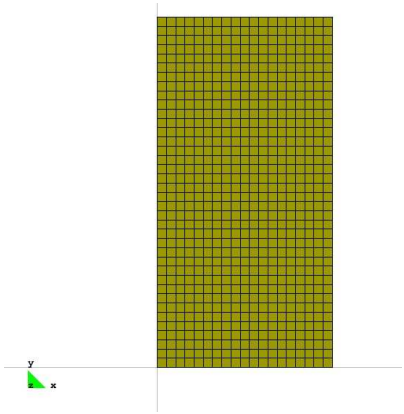

Figure 7- 7 Finite element mesh.

At time t=0, a constant initial liquid pressure u_l of -1.8MPa and a constant porosity equal to 0.468 are imposed in the entire specimen. Pore air pressure remains constant in all the simulation (u_a=0.1 MPa), which implies an initial value of matric suction equal to 1.9 MPa (s=u_a-u_l). An initial isotropic stress state with a mean total stress p=0.7 MPa is imposed in the entire sample. This leads to an initial value of mean net stress equal to 0.6 MPa throughout the sample. This condition is maintained until t=600s.

Mechanical boundary conditions are shown in Figure 7-8a. Null vertical displacements u_y are imposed at the bottom of the FE mesh (the mid-plane of the soil sample) and null horizontal displacements u_x are assumed on the vertical axis of radial symmetry (with no shear stresses on either of these boundaries). Stress-controlled boundaries are applied on the top boundary and on the outer vertical boundary, with normal total stresses of 0.7 MPa on both boundaries and no shear stresses. This means, with u_a=0.1 MPa, that the

"global" stress state for the sample is isotropic, with a mean net stress of 0.6 MPa, but it will be shown later that, as the wetting process develops, a complex non-uniform, non-isotropic field of total (and net) stresses develops within the sample.

From time t=600s to t=4.976.700s a uniform rate of increase of pore liquid pressure from -1.8MPa to 0.04MPa is imposed at the top boundary. The simulation therefore consists of a gradual wetting from both top and bottom of the soil sample (given the assumed plane of symmetry at the mid-height) from a matric suction of 1.9MPa to 0.06MPa, with a constant "global" mean net stress of 0.6MPa. Temperature is assumed constant in all calculations. The assumption of stress-controlled mechanical boundary conditions on the top boundary and on the outer vertical boundary means that both boundaries are considered as flexible. In particular, the vertical displacement of the top boundary does not remain uniform as the simulation progresses. This would not be a realistic representation of the conditions on a real triaxial test specimen in the laboratory, where uniform vertical displacements would normally be imposed at both top and bottom boundaries. However, this rather unrealistic aspect of the boundary value problem is unimportant, because this is a purely fictitious exercise, intended solely to provide evidence of successful working of the FE code following implementation of the new constitutive model.

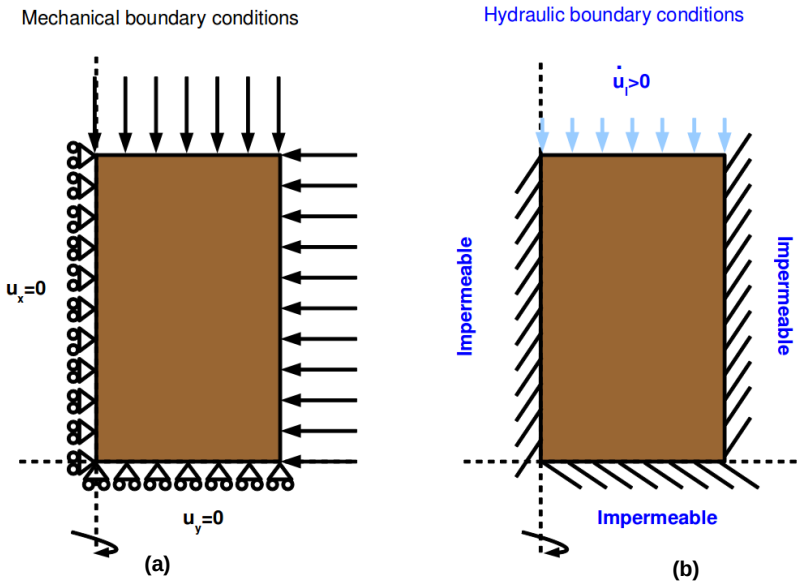

Figure 7- 8 Assumed boundary conditions.

7.9.2. Model parameter values

Basic physical properties used in the analysis are listed in Table 7.8.

Table 7. 6 Physical properties.

Parameter	***Symbol***	***Value***	***Units***
Water density	ρ_{w0}	*1000*	*kg m^{-3}*
Water viscosity	μ_{w0}	*1e-06*	*kPa s*
Intrinsic permeability at reference porosity[1]	$(k_{11})_0=(k_{22})_0=(k_{33})_0$	*3.0e-19*	*m^2*
Solid density	ρ_{s0}	*2.773*	*kg m^{-3}*

[1]*Further details on the adopted value of intrinsic permeability for Boom clay can be found in Romero (1999).*

As mentioned in Section 7.3.1, CODE_BRIGHT allows for different laws to describe the dependence of permeability on pore structure and degree of saturation. In this FE simulation, the adopted variation of intrinsic permeability *k* with porosity *n* is given by (7.23) (*Kozeny's model*).

$$\mathbf{k} = \mathbf{k_0} \frac{n^3}{(1-n)^2} \frac{(1-n_0)^2}{n_0^3} \qquad (7.\ 23)$$

where n_0 is a reference porosity (i.e. 0.468 for this case), $\boldsymbol{k_0}$ is the intrinsic permeability tensor at the reference porosity n_0 (see Table 7.6).

The relative permeability of the liquid phase k_{rl} varies with degree of saturation S_r according to (7.24) (*generalised power law*) (see also Equations (7.7) and (7.8)).

$$k_{rl} = \tilde{A}\left(\frac{S_r - S_{rl}}{S_{rs} - S_{rl}}\right)^{\tilde{\lambda}} = \tilde{A} S_e^{\tilde{\lambda}} \qquad (7.\ 24)$$

where $\tilde{\lambda}$ and $\tilde{A}$ are two model parameters (taking values, for this case, of 3 and 1 respectively), S_{rl} is the residual saturation (fixed to 0.01 for this case) and S_{rs} is the maximum saturation (fixed to 1 in this case).

Values used for the parameters within the extended 3D mechanical-water retention constitutive model of Wheeler et al. (2003) are given in Table 7.9, including the initial state. To ensure that the parameter values were realistic they were selected as an attempt to represent approximately the compacted Boom clay tested by Romero (1999). However, it was not possible to perform a rigorous calibration exercise, using the procedure set out in Section 2.7.4, because the experimental data available from Romero (1999) did not provide all the appropriate information. The set of values listed in Table 7.9 should therefore be viewed simply as a fictitious but realistic set of model parameter values.

Table 7. 7 Initial state and constitutive model parameters used in the modelling.

$\overline{p}$ =0.6 MPa	s=1.8 MPa	S_l=0.47	e=0.879
$p_0^*=p^*$=1.4 MPa	$s_D^*=s^*$=0.8 MPa		
λ=0.1	λ_s=0.096	κ_s=0.023	κ=0.015
k_1=0.66	k_2=0.73	M=0.77	υ^1=0.3

[1]*Poisson's ratio.*

Note also that there are different expressions of $g(\theta)$ (see Equation (5.1)) for different failure criteria. The function for $g(\theta)$ assumed here, however, corresponds to von Misses failure criteria (i.e. $g(\theta)$=1 see Appendix A.1 for further details).

7.9.3. Modelling and discussion

This section presents the results obtained from the FE simulations of the boundary value problem defined in Section 7.9.1 and using the implemented constitutive model with the model parameter values shown in Section 7.9.2. A discussion of these results is also included, presented in four parts. The first part shows the outputs of the solution from CODE_BRIGHT illustrated by contours plots at the final time (all these plots have been developed using GiD as a graphical interface, http://gid.cimne.upc.es). The second part of the results shows the temporal variation of several variables at three different points within the soil sample. The remaining two parts present the variation of several variables across two fixed cross sections (vertical and horizontal) at different times.

7.9.3.1. Results at final time

Figure 7-9 illustrates the contour plots of pore liquid pressure at final time. As expected, the final value of pore liquid pressure on the top of the sample corresponds to the final value of u_l (0.04 MPa) imposed with the hydraulic boundary condition (see Section 7.9.1). As a consequence of considering pore air pressure constant at all nodes throughout the test at a value of 0.1 MPa, the value of matric suction reached at the top of the sample is 0.06 MPa. At the bottom of the finite element mesh (the mid-plane of the sample), however, the value of matric suction is significantly higher which can be explained by the fact that wetting progresses relatively slowly down through the sample, due the low permeability values used for Boom clay (intrinsic permeability of $3 \cdot 10^{-19} m^2$, see Table 7.6). The variation of pore liquid pressure across the finite element mesh is qualitatively the expected one, showing a smooth transition from the imposed value on the top of the specimen to the value reached at the bottom of the mesh.

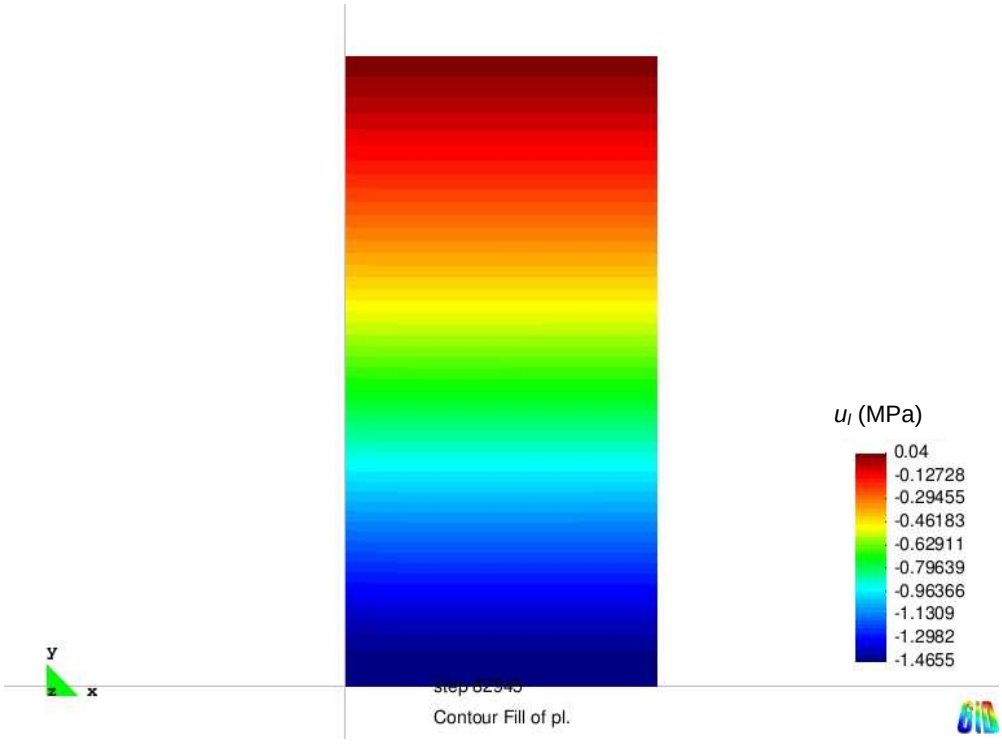

Figure 7- 9 Computed results at final time for liquid pressure.

Figure 7-10 presents equivalent results for degree of saturation (Figure 7-10a) and the hardening parameter s_D^* associated with the *SD* yield surface (Figure 7-10b). Yielding on the *SD* yield surface gives irreversible increases of degree of saturation and the variation of this hardening parameter s_D^* complements, therefore, information on degree of saturation. As expected, the observed value of the degree of saturation is significantly higher at the top of the soil sample (i.e. 0.94) than its corresponding value at the bottom (i.e. 0.49). This general behaviour is in accordance with prior comments made on the pore liquid pressure and the large variation of S_r over the sample height is essentially a consequence of the low permeability of Boom clay. It is interesting to note that this final value of the degree of saturation at the bottom of the FE mesh is slightly higher than the initial value (i.e. 0.47, see Table 7.7), meaning that water has already reached the bottom of the FE mesh at this final time (i.e. t=82.945min). It is also interesting to remember that irreversible increases of S_r took place from the start of the wetting, because the initial state was at the corner between the *LC* and *SD* yield surfaces (see Table 7.7) and simultaneous yielding on both yield surfaces occurred from the beginning of the wetting. This aspect is further discussed in the following section when showing the temporal results.

Close inspection of Figure 7-10 shows that the contours of S_r and s_D^* are not exactly horizontal, and therefore slight variation of each of these two parameters with radius is

predicted. Although this may initially appear surprising, it is a perfectly correct feature of the predictions. It is shown below that other variables show greater variation with radius, and the explanation for this behaviour is presented in Section 7.9.3.4.

Figure 7-11 presents equivalent results for void ratio (Figure 7-11a) and hardening parameter p_0^* associated with the *LC* yield surface (Figure 7-11b). Yielding on the *LC* surface results in irreversible decreases of void ratio and variation of this hardening parameter p_0^* complements, therefore, information on void ratio. Also as expected, the observed value of the void ratio is significantly lower at the top of the soil sample (i.e. 0.652) than its corresponding value at the bottom (i.e. 0.876). This shows that the simulation is predicting collapse compression on wetting, and this is obviously greatest at the top of the sample, where wetting has progressed furthest. The final value of void ratio at the bottom of the FE mesh is slightly lower than the initial value of void ratio (i.e. 0.879, see Table 7.7) meaning again that water has already reached the bottom of the mesh at this final time (i.e. t=82.945min) and collapse compression behaviour has commenced at the bottom of the mesh by the end of the test.

Figure 7-11b shows that the hardening parameter p_0^* has reduced in value due to the wetting process, particularly towards the top of the sample where the wetting has progressed further. This reduction of p_0^*, even though yielding on the *LC* surface is occurring (producing collapse compression), is entirely as expected. Mean Bishop's stress p^* is reducing during wetting, but with the stress point remaining at the corner of *SD* and *LC* yield surfaces, and simultaneous yielding on both surfaces occurring throughout. The net inward movement of the *LC* surface during this process (indicated by the reduction of p_0^*), which keeps the stress point on the *LC* surface, is made up of a large inward coupled movement of the *LC* surface due to the plastic increase of S_r associated with yielding on the *SD* surface and a smaller direct outward movement of the *LC* surface due to yielding on the *LC* surface itself. It is only the latter component that is associated with the occurrence of plastic volumetric strain.

Inspection of Figure 7-11 shows that contours of void ratio and of hardening parameter p_0^* are clearly not horizontal, indicating significant variation with radius of these two variables. This is not an error in the FE predictions, and neither is it specifically associated with the use of the Wheeler et al. (2003) constitutive model (qualitatively similar variations of void ratio with radius were predicted with an equivalent FE simulation employing the Barcelona Basic Model as the mechanical constitutive model). A full explanation for the predicted variations with radius is given in Section 7.9.3.4.

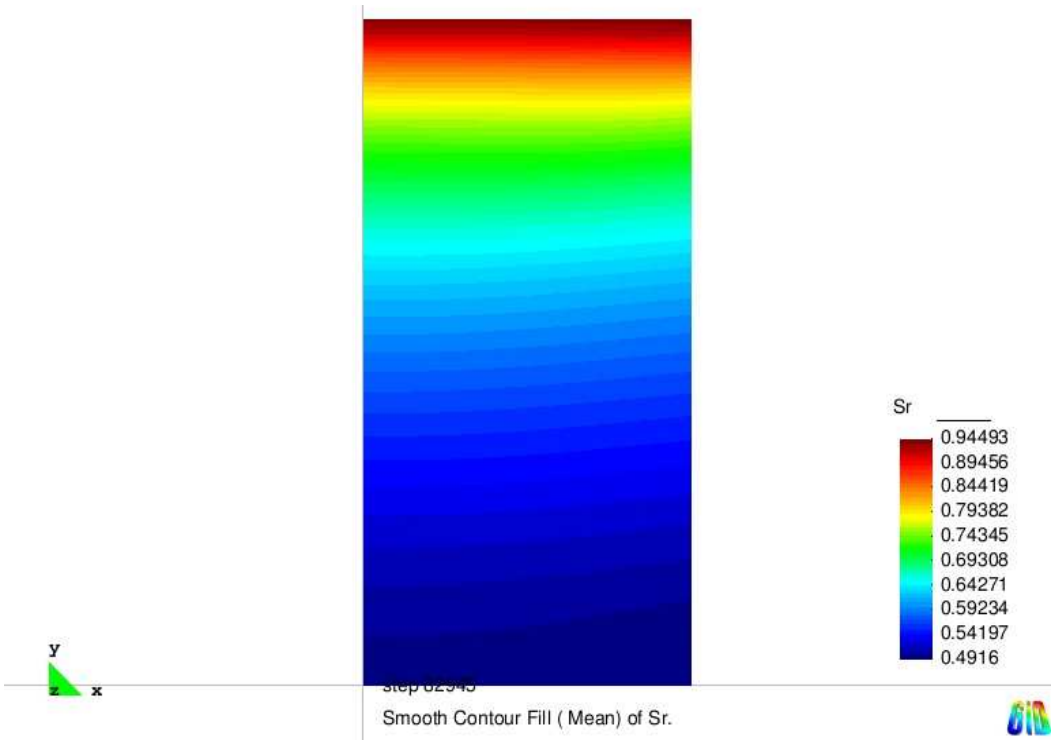

(a)

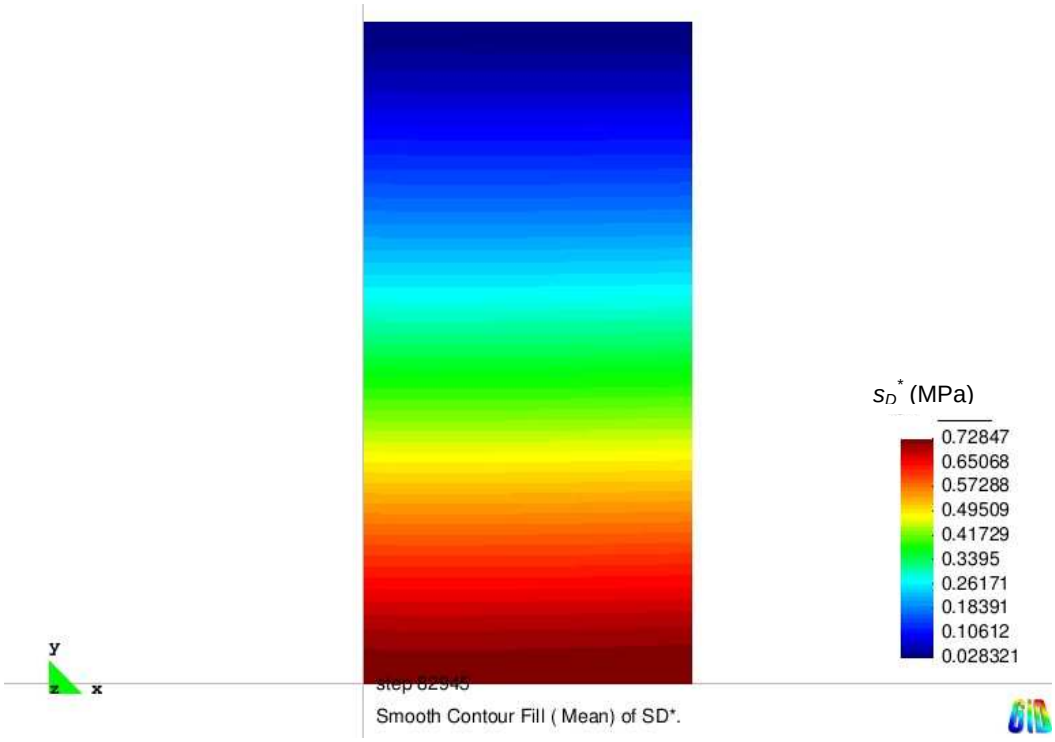

(b)

Figure 7- 10 Computed results at final time; (a) degree of saturation S_r; (b) hardening parameter s_D^*.

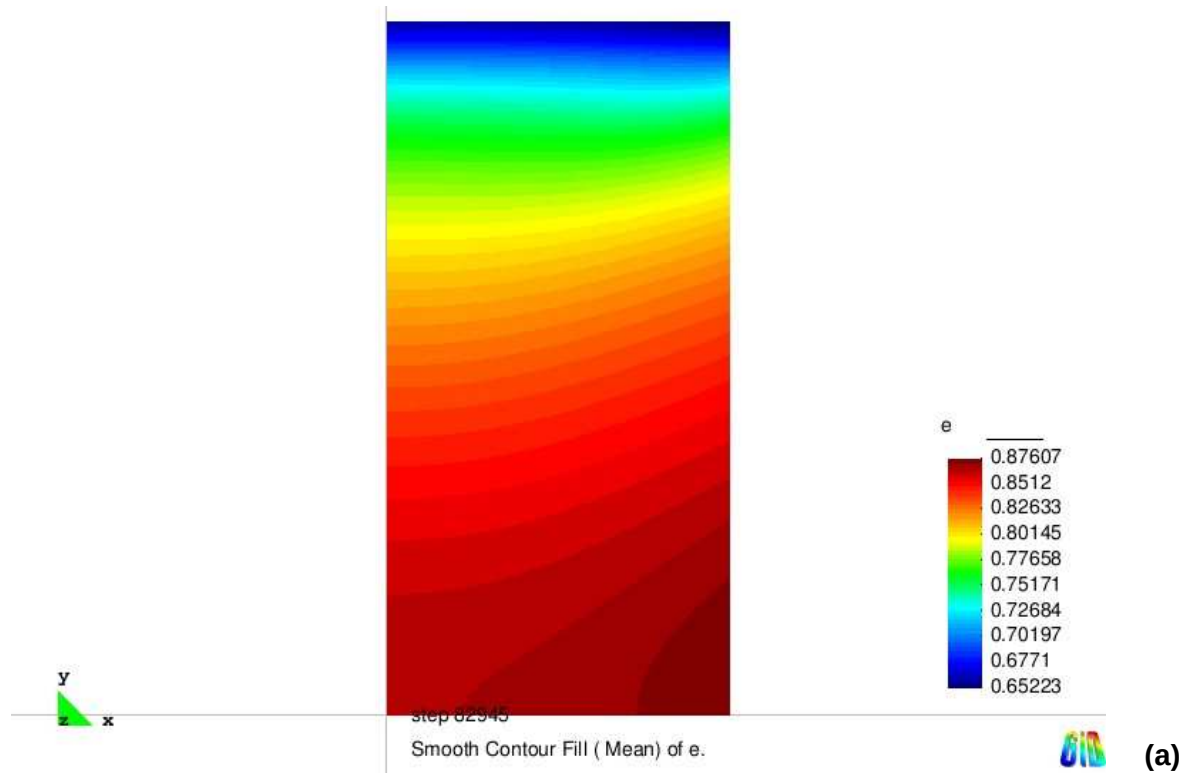

(a)

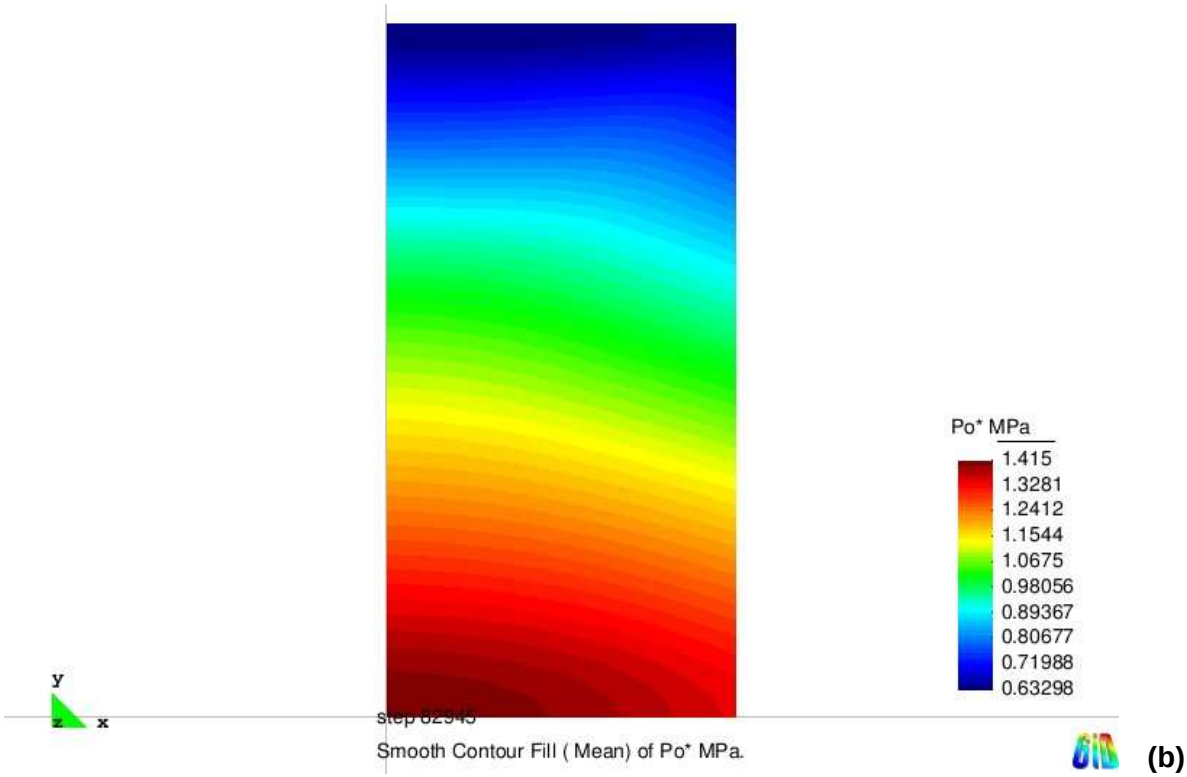

(b)

Figure 7- 11 Computed results at final time; (a) void ratio e; (b) hardening parameter p_0^*.

Figure 7-12 presents the results for horizontal displacements (Figure 7-12a) and vertical displacements (Figure 7-12b). As expected, horizontal displacements are effectively zero (i.e. $3.2 \cdot 10^{-17}$ m) along the axisymmetric vertical axis, and vertical displacements are

effectively zero ($5.8 \cdot 10^{-06}$ m) on the bottom boundary of the FE mesh, as imposed with the mechanical boundary conditions (see Figure 7-8). Horizontal displacements throughout the FE mesh are towards the axisymmetric vertical axis (i.e. negatives values of horizontal displacements) and vertical displacements are downwards (negative values of vertical displacement). This is simply a consequence of the occurrence of wetting-induced collapse compression producing compression in both horizontal and vertical directions. Horizontal displacements are largest in the upper part of the sample, where wetting has progressed further and the collapse compression is greatest. Vertical displacements are also greatest at the top of the mesh, but this simply reflects the accumulated vertical compression between the bottom of the mesh (which is assumed not to displace vertically) and the point in question.

Both horizontal and vertical displacements show significant variation with radius (contours of u_x and u_y are not horizontal in Figure 7-12). This is discussed further below. Figure 7-13 shows the final deformed shape of the sample (compared against the original shape). This highlights the marked reduction of sample diameter in the upper part of the sample, where large wetting induced collapse compression has occurred, leading to compressive straining in both vertical and horizontal directions. Figure 7-13 also shows the marked non-uniformity of vertical displacement across the top boundary of the sample, as a consequence of imposing a flexible stress-controlled boundary condition on this boundary.

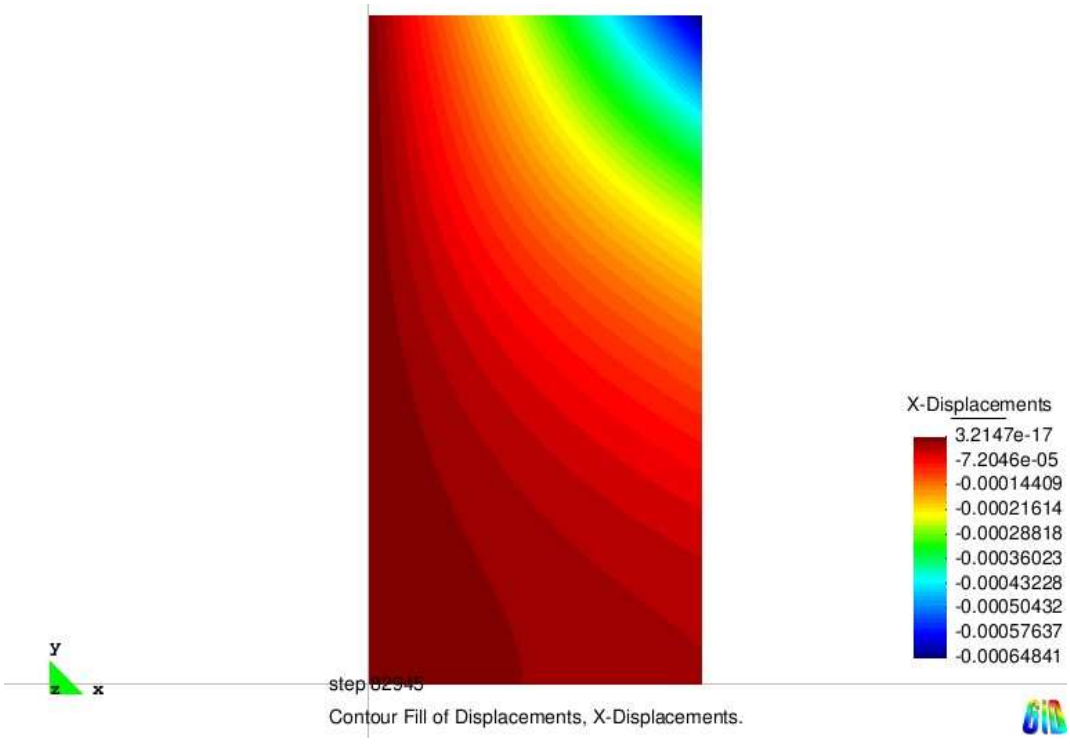

(a)

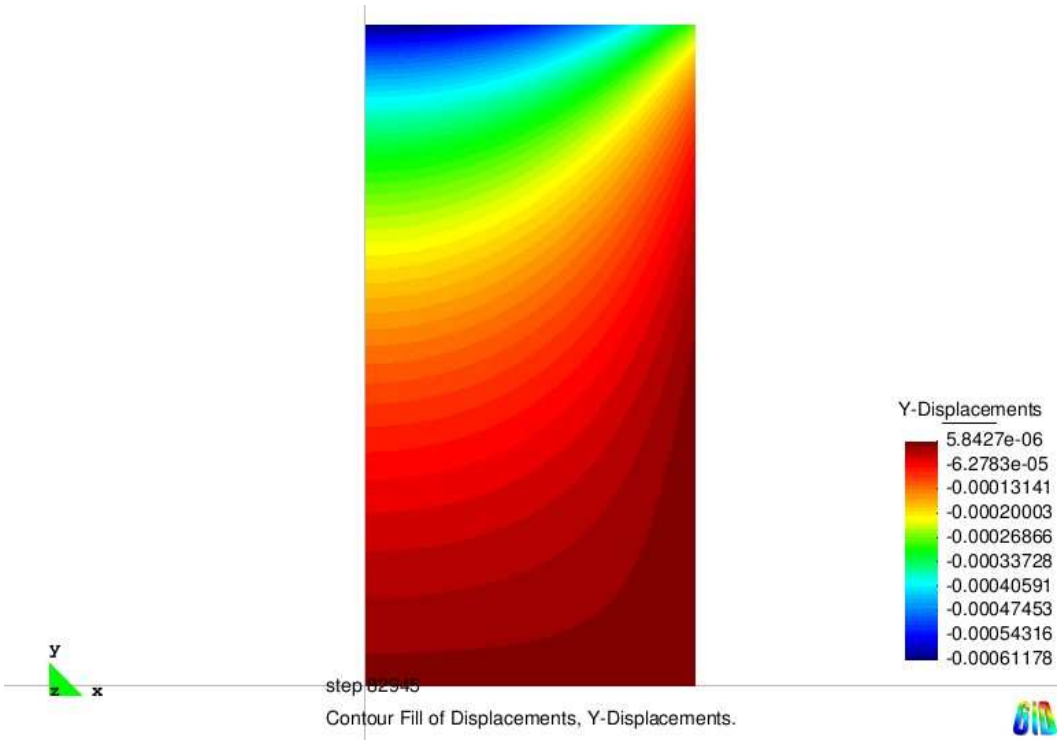

(b)

Figure 7- 12 Computed results at final time; (a) horizontal displacements u_x; (b) vertical displacements u_y.

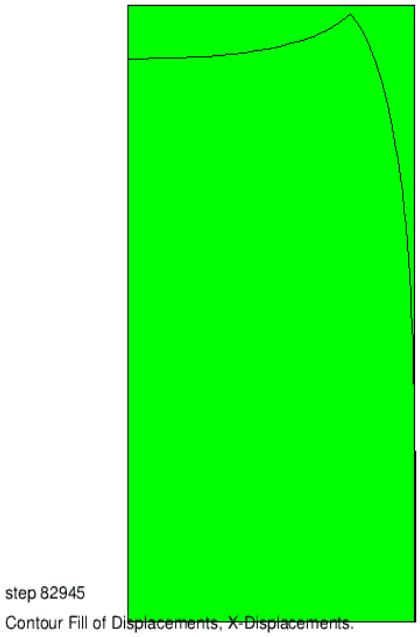

Figure 7- 13 Original and deformed sample.

7.9.3.2. Temporal evolution at fixed positions

This section examines temporal evolutions of pore liquid pressure, void ratio, degree of saturation, vertical displacement and horizontal displacement, at three selected points shown as *A*, *B* and *C* in Figure 7-14.

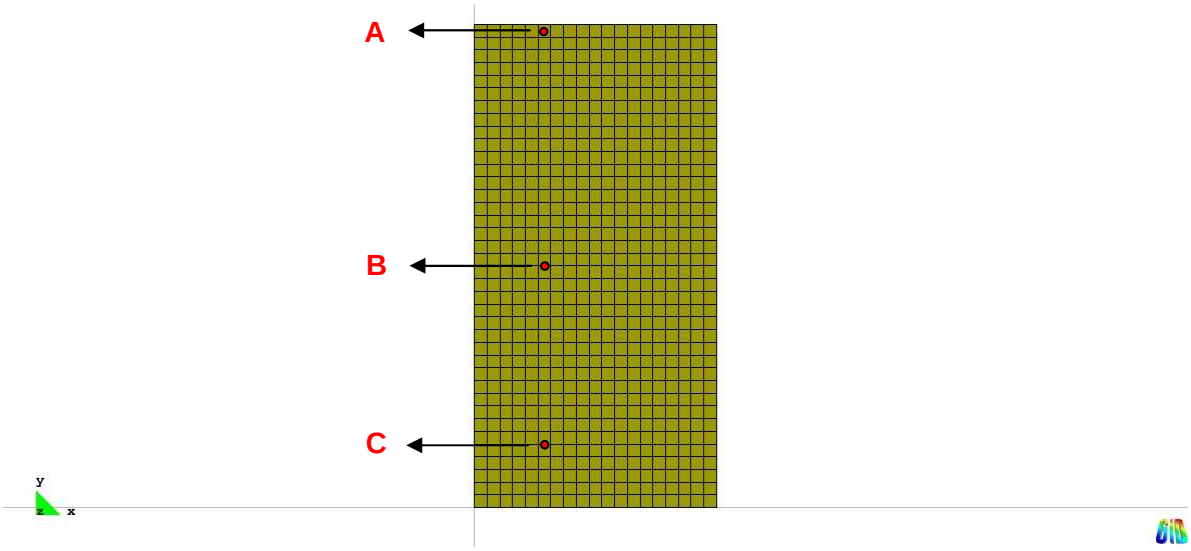

Figure 7- 14 Positions of A, B and C in the finite element mesh.

Figure 7-15 shows how the pore liquid pressure u_l varies with time at points *A*, *B* and *C*. As expected, at *A* (the highest position analysed, almost at the top of the soil sample) the variation of pore liquid pressure changes from the initial value u_l=-1.8 MPa to almost the final value imposed on the top boundary (u_l=0.04 MPa) (see Section 7.9.1). As illustrated in Figure 7-15, pore liquid pressure initially shows no change at points *B* and *C*, before finally starting to rise, first at *B* and then at *C*. This is entirely to be expected, with pore liquid pressure rising later the greater the distance from the boundary where wetting is applied.

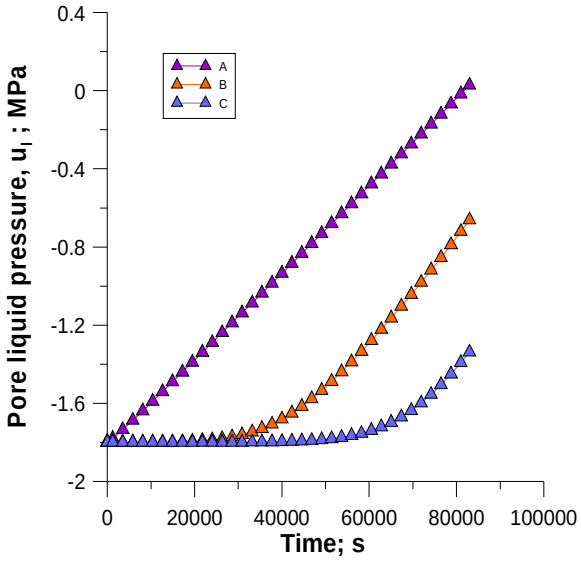

Figure 7- 15 Temporal evolution of pore liquid pressure u_l at points A, B and C.

Figure 7-16a gives information on void ratio and Figure 7-16b on degree of saturation changes against time at points *A*, *B* and *C*. As expected, degree of saturation starts to rise

earlier and shows a greater final rise the closer the point is to the top boundary. Similarly, void ratio starts to fall earlier and shows a greater final fall the closer the point is to the top boundary. This simply reflects the gradual progression of wetting, and associated collapse compression, downwards through the sample from the top boundary where the wetting is imposed.

Figure 7-17 plots computed horizontal (Figure 7-17a) and vertical (Figure 7-17b) displacements against time for points *A*, *B* and *C*. Again it is possible to observe the effect of the wetting gradually progressing down through the sample.

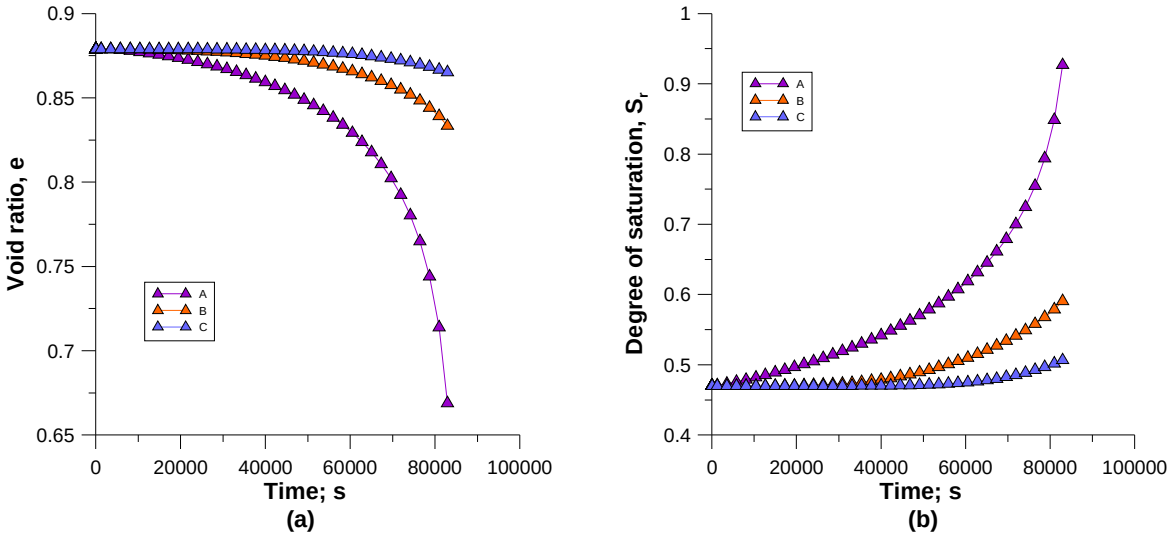

Figure 7- 16 Temporal evolution analysis at points A, B and C: (a) void ratio e; (b) degree of saturation S_r.

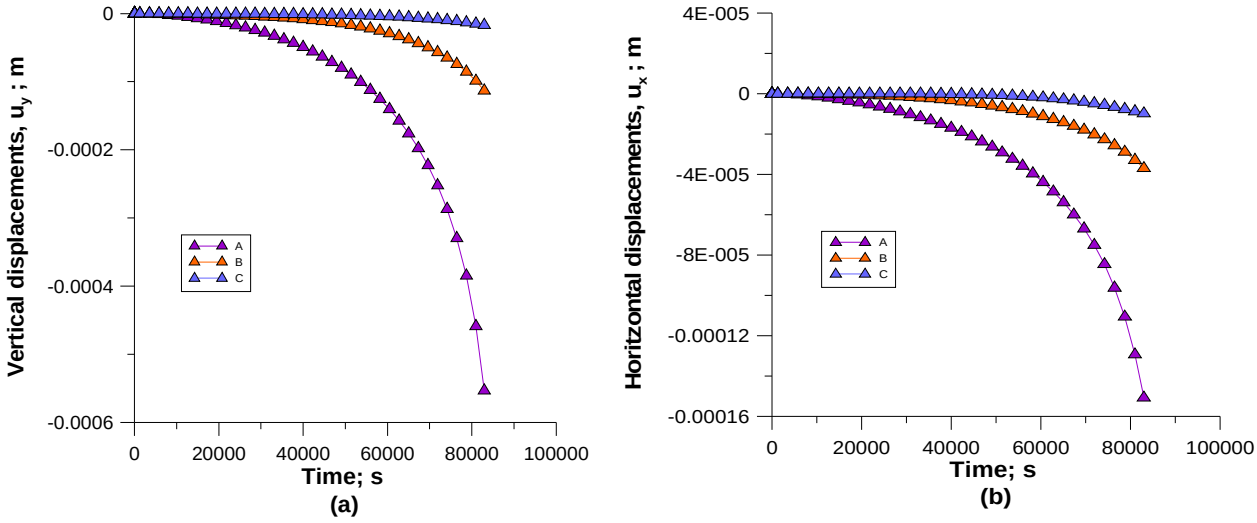

Figure 7- 17 Temporal evolution analysis at points A, B and C: (a) vertical displacements u_y; (b) horizontal displacements u_x.

7.9.3.3. Results from a vertical cross section at different times

This section shows the evolution, at different times, of several key variables of the model along the vertical cross section *YY* illustrated in Figure 7-18.

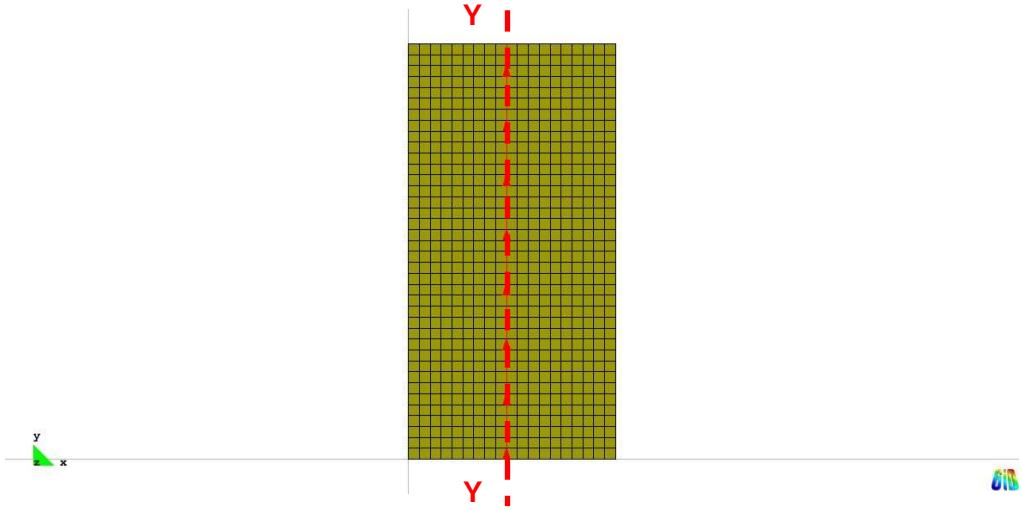

Figure 7- 18 Vertical cross section YY.

Figure 7-19 examines how the pore liquid pressure varies along *YY* at four different times (t_1, t_2, t_3 and t_4 where t_1=0min is the starting time of the test, t_4=82.945min corresponds to the final time, t_2=35.438min and t_3=62.778min are two intermediate time values). At t_1, the value of pore liquid pressure is constant for the full vertical cross section *YY* and is equal to the imposed initial value (u_l=-1.8MPa). At t_2, the influence of the wetting from the top boundary has reached approximately half way down through the mesh, with pore liquid pressure still unchanged (u_l=-1.8MPa) in the lower part of the finite element mesh. By the final time t_4 the influence of the wetting has reached all parts of the specimen, although the rise of pore water pressure is still relatively small at the base of the FE mesh.

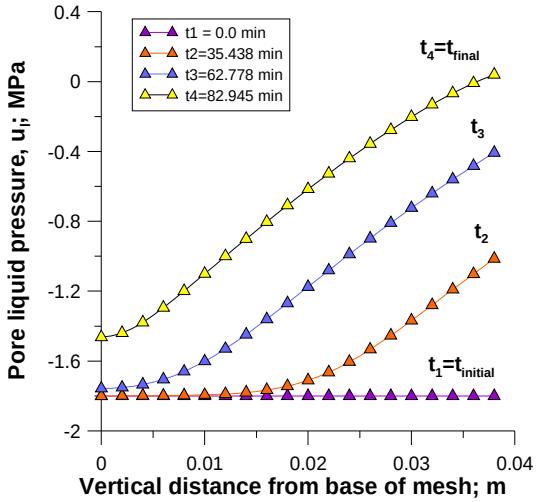

Figure 7- 19 Computed results of pore liquid pressure for vertical cross section YY at different times.

Figures 7-20, 7-21 and 7-22 show, for the vertical cross section *YY*, the variations of void ratio *e*, hardening parameter p_0^*, degree of saturation S_r, hardening parameter s_D^*, vertical displacement u_y and horizontal displacement u_x, at times t_1, t_2, t_3 and t_4. All the variations shown in Figures 7-20 to 7-22 are consistent with wetting and associated collapse compression gradually progressing downwards through the soil from the top boundary.

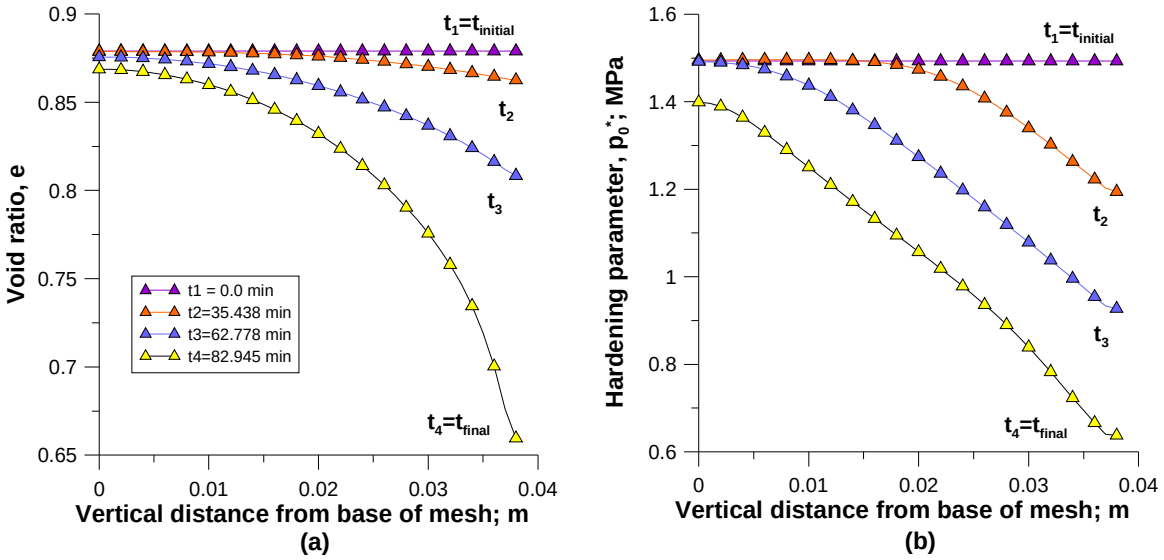

Figure 7- 20 Computed results for vertical cross section YY at different times: (a) void ratio e; (b) hardening parameter p_0^*.

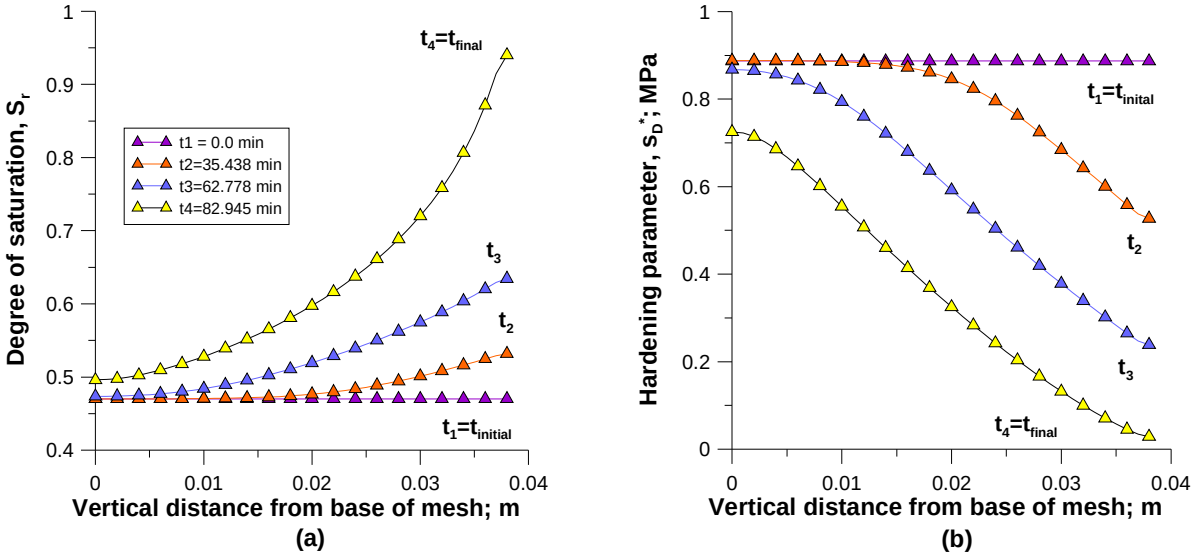

Figure 7- 21 Computed results for vertical cross section YY at different times: (a) degree of saturation S_r; (b) hardening parameter s_D^*.

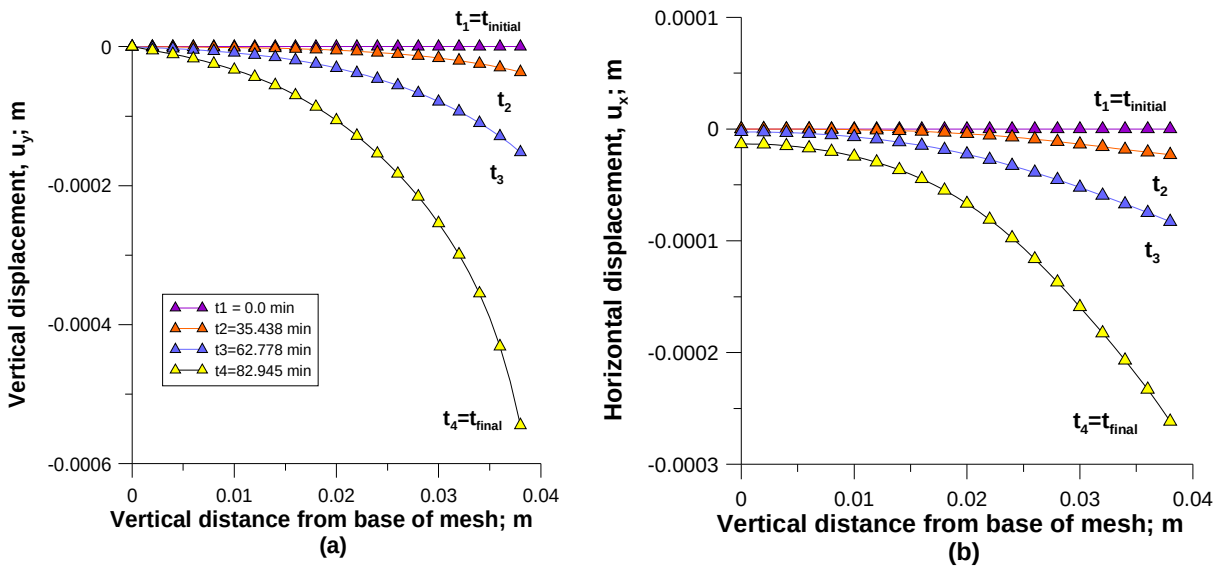

Figure 7- 22 Computed results for vertical cross section YY at different times: (a) vertical displacements u_y; (b) horizontal displacements u_x.

7.9.3.4. Results from an horizontal cross section at different times

This section shows the evolution of several key variables of the model along the horizontal cross section *XX* illustrated in Figure 7-23. The analysis is made for the four same times presented in the previous section (i.e. t_1, t_2, t_3 and t_4).

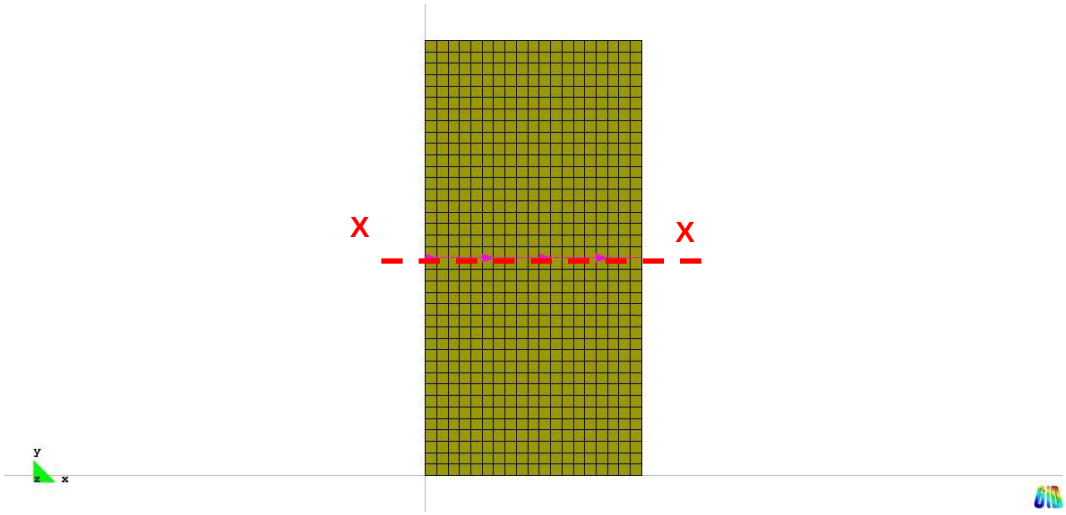

Figure 7- 23 Horizontal cross section XX.

Figure 7-24 presents how the pore liquid pressure varies across the horizontal cross section *XX* at the four mentioned times (t_1, t_2, t_3 and t_4). As expected, the initial value of pore liquid pressure (i.e. u_l=-1.8MPa) is observed along the horizontal cross section for t=0min. As time progresses the value of u_l gradually increases (as expected), and at any particular time there is no noticeable variation of u_l with radius.

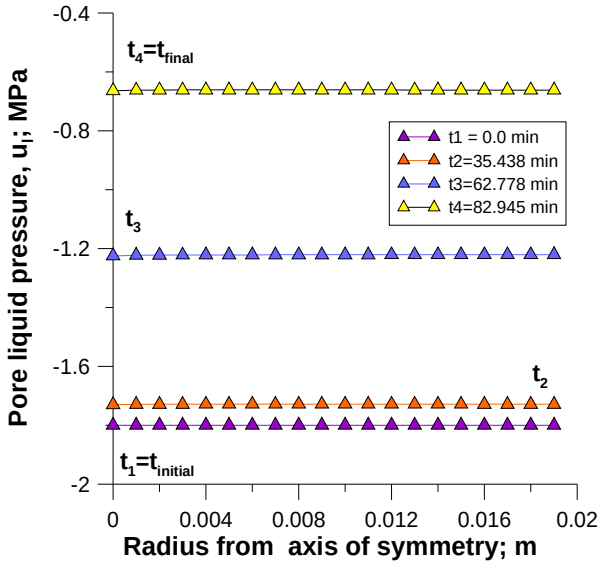

Figure 7- 24 Computed results of pore liquid pressure for horizontal cross section XX at different times.

Figure 7-25 and 7-26 show how the void ratio e, hardening parameter p_0^*, degree of saturation S_r, hardening parameter s_D^* vary with radius across the cross-section XX at the four different times t_1, t_2, t_3 and t_4. The figures clearly show the expected increase of S_r and decrease of e with time, as wetting progresses at the level of cross-section XX. However, what is also clear from Figure 7-25, is that, at any given time after the start of wetting, void ratio e and hardening parameter p_0^* show significant variation with radius. Close inspection of Figure 7-26 shows that degree of saturation S_r and hardening parameter s_D^* also vary slightly with radius (the latter is almost imperceptible).

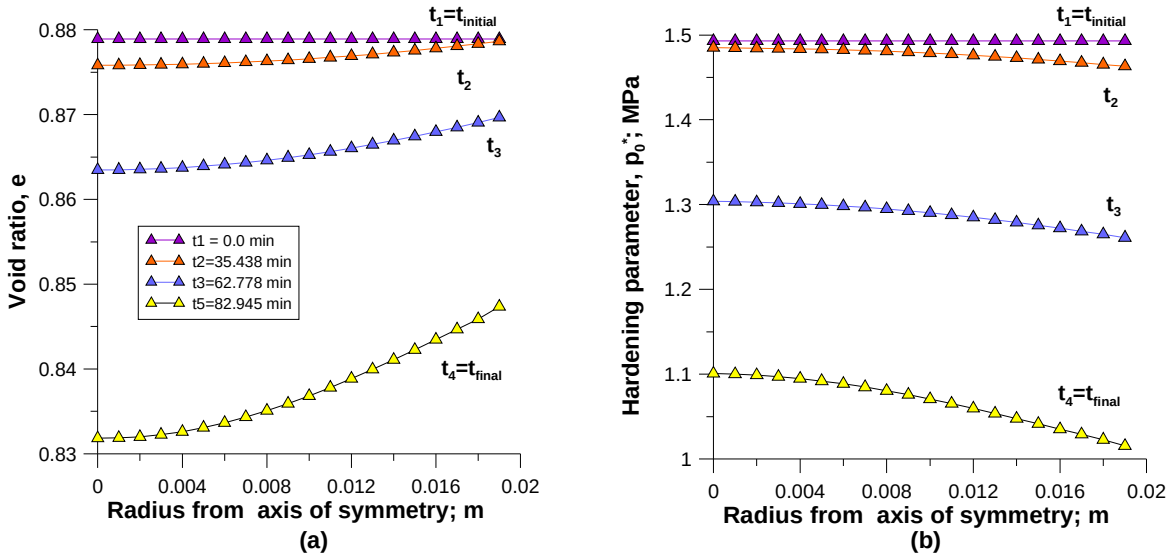

Figure 7- 25 Computed results for horizontal cross section XX at different times: (a) void ratio e; (b) hardening parameter p_0^*.

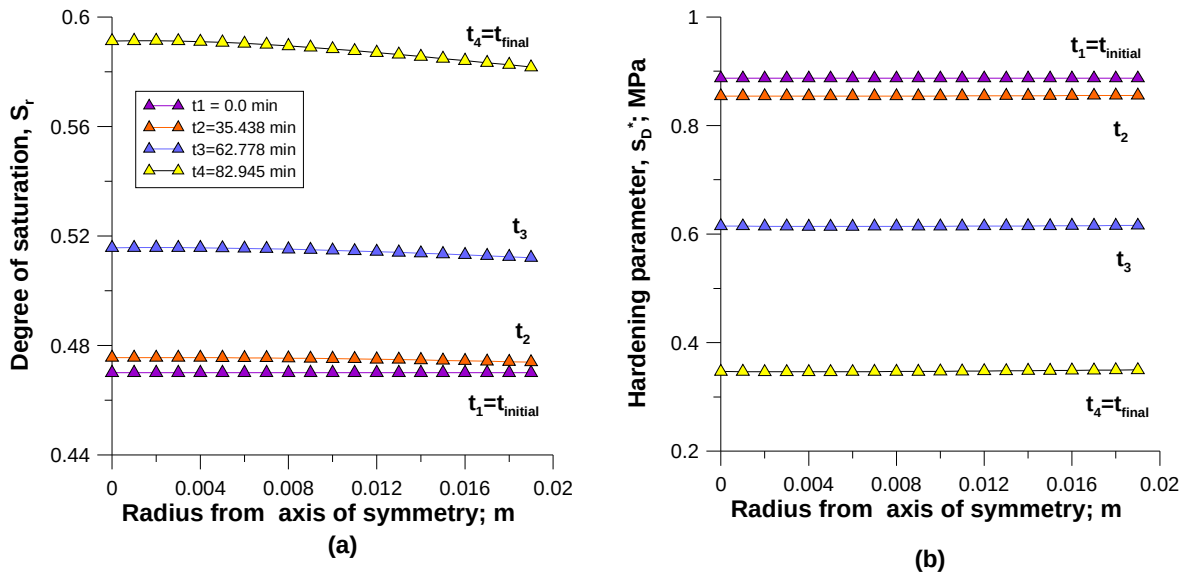

Figure 7- 26 Computed results for horizontal cross section XX at different times: (a) degree of saturation S_r; (b) hardening parameter s_D^*.

The variations with radius of void ratio *e*, degree of saturation S_r and other variables shown in Figures 7-25 and 7-26 and also apparent in various contours plots such as Figure 7-11 and 7-10, are a consequence of the fact that, as wetting progresses, a spatially varying total stress field (and, hence, net stress field) develops within the sample. Inspection of Figure 7-13 (the deformed shape of the sample) shows that, with wetting progressing faster at the top of the soil sample than at the mid-plane (represented by the bottom of the FE mesh), at any given time there will be greater radial compression at the top than at the mid-plane. This strain pattern produces changes in the total stress field within the statically indeterminate problem. For example, shear stresses will develop on horizontal planes, as the soil closer to the top boundary attempts to deform horizontally (due to wetting induced collapse compression) and is restrained by the soil below. As this process develops mean total stress *p* (and mean net stress $\overline{p}$) becomes non-uniform throughout the sample and deviator stress *q* becomes non-zero and non-uniform.

Given the development of shear stresses on horizontal planes described above (and development of complementary shear stresses on vertical planes), rotation of principal stress directions also occurs within the interior of the sample, with axial (vertical) and radial (horizontal) stresses no longer principal stresses. The out-of-plane (circumferential) stress remains a principal stress. At any point within the interior of the sample all three principal stresses can be different in magnitude, and mean net stress $\overline{p}$, scalar value of deviatoric stress *q* and Lode angle θ all vary both spatially and temporally.

Figure 7-27 shows the variation of mean net stress $\bar{p}$ and scalar value of deviatoric stress *q* (defined in Appendix A.1 by Equation (A1.23)) with radius across the horizontal cross section *XX* at the four different times t_1, t_2, t_3 and t_4. This shows that initially (at $t=t_1$) mean net stress $\bar{p}$ is uniform across the cross-section at $\bar{p}$=0.6 MPa and deviatoric stress *q* is zero across the cross-section (this applies through the entire sample at $t=t_1=0$). However, as time progresses, $\bar{p}$ becomes non-uniform, with higher values close to axis of symmetry and lower values towards the outer boundary. At the same time, significant values of deviatoric stress *q* develop. At times t_3 and t_4, values of *q* are highest on the axis of symmetry and at the outer boundary, with a near isotropic stress state ($q\cong0$) at an intermediate radius of approximately 0.013 m. At time t_4, the plot of *q* against radius appears to have a discontinuity of gradient at the point where *q* is zero. However, this is simply a consequence of the use of the generalised scalar value of q (which is always positive for anisotropic stress states) and the fact that the stress path passes through the origin in the deviatoric plane at this point (with a 180° change in Lode angle).

The fact that the mean net stress $\bar{p}$ and deviatoric stress q both vary with radius once wetting commences, explains the observed variation with radius of variables such as void ratio *e* and degree of saturation S_r. As points at different radii are following different imposed net stress paths it is inevitable that the mechanical and water retention responses of the soil at these different points will differ. In particular, mean net stress $\bar{p}$ is highest close to the axis of radial symmetry (see Figure 7-27a) and relatively high values of deviatoric stress *q* also occur close to the axis of symmetry (see Figure 7-27b), and these facts explain why collapse compression is greatest close to the axis of symmetry (see lower values of void ratio close to the axis of symmetry in Figure 7-25a and Figure 7-11a). A FE simulation of the same boundary value problem but using BBM as the mechanical constitutive model produced the same qualitative variation of void ratio with radius. It is important therefore to appreciate that the prediction of soil response varying with radius is not a consequence of the choice of constitutive model.

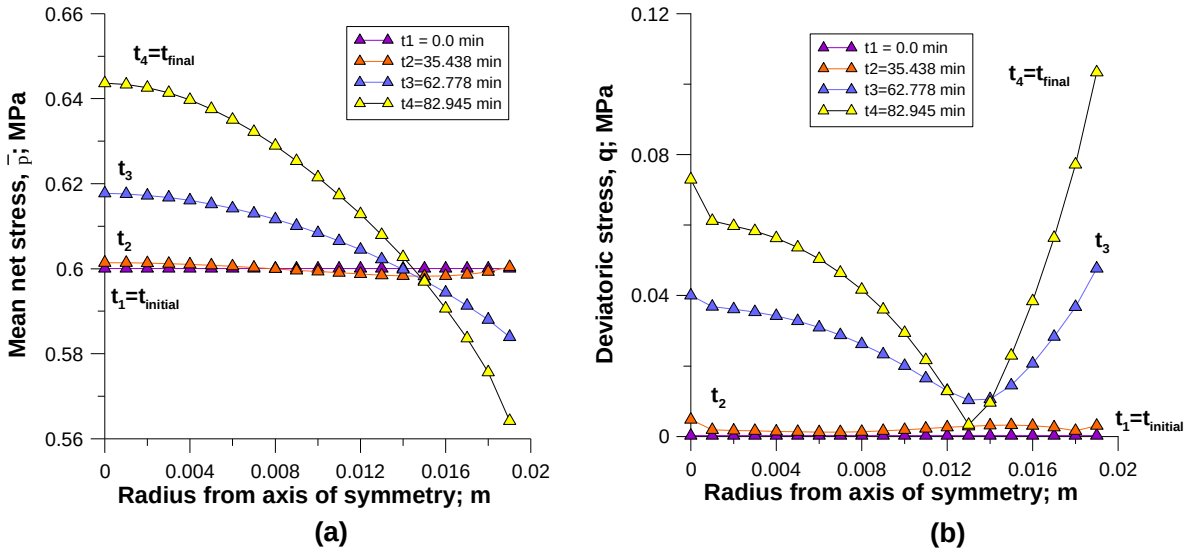

Figure 7- 27 Computed results for horizontal cross section XX at different times: (a) mean net stress $\bar{p}$; (b) deviatoric stress q.

Figure 7-28 shows the predicted variations of vertical displacement u_y and horizontal displacement u_x with radius across the horizontal cross section *XX* at the four different times t_1, t_2, t_3 and t_4.

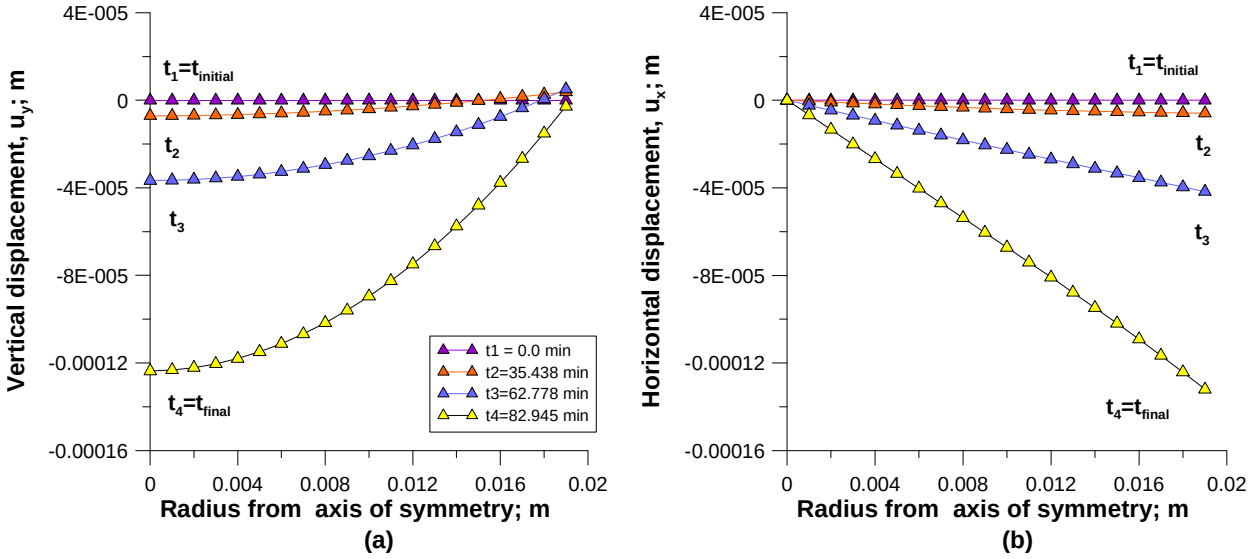

Figure 7- 28 Computed results for horizontal cross section XX at different times: (a) vertical displacements u_y; (b) horizontal displacements u_x.

7.9.3.5. Final discussion

Sections 7.9.3.1 to 7.9.3.4 showed that the results of the FE simulation of this boundary value problem were qualitatively sensible. This included the prediction of variables such as void ratio *e* and degree of saturation S_r varying with radius once the wetting

commenced (this was shown to be consistent with the development of a non-uniform net stress field and it also occurred when a more conventional mechanical constitutive model was used within the FE code). The fact that the results of FE simulations for a boundary value problem involving both spatial and temporal variation of variables are qualitatively sensible suggests that the FE code is working correctly following the implementation of the following implementation of the generalised 3D version of the Wheeler et al. (2003) constitutive model.

Figure 7-29 shows the variation of void ratio from the FE results at individual points *A*, *B* and *C* (see Figure 7-14) plotted against the corresponding values of p^* and s^* at these points, by representing the two orthogonal 2-dimensional views of e:lnp^*:lns^* introduced in Sections 2.7.2 and 4.4. Figure 7-30 shows the corresponding variation of degree of saturation from the FE results at points *A*, *B* and *C*. Also shown in these figures, by dashed lines, are the two dimensional views of the unique planar surfaces in e:lnp^*:lns^* and S_r:lnp^*:lns^* spaces predicted by the constitutive model for both isotropic stress states and for critical states (assuming simultaneous yielding on both *LC* and *SD* yield surfaces, as was occurring throughout the FE simulation).

If the stress states at points *A*, *B* and *C* had remained isotropic throughout the FE simulation of wetting (as s^* and p^* both decreased), the FE results shown in Figures 7-29 and 7-30 should have exactly followed the dashed lines corresponding to the constitutive model predictions for isotropic stress states. However, the FE simulation shows deviatoric stress q gradually developing as the wetting progresses. As a consequence, the expected behaviour is that the FE simulation results shown in Figures 7-29 and 7-30 should gradually drift away from the dashed lines corresponding to isotropic stress states and move slightly towards the dashed lines corresponding to critical states. Careful inspection of the FE results shown in Figures 7-29 and 7-30 shows that this is precisely what happens. The FE results only move very slightly towards the dashed lines corresponding to critical states, because deviator stresses remain much lower than those corresponding to critical states.

Overall, therefore, the evidence presented in Section 7.9 reinforces the conclusion that the implementation of the new constitutive model within the FE code is working correctly during the solution of a boundary value problem involving both spatial and temporal variations of variables.

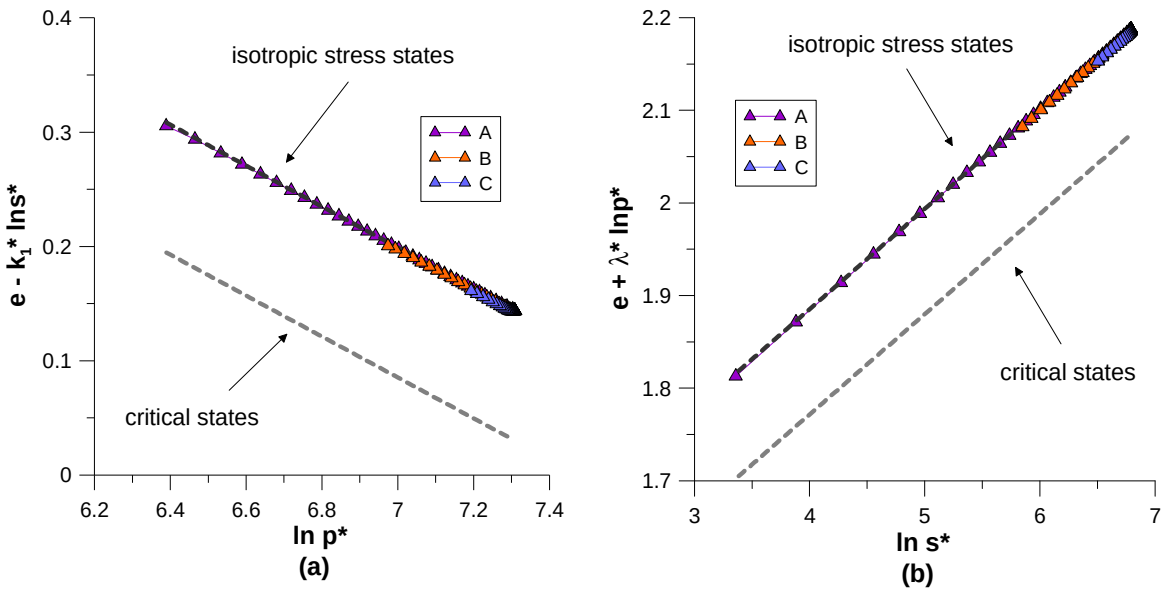

Figure 7- 29 Orthogonal 2-dimensional views of FE predictions in the e:lnp:lns* space for A, B and C.*

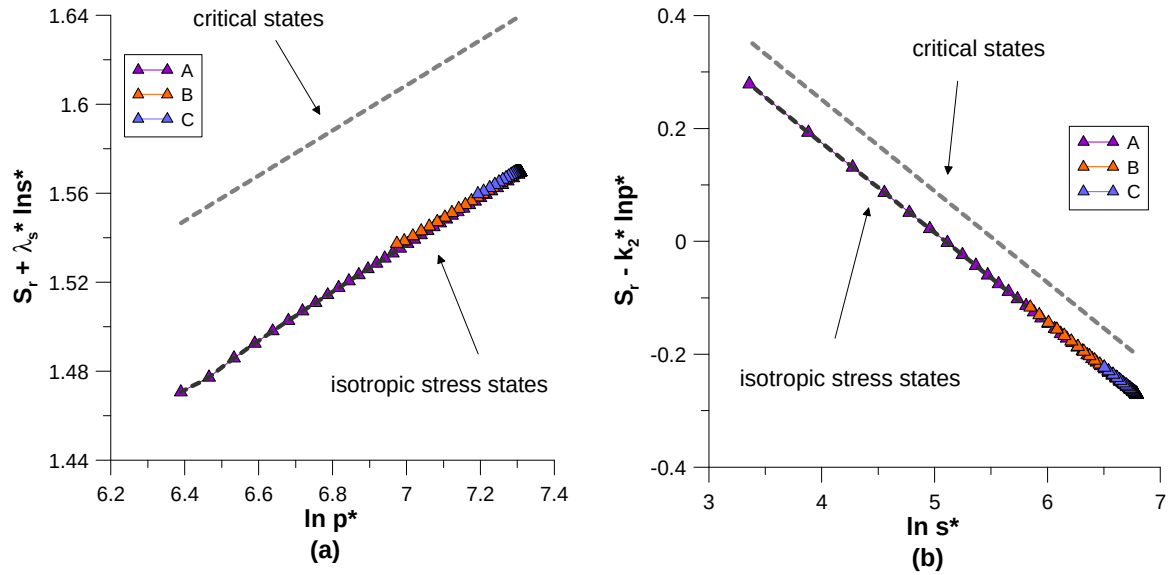

Figure 7- 30 Orthogonal 2-dimensional views of FE predictions in the Sr:lnp:lns* space for A, B and C.*

Chapter 8

CONCLUSIONS AND RECOMMENDATIONS

8. Conclusions and recommendations

The following sections are intended to summarise the main conclusions of the research described within this thesis including some suggestions and recommendations for the future work.

8.1. Constitutive modelling

8.1.1. Isotropic normal compression relationships

Two unique normal compression relationships predicted by the model for simultaneous yielding on the *LC* and *SD* yield surfaces were presented in Chapter 2: one of them linking specific volume v to mean Bishop's stress p^* and modified suction s^*, and the other one linking degree of saturation S_r to p^* and s^*. They define two planar surfaces, one in v:lnp^*:lns^* space and one in S_r:lnp^*:lns^* space. A limitation on these relationships predicted was that the soil remains under unsaturated conditions (i.e. $0<S_r<1$).

The model prediction of unique planar surfaces in v:lnp^*:lns^* space and in S_r:lnp^*:lns^* space during simultaneous yielding on *LC* and *SD* was validated against the experimental results of Sivakumar (1993) on compacted speswhite kaolin. The fact that the proposed planar surfaces for v and S_r provided an excellent match to the experimental results of Sivakumar (1993) was a significant component of experimental validation of the Wheeler et al. (2003) model. The predicted existence and predicted form of the two unique planar surfaces arose from the combination of several key components of the model, most notably the existence and assumed mathematical forms of the two coupling relationships in the model (Equations (2-20) and (2-22)) something that was not entirely clear at the time of the original formulation of the model by Wheeler et al. (2003).

Furthermore, it was shown that presenting experimental normal compression results in these spaces (i.e. v:lnp^*:lns^* and S_r:lnp^*:lns^*) gave an ideal method for determining the soil parameters employed within the coupled model. Based on this result, a new methodology was proposed to calibrate the constitutive model against experimental data, which was demonstrated with the experimental data of Sivakumar (1993).

8.1.2. Critical state relationships

The previous analysis under isotropic normal compression conditions was extended to critical states. Assuming again simultaneous yielding on the *LC* and *SD* surfaces, and that the soil remained under unsaturated conditions (i.e. $0<S_r<1$), a pair of critical state relationships expressing the ultimate values of specific volume and of degree of

saturation, in terms of mean Bishop's stress and modified suction variations, were developed from the model equations. The representation of these critical state relationships in v:lnp^*:lns^* and S_r:lnp^*:lns^* spaces showed a second pair of unique planar surfaces. Equivalent to the work presented when developing the isotropic normal compression relationships, the experimental critical state data of Sivakumar (1993) were plotted in these spaces. The results showed a very satisfactory fit to the experimental data.

In particular the results showed that the two planar surfaces for v were parallel, as predicted by the model, but that the vertical spacing between the critical state and isotropic normal compression surfaces for v was significantly overpredicted by the model (by a factor of approximately 2). As mentioned in Chapter 4, this is a common observation when the predictions of Modified Cam Clay (*MCC*) are compared with experimental data for saturated soils. It can therefore be viewed as a weakness of *MCC* that has been transferred through to the extended version of the Wheeler et al. (2003) model, by the assumption of *MCC* as the saturated base model.

The experimental results of Sivakumar (1993) presented also showed that the two planar surfaces for S_r were parallel, as predicted by the model. It was observed in this case that the vertical spacing between the critical state and isotropic normal compression surfaces for S_r predicted by the model provided a good match to the experimental results.

The relationships proposed and experimentally validated using the Sivakumar (1993) data, provided an easy and understandable framework to represent aspects of the observed coupling between mechanical and water retention behaviour in unsaturated soils. Both pairs of planar surfaces (i.e. isotropic normal compression planar surfaces for v and S_r, and critical state planar surfaces for v and S_r) using the Wheeler et al. (2003) constitutive model (and the extension of the model to triaxial stress states) were presented in a rather simple mathematical form and, as illustrated with the results of Sivakumar (1993), were capable of capturing well the variations of void ratio and degree of saturation when irreversible changes of both variables took place due to simultaneous yielding on *SD* and *LC* yield surfaces. The way in which these mathematical expressions were presented showed a useful parallelism with the Cam Clay family of models, in describing void ratio changes under isotropic stress conditions and at critical states, but also, in this case, extended to include degree of saturation changes under isotropic stress conditions and at critical states. Although not all the predictions presented showed an excellent match with the experimental data of Sivakumar (in particular the over-prediction of the spacing between the normal compression and critical state surfaces for v), this new

approach is thought to be a significant contribution to understanding and modelling of the coupling between mechanical and water retention behaviour in unsaturated soils.

8.1.3. 3D extended version of the constitutive model

Before implementing the coupled mechanical- water retention constitutive model into a finite element program it was necessary to extend the formulation to 3D stress conditions (the original formulation proposed by Wheeler and co-workers was presented only for isotropic stress conditions). The 3D extended version of the fully coupled model was proposed in Chapter 5 and validated against experimental data of seventeen triaxial tests performed by Sivakumar (1993).

The generalised 3D model was formulated in terms of the three invariants (p^*, J, θ) (where: p^* is the first invariant of the Bishop's stress tensor: $p^*=1/3(\sigma_1^*+\sigma_2^*+\sigma_3^*)$; J is the second invariant of the deviatoric Bishop's stress tensor: $s_{ij}^*=\sigma_{ij}^*-\delta_{ij}p^*$ and θ is the Lode angle) and the modified suction (s^*).

The generalised version of the constitutive model was afterwards partially validated against experimental results of Sivakumar (1993) involving isotropic and triaxial stress paths at three different constant values of suction (100 kPa, 200 kPa and 300 kPa). Overall, the model predictions provided a reasonable match to the mechanical and water retention behaviour observed in the experimental tests of Sivakumar (1993). The significant mis-matches between model predictions and experimental results arose because the spacing between normal compression planar surface and critical state planar surface in the v:lnp^*:lns^* space is over-predicted and because the development of shear strain during plastic straining is not accurately predicted. These weaknesses are also apparent in the Modified Cam Clay model for saturated soils which has been used as the saturated base model in the extension of the Wheeler et al. (2003) model to triaxial stress states. The weaknesses seem to arise because of the choice of elliptical cross-sections of the *LC* yield surface and the use of an associated flow rule on this surface.

From the comparison of model simulations with the experimental results of Sivakumar (1993) it appears that the extended model of Wheeler et al (2003) is able to represent the mechanical and water retention behaviour of unsaturated soils with the same level of success as can be achieved by Modified Cam Clay in representing the mechanical behaviour of saturated soils. If this is true, it represents a major success on the part of the Wheeler et al. (2003) model.

It should, however, be appreciated that the comparison of model predictions with the experimental results of Sivakumar (1993), presented in this research, represents only a partial validation of the extended model of Wheeler et al. (2003). In particular, the results of Sivakumar (1993) do not show directly the effects of hydraulic hysteresis on water retention and mechanical behaviour, because Sivakumar's tests did not generally involve reversals of suction (the tests shown here involved wetting during the initial equalization stage and then constant suction during the remainder of each test). This absence of the effects of hydraulic hysteresis on the soil behaviour reported in the tests of Sivakumar (1993) means that the mechanical behaviour in these tests can be adequately represented by a more conventional unsaturated elasto-plastic mechanical constitutive model expressed in terms of net stresses and suction (see, for example, Wheeler and Sivakumar, 1995). The additional achievement of the extended Wheeler et al. (2003) model in simulating these tests is that it is also able to accurately predict the variation of degree of saturation S_r.

Full validation of the extended model of Wheeler et al. (2003) will require comparison with experimental results involving strong reversals of suction, where the impact of hydraulic hysteresis on water retention and mechanical behaviour is crucial. Inability to model properly this type of situation was identified by Wheeler et al. (2003) as a weakness of existing mechanical constitutive models expressed in terms of net stresses and suction, and was the motivation behind their development of a new model. However, it is reassuring to see, in the partial validation of the extended Wheeler et al. (2003) model against the experimental results of Sivakumar (1993) presented here, that in developing a model capable of dealing with the complexities of the effects of hydraulic hysteresis on mechanical behaviour it has not been necessary to sacrifice any accuracy in the modelling of unsaturated soil behaviour when hydraulic hysteresis is not involved.

8.2. Numerical modelling

8.2.1. Numerical integration

The fundamental elasto-plastic components of the constitutive model (i.e. flow rules, hardening laws, plastic multipliers and elastic and elasto-plastic relationships) were presented in Chapter 3 for isotropic stress conditions along with a methodology to identify the elasto-plastic mechanism active. These ideas were then extended in Chapter 5 to the 3D version of the constitutive model, and were, afterwards, combined in Chapter 6 to present a complete strain-driver algorithmic formulation that enabled the update of the stress state variables (i.e. Bishop's stress tensor, modified suction, net stress tensor and

matric suction); updating also degree of saturation and void ratio. This was achieved by expressing the equations of the problem in terms of strain and matric suction increments, which are the driven or known inputs of the algorithmic scheme described.

8.2.2. Explicit strain-driver algorithms

Two different numerical approaches to integrate the new constitutive model (i.e. first order error forward Euler and second order error modified Euler) were presented in Chapter 6. Several aspects of their computational performance were discussed, highlighting the consistency of the computed results.

The complexity associated with the mathematical equations involved in the integration of the constitutive model of Wheeler et al. (2003) justified the extensive analysis of verification and checking presented in Chapter 6. This checking process was an important step before including this strain-driver algorithm into the finite element program CODE_BRIGHT. All the information presented in the analysis complemented prior discussions on the formulation proposed to numerically integrate the constitutive model. It was shown that, for the set of stress paths analysed (involving both one plastic mechanism and two plastic mechanisms acting simultaneously), the computed results obtained were consistent. This suggests that the constitutive model has been correctly integrated. The algorithm was then implemented in the finite element program CODE_BRIGHT to solve boundary value problems.

8.3. Implementation into CODE_BRIGHT

In Chapter 7, the strain-driver formulation presented and analysed within Chapter 6 was implemented into CODE_BRIGHT. Some aspects of the existing finite element program had to be extended in order to implement the new strain-driver scheme. Furthermore, some modifications of the strain-driver algorithm were also necessary to control the strain and matric suction increment sizes. A study of the computational performance of the implemented constitutive model was also conducted in Chapter 7, and the chapter then finished with the analysis of a simple boundary value problem.

8.3.1. Computational performance of the implemented constitutive model

The main modification in the proposed explicit algorithm was the inclusion of a subdividing strategy for strain and suction increments (i.e. *substepping*). The new implemented subroutine allowed the subdivision of the strain and suction increments into a specified number of substeps (referred to as *Nsubs*) in order to provide smoother computations to the non-linear solution. As mentioned above, re-arrangements were also necessary within

CODE_BRIGHT, which essentially were associated with updating of the degree of saturation, as the implemented constitutive model updates both types of state variable (stresses and degree of saturation) with no need of a separate model for the water retention behaviour.

Because of these modifications to the strain-driver subroutine and to the main finite element program, an analysis of computational aspects was presented, studying the performance of the new implemented model. The first part of the analysis consisted of studying the influence of the number of substeps on the CPU time. Also, the relative error of the computed void ratio and degree of saturation were related to the number of substeps adopted. A simple stress path involving isotropic loading and subsequent shearing at constant matric suction of a cylindrical sample was used in the analysis. As expected, an increase of the CPU time required for the computations was generally observed when increasing the number of substeps. This analysis essentially confirmed that the computed results from the newly implemented constitutive model were consistent, suggesting that the algorithm has been correctly implemented within the finite element program.

The previous investigation was complemented with a second analysis, intended to provide (partial) verification that the generalized 3D version of the Wheeler et al. (2003) model has been correctly implemented within the FE code. This was achieved by performing a finite element simulation of a problem where the results could be compared with corresponding results produced directly with the strain-driver algorithm. The output from the driver algorithm was itself previously verified by checking that isotropic loading states and critical states involving simultaneous yielding on *LC* and *SD* surfaces were correctly predicted to fall on the appropriate planar surfaces in v:lnp^*:lns^* and S_r:lnp^*:lns^* spaces (see Sections 5.5 and 6.6). Of course, using the output from the strain-driver algorithm as the reference against which the FE simulations were compared placed considerable restriction on the type of problem that could be analysed. In particular, the boundary value problem studied with the FE code had to be one where there was no spatial variation of suction or of other variables, so that it was essentially the same as a single element simulation (rather than a true boundary problem). This fact that the problem analysed involved no spatial variation of any variable means that this exercise can only be considered as partial verification of the correct FE implementation of the constitutive model.

The analysis showed that FE simulations were indistinguishable from strain-driver simulations in all respects, including the predicted stress path in the q:p^* plane, the predicted variations of void ratio e and degree of saturation S_r and the development of

shear strain (and hence axial strain). Given that the results of the strain-driver algorithm had already been verified, this comparison provided verification (at least for the limited condition of a boundary value problem involving no spatial variation of variables) of correct implementation in the finite element code.

8.3.2. Boundary value problem

A FE simulation of a simple boundary value problem, incorporating spatial variation of suction and other variables and therefore full solution of the coupled hydro-mechanical governing equations was presented in Chapter 7. The objective was simply to demonstrate the FE code, incorporating the extended 3D version of the Wheeler et al. (2003) constitutive model, working on a full boundary value problem. As the full boundary value problem analysed involved highly complex non-linear constitutive relations there was no analytical solution against which the FE results could be compared. Neither was there an alternative numerical solution against which the results could be compared. This exercise did not, therefore, constitute a formal verification of the correct implementation of the new constitutive model with the FE code. All that could be checked was that the FE code ran satisfactorily and that the results were qualitatively sensible. This provided increased confidence, but not formal verification, that the constitutive model has been correctly implemented in the FE code.

The results of the FE simulation of this boundary value problem were qualitatively sensible (Sections 7.9.3.1 to 7.9.3.4). This included the prediction of variables such as void ratio e and degree of saturation S_r varying with radius once the wetting commenced (this was shown to be consistent with the development of a non-uniform net stress field and it also occurred when a more conventional mechanical constitutive model was used within the FE code). The fact that the results of FE simulations for a boundary value problem involving both spatial and temporal variation of variables were qualitatively sensible suggested that the FE code is working correctly following the implementation of the following implementation of the generalised 3D version of the Wheeler et al. (2003) constitutive model.

A final analysis supporting that the FE implementation of the new constitutive model is working correctly was provided at the end of Chapter 7 by representing the two orthogonal 2-dimensional views of e:lnp^*:lns^* and S_r:lnp^*:lns^* spaces (see Figures 7-29 and 7-30). The two dimensional views of the unique planar surfaces in e:lnp^*:lns^* and S_r:lnp^*:lns^* spaces predicted by the constitutive model for both isotropic stress states and for critical states were also shown in these figures by dashed lines (assuming simultaneous yielding on

both *LC* and *SD* yield surfaces, as was occurring throughout the FE simulation). If the stress states of the simulations plotted had remained isotropic throughout the FE simulation of wetting, the FE results should have exactly followed the dashed lines corresponding to the constitutive model predictions for isotropic stress states. However, the FE simulation showed deviatoric stress q gradually developing as the wetting progressed. As a consequence, the expected behaviour is that the FE simulation results should gradually drift away from the dashed lines corresponding to isotropic stress states and move slightly towards the dashed lines corresponding to critical states. Careful inspection of the FE results showed that this was precisely the case. The FE results only moved very slightly towards the dashed lines corresponding to critical states, because deviator stresses remained much lower than those corresponding to critical states.

Overall, therefore, the evidence presented in Section 7.9 reinforces the conclusion that the implementation of the new constitutive model within the FE code is working correctly during the solution of a boundary value problem involving both spatial and temporal variations of variables.

8.4. Recommendations for future work

The extension, integration and further validation of the 3D version of the constitutive model presented in this thesis has helped to identify issues of the formulation that could be improved. In particular, the strain-driver formulation that was developed provides a mathematical framework to implement the constitutive model into a finite element program. There are obviously other types of algorithm that could be adopted; for example explicit formulations with automatic error control, such as those originally proposed by Sloan (1987); or implicit integration schemes. Also several improvements related to different computational aspects of the algorithms proposed are yet to be addressed. Now that the constitutive model has been successfully implemented in a finite element program, further analyses of different boundary problems would also be desirable. A more detailed discussion on possible new lines of future investigation is given below.

8.4.1. Constitutive modelling

The fully coupled constitutive model proposed by Wheeler et al. (2003) has now been extended to 3D stress conditions and has been partially validated against the experimental data provided in Sivakumar (1993). An interesting following step would be to investigate the possibility of including in the model other types of coupling, such as temperature and chemical effects. Also interesting would be to examine the response considering other possible formulations including, for instance, visco-plasticity.

The inconsistency identified in the Wheeler et al. (2003) constitutive model associated with occurrence of plastic volumetric strains while the soil is fully saturated or fully dry (see Section 2.6.3), should be further investigated in order to find a more satisfactory alternative than simply assuming κ_s=0. Related to this, it may be desirable to explore and analyse other possibilities in describing the water retention behaviour.

An important future research is the full experimental validation of the extended model of Wheeler et al. (2003) by further investigating the effects of hydraulic hysteresis on water retention and mechanical behaviour. As described above, full validation of the new extended model will require comparison with experiments involving strong reversals of suction, where the impact of hydraulic hysteresis on water retention and mechanical behaviour is crucial.

It would be an interesting future line of research to investigate further the validity of the isotropic normal compression and critical states relationships developed for the void ratio (and for the degree of saturation) by comparing them against more experimental results on unsaturated soils such as those recently presented in the work of Raveendiraraj (2009).

8.4.2. Algorithmic formulation

It would be very interesting to integrate this constitutive model using an automatic substepping algorithm similar to those proposed in Sloan et al. (1987) and subsequent papers. This integration scheme would optimise the efficiency of the computation as it would control, automatically, the size of the strain (and matric suction) increments depending on the non-linearity of the problem (see, for instance, Sheng et al., 2003) whilst maintaining second order accuracy.

Another important improvement that may be addressed is associated with the proposed intersection method between the stress path and the different surfaces. This intersection takes place when changing from elastic to elasto-plastic behaviour and it may be of interest to extend the analysis presented here using other intersection schemes such as those proposed in Abbo (1997).

Also another important aspect that still needs to be addressed is the inclusion in the algorithmic formulation (and subsequent full implementation) of the cases where S_r=1 or S_r=0.

8.4.3. Finite element implementation

Finally, another important area of further research would be to extend the analysis of boundary value problems using this and others constitutive models. Indeed, it would be an interesting future line of investigation to compare the solution obtained by solving a well-defined boundary value problem when using the new implemented model presented in this research and when using other more conventional mechanical and water retention constitutive models such as the Barcelona Basic Model and the van Genuchten equation respectively.

REFERENCES

References

Abbo, A. J. (1997). Finite element algorithms for elastoplasticity and consolidation. *PhD thesis*, University of Newcastle, Australia.

Alonso E.E. (1993). Unsaturated soils: recent developments and applications. Constitutive models of unsaturated soils. *Civil Engineering European Courses,* UPC, Barcelona, Spain.

Alonso, E. E., Gens, A. and Hight, D. W. (1987). Special problem soils. *General Rep. Proc., 9th European Conf. Soil Mechanics and Foundation Engineering*, Dublin, Vol. 3, pp.1087–1146.

Alonso, E.E., Gens, A., Josa, A. (1990). A constitutive model for partially saturated soils. *Géotechnique*, Vol.40 (3), pp. 405-430.

Baker, R. and Frydman, S. (2009). Unsaturated soil mechanics: Critical review of physical foundations. *Engng Geol.*, 106:26-39.

Barrera, M. (2002). Estudio experimental del comportamiento hidro-mecánico de suelos colapsables. *PhD thesis*, Universitat Politècnica de Catalunya, Spain.

Bishop, A. W. (1959). The principle of effective stress. *Teknisk Ukeblad*, Vol. 39, pp.859–863.

Burland, J. B. (1965). Some aspects of the mechanical behaviour of partly saturated soils. *Moisture Equilibria and Moisture Changes in the Soils Beneath Covered Areas*, G. D. Aitchison, ed., Butterworth, Sydney, Australia, pp.270–278.

Buscarnera, G. and Nova, R. (2009). An elasto-plastic strain hardening model for soil allowing for hydraulic bonding debonding effects. *Int. J. Numer. Anal. Methods Geomechanics*, 33: 1055–1086.

CODE_BRIGHT User's Manual (2011). Universitat Politècnica de Catalunya, Spain.

Crisfield, M. (1991). Non-linear finite element analysis of solids and structures Vol 1. *John Wiley & Sons Edit*.

Cui, Y.J. and Delage, P. (1996). Yielding and plastic behaviour of unsaturated compacted silt. *Géotechnique,* Vol. 46 (2), pp. 291-311.

Escario, V. and Saez, J. (1986). The shear strength of partly saturated soils, *Géotechnique*, Vol. 36(3), pp. 453-456.

François, B. (2008). Thermo-plasticity of fine-grained soils at various saturation statesApplication to nuclear waste disposal. *PhD thesis*, Ecole Polytechnique Fédérale de Lausanne, Switzerland.

Fredlund, D.G. and Morgenstern, N.R. (1976). Constitutive relations for volume change in unsaturated soils. *Canadian Geotechnical Journal*, Vol.13 (3), pp.261–276.

Fredlund, D.G. and Morgenstern, N.R. (1977). Stress state variables for unsaturated soils. *ASCE Journal of Geotechnical Engineering*. Vol. 103(5), pp. 447-466.

Gallipoli, D., Gens, A., Chen, G. and D'Onza, F. (2008). Modelling unsaturated soil behaviour during normal consolidation and at critical state, *Computers and Geotechnics*, Vol. 35 (6), pp.825-834.

Gallipoli, D., Wheeler, S. J. and Karstunen, M. (2003a). Modelling the variation of degree of saturation in a deformable unsaturated soil. *Géotechnique,* Vol. 53(1), pp. 105–112.

Gallipoli, D., Gens, A., Sharma, R. S. and Vaunat, J. (2003b). An elasto-plastic model for unsaturated soil incorporating the effect of suction and degree of saturation on mechanical behaviour. *Géotechnique,* Vol. 53(1), pp. 123-135.

Gens, A. (1996). Constitutive modelling: Application to compacted soils. In: *Unsaturated Soils* (Alonso, E.E. and Delage, P., eds), Balkema, Rotterdam, Vol. 3, pp. 1179-1200.

Gens A. (2009). Some issues in constitutive modelling of unsaturated soils. In: *Unsaturated Soils – Theoretical and Numerical Advances in Unsaturated Soil Mechanics* (Buzzi, O., Fityus, S.G. and Sheng, D., eds), CRC Press, pp. 613-626.

Gens, A. (2010). Soil-environment interactions in geotechnical engineering. *Géotechnique,* Vol. 60(1), pp. 3–74 (*47th Rankine Lecture*).

Gens, A. and Olivella, S. (2001). THM phenomena in saturated and unsaturated porous media. Fundamentals and formulation. *Revue Française de Génie Civil*, Vol 5, Nº 6, pp. 693-717.

Gens, A. and Potts, D. (1988). Critical state models in computational geomechanics, *Engineering Computations*, Vol.5, pp.178-197.

Gens, A., Sánchez, M. and Sheng, D. (2006). On constitutive modelling of unsaturated soils, *Acta Geotechnica*, 1: 137-147.

Guimarães, L. N. (2002). Análisis multi-componente no isotermo en medio poroso deformable no saturado. *PhD thesis*, Universitat Politècnica de Catalunya, Spain.

Hill, R. (1950). The Mathematical Theory of Plasticity. *Clarendon Press*, Oxford.

Houlsby, G. T. (1997). The work input to an unsaturated granular material. *Géotechnique,* Vol. 47(1), pp. 193–196.

Hueckel, T. (1992). Water-mineral interaction in hygromechanics of clays exposed to environmental loads: a mixture-theory approach. *Canadian Geotechnical Journal,* Vol. 29, pp. 1071-1086.

Jennings, J. E. B. and Burland, J. B. (1962). Limitations to the use of effective stresses in unsaturated soils. *Géotechnique,* Vol.12, pp. 125–144.

Jommi, C. (2000). Remarks on the constitutive modelling of unsaturated soils. *Proceedings of the international workshop on unsaturated soils*, Trento, pp. 139–153.

Josa, A. (1988). Un modelo elastoplastico para suelos no saturados. *PhD thesis*, Universitat Politècnica de Catalunya, Spain.

Josa, A., Balmaceda, A., Gens, A. and Alonso, E. E. (1992). An elasto-plastic model for partially saturated soils exhibiting a maximum of collapse. *Proc. 3rd Int. Conf. Computational Plasticity*, Barcelona 1, 815–826.

Juang, C.H. and Holtz, R.D. (1986). A probabilistic permeability model and the pore size density function. *International Journal of Numerical and Analytical Methods in Geomechanics*, Vol.10, pp. 543-553.

Khalili N, Geiser F, Blight GE. (2004). Effective stress in unsaturated soils: Critical review with new evidence. *International Journal of Geomechanics* (ASCE); 4(2): 115-126.

Lloret A. and Ledesma A. (1993). Finite element analysis of deformations of unsaturated soils. *Civil Engineering European Courses*, Barcelona, Spain.

Lloret M., Sánchez M. and Wheeler S.J (2008a). Considering the coupling of water retention and mechanical behaviour in unsaturated soils. *3rd International Workshop of*

young doctors W(H)YDOC 08'. Pereira, De Gennaro and Delage (Eds), Ecole des ponts-Paris Tech, France.

Lloret M., Sánchez M., Wheeler S.J. and Karstunen M. (2008b). Generalised elasto-plastic stress-strain relations of a fully coupled hydro-mechanical model. *1st European Conference on Unsaturated Soils*. Durham, UK.

Manzanal, D. (2008). Constitutive model based on generalized plasticity incorporating state parameter for saturated and unsaturated sand *PhD thesis*, Universisad Politécnica de Madrid, Spain.

Marques, J. M. M. C. (1984). Stress computation in elastoplasticity. *Engineering Computations*, Vol.1(4), pp. 2–51.

McGown, A. and Collins, K. (1975). The microfabrics of some expansive and collapsing soils. *Proc. 5th Panamerican Am. Conf. Soil Mechanics and Foundation Engineering*, Buenos Aires, 1:323-332.

Muir Wood D. (1990). Soil Behaviour and Critical State Soil Mechanics. *Cambridge University Press*, Cambridge, UK.

Nuth, M. and Laloui, L. (2008a). Effective stress concept in unsaturated soils: Clarification and validation of a unified framework. *International Journal for Numerical and Analytical Methods in Geomechanics*, 32; pp. 771-801.

Nuth M. and Laloui L. (2008b). Advances in modelling hysteretic water retention curve in deformable soils, *Computers and Geotechnics*, Vol 35(6); pp. 835-844.

Olivella, S. (1995). Non-isothermal multiphase flow of brine and gas through saline media. *PhD thesis*, Universitat Politècnica de Catalunya. Spain.

Olivella, S., Carrera J., Gens, A. and Alonso, E.E. (1994). Non-isothermal multiphase flow of brine and gas through saline media. *Transport in porous media*, 15, pp. 271-293.

Olivella, S., Gens, A., Carrera, J. and Alonso, E.E. (1996). Numerical formulation for a simulator (CODE-BRIGHT) for the coupled analysis of saline media. *Engineering Computations*, 13, 7, pp. 87-112.

Oliver, X. and Agelet, C. (2003). Mecànica de medis continus per a enginyers. *Edicions UPC S.L.* Barcelona, Spain.

Potts, D. and Gens, A. (1985). A critical assessment of methods of correcting for drift from the yield surface in elasto-plastic finite element analysis. *International Journal for Numerical and Analytical Methods in Geomechanics*, Vol (9); pp. 149-159.

Potts, D. and Zdravković, L. (1999). Finite element analysis in geotechnical engineering: theory*, Thomas Telford*, London, UK.

Prager, W. (1949). Recent developments in mathematical theory of plasticity. *Journal of Applied Physics*, 20(3): 239-241.

Prat, P. (2003). Ecuaciones Constitutivas. ELASTICIDAD y PLASTICIDAD, *Apunts de l'assignatura de Mecànica del sòl de la E.T.S. d'enginyers de camins de la UPC,* Spain.

Raveendiraraj, A. (2009). Coupling of mechanical behaviour and water retention behaviour in unsaturated soils. *PhD thesis*, University of Glasgow, UK.

Review Panel Statement. (1965). Engineering Concepts of Moisture Equilibria and Moisture Changes in Soils, *Proc. Conf. On Moisture Equilibria and Moisture Changes in Soil Beneath Covered Areas*, London, UK.

Ribes, L. (2010). ELASTICITY AND INESLASTICITY, *Course notes.* Facultat de Física, Universitat de Barcelona (UB), Spain.

Romero, E. (1999). Characterisation and thermo-hydro-mechanical behaviour of unsaturated Boom clay: an experimental study. *PhD thesis*, Universitat Politècnica de Catalunya, Spain.

Romero, E. and Vaunat, J. (2000). Retention curves of deformable clays. *Experimental evidence and theoretical approaches in unsaturated soils* (eds. A. Tarantino and C. Mancuso), Rotterdam: Balkema, pp. 91–106.

Roscoe K.H. and Burland J.B. (1968). On the generalised stress-strain behavior of wet clay. Engineering Plasticity (eds Heyman J & Leckie FA), *Cambridge University Press*, Cambridge: 535-609.

Roscoe K.H, Schofield A.N. and Wroth C.P. (1958). On the yielding of soils. *Géotechnique*, Vol.8, pp. 22-52.

Sánchez, M. (2004).Thermo-Hydro-Mechanical coupled analysis in low permeability media. *PhD thesis*, Universitat Politècnica de Catalunya, Spain.

Sánchez M, Gens A, Guimarães L do N and Olivella S. (2005). A double structure generalized plasticity model for expansive materials. *Int. J. Numer. Anal. Methods Geomechanics*, 29:751-787.

Sharma, R. S. (1998). Mechanical behaviour of unsaturated highly expansive clays. D*Phil thesis*, University of Oxford, UK.

Sheng, D., Sloan, S.W. and Gens, A. (2004). A constitutive model for unsaturated soils: thermomechanical and computational aspects. *Computational Mechanics*, 33: 453-465.

Sheng, D., Gens, A., Fredlund, D.G. and Sloan, S.W. (2008). Unsaturated soils: from constitutive modelling to numerical algorithms. *Computers and Geotechnics*, 35: 810-824.

Sheng D., Sloan S. W., Gens A. and Smith D. W. (2003a). Finite element formulation and algorithms for unsaturated soils. Part I: Theory. *Int. J. Numer. Anal. Meth. Geomech.*, 27:745-765.

Sheng D., Sloan S. W., Gens A. and Smith D. W. (2003b). Finite element formulation and algorithms for unsaturated soils. Part II: Verification and application. *Int. J. Numer. Anal. Meth. Geomech.,* 27:767-790.

Simo, J. and Hughes, T. (1998). Computational Inelasticity. *Springer-Verlag*.

Sivakumar, V. (1993). A critical state framework for unsaturated soil. *PhD thesis*, University of Sheffield, UK.

Sloan S. W. (1987). Substepping schemes for the numerical integration of elastoplastic stress-strain relations. *Int. J. Numer. Methods Eng*. 24: 893-911.

Sloan S. W., Abbo A. J. and Sheng D. (2001) Refined explicit integration of elastoplastic models with automatic error control. *Engineering Computations* 18(1/2): 121-154.

Solowsky W.T., (2008). Unsaturated soils:constitutive modelling and explicit stress integration. *PhD thesis*, University of Durham, UK.

Solowsky W.T. and Gallipoli D. (2010a). Explicit stress integration with error control for the Barcelona Basic Model. Part I: Algorithms formulations. *Computers and Geotechnics*, 37(1-2): 59-67.

Solowsky W.T. and Gallipoli D. (2010b). Explicit stress integration with error control for the Barcelona Basic Model. Part II: Algorithms efficiency and accuracy. *Computers and Geotechnics*, 37(1-2): 68-81.

Stepkowska, E.T. (1990). Aspects of clay/electrolyte/water system with special reference to the geotechnical properties of clays. *Engineering geology*, 28:249-267.

Sun, D. and Xiang, L. (2007). An Elastoplastic Hydro-mechanical Model for Unsaturated Soils. *International Conference on Computational Science*, Vol.3, pp. 1138-1145

Tamagnini, C., Castellanza, R. and Nova, R. (2002). Implicit integration of constitutive equations in computational plasticity. *Revue Française de Génie Civil*, Vol 6, Nº5, pp 1051- 1067.

Tamagnini, R. and Pastor, M. (2005). A thermodynamically based model for unsaturated soil: a new framework for generalized plasticity. In: Mancuso C, Tarantino A (eds) Unsaturated soils. *Advances in testing, modelling and engineering applications*. Balkema, Leiden, pp.121–134.

Tarantino, A. (2007). Coupling between mechanical and water retention behaviour in unsaturated soils. *Presentation during MUSE school in Naples* (May be downloaded from MUSE website muse.dur.ac.uk).

Tarantino, A. and Tombolato, S. (2005). Coupling of hydraulic and mechanical behaviour in unsaturated compacted clay. *Géotechnique,* Vol. 55(4), pp. 307–317.

Tarantino, A. Mongiovì, L. and Bosco, G. (2000). An experimental investigation on the independent isotropic stress variables for unsaturated soils. *Géotechnique,* Vol. 50(3), pp. 275–282.

Terzaghi, K. (1936). The shearing resistance of saturated soils and the angle between the planes of shear. *Proc. 1st Int. Conf. Soil Mech. Found. Engng*, Cambridge, MA 1, 54–56.

Vanapalli, S.K. (2009). Shear strength of unsaturated soils and its applications in geotechnical engineering practice. . In: *Unsaturated Soils – Theoretical and Numerical Advances in Unsaturated Soil Mechanics* (Buzzi, O., Fityus, S.G. and Sheng, D., eds), CRC Press, pp. 613-626.

Vaunat, J., Romero, E. and Jommi, C. (2000). An elasto-plastic hydro mechanical model for unsaturated soils. *In Experimental evidence and theoretical approaches in unsaturated soils* (eds. A. Tarantino and C. Mancuso), Rotterdam: Balkema, pp. 121–138.

Wheeler, S.J. (1991). An alternative framework for saturated soil behaviour. *Géotechnique*, Vol. 41 (2), pp. 257–261.

Wheeler, S.J. (2009). Personal communication.

Wheeler, S. J., Gallipoli, D. and Karstunen, M. (2002). Comments on use of the Barcelona basic model for unsaturated soils. *International Journal for Numerical and Analytical Methods in Geomechanics* Vol. 26(15), pp. 1561-1571.

Wheeler, S.J. and Karube, D. (1996). Constitutive modelling. In: *Unsaturated Soils* (Alonso, E.E. and Delage, P, eds), Balkema, Rotterdam, vol.3, pp. 1323–1356.

Wheeler, S. J., Sharma, R. S. and Buisson, M. S. R. (2003). Coupling of hydraulic hysteresis and stress–strain behaviour in unsaturated soils. *Géotechnique,* Vol.53(1), pp. 41-54.

Wheeler, S. J. and Sivakumar, V. (1995). An elasto-plastic critical state framework for unsaturated soil. *Géotechnique,* Vol. 45(1), pp. 35–53.

Wheeler, S. J. and Sivakumar, V. (2000). Influence of compaction procedure on the mechanical behaviour of an unsaturated compacted clay. Part 2: Shearing and constitutive modelling. *Géotechnique,* Vol. 50(4), pp. 369–376.

Yoshimi, V. and Osterberg, J.O. (1963). Compression of partially saturated cohesive soils. *Journal of the Soil Mechanics and Foundations Division, ASCE*, Vol. 89, SM.

APPENDIX A1

Appendix A1: Stress conventions and stress-strain relationships

A1.1 Stress conventions

The total stresses are forces per unit area and can be defined as:

$$\sigma_{ij} = \lim_{A_i \to 0} \left(\frac{F_j}{A_i} \right) \qquad \textit{(A1. 1)}$$

where F_j is the force in the direction j and A_i is the area normal to the direction i.

The total stresses can be represented in the three dimensions by a symmetric 3x3 tensor:

$$\sigma_{ij} = \begin{pmatrix} \sigma_{xx} & \tau_{xy} & \tau_{xz} \\ & \sigma_{yy} & \tau_{yz} \\ sym & & \sigma_{zz} \end{pmatrix} \qquad \textit{(A1. 2)}$$

and, in a more compact form, as a vector (which is the general formulation adopted in this research):

$$\boldsymbol{\sigma}^T = \begin{pmatrix} \sigma_{xx} & \sigma_{yy} & \sigma_{zz} & \tau_{xy} & \tau_{xz} & \tau_{yz} \end{pmatrix} \qquad \textit{(A1. 3)}$$

As mentioned in the text, soil mechanics sign convention is adopted in this work with positive compression.

The stress tensor can be also expressed in terms of three independent invariants. A possible way to express these invariants is given below:

$$I_1 = tr(\boldsymbol{\sigma}) = \sigma_{xx} + \sigma_{yy} + \sigma_{zz} \qquad \textit{(A1. 4)}$$

where *tr(.)* is the trace of the tensor (i.e. sum of the diagonal terms).

$$I_2 = \frac{1}{2}\sigma_{ij}\sigma_{ji} = \frac{1}{2} tr(\boldsymbol{\sigma})^2 \qquad \textit{(A1. 5)}$$

$$I_3 = \frac{1}{3}\sigma_{ij}\sigma_{kl}\sigma_{li} = \frac{1}{3} tr(\boldsymbol{\sigma})^3 \qquad \textit{(A1. 6)}$$

In soil mechanics, however, it is common to express these invariants in terms of the mean total stress p, the deviatoric stress q and the Lode angle θ. The mean total stress p is simply defined as:

$$p = \frac{I_1}{3} = \frac{1}{3}\left(\sigma_{xx} + \sigma_{yy} + \sigma_{zz}\right) \qquad \textit{(A1. 7)}$$

On the other hand, the total stress tensor can be decomposed into the deviatoric stress tenor and the hydrostatic stress tensor as:

$$\sigma_{ij} = s_{ij} + p\delta_{ij} = \begin{pmatrix} \sigma_{xx} - p & \tau_{xy} & \tau_{xz} \\ & \sigma_{yy} - p & \tau_{yz} \\ sym & & \sigma_{zz} - p \end{pmatrix} + \begin{pmatrix} p & 0 & 0 \\ & p & 0 \\ sym & & p \end{pmatrix} \qquad \textit{(A1. 8)}$$

The second invariant of the deviatoric stress tensor s_{ij} can be written as:

$$\bar{J} = \frac{1}{2} tr\left(\mathbf{s}\right)^2 = \frac{1}{6}\left[\left(\sigma_{xx} - \sigma_{yy}\right)^2 + \left(\sigma_{yy} - \sigma_{zz}\right)^2 + \left(\sigma_{zz} - \sigma_{xx}\right)^2 + \left(\tau_{xy}^2 + \tau_{yz}^2 + \tau_{zx}^2\right)\right] \qquad \textit{(A1. 9)}$$

From where the following expression of the scalar deviatoric stress q is obtained:

$$q = \sqrt{3}\sqrt{\bar{J}} \qquad \textit{(A1. 10)}$$

Note that depending on the definition of second invariant of the deviatoric stress tensor, the scalar may be also written as:

$$q = \sqrt{3}\bar{J}_2 \qquad \textit{(A1. 11)}$$

where,

$$\bar{J}_2 = \left\{\frac{1}{6}\left[\left(\sigma_{xx} - \sigma_{yy}\right)^2 + \left(\sigma_{xx} - \sigma_{zz}\right)^2 + \left(\sigma_{yy} - \sigma_{zz}\right)^2 + \left(\tau_{xy}^2 + \tau_{xz}^2 + \tau_{yz}^2\right)\right]\right\}^{\frac{1}{2}} \qquad \textit{(A1. 12)}$$

If σ_1, σ_2, and σ_3 are the principal stresses of the stress tensor σ_{ij} (with $\sigma_1 > \sigma_2 > \sigma_3$) the expression of the third quantity referred to as Lode angle is written as:

$$\theta = \tan^{-1}\left[-\frac{1}{\sqrt{3}}\left(\frac{\sigma_1 - 2\sigma_2 + \sigma_3}{\sigma_1 - \sigma_3}\right)\right] \qquad \textit{(A1. 13)}$$

Function $g(\theta)$ has different expressions for different failure criteria (see Alonso, 1993 for further details).

$$g(\theta) = c = \text{constant} \qquad \text{Von Mises} \qquad (A1.\ 14)$$

$$g(\theta) = \frac{c}{\cos\theta} \qquad \text{Tresca} \qquad (A1.\ 15)$$

$$g(\theta) = \frac{\sin\phi}{\cos\theta + \frac{1}{\sqrt{3}}\sin\theta\sin\phi} \qquad \text{Mohr-Coulomb} \qquad (A1.\ 16)$$

where Φ is the friction angle.

Note that for triaxial stress conditions ($\sigma_2=\sigma_3$) and then θ=-30°. Then, for this particular stress condition:

$$g(\theta) = g(-30°) = \frac{M}{\sqrt{3}} \qquad (A1.\ 17)$$

where M is the gradient of the critical state line.

Instead of total stresses, the constitutive model used within this research employs the Bishop's stress tensor σ^*_{ij} as state variable. From the expression of the Bishop's stresses σ^*_{ij} defined in Chapter 2:

$$\sigma^*_{ij} = \sigma_{ij} - \delta_{ij}u_a + \delta_{ij}S_r\left(u_a - u_w\right) = \bar{\sigma}_{ij} + \delta_{ij}S_r s \qquad (A1.\ 18)$$

where δ_{ij} is the Kronecker delta, u_a is the pore air pressure, u_w is the pore water pressure, S_r is the degree of saturation, s is matric suction and $\bar{\sigma}_{ij}$ is the net stress tensor.

Equation (A1.18) can also be expressed in terms of the following tensor:

$$\sigma^*_{ij} = \begin{pmatrix} \sigma^*_{xx} & \tau_{xy} & \tau_{xz} \\ & \sigma^*_{yy} & \tau_{yz} \\ sym & & \sigma^*_{zz} \end{pmatrix} \qquad (A1.\ 19)$$

Equivalent expressions of the invariants for the Bishop's tensor can be also developed. The mean Bishop's stress takes the following form:

$$p = \frac{1}{3}\left(\sigma_{xx}^{*} + \sigma_{xx}^{*} + \sigma_{xx}^{*}\right) \qquad \textit{(A1. 20)}$$

The deviatoric Bishop's stress tensor is defined as:

$$\sigma_{ij}^{*} = s_{ij}^{*} + p^{*}\delta_{ij} = \begin{pmatrix} \sigma_{xx}^{*} - p^{*} & \tau_{xy} & \tau_{xz} \\ & \sigma_{yy}^{*} - p^{*} & \tau_{yz} \\ sym & & \sigma_{zz}^{*} - p^{*} \end{pmatrix} + \begin{pmatrix} p^{*} & 0 & 0 \\ & p^{*} & 0 \\ sym & & p^{*} \end{pmatrix} \qquad \textit{(A1. 21)}$$

The second invariant J of the Bishop's deviatoric stress tensor s^{*}_{ij} can be written as:

$$J = \frac{1}{2} tr\left(\mathbf{s}^{*}\right)^{2} = \frac{1}{6}\left[\left(\sigma_{xx}^{*} - \sigma_{yy}^{*}\right)^{2} + \left(\sigma_{yy}^{*} - \sigma_{zz}^{*}\right)^{2} + \left(\sigma_{zz}^{*} - \sigma_{xx}^{*}\right)^{2} + \left(\tau_{xy}^{2} + \tau_{yz}^{2} + \tau_{zx}^{2}\right)\right] \qquad \textit{(A1. 22)}$$

From where the following expression of the scalar deviatoric stress q is obtained:

$$q = \sqrt{3}\sqrt{J} \qquad \textit{(A1. 23)}$$

A1.2 Stress-strain relationships

The total stresses can be related to the strains with the elasticity tensor:

$$\boldsymbol{\sigma} = \mathbf{D}^{e} d\boldsymbol{\varepsilon} \qquad \textit{(A1. 24)}$$

where

$$\mathbf{D}^{e} = \begin{pmatrix} E_{11} & E_{12} & E_{13} & 0 & 0 & 0 \\ & E_{22} & E_{23} & 0 & 0 & 0 \\ & & E_{33} & 0 & 0 & 0 \\ & sym & & E_{44} & 0 & 0 \\ & & & & E_{55} & 0 \\ & & & & & E_{66} \end{pmatrix} \qquad \textit{(A1. 25)}$$

where

$E_{11}=E_{22}=E_{33}=K+4/3G$ *(A1. 26)*

$E_{44}=E_{55}=E_{66}=G$ *(A1. 27)*

$E_{12}=E_{23}=E_{13}=K-2/3G$ *(A1. 28)*

where G is the elastic shear modulus:

$$G = 3\frac{1-2\upsilon}{2(1+\upsilon)}K \qquad \textit{(A1. 29)}$$

where υ is the Poisson's ratio and *K* is the the elastic bulk modulus which are related with the Young's modulus *E* by:

$$E = 3K(1-2\nu) \qquad \textit{(A1. 30)}$$

APPENDIX A2

Appendix A2: Strain-driver formulation

The stress-strain relationships for isotropic stress conditions described within Chapter 3 are a particular case of the stress-strain relationships for the generalised 3D model described in Chapter 5. Because of that, only the stress-strain relationships corresponding to the most general case of the 3D stress conditions is included below.

A2.1 Generalised stress-strain relationships

The expression of the Bishop's stress tensor σ^*_{ij} was presented in Appendix A.1 and is repeated here in order to facilitate the development below. Also the expression of modified suction s^* and the compact form of the generalised stress $\tilde{\boldsymbol{\sigma}}^*$ and generalised strain $d\tilde{\boldsymbol{\varepsilon}}$ (introduced in Chapters 2 and 5 respectively) are repeated here.

$$\sigma^*_{ij} = \sigma_{ij} - \delta_{ij} u_a + \delta_{ij} S_r \left(u_a - u_w\right) = \bar{\sigma}_{ij} + \delta_{ij} S_r s \qquad \text{(A2. 1)}$$

where δ_{ij} is the Kronecker delta, u_a is the pore air pressure, u_w is the pore water pressure, S_r is the degree of saturation, s is matric suction and $\bar{\sigma}_{ij}$ is the net stress tensor.

$$s^* = n\left(u_a - u_w\right) = ns \qquad \text{(A2. 2)}$$

where n is the porosity.

$$\tilde{\boldsymbol{\sigma}}^* = \left(\sigma^*_{xx} \quad \sigma^*_{yy} \quad \sigma^*_{zz} \quad \tau_{xy} \quad \tau_{yz} \quad \tau_{xz} \quad s^*\right)^T \qquad \text{(A2. 3)}$$

$$d\tilde{\boldsymbol{\varepsilon}} = \left(d\,\varepsilon_{xx} \quad d\varepsilon_{yy} \quad d\varepsilon_{zz} \quad d\gamma_{xy} \quad d\gamma_{yz} \quad d\gamma_{xz} \quad -dS_r\right)^T \qquad \text{(A2. 4)}$$

A2.1.1 Elastic behaviour

For elastic behaviour the generalised stress increment can be related to the generalised strain increment by:

$$d\tilde{\boldsymbol{\sigma}}^* = \mathbf{D}^*_e d\tilde{\boldsymbol{\varepsilon}} \qquad \text{(A2. 5)}$$

where $\boldsymbol{D_e}^*$ is the generalised elastic matrix and takes the following form:

$$\mathbf{D}_e^* = \begin{pmatrix} E_{11} & E_{12} & E_{13} & 0 & 0 & 0 & 0 \\ & E_{22} & E_{23} & 0 & 0 & 0 & 0 \\ & & E_{33} & 0 & 0 & 0 & 0 \\ & & & E_{44} & 0 & 0 & 0 \\ & sym & & & E_{55} & 0 & 0 \\ & & & & & E_{66} & 0 \\ & & & & & & E_{77} \end{pmatrix} = \begin{pmatrix} \mathbf{D}_{e\ 6x6} & \mathbf{0} \\ \mathbf{0} & \gamma_{e\ 1x1} \end{pmatrix} \quad \text{(A2. 6)}$$

where

$E_{11}=E_{22}=E_{33}=K'+4/3G'=(v/\kappa)p^*+4/3G'$ (A2. 7)

$E_{44}=E_{55}=E_{66}=G'=3K'(1-2\nu)/(2(1+\nu))$ (A2. 8)

$E_{12}=E_{23}=E_{13}=K'-2/3G'$ (A2. 9)

$E_{77}=\gamma_e=(1/\kappa_s)s^*$ (A2. 10)

where K' is the elastic bulk modulus, G' is the elastic shear modulus and ν the Poisson's ratio.

A2.1.2 Elasto-plastic behaviour

When a plastic mechanism is active, it is also possible to obtain a general expression to compute the increments of generalised stresses:

$$d\tilde{\boldsymbol{\sigma}}^* = \mathbf{D}_{ep}^* d\tilde{\boldsymbol{\varepsilon}} \quad \text{(A2. 11)}$$

As summarised below, the form of $\boldsymbol{D}_{ep}^*$ depends on which plastic mechanism(s) is (are) active (i.e. the *LC* plastic mechanism alone, the *SD* or *SI* mechanism alone, or both *LC* and *SD* or *SI* plastic mechanisms active simultaneously).

A2.1.2.1 Yielding on the LC yield surface alone

When yielding on the *LC* surface alone is taking place:

$$d\tilde{\boldsymbol{\sigma}}^* = \mathbf{D}_e^* d\tilde{\boldsymbol{\varepsilon}}^e = \mathbf{D}_e^* \left(d\tilde{\boldsymbol{\varepsilon}} - d\tilde{\boldsymbol{\varepsilon}}_{LC}^p \right) \quad \text{(A2. 12)}$$

where the subscript *LC* indicates the plastic mechanism that is active.

Using now the flow rule (5.10) for this case considered:

$$d\tilde{\boldsymbol{\sigma}}^{*} = \mathbf{D}_{e}^{*}\left(d\tilde{\boldsymbol{\varepsilon}} - d\chi_{LC}^{LC}\mathbf{m}_{LC}\right) \qquad \textit{(A2. 13)}$$

The plastic multiplier associated with yielding on the *LC* surface alone $d\chi^{LC}{}_{LC}$ can be determined by imposing the consistency condition on the *LC* yield surface:

$$dF_{LC} = \left(\frac{\partial F_{LC}}{\partial \boldsymbol{\sigma}^{*}}\right)^{T} d\boldsymbol{\sigma}^{*} + \frac{\partial F_{LC}}{\partial p_{0}^{*}} dp_{0}^{*} = 0 \qquad \textit{(A2. 14)}$$

Combining with (A2.13) and the hardening law (2.29) with dS_r^p set to zero (see Section 2.6.4 in Chapter 2):

$$\left(\frac{\partial F_{LC}}{\partial \boldsymbol{\sigma}^{*}}\right)^{T} \mathbf{D}_{e}^{*}\left(d\boldsymbol{\varepsilon} - d\chi_{LC}^{LC}\frac{\partial F_{LC}}{\partial \boldsymbol{\sigma}^{*}}\right) + \frac{\partial F_{LC}}{\partial p_{0}^{*}} p_{0}^{*}\left[\nu\frac{\mathbf{m}^{T} d\chi_{LC}^{LC}\dfrac{\partial F_{LC}}{\partial \boldsymbol{\sigma}^{*}}}{\lambda - \kappa}\right] = 0 \qquad \textit{(A2. 15)}$$

where $\boldsymbol{m}^{T}$=(1,1,1,0,0,0).

Isolating the $d\chi^{LC}{}_{LC}$ the following expression for this plastic multiplier can be obtained:

$$d\chi_{LC}^{LC} = \frac{\mathbf{a}_{LC}^{T} d\boldsymbol{\varepsilon}}{h_{LC}} \qquad \textit{(A2. 16)}$$

where

$$\mathbf{a}_{LC}^{T} = \left(\frac{\partial F_{LC}}{\partial \boldsymbol{\sigma}^{*}}\right)^{T} \mathbf{D}_{e} \qquad \textit{(A2. 17)}$$

$$h_{LC} = \left(\frac{\partial F_{LC}}{\partial \boldsymbol{\sigma}^{*}}\right)^{T} \mathbf{D}_{e} \frac{\partial F_{LC}}{\partial \boldsymbol{\sigma}^{*}} - \frac{\partial F_{LC}}{\partial p_{0}^{*}} \frac{\nu}{\lambda - \kappa} p_{0}^{*} \mathbf{m}^{T} \frac{\partial F_{LC}}{\partial \boldsymbol{\sigma}^{*}} \qquad \textit{(A2. 18)}$$

where the subscript *LC* indicates that the *LC* mechanism is active.

Substituting this expression of the plastic multiplier into (A2.13):

$$d\tilde{\boldsymbol{\sigma}}^{*} = \mathbf{D}_{e}^{*}\left(d\tilde{\boldsymbol{\varepsilon}} - \frac{\mathbf{a}_{LC}^{T} d\boldsymbol{\varepsilon}}{h_{LC}}\mathbf{m}_{LC}\right) = \mathbf{D}_{ep}^{*\ LC} d\tilde{\boldsymbol{\varepsilon}} \qquad \textit{(A2. 19)}$$

where,

$$\mathbf{D}_{ep}^{*\,LC} = \begin{pmatrix} \mathbf{A}_{LC} & \mathbf{0} \\ \mathbf{0} & D_{LC} \end{pmatrix} \qquad \textit{(A2. 20)}$$

with

$$\left(\mathbf{A}_{LC}\right)_{6x6} = \mathbf{D}_e \left(\mathbf{Id}_{6x6} - \frac{\partial F_{LC}}{\partial \boldsymbol{\sigma}^*} \frac{\mathbf{a}_{LC}^T}{h_{LC}} \right) \qquad \textit{(A2. 21)}$$

$$\left(D_{LC}\right)_{1x1} = \gamma_e = \left(1/\kappa_s\right) s^* \qquad \textit{(A2. 22)}$$

A2.1.2.2 Yielding on the SD or SI yield surface alone

When yielding on only *β=SD* or *SI* is taking place:

$$d\tilde{\boldsymbol{\sigma}}^* = \mathbf{D}_e^* d\tilde{\boldsymbol{\varepsilon}}^e = \mathbf{D}_e^* \left(d\tilde{\boldsymbol{\varepsilon}} - d\tilde{\boldsymbol{\varepsilon}}_\beta^p \right) \qquad \textit{(A2. 23)}$$

where the subscript *β* indicates the plastic mechanism active.

Employing now the flow rule (5.12) for yielding on only *SD* or *SI*:

$$d\tilde{\boldsymbol{\sigma}}^* = \mathbf{D}_e^* \left(d\tilde{\boldsymbol{\varepsilon}} - d\chi_\beta^\beta \mathbf{m}_\beta \right) \qquad \textit{(A2. 24)}$$

The plastic multiplier associated with yielding on the *SD* or *SI* surface alone $d\chi^{\beta}_{\beta}$ can be determined by imposing the consistency condition on the *β=SD* or *SI*:

$$dF_\beta = \frac{\partial F_\beta}{\partial s^*} ds^* + \frac{\partial F_\beta}{\partial s_\beta^*} ds_\beta^* = 0 \qquad \textit{(A2. 25)}$$

Combining with (A2.24) and the hardening law (2.29) with $d\varepsilon_v^p$ set to zero (see Section 2.6.4):

$$\frac{\partial F_\beta}{\partial s^*} \gamma_e \left(dS_r - d\chi_\beta^\beta \frac{\partial F_\beta}{\partial s^*} \right) + \frac{\partial F_\beta}{\partial s_\beta^*} s_\beta^* \left[- \frac{d\chi_\beta^\beta \frac{\partial F_\beta}{\partial s^*}}{\lambda_s - \kappa_s} \right] = 0 \qquad \textit{(A2. 26)}$$

Isolating the $d\chi^{\beta}_{\beta}$ the following expression for this plastic multiplier can be obtained:

$$d\chi_\beta^\beta = \frac{d_\beta dS_r}{h_\beta} \qquad \textit{(A2. 27)}$$

$$d_\beta = \frac{\partial F_\beta}{\partial s^*}\gamma_e \qquad \text{(A2. 28)}$$

$$h_\beta = -\frac{\partial F_\beta}{\partial s^*}\gamma_e \frac{\partial F_\beta}{\partial s^*} + \frac{\partial F_\beta}{\partial s^*_\beta} s^*_\beta \frac{1}{\lambda_s - \kappa_s}\frac{\partial F_\beta}{\partial s^*} \qquad \text{(A2. 29)}$$

where the subscript β indicates that the *SD* or *SI* mechanism is active.

Substituting this expression of the plastic multiplier into (A2.24):

$$d\tilde{\boldsymbol{\sigma}}^* = \mathbf{D}^*_e\left(d\tilde{\boldsymbol{\varepsilon}} - \frac{d_\beta dS_r}{h_\beta}\mathbf{m}_\beta\right) = \mathbf{D}^{*\,\beta}_{ep} d\tilde{\boldsymbol{\varepsilon}} \qquad \text{(A2. 30)}$$

where,

$$\mathbf{D}^{*\,\beta}_{ep} = \begin{pmatrix} \mathbf{A}_\beta & \mathbf{0} \\ \mathbf{0} & D_\beta \end{pmatrix} \qquad \text{(A2. 31)}$$

with

$$\left(\mathbf{A}_\beta\right)_{6x6} = \mathbf{D}_e \qquad \text{(A2. 32)}$$

$$\left(D_\beta\right)_{1x1} = \gamma_e\left(1 + \frac{\partial F_\beta}{\partial s^*}\frac{d_\beta}{h_\beta}\right) \qquad \text{(A2. 33)}$$

A2.1.2.3 Simultaneous yielding on the LC and SD or SI yield surfaces

When simultaneous yielding is taking place:

$$d\tilde{\boldsymbol{\sigma}}^* = \mathbf{D}^*_e d\tilde{\boldsymbol{\varepsilon}}^e = \mathbf{D}^*_e\left(d\tilde{\boldsymbol{\varepsilon}} - d\tilde{\boldsymbol{\varepsilon}}^p_{LC+\beta}\right) \qquad \text{(A2. 34)}$$

where the subscript β indicates that yielding on the *SD* or *SI* surface is active while the subscript *LC* indicates that yielding on the *LC* surface is also active.

Considering now the flow rule (5.14):

$$d\tilde{\boldsymbol{\sigma}}^* = \mathbf{D}^*_e\left(d\tilde{\boldsymbol{\varepsilon}} - d\chi^{LC+\beta}_\beta \mathbf{m}_\beta - d\chi^{LC+\beta}_{LC}\mathbf{m}_{LC}\right) \qquad \text{(A2. 35)}$$

The plastic multiplier $d\chi_\beta^{LC+\beta}$ associated with yielding on β and the one $d\chi_{LC}^{LC+\beta}$ associated with yielding on *LC* when simultaneous yielding on two surfaces is occurring can be

determined by imposing the consistency condition on the *LC* and on the *β* yield surfaces at the same time:

$$dF_{LC} = \left(\frac{\partial F_{LC}}{\partial \boldsymbol{\sigma}^*}\right)^T d\boldsymbol{\sigma}^* + \frac{\partial F_{LC}}{\partial p_0^*} dp_0^* = 0 \qquad \textit{(A2. 36)}$$

$$dF_{\beta} = \frac{\partial F_{\beta}}{\partial s^*} ds^* + \frac{\partial F_{\beta}}{\partial s_{\beta}^*} ds_{\beta}^* = 0 \qquad \textit{(A2. 37)}$$

Combining with (A2.34) and using the hardening laws (2.29) and (2.30), and following the equivalent procedure showed for yielding on the *LC* yield surface alone and yielding on the *SD* or *SI* yield surface alone, the expression for each plastic multiplier can be obtained:

$$d\chi_{LC}^{LC+\beta} = \frac{\mathbf{a}_{LC+\beta}^T d\boldsymbol{\varepsilon} + b_{LC+\beta} dS_r}{h_{LC+\beta}} \qquad \textit{(A2. 38)}$$

$$d\chi_{\beta}^{LC+\beta} = \frac{\mathbf{c}_{LC+\beta}^T d\boldsymbol{\varepsilon} + d_{LC+\beta} dS_r}{h_{LC+\beta}} \qquad \textit{(A2. 39)}$$

where the subscript *LC+β* indicates that the *LC* and *β* mechanisms are both active and,

$$\mathbf{a}_{LC+\beta}^T = \left(\frac{\partial F_{LC}}{\partial \boldsymbol{\sigma}^*}\right)^T \mathbf{D}_e \left(\frac{\partial F_{\beta}}{\partial s^*} \gamma_e \frac{\partial F_{\beta}}{\partial s^*} - \frac{\partial F_{\beta}}{\partial s_{\beta}^*} s_{\beta}^* \frac{1}{\lambda_s - \kappa_s} \frac{\partial F_{\beta}}{\partial s^*}\right) \qquad \textit{(A2. 40)}$$

$$b_{LC+\beta} = -k_1 \frac{\partial F_{\beta}}{\partial s^*} \gamma_e \frac{\partial F_{LC}}{\partial p_0^*} \frac{p_0^*}{\lambda_s - \kappa_s} \frac{\partial F_{\beta}}{\partial s^*} \qquad \textit{(A2. 41)}$$

$$\mathbf{c}_{LC+\beta}^T = k_2 \left(\frac{\partial F_{LC}}{\partial \boldsymbol{\sigma}^*}\right)^T \mathbf{D}_e \frac{\partial F_{\beta}}{\partial s_{\beta}^*} \nu \frac{s_{\beta}^*}{\lambda - \kappa} \mathbf{m}^T \frac{\partial F_{LC}}{\partial \boldsymbol{\sigma}^*} \qquad \textit{(A2. 42)}$$

$$d_{LC+\beta} = \frac{\partial F_{\beta}}{\partial s^*} \gamma_e \left(-\left(\frac{\partial F_{LC}}{\partial \boldsymbol{\sigma}^*}\right)^T \mathbf{D}_e \frac{\partial F_{LC}}{\partial \boldsymbol{\sigma}^*} + \frac{\partial F_{LC}}{\partial p_0^*} \frac{\nu}{\lambda - \kappa} p_0^* \mathbf{m}^T \frac{\partial F_{LC}}{\partial \boldsymbol{\sigma}^*}\right) \qquad \textit{(A2. 43)}$$

where

$$h_{LC+\beta}=\left[-\left(\frac{\partial F_{LC}}{\partial \boldsymbol{\sigma}^*}\right)^T \mathbf{D}_e \frac{\partial F_{LC}}{\partial \boldsymbol{\sigma}^*}+\frac{\partial F_{LC}}{\partial p_0^*}\frac{\nu}{\lambda-\kappa}p_0^*\mathbf{m}^T\frac{\partial F_{LC}}{\partial \boldsymbol{\sigma}^*}\right]\left[-\frac{\partial F_\beta}{\partial s^*}\gamma_e\frac{\partial F_\beta}{\partial s^*}+\frac{\partial F_\beta}{\partial s_\beta^*}\frac{s_\beta^*}{\lambda_s-\kappa_s}\frac{\partial F_\beta}{\partial s^*}\right]$$
$$-k_1k_2\frac{\partial F_\beta}{\partial s_\beta^*}p_0^*\frac{\nu}{\lambda-\kappa}\frac{s_\beta^*}{\lambda_s-\kappa_s}\frac{\partial F_{LC}}{\partial p_0^*}\mathbf{m}^T\frac{\partial F_{LC}}{\partial \boldsymbol{\sigma}^*}\frac{\partial F_\beta}{\partial s^*} \qquad \textit{(A2. 44)}$$

where $\boldsymbol{m}^T$ is an auxiliary vector $\boldsymbol{m}^T$=(1,1,1,0,0,0).

Substituting both expressions of the plastic multipliers into (A2.35):

$$d\tilde{\boldsymbol{\sigma}}^*=\mathbf{D}_e^*\left(d\tilde{\boldsymbol{\varepsilon}}-\frac{\mathbf{c}_{LC+\beta}^T d\boldsymbol{\varepsilon}+d_{LC+\beta}dS_r}{h_{LC+\beta}}\mathbf{m}_\beta-\frac{\mathbf{a}_{LC+\beta}^T d\boldsymbol{\varepsilon}+b_{LC+\beta}dS_r}{h_{LC+\beta}}\mathbf{m}_{LC}\right)=\mathbf{D}_{ep}^{*\ LC+\beta}d\tilde{\boldsymbol{\varepsilon}} \qquad \textit{(A2. 45)}$$

where,

$$\mathbf{D}_{ep}^{*\ LC+\beta}=\begin{pmatrix}\mathbf{A}_{LC+\beta} & \mathbf{B}_{LC+\beta}\\ \mathbf{C}^T{}_{LC+\beta} & D_{LC+\beta}\end{pmatrix} \qquad \textit{(A2. 46)}$$

with

$$\left(\mathbf{A}_{LC+\beta}\right)_{6x6}=\mathbf{D}_e\left(\mathbf{Id}_{6x6}-\frac{\partial F_{LC}}{\partial \boldsymbol{\sigma}^*}\frac{\mathbf{a}_{LC+\beta}^T}{h_{LC+\beta}}\right) \qquad \textit{(A2. 47)}$$

$$\left(\mathbf{B}_{LC+\beta}\right)_{6x1}=\mathbf{D}_e\left(\frac{\partial F_{LC}}{\partial \boldsymbol{\sigma}^*}\frac{b_{LC+\beta}}{h_{LC+\beta}}\right) \qquad \textit{(A2. 48)}$$

$$\left(\mathbf{C}_{LC+\beta}\right)_{1x6}^T=-\gamma_e\left(\frac{\partial F_\beta}{\partial s^*}\frac{\mathbf{c}_{LC+\beta}^T}{h_{LC+\beta}}\right) \qquad \textit{(A2. 49)}$$

$$\left(D_{LC+\beta}\right)_{1x1}=\gamma_e\left(1+\frac{\partial F_\beta}{\partial s^*}\frac{d_{LC+\beta}}{h_{LC+\beta}}\right) \qquad \textit{(A2. 50)}$$

A2.1.3 Drift correction method

From a given initial state *A* lying on the yield surface, an increment of load is considered causing elasto-plastic yielding from *A* to *B*. As yielding takes place, the position of the yield surface changes from F_A to F_B. Due to the tendency to drift, the predicted (generalised) stress state in *B* does not necessarily lie on this new yield surface (Potts and Gens, 1985). The stress state should then be corrected to effectively be on the yield

surface using a drift correction method. The main mathematical expressions and details and of how this method is applied within the implemented constitutive model are described in Chapter 6 (see Section 6.5.1). Only the mathematical development for the most general case of simultaneous yielding on *LC* and *SD* or *SI* yield surfaces is presented below.

A key issue of the proposed method is to consider that during the projection back of the (generalised) stresses to the yield surface, an associated change in the elastic (generalised) strains takes place. This leads to:

$$\Delta\tilde{\boldsymbol{\varepsilon}}^{e} = \left(\mathbf{D}_{\mathbf{e}}^{*}\right)^{-1}\left(\tilde{\boldsymbol{\sigma}}_{C}^{*} - \tilde{\boldsymbol{\sigma}}_{B}^{*}\right) \qquad \textit{(A2. 51)}$$

where $\tilde{\boldsymbol{\sigma}}_{B}^{*}$ and $\tilde{\boldsymbol{\sigma}}_{C}^{*}$ are, respectively, the generalised stress to be corrected and the corrected generalised stress. The assumption of no changes in the total generalised strains during the correction process implies that the elastic (generalised) strain change must be balanced by an equal and opposite change in the plastic (generalised) strains (Potts and Gens, 1985).

$$\Delta\tilde{\boldsymbol{\varepsilon}}^{total} = 0 \Rightarrow \Delta\tilde{\boldsymbol{\varepsilon}}^{e} = -\Delta\tilde{\boldsymbol{\varepsilon}}^{p} \qquad \textit{(A2. 52)}$$

Note that now the expression of the generalised strains (A2.52) includes changes in both, plastic strain and plastic variations of the degree of saturation. This is because the case analysed involves yielding simultaneous on two yield surfaces.

The (generalised) plastic strain increments are proportional to the gradient of the pertinent yield surface according to:

$$\Delta\tilde{\boldsymbol{\varepsilon}}_{LC}^{p} = \alpha_{LC}^{LC+\beta}\mathbf{m}_{LC} \qquad \textit{(A2. 53)}$$

$$\Delta\tilde{\boldsymbol{\varepsilon}}_{\beta}^{p} = \alpha_{\beta}^{LC+\beta}\mathbf{m}_{\beta} \qquad \textit{(A2. 54)}$$

where ${\alpha_{LC}}^{LC+\beta}$ and ${\alpha_{\beta}}^{LC+\beta}$ are the two scalar quantities unknown. Combining previous expressions the following equation expressing the corrected generalised stress is obtained:

$$\tilde{\boldsymbol{\sigma}}_{C}^{*} = \tilde{\boldsymbol{\sigma}}_{B}^{*} - \mathbf{D}_{\mathbf{e}}^{*}\left(\alpha_{LC}^{LC+\beta}\mathbf{m}_{LC} + \alpha_{\beta}^{LC+\beta}\mathbf{m}_{\beta}\right) \qquad \textit{(A2. 55)}$$

Note that in here, all terms of the generalised stress tensor are corrected. This involves, those terms related to the Bishop's stress tensor and those associated with modified suction (because irreversible changes occur on both, strains and degree of saturation).

There will be also a variation on the position of the yield surfaces given by

$$\mathbf{h}_C = \mathbf{h}_B + \Delta\mathbf{h} = \mathbf{h}_B + \Delta\boldsymbol{\alpha}_j^T \bar{\mathbf{B}} \quad \text{with} \quad \text{j} = LC, \beta, LC+\beta \text{ where } \beta = SD/SI \qquad \textit{(A2. 56)}$$

with $j=LC+\beta$ and

$$\Delta\boldsymbol{\alpha}_{LC+\beta}^T = \begin{pmatrix} \alpha_{LC}^{LC+\beta} & \alpha_{\beta}^{LC+\beta} \end{pmatrix} \qquad \textit{(A2. 57)}$$

Imposing that the corrected (generalised) stress state is on the *LC* yield surface and also on the *SD/SI* yield surface:

$$F_{LC}\left(\tilde{\boldsymbol{\sigma}}_C^*, \mathbf{h}_C\right) = 0 \qquad \textit{(A2. 58)}$$

$$F_{\beta}\left(\tilde{\boldsymbol{\sigma}}_C^*, \mathbf{h}_C\right) = 0 \qquad \textit{(A2. 59)}$$

Expanding Taylor's series in both yield surfaces and neglecting second order terms, the following system of equations is obtained:

$$F_{LC}\left(\tilde{\boldsymbol{\sigma}}_C^*, \mathbf{h}_C\right) \approx F_{LC}\left(\tilde{\boldsymbol{\sigma}}_B^*, \mathbf{h}_B\right) + \mathbf{m}_{LC}^T \delta\tilde{\boldsymbol{\sigma}}^* + \frac{\partial F_{LC}}{\partial p_0^*}\delta p_0^* \qquad \textit{(A2. 60)}$$

$$F_{\beta}\left(\tilde{\boldsymbol{\sigma}}_C^*, \mathbf{h}_C\right) \approx F_{\beta}\left(\tilde{\boldsymbol{\sigma}}_B^*, \mathbf{h}_B\right) + \mathbf{m}_{\beta}^T \delta\tilde{\boldsymbol{\sigma}}^* + \frac{\partial F_{\beta}}{\partial s_{\beta}^*}\delta s_{\beta}^* \qquad \textit{(A2. 61)}$$

Re-arranging:

$$\alpha_{LC}^{LC+\beta} = \frac{a_1 F_{LC}\left(\tilde{\boldsymbol{\sigma}}_B^*, \mathbf{h}_B\right) + a_2 F_{\beta}\left(\tilde{\boldsymbol{\sigma}}_B^*, \mathbf{h}_B\right)}{h_{LC+\beta}} \qquad \textit{(A2. 62)}$$

$$\alpha_{\beta}^{LC+\beta} = \frac{a_3 F_{LC}\left(\tilde{\boldsymbol{\sigma}}_B^*, \mathbf{h}_B\right) + a_4 F_{\beta}\left(\tilde{\boldsymbol{\sigma}}_B^*, \mathbf{h}_B\right)}{h_{LC+\beta}} \qquad \textit{(A2. 63)}$$

where

$$h_{LC+\beta} = \left[-\left(\frac{\partial F_{LC}}{\partial \boldsymbol{\sigma}^*} \right)^T \mathbf{D}_e \frac{\partial F_{LC}}{\partial \boldsymbol{\sigma}^*} + \frac{\partial F_{LC}}{\partial p_0^*} \frac{v}{\lambda - \kappa} p_0^* \mathbf{m}^T \frac{\partial F_{LC}}{\partial \boldsymbol{\sigma}^*} \right] \left[-\frac{\partial F_\beta}{\partial s^*} \gamma_e \frac{\partial F_\beta}{\partial s^*} + \frac{\partial F_\beta}{\partial s_\beta^*} \frac{s_\beta^*}{\lambda_s - \kappa_s} \frac{\partial F_\beta}{\partial s^*} \right]$$
$$-k_1 k_2 \frac{\partial F_\beta}{\partial s_\beta^*} p_0^* \frac{v}{\lambda - \kappa} \frac{s_\beta^*}{\lambda_s - \kappa_s} \frac{\partial F_{LC}}{\partial p_0^*} \mathbf{m}^T \frac{\partial F_{LC}}{\partial \boldsymbol{\sigma}^*} \frac{\partial F_\beta}{\partial s^*} \qquad \textit{(A2. 64)}$$

(Note that $h_{LC+\beta}$ takes the same form as the expression for the plastic multiplier when *LC+β* is active, see (A2.44)).

$$a_1 = \frac{\partial F_\beta}{\partial s^*} \gamma_e \frac{\partial F_\beta}{\partial s^*} - \frac{\partial F_\beta}{\partial s_\beta^*} \frac{s_\beta^*}{\lambda_s - \kappa_s} \frac{\partial F_\beta}{\partial s^*} \qquad \textit{(A2. 65)}$$

$$a_2 = \frac{\partial F_{LC}}{\partial p_0^*} \frac{p_0^*}{\lambda_s - \kappa_s} k_1 \frac{\partial F_\beta}{\partial s^*} \qquad \textit{(A2. 66)}$$

$$a_3 = \frac{\partial F_\beta}{\partial s_\beta^*} v k_2 \frac{s_\beta^*}{\lambda - \kappa} \mathbf{m}^T \frac{\partial F_{LC}}{\partial \boldsymbol{\sigma}^*} \qquad \textit{(A2. 67)}$$

$$a_4 = \left(\frac{\partial F_{LC}}{\partial \boldsymbol{\sigma}^*} \right)^T \mathbf{D}_e \frac{\partial F_{LC}}{\partial \boldsymbol{\sigma}^*} - \frac{\partial F_{LC}}{\partial p_0^*} \frac{v}{\lambda - \kappa} p_0^* \mathbf{m}^T \frac{\partial F_{LC}}{\partial \boldsymbol{\sigma}^*} \qquad \textit{(A2. 68)}$$

APPENDIX A3

Appendix A3: Stress-driver formulation

A3.1 Stress-strain relationships

The stress-strain relationships for isotropic stress conditions described within Chapter 3 are a particular case of the stress-strain relationships for the generalised 3D model described in Chapter 5. Because of that, only the stress-strain relationships corresponding to the most general case of the 3D stress conditions is included below.

In general, it is possible to consider the following equations. Firstly from the definitions of Bishop's stress tensor and modified suction, one may write the total variations of these variables as:

$$d\boldsymbol{\sigma}^{*} = d\overline{\boldsymbol{\sigma}} + \mathbf{m}\left(S_r ds + s dS_r\right) \qquad \textit{(A3. 1)}$$

$$ds^{*} = \frac{e}{1+e} ds - \frac{s}{1+e} \mathbf{m}^{T} d\boldsymbol{\varepsilon} \qquad \textit{(A3. 2)}$$

where $\boldsymbol{m}^{T}$=(1,1,1,0,0,0).

On the other hand,

$$d\boldsymbol{\sigma}^{*} = \mathbf{A}^{j}_{6x6} d\boldsymbol{\varepsilon} + \mathbf{B}^{j}_{6x1}\left(-dS_r\right)) \qquad \textit{(A3. 3)}$$

$$ds^{*} = \mathbf{C}^{j}_{1x6} d\boldsymbol{\varepsilon} + D^{j}_{1x1}\left(-dS_r\right) \qquad \textit{(A3. 4)}$$

where the superscript *j* indicates the current type of material behaviour (i.e. elastic, yielding on the *LC* yield surface alone, yielding on the *SD/SI* yield surface alone or simultaneous yielding on the *LC* and *SD/SI* yield surfaces) and the different expressions of ***A***, ***B***, ***C*** and *D* take the form showed in Appendix A.2.

Expressions (A3.1), (A3.2), (A3.3) and (A3.4) define a system of equations with six unknowns: increment of Bishop's stress $d\boldsymbol{\sigma}^{*}$ (which, in turn, has six components), increment of net stress $d\overline{\boldsymbol{\sigma}}$ (which, in turn, has six components), strain increment $d\boldsymbol{\varepsilon}$ (which, in turn, has six components), increment of matric suction *ds* (scalar), increment of modified suction ds^{*} (scalar) and increment of degree of saturation dS_r (scalar). If a pair of these six unknowns is assumed to be known, it should be then possible to express these equations as functions of these pair of known variables. For instance, if it is assumed that $d\overline{\boldsymbol{\sigma}}$ and *ds* are known (i.e. stress-driver type algorithms), the remaining four unknowns

can be expressed (by employing these four equations (A3.1), (A3.2), (A3.3) and (A3.4)) in terms of $d\overline{\boldsymbol{\sigma}}$ and ds. This is exaclty the aim of the mathematical development given below. In particular, to find an expression of $d\boldsymbol{\sigma}^*$ and ds^* in terms of the driven variables in terms of $d\overline{\boldsymbol{\sigma}}$ and ds.

Isolating dS_r from (A3.4):

$$\left(-dS_r\right)=\left(D_{1x1}^{j}\right)^{-1}ds^{*}-\left(D_{1x1}^{j}\right)^{-1}\mathbf{C}_{1x6}^{j}d\boldsymbol{\varepsilon} \qquad \textit{(A3. 5)}$$

Isolating $d\boldsymbol{\varepsilon}$ from (A3.3):

$$d\boldsymbol{\varepsilon}=\left(\mathbf{A}_{6x6}^{j}\right)^{-1}\left(d\boldsymbol{\sigma}^{*}-\mathbf{B}_{6x1}^{j}\left(-dS_r\right)\right) \qquad \textit{(A3. 6)}$$

Combining both equations it is possible to express $d\boldsymbol{\varepsilon}$ and dS_r in terms of ds^* and $d\boldsymbol{\sigma}^*$:

$$\left(-dS_r\right)=\left(D_{1x1}^{j}\right)^{-1}ds^{*}-\left(D_{1x1}^{j}\right)^{-1}\mathbf{C}_{1x6}^{j}\left(\left(\mathbf{A}_{6x6}^{j}\right)^{-1}\left(d\boldsymbol{\sigma}^{*}-\mathbf{B}_{6x1}^{j}\left(-dS_r\right)\right)\right) \qquad \textit{(A3. 7)}$$

$$d\boldsymbol{\varepsilon}=\left(\mathbf{A}_{6x6}^{j}\right)^{-1}\left(d\boldsymbol{\sigma}^{*}-\mathbf{B}_{6x1}^{j}\left(\left(D_{1x1}^{j}\right)^{-1}ds^{*}-\left(D_{1x1}^{j}\right)^{-1}\mathbf{C}_{1x6}^{j}d\boldsymbol{\varepsilon}\right)\right) \qquad \textit{(A3. 8)}$$

Re-arranging:

$$\left(-dS_r\right)=\left(1-\left(D_{1x1}^{j}\right)^{-1}\mathbf{C}_{1x6}^{j}\left(\mathbf{A}_{6x6}^{j}\right)^{-1}\mathbf{B}_{6x1}^{j}\right)^{-1}\left(\left(D_{1x1}^{j}\right)^{-1}ds^{*}-\left(D_{1x1}^{j}\right)^{-1}\mathbf{C}_{1x6}^{j}\left(\mathbf{A}_{6x6}^{j}\right)^{-1}d\boldsymbol{\sigma}^{*}\right)$$

(A3. 9)

$$d\boldsymbol{\varepsilon}=\left(\left(\mathbf{I}_{6x6}-\left(\mathbf{A}_{6x6}^{j}\right)^{-1}\mathbf{B}_{6x1}^{j}\left(D_{1x1}^{j}\right)^{-1}\mathbf{C}_{1x6}^{j}\right)\right)^{-1}\left(\left(\mathbf{A}_{6x6}^{j}\right)^{-1}d\boldsymbol{\sigma}^{*}-\left(\mathbf{A}_{6x6}^{j}\right)^{-1}\mathbf{B}_{6x1}^{j}\left(D_{1x1}^{j}\right)^{-1}ds^{*}\right)$$

(A3. 10)

In order to facilitate the development let's consider the following notation:

$$\mathbf{E}_{6x6}=\left(\left(\mathbf{I}_{6x6}-\left(\mathbf{A}_{6x6}^{j}\right)^{-1}\mathbf{B}_{6x1}^{j}\left(D_{1x1}^{j}\right)^{-1}\mathbf{C}_{1x6}^{j}\right)\right)^{-1}\left(\mathbf{A}_{6x6}^{j}\right)^{-1} \qquad \textit{(A3. 11)}$$

$$\mathbf{F}_{6x1}=-\left(\left(\mathbf{I}_{6x6}-\left(\mathbf{A}_{6x6}^{j}\right)^{-1}\mathbf{B}_{6x1}^{j}\left(D_{1x1}^{j}\right)^{-1}\mathbf{C}_{1x6}^{j}\right)\right)^{-1}\left(\mathbf{A}_{6x6}^{j}\right)^{-1}\mathbf{B}_{6x1}^{j}\left(D_{1x1}^{j}\right)^{-1} \qquad \textit{(A3. 12)}$$

$$G_{1x1}=\left(1-\left(D_{1x1}^{j}\right)^{-1}\mathbf{C}_{1x6}^{j}\left(\mathbf{A}_{6x6}^{j}\right)^{-1}\mathbf{B}_{6x1}^{j}\right)^{-1}\left(D_{1x1}^{j}\right)^{-1} \qquad \textit{(A3. 13)}$$

$$\mathbf{H}_{1x6}^{j}=\left(1-\left(D_{1x1}^{j}\right)^{-1}\mathbf{C}_{1x6}^{j}\left(\mathbf{A}_{6x6}^{j}\right)^{-1}\mathbf{B}_{6x1}^{j}\right)^{-1}\left(D_{1x1}^{j}\right)^{-1}\mathbf{C}_{1x6}^{j}\left(\mathbf{A}_{6x6}^{j}\right)^{-1} \quad \textit{(A3. 14)}$$

Equations (A3.9) and (A3.10) can be expressed in a more compact way as:

$$\left(-dS_r\right)=G_{1x1}^{j}ds^{*}+\mathbf{H}_{1x6}^{j}d\boldsymbol{\sigma}^{*} \quad \textit{(A3. 15)}$$

$$d\boldsymbol{\varepsilon}=\mathbf{E}_{6x6}^{j}d\boldsymbol{\sigma}^{*}+\mathbf{F}_{6x1}^{j}ds^{*} \quad \textit{(A3. 16)}$$

Inserting now (A3.15) into (A3.1) and (A3.16) into (A3.2) respectively:

$$d\boldsymbol{\sigma}^{*}=d\overline{\boldsymbol{\sigma}}+\mathbf{m}\left(S_r ds-s\left(G_{1x1}^{j}ds^{*}+\mathbf{H}_{1x6}^{j}d\boldsymbol{\sigma}^{*}\right)\right) \quad \textit{(A3. 17)}$$

$$ds^{*}=\frac{e}{1+e}ds-\frac{s}{1+e}\mathbf{m}^{T}\left(\mathbf{E}_{6x6}^{j}d\boldsymbol{\sigma}^{*}+\mathbf{F}_{6x1}^{j}ds^{*}\right) \quad \textit{(A3. 18)}$$

Re-arrenging in (A3.17):

$$d\boldsymbol{\sigma}^{*}=\left(\mathbf{I}_{6x6}+\mathbf{m}s\mathbf{H}_{1x6}^{j}\right)^{-1}\left(d\overline{\boldsymbol{\sigma}}+\mathbf{m}S_r ds-\mathbf{m}sG_{1x1}^{j}ds^{*}\right) \quad \textit{(A3. 19)}$$

Re-arrenging (A3.18):

$$ds^{*}=\left(1+\frac{s}{1+e}\mathbf{m}^{T}\mathbf{F}_{6x1}^{j}\right)^{-1}\left(\frac{e}{1+e}ds-\frac{s}{1+e}\mathbf{m}^{T}\mathbf{E}_{6x6}^{j}d\boldsymbol{\sigma}^{*}\right) \quad \textit{(A3. 20)}$$

Using now the following notation in the previous equations:

$$\overline{\mathbf{A}}_{6x6}^{j}=\left(\mathbf{I}_{6x6}+\mathbf{m}s\mathbf{H}_{1x6}^{j}\right)^{-1} \quad \textit{(A3. 21)}$$

$$\overline{B}_{1x1}^{j}=\left(1+\frac{s}{1+e}\mathbf{m}^{T}\mathbf{F}_{6x1}^{j}\right)^{-1} \quad \textit{(A3. 22)}$$

$$d\boldsymbol{\sigma}^{*}=\overline{\mathbf{A}}_{6x6}^{j}d\overline{\boldsymbol{\sigma}}+\overline{\mathbf{A}}_{6x6}^{j}\mathbf{m}S_r ds-\overline{\mathbf{A}}_{6x6}^{j}\mathbf{m}sG_{1x1}^{j}ds^{*} \quad \textit{(A3. 23)}$$

$$ds^{*}=\overline{B}_{1x1}^{j}\frac{e}{1+e}ds-\overline{B}_{1x1}^{j}\frac{s}{1+e}\mathbf{m}^{T}\mathbf{E}_{6x6}^{j}d\boldsymbol{\sigma}^{*} \quad \textit{(A3. 24)}$$

Inserting (A3.23) into (A3.24):

$$ds^* = \bar{B}^j_{1x1}\frac{e}{1+e}ds - \bar{B}^j_{1x1}\frac{s}{1+e}\mathbf{m}^T\mathbf{E}^j_{6x6}\left(\bar{\mathbf{A}}^j_{6x6}d\bar{\boldsymbol{\sigma}} + \bar{\mathbf{A}}^j_{6x6}\mathbf{m}sS_r ds - \bar{\mathbf{A}}^j_{6x6}\mathbf{m}sG^j_{1x1}ds^*\right) \quad \textit{(A3. 25)}$$

Inserting (A3.24) into (A3.23):

$$d\boldsymbol{\sigma}^* = \bar{\mathbf{A}}^j_{6x6}d\bar{\boldsymbol{\sigma}} + \bar{\mathbf{A}}^j_{6x6}\mathbf{m}sS_r ds - \bar{\mathbf{A}}^j_{6x6}\mathbf{m}sG^j_{1x1}\left(\bar{B}^j_{1x1}\frac{e}{1+e}ds - \bar{B}^j_{1x1}\frac{s}{1+e}\mathbf{m}^T\mathbf{E}^j_{6x6}d\boldsymbol{\sigma}^*\right) \quad \textit{(A3. 26)}$$

Re-arranging both previous equations it is possible to obtained the general final expression of $d\boldsymbol{\sigma}^*$ and ds^* in terms of the driven variables in terms of $d\bar{\boldsymbol{\sigma}}$ and ds.

$$ds^* = Q^j_{1x1}ds + \mathbf{W}^j_{6x1}d\bar{\boldsymbol{\sigma}} \quad \textit{(A3. 27)}$$

where,

$$Q^j_{1x1} = \left(1 - \bar{B}^j_{1x1}\frac{s}{1+e}\mathbf{m}^T\mathbf{E}^j_{6x6}\bar{\mathbf{A}}^j_{6x6}\mathbf{m}sG^j_{1x1}\right)^{-1}\left(\bar{B}^j_{1x1}\frac{e}{1+e} - \bar{B}^j_{1x1}\frac{s}{1+e}\mathbf{m}^T\mathbf{E}^j_{6x6}\bar{\mathbf{A}}^j_{6x6}\mathbf{m}S_r\right) \quad \textit{(A3. 28)}$$

$$\mathbf{W}^j_{1x6} = \left(1 - \bar{B}^j_{1x1}\frac{s}{1+e}\mathbf{m}^T\mathbf{E}^j_{6x6}\bar{\mathbf{A}}^j_{6x6}\mathbf{m}sG^j_{1x1}\right)^{-1}\left(-\bar{B}^j_{1x1}\frac{s}{1+e}\mathbf{m}^T\mathbf{E}^j_{6x6}\bar{\mathbf{A}}^j_{6x6}\right) \quad \textit{(A3. 29)}$$

$$d\boldsymbol{\sigma}^* = \mathbf{Y}^j_{6x6}d\bar{\boldsymbol{\sigma}} + \mathbf{Z}^j_{6x1}ds \quad \textit{(A3. 30)}$$

where,

$$\mathbf{Y}^j_{6x6} = \left(\mathbf{I}_{6x6} - \bar{\mathbf{A}}^j_{6x6}\mathbf{m}sG^j_{1x1}\bar{B}^j_{1x1}\frac{s}{1+e}\mathbf{m}^T\mathbf{E}^j_{6x6}\right)^{-1}\bar{\mathbf{A}}^j_{6x6} \quad \textit{(A3. 31)}$$

$$\mathbf{Z}^j_{6x1} = \left(\mathbf{I}_{6x6} - \bar{\mathbf{A}}^j_{6x6}\mathbf{m}sG^j_{1x1}\bar{B}^j_{1x1}\frac{s}{1+e}\mathbf{m}^T\mathbf{E}^j_{6x6}\right)^{-1}\left(\bar{\mathbf{A}}^j_{6x6}\mathbf{m}S_r - \bar{\mathbf{A}}^j_{6x6}\mathbf{m}sG^j_{1x1}\bar{B}^j_{1x1}\frac{e}{1+e}\right) \quad \textit{(A3. 32)}$$

APPENDIX A4

Appendix A4: Total stress in terms of strain and fluid pressure variations

In order to implement the Wheeler et al. (2003) constitutive model into CODE_BRIGHT it is useful to express some of the equations of this constitutive model in such a way that make them compatible with the current formulation of CODE_BRIGHT. In particular, it is convenient to express the total stress tensor variations in terms of strain and fluid pressure changes using the relationships proposed within the constitutive model. The mathematical development to find these expressions is detailed in the following.

Using the definition of Bishop's stresses given in Chapter 2, temporal variations of total stresses can be expressed as:

$$\dot{\boldsymbol{\sigma}} = \dot{\boldsymbol{\sigma}}^{*} + \mathbf{m}\dot{u}_g - \mathbf{m}\dot{S}_r\left(u_g - u_l\right) - \mathbf{m}S_r\left(\dot{u}_g - \dot{u}_l\right) \qquad \textit{(A4. 1)}$$

where ***m*** is the auxiliary vector (1,1,1,0,0,0), ***σ*** is the total stress tensor, ***σ**** is the Bishop's stress tensor, u_l and u_g are the liquid and gas pressures, respectively, and the upper dot indicates temporal variations.

Employing also the expression of the generalised constitutive stiffness matrix introduced in Chapter 5, the Bishop's stress changes can be expressed as:

$$\dot{\boldsymbol{\sigma}}^{*} = \mathbf{A}^{j}_{6x6}\dot{\boldsymbol{\varepsilon}} + \mathbf{B}^{j}_{1x6}\left(-\dot{S}_r\right) \qquad \textit{(A4. 2)}$$

where *j* indicates the elasto-plastic mechanism active, and ***A*** and ***B*** take the form shown in Appendix A.2.

On the other hand, temporal variations of degree of saturation can be expressed with an equivalent expression to the one developed in Chapter 6:

$$-\dot{S}_r = \left(D^j\right)^{-1}\left[\frac{e}{1+e}\left(\dot{u}_g - \dot{u}_l\right) + \left(\frac{-\left(u_g - u_l\right)}{1+e}\mathbf{m}^T - \mathbf{C}^j\right)\dot{\boldsymbol{\varepsilon}}\right] \qquad \textit{(A4. 3)}$$

where *T* indicates transposed, *j* indicates the elasto-plastic mechanism active, and *D* and ***C*** take the form shown in Appendix A.2.

Inserting (A4.2) into the general expression of the total stress tensor variations (A4.1):

$$\dot{\boldsymbol{\sigma}} = \mathbf{A}^{j}_{6x6}\dot{\boldsymbol{\varepsilon}} + \mathbf{B}^{j}_{1x6}\left(-\dot{S}_r\right) + \mathbf{m}\dot{u}_g - \mathbf{m}\dot{S}_r\left(u_g - u_l\right) - \mathbf{m}S_r\left(\dot{u}_g - \dot{u}_l\right) \qquad \textit{(A4. 4)}$$

Re-arranging:

$$\dot{\boldsymbol{\sigma}} = \mathbf{A}^{j}_{6x6}\dot{\boldsymbol{\varepsilon}} + \left(\mathbf{B}^{j}_{1x6} + \mathbf{m}\left(u_g - u_l\right)\right)\left(-\dot{S}_r\right) + \mathbf{m}\dot{u}_g - \mathbf{m}S_r\left(\dot{u}_g - \dot{u}_l\right) \qquad \textit{(A4. 5)}$$

Substituting now the variations of degree of saturation given by (A4.3) into (A4.5):

$$\dot{\boldsymbol{\sigma}} = \mathbf{A}^{j}_{6x6}\dot{\boldsymbol{\varepsilon}} + \left(\mathbf{B}^{j}_{1x6} + \mathbf{m}\left(u_g - u_l\right)\right)\left(\left(D^{j}\right)^{-1}\left[\frac{e}{1+e}\left(\dot{u}_g - \dot{u}_l\right) + \left(\frac{-\left(u_g - u_l\right)}{1+e}\mathbf{m}^{T} - \mathbf{C}^{j}\right)\dot{\boldsymbol{\varepsilon}}\right]\right) +$$

$$+\mathbf{m}\dot{u}_g - \mathbf{m}S_r\left(\dot{u}_g - \dot{u}_l\right) \qquad \textit{(A4. 6)}$$

Re-arranging terms, the following expression of the total stress temporal variations in terms of the temporal variations of strains and fluid pressures:

$$\dot{\boldsymbol{\sigma}} = \boldsymbol{\Lambda}_1\dot{\boldsymbol{\varepsilon}} + \boldsymbol{\gamma}_1\dot{u}_g + \boldsymbol{\gamma}_2\dot{u}_l \qquad \textit{(A4. 7)}$$

where the 6x6 matrix $\boldsymbol{\Lambda_1}$ and the 6x1 vectors $\boldsymbol{\gamma_1}$ and $\boldsymbol{\gamma_2}$ take the form:

$$\boldsymbol{\Lambda}_1 = \mathbf{A}^{j}_{6x6} + \left(\mathbf{B}^{j}_{1x6} + \mathbf{m}\left(u_g - u_l\right)\right)\left(D^{j}\right)^{-1}\left(\frac{-\left(u_g - u_l\right)}{1+e}\mathbf{m}^{T} - \mathbf{C}^{j}\right) \qquad \textit{(A4. 8)}$$

$$\boldsymbol{\gamma}_1 = \left(\mathbf{B}^{j}_{1x6} + \mathbf{m}\left(u_g - u_l\right)\right)\left(D^{j}\right)^{-1}\frac{e}{1+e} + \mathbf{m} - \mathbf{m}S_r \qquad \textit{(A4. 9)}$$

$$\boldsymbol{\gamma}_2 = -\left(\mathbf{B}^{j}_{1x6} + \mathbf{m}\left(u_g - u_l\right)\right)\left(D^{j}\right)^{-1}\frac{e}{1+e} + \mathbf{m}S_r \qquad \textit{(A4. 10)}$$